



Norwegian University of  
Science and Technology

# Fatigue Properties of Corrugated Sheathing for Subsea Power Cables

**Bjørnar Fugløy**

Mechanical Engineering

Submission date: June 2017

Supervisor: Odd Magne Akselsen, MTP

Norwegian University of Science and Technology  
Department of Mechanical and Industrial Engineering



## Abstract

A high voltage subsea power cable consists of several different layers with different purposes. One layer is a metallic tubular sheathing with the main purpose to act as a moisture-blocking barrier to prevent moisture ingress towards the cable core. Unlike a static cable, which normally utilizes a smooth tubular sheathing, the dynamic cable is exposed to various hanging configurations and fatigue loading. Hence, a need for a more flexible but also fatigue resistant sheathing has arose. Thus, metallic corrugated tubular sheathing (MCTS) has been introduced as a candidate, due to high flexibility, good mechanical strength and favourable fatigue resistant.

This master thesis investigates, on commission from Nexans, a MCTS with respect to how various geometrical parameters, that is corrugation pitch ( $P$ ), amplitude ( $A$ ), sheath thickness ( $t$ ) and helical inclination angle influences the developed strain along the corrugation geometry. The obtained results can be utilized as a parameter to predict the MCTS fatigue properties.

In this thesis, the MCTS was 3D modelled and parametrized, thereafter a finite element approach was utilized to expose the MCTS models to static axial and bending analysis and quasi-static four-point bending analysis. Variations in local geometry parameters were analysed and evaluated based on developed strain. When changing the different geometrical parameters, variations in developed strain occurred. Local developed strain values were further compared to global strain values obtained by exposing a smooth tubular sheathing to similar boundary conditions as the corrugated models.

Finite element analysis (FEA) indicated that the most suitable corrugation geometry for fatigue life based on global and local strain development fields in the corrugation was a MCTS inherent with a thin wall thickness, a low  $P/A$  ratio and a high  $A$ -value. Considering the most suitable corrugation wave pattern, the FEA indicated that both annular and helical were favourable. However, if selecting a helical wave pattern, the helical inclination angle should remain small, due to the presence of a relatively high shear strain sensitivity when introducing a helical wave pattern.

A prime design example considering fatigue life, based on the FEA results, may be a MCTS comprising of  $t = 0.7\text{mm}$ ,  $P/A = 2.0$ ,  $A = 5.0\text{mm}$  and a corrugation geometry holding either an annular or helical wave pattern, where the helical pattern should hold a low inclination angle.



## Sammendrag

En undervanns høyspent strømkabel er inndelt i forskjellige lag, hvor hvert lag utøver et spesielt formål. Ett av disse lagene er en metallisk tynnvegget rørformet kledning med den hensikt å operere som en fuktighetsbarriere, hvor fukt hindres i å komme i kontakt med kabelkjernen. I motsetning til en statisk kabel, som normalt benytter en rett og jevn rørformet kledning, blir den dynamiske kabelen utsatt for ulike hengende konfigurasjoner og utmatting. Det har derfor oppstått et behov for en mer fleksibel, men samtidig utmattingsresistent kledning. Dette har ført til at metallisk korrugert rørformet kledning (MKRK) har blitt introdusert som en mulig kandidat, hovedsakelig på grunn av dens høye fleksibilitet, mekaniske styrke og gode utmattingssegenskaper.

Denne masteroppgaven undersøker, på oppdrag fra Nexans, MKRK med hensyn til hvordan ulike geometriske parametere, det vil si amplituden (A) og lengden (P) på hver enkelt korrugering, veggtykkelse (t), og innvirkningen en spiralformet korrugering med stigningsvinkel har med hensyn til utviklet tøyning langs kledningens overflate. De oppnådde tøyningresultatene kan benyttes som en parameter til å forutsi utmattingssegenskapene til MKRK.

MKRK ble 3D modellert og parametrisert, før simuleringer ved hjelp av elementmetoden ble benyttet til å utsette MKRK-modellene for statisk aksial- og bøyingsanalyse etterfulgt av kvasistatisk firepunkts bøyingsanalyse. Variasjoner i lokale geometriske parametere ble analysert og evaluert med hensyn til utviklet tøyning. Lokale utviklede tøyingsverdier ble deretter sammenlignet med globale tøyingsverdier innhentet fra en rett jevn rørformet kledning utsatt for samme type grensebetingelser og forskyvninger som de korrugerte modellene.

Elementanalysene indikerte at den mest hensiktsmessige korrugeringsgeometrien med hensyn til utmatting, basert på lokal og global tøyingsutvikling i korrugeringsgeometrien, var en MKRK med tynn veggtykkelse, et lavt P/A forhold og en høy A-verdi. Videre indikerte elementanalysene at både en ringformet og en spiralformet bølgeform var gunstig med tanke på utmatting. Imidlertid bør en spiralformet bølgeform inneha en lav stigningsvinkel, siden andelen utviklet skjærtøyning viste seg å være nokså høy og lineært stigende ved økende stigningsvinkel. Et utmerket designeksempel med hensyn til utmatting, basert på resultatene fra elementanalysene, kan være en MKRK bestående av  $t = 0.7\text{mm}$ ,  $P/A = 2.0$ ,  $A = 5.0\text{mm}$  og et ringformet eller spiralformet bølgemønster med en iboende lav stigningsvinkel.



## Preface

This report is the result of the master's thesis accomplished during the spring 2017 at the Norwegian University of Science and Technology of the 2-year master program at the Department of Mechanical and Industrial Engineering (MTP). The master thesis is weighted 30 credits and is a continuation of the pre-project thesis accomplished during the third semester.

This master thesis is written for the Department of Mechanical and Industrial Engineering in collaboration with Nexans and SINTEF. The report describes the possible usage of metallic tubular corrugated sheathing (MCTS) within a high voltage dynamic subsea power cable. The main objective has been to investigate the MCTS behaviour when exposed to controlled axial and bending analysis, and how variation of geometrical parameters influences developed strain along the corrugated geometry, which again can be used as a parameter to predict its fatigue properties.

Prior of this thesis I had minor experience and knowledge with the software's NX and ABAQUS, which, respectively, was the modelling- and simulation programs utilized to make the corrugated geometry and perform the axial and bending analysis through a finite element approach. A large amount of time has therefor been used to familiarize oneself with this two software's and utilize them in a satisfactory manner.

Working with both the 3D modelling and FEA in this thesis has been challenging and a trial of patience. Thus, a great number of trial and error and hours spent, lies behind the obtained results in this thesis. The 3D modelling was especially challenging due to the complex geometry created by the corrugation and the later introduction of helical inclination. The FEA was mainly challenging due to the small amount of personal computer resources available considering the complex geometry and often large models required. Also, this topic had never been investigated by SINTEF before, leading to a path of research which had to be mapped while walked.

Trondheim, 25.06.2017



Bjørnar Fugløy





## Acknowledgement

This master's thesis has been an adventure from start to finish. I have been given the opportunity to specialize myself within advanced non-linear finite element analysis, and simultaneously explore and research the significance of adding corrugation to a metallic tube with respect to its fatigue properties.

First I would like to express my gratitude to my main technical advisor, Research Scientist Antonio Alvaro at SINTEF Material and Chemistry at the Department of Materials and Nanotechnology. He has always been available for technical discussions related to the research or technical approach in the thesis, although he had paternity leave most of the time.

I would also like to thank my other supervisors at SINTEF Material and Chemistry at the Department of Materials and Nanotechnology for valuable technical discussions, advices and technical input throughout this thesis. They have all been available and interested in solving any type of problem encountered during the thesis. These supervisors comprise of Senior Research Specialist Bård Nyhus, Senior Engineer Vidar Osen and Senior Research Scientist Odd Mange Akselsen.

I would also like to express my gratitude towards Professor Sigmund Kyrre Ås, at the Department of Marine Technology at NTNU, who was so accommodating performing X-ray diffraction measurements on behalf of me and my thesis.

I would also like to thank the company Nexans for the opportunity to work with this thesis. Finally, I would like to thank my supervisor in Nexans, Research and Development Metallurgist Audun Johanson, for his technical inputs and prime collaboration throughout the thesis.

It has been a thoroughly pleasure to work with and explore the field of Dynamic High Voltage Subsea Power Cables and the technical topic: *Corrugated Sheathing*.



# Table of contents

<b>1</b>	<b>INTRODUCTION.....</b>	<b>1</b>
1.1	BACKGROUND AND MOTIVATION.....	1
1.2	PROBLEM DESCRIPTION.....	2
1.3	PROJECT SCOPE.....	3
1.3.1	<i>Objectives</i> .....	3
1.4	THESIS STRUCTURE.....	4
<b>2</b>	<b>HIGH VOLTAGE SUBMARINE POWER CABLES .....</b>	<b>7</b>
2.1	GENERAL.....	7
2.1.1	<i>Static Cables</i> .....	7
2.1.2	<i>Dynamic Cables</i> .....	7
2.2	TYPES AND STRUCTURE.....	10
2.2.1	<i>HVAC and HVDC</i> .....	10
2.2.2	<i>Cable Layering</i> .....	11
2.3	METALLIC CORRUGATED TUBULAR SHEATHING WITHIN A DYNAMIC HV SUBMARINE POWER CABLE.....	14
2.3.1	<i>Usage</i> .....	14
2.3.2	<i>Lead Sheath</i> .....	15
2.3.3	<i>Aluminium Sheath</i> .....	15
2.3.4	<i>Copper Sheath</i> .....	15
2.3.5	<i>Stainless Steel Sheath</i> .....	16
2.3.6	<i>Corrugation shapes</i> .....	16
2.3.7	<i>Corrugation Profile Definition</i> .....	17
2.3.8	<i>Corrugation Effects</i> .....	17
2.4	NEXANS PRODUCTION LINE FOR SHEATHING OF SUBMARINE POWER CABLE.....	19
2.4.1	<i>UNIWEMA® HV</i> .....	19
2.4.2	<i>Corrugation Unit</i> .....	20
2.4.3	<i>Technical Data</i> .....	21
<b>3</b>	<b>MATERIAL BEHAVIOUR OF A METALLIC CORRUGATED TUBULAR SHEATHING.....</b>	<b>23</b>
3.1	STRESS.....	23
3.1.1	<i>Cauchy Stress Tensor</i> .....	23
3.1.2	<i>Principal Stress</i> .....	24
3.2	STRAIN.....	25

3.2.1	<i>Logarithmic Strain</i> .....	25
3.2.2	<i>Principal Strain</i> .....	26
3.3	STRAIN HARDENING.....	27
3.3.1	<i>Isotropic</i> .....	27
3.3.2	<i>Kinematic</i> .....	27
<b>4</b>	<b>LOAD IMPACT AND FATIGUE OF METALLIC CORRUGATED TUBULAR SHEATHING</b> .....	<b>29</b>
4.1	GLOBAL BEHAVIOUR .....	29
4.2	MINIMUM BENDING RADIUS .....	30
4.3	DYNAMICAL BENDING, AXIAL AND FRICTION FORCES .....	31
4.3.1	<i>Friction Reducing Layer</i> .....	32
4.4	HYDROSTATIC PRESSURE.....	33
4.4.1	<i>Hoop Stress</i> .....	34
4.5	STRESS AND STRAIN COMPONENT SIGNS .....	38
4.6	FATIGUE .....	40
4.6.1	<i>Fatigue Loads</i> .....	40
4.6.2	<i>Fatigue Resistance</i> .....	40
4.6.3	<i>Strain-based Fatigue Approach</i> .....	40
4.6.4	<i>Strain vs Life Curves</i> .....	40
4.7	RESIDUAL STRESSES .....	42
4.7.1	<i>Welding</i> .....	44
4.7.2	<i>Cold Working</i> .....	45
4.7.3	<i>Stress Relief</i> .....	46
4.7.4	<i>Measurement – X-ray Diffraction</i> .....	46
<b>5</b>	<b>EXPERIMENTAL WORK</b> .....	<b>51</b>
5.1	MATERIAL AND GEOMETRICAL CHARACTERIZATION OF TEST TUBES .....	51
5.2	X-RAY DIFFRACTION .....	54
<b>6</b>	<b>FINITE ELEMENT METHOD – THEORY AND UTILIZED TOOLS</b> .....	<b>57</b>
6.1	SOFTWARE .....	57
6.1.1	<i>NX</i> .....	57
6.1.2	<i>Abaqus FEA</i> .....	57
6.2	GENERAL.....	58
6.2.1	<i>Governing Equations</i> .....	58
6.3	NONLINEAR FEM.....	59

6.4	ELEMENTS .....	61
6.4.1	<i>General-Purpose Conventional Shell Elements</i> .....	61
6.4.2	<i>Reduced Integration</i> .....	62
6.4.3	<i>Hourglassing</i> .....	62
6.5	MULTIPOINT CONSTRAINT .....	64
6.6	CONTACT INTERACTION.....	65
6.7	ABAQUS/STANDARD VS ABAQUS/EXPLICIT .....	67
6.7.1	<i>Time Integration</i> .....	67
6.7.2	<i>Explicit – Stability</i> .....	68
6.7.3	<i>Explicit – Energy Balance</i> .....	69
6.8	QUASI-STATIC ANALYSIS IN ABAQUS/EXPLICIT .....	70
6.8.1	<i>Load Rate</i> .....	70
6.8.2	<i>Modal Analysis</i> .....	71
<b>7</b>	<b>FINITE ELEMENT METHOD – PRE-PROCESSING, EVALUATION AND SIMULATION.....</b>	<b>73</b>
7.1	3D MODEL – ANNULAR METALLIC CORRUGATED TUBULAR SHEATHING .....	73
7.1.1	<i>Parametrization</i> .....	73
7.2	3D MODEL – HELICAL METALLIC CORRUGATED TUBULAR SHEATHING .....	75
7.2.1	<i>Parametrization</i> .....	75
7.3	UNITS .....	78
7.4	MATERIAL MODELS .....	79
7.4.1	<i>X70 Steel</i> .....	79
7.4.2	<i>AISI316</i> .....	79
7.4.3	<i>XLPE</i> .....	80
7.4.4	<i>Strain Hardening Model</i> .....	80
7.5	STATIC AXIAL ANALYSIS.....	81
7.5.1	<i>Design Input</i> .....	82
7.5.2	<i>Boundary conditions</i> .....	82
7.5.3	<i>Mesh</i> .....	83
7.6	STATIC BENDING ANALYSIS .....	85
7.6.1	<i>Design input</i> .....	85
7.6.2	<i>Boundary Conditions</i> .....	86
7.6.3	<i>Mesh</i> .....	88
7.7	QUASI-STATIC FOUR-POINT BENDING ANALYSIS .....	91
7.7.1	<i>Design Input</i> .....	91
7.7.2	<i>Modal Analysis</i> .....	91

7.7.3	<i>Boundary Conditions</i> .....	92
7.7.4	<i>Contact</i> .....	95
7.7.5	<i>Mesh</i> .....	95
<b>8</b>	<b>X-RAY DIFFRACTION – RESULTS.....</b>	<b>97</b>
8.1	TUBE (1 – 2).....	97
8.1.1	<i>Welding Seam – Residual Stresses at Wave Crest Top</i> .....	97
8.1.2	<i>Weld-free Areas – Residual Stresses at Wave Crest Top</i> .....	99
8.2	TUBE (2 – 2).....	101
8.2.1	<i>Welding Seam – Residual Hoop and Shear Stresses at Wave Crest and Wave Trough</i>	101
8.2.2	<i>Weld-free Areas – Residual Hoop and Shear Stresses at Wave Crest Top</i> .....	106
<b>9</b>	<b>FINITE ELEMENT METHOD – POSTPROCESSING AND RESULTS.....</b>	<b>109</b>
9.1	STATIC AXIAL ANALYSIS.....	109
9.1.1	<i>Strain Development</i> .....	109
9.1.2	<i>Wave Crest vs Wave Trough</i> .....	110
9.1.3	<i>Thickness Sensitivity</i> .....	110
9.1.4	<i>Amplitude Sensitivity</i> .....	111
9.1.5	<i>Reaction Force</i> .....	114
9.1.6	<i>Diameter Variation</i> .....	115
9.1.7	<i>Helical Inclination Angle Sensitivity</i> .....	116
9.2	STATIC BENDING ANALYSIS.....	117
9.2.1	<i>Strain Development</i> .....	117
9.2.2	<i>Helical Inclination Angle Sensitivity</i> .....	121
9.2.3	<i>Shear Strain Sensitivity</i> .....	122
9.2.4	<i>Ovality</i> .....	123
9.3	QUASI-STATIC FOUR-POINT BENDING.....	124
9.3.1	<i>Static Bending Analysis</i> .....	124
9.3.2	<i>Modal Analysis</i> .....	125
9.3.3	<i>Strain Development without Insulation</i> .....	127
9.3.4	<i>Strain development with insulation</i> .....	129
9.3.5	<i>Force-Displacement</i> .....	133
9.3.6	<i>Internal vs Kinetic Energy</i> .....	135
<b>10</b>	<b>DISCUSSION .....</b>	<b>139</b>
10.1	EXPERIMENTAL WORK.....	139
10.1.1	<i>Choice of Measurement Technique</i> .....	139
10.1.2	<i>Measurement Results</i> .....	140

10.2	STATIC AND QUASI-STATIC ANALYSIS.....	143
10.2.1	<i>Static Axial analysis</i> .....	143
10.2.2	<i>Static Bending Analysis</i> .....	144
10.2.3	<i>Quasi-Static Four-Point Bending Analysis</i> .....	146
<b>11</b>	<b>CONCLUSION AND FURTHER WORK .....</b>	<b>149</b>
11.1	CONCLUSION.....	149
11.2	FURTHER WORK.....	151
<b>12</b>	<b>BIBLIOGRAPHY .....</b>	<b>153</b>
<b>APPENDIX A</b>	<b>RISK ASSESSMENT.....</b>	<b>157</b>
<b>APPENDIX B</b>	<b>TUBE SPECIMENS.....</b>	<b>161</b>
<b>APPENDIX C</b>	<b>UTILIZED X-RAY DIFFRACTION PARAMETERS .....</b>	<b>163</b>
<b>APPENDIX D</b>	<b>X-RAY DIFFRACTION RESULTS.....</b>	<b>165</b>





# List of Figures

Figure 1: Bending stiffener [2]..... 7

Figure 2: Various dynamic HV submarine power cable hanging configurations [4] ..... 8

Figure 3: Parameters exposing a dynamic HV submarine power cable after installation [3].... 9

Figure 4: Static HV submarine power cable - HVDC (left) [10] and HVAC (right) [11]..... 11

Figure 5: Dynamic HV submarine power cables with corrugated sheathing [11] ..... 14

Figure 6: An annular pattern to the left and a helical pattern to the right ..... 16

Figure 7: Corrugation profile definition..... 17

Figure 8: UNIWEMA® HV manufacturing layout [19]..... 19

Figure 9: Forming table [19] ..... 19

Figure 10: Welding station [19] ..... 20

Figure 11: Split clam caterpillar capstan [19] ..... 20

Figure 12: Corrugation unit [19] ..... 21

Figure 13: The stress components acting on a solid 3D infinite small element [22] ..... 24

Figure 14: The effect of an isotropic strain hardening on the yield locus [27] ..... 27

Figure 15: The effect of a kinematic strain hardening on the yield locus [27] ..... 28

Figure 16: Dislocation pile-up [22]..... 28

Figure 17: Global axial displacement..... 29

Figure 18: Global tube bending..... 29

Figure 19: Minimum bending radius..... 30

Figure 20: Wall element of a pressurized thin-walled cylinder [32]..... 35

Figure 21: Free body diagram of a thin-walled pressurized cylinder [32]..... 36

Figure 22: Stress through the MCTS wall thickness including bending stress ( $\sigma_b$ ) and membrane stress ( $\sigma_m$ ) ..... 39

Figure 23: Elastic, plastic and total strain amplitudes vs number of cycles N [35] ..... 41

Figure 24: Mean stress effect [15]..... 41

Figure 25: Force and moment equilibrium on a cut *AB* through a material [22]..... 42

Figure 26: Residual stresses within grains in a polycrystalline material deformed plastically during tensile loading [22] .....	43
Figure 27: Heat source and three distinct weldment regions in a fusion weld, that is FZ, HAZ and BM [36] .....	44
Figure 28: Typical residual stress pattern in a welded plate [22].....	45
Figure 29: Residual stress pattern after plastically sheet bending [26].....	45
Figure 30: Residual stresses that might arise from the corrugation cold forming process .....	46
Figure 31: X-ray diffraction of crystallographic planes characterized by Bragg’s law of reflection [37].....	47
Figure 32: Visualization of measured global geometrical test tube parameters .....	53
Figure 33: X-ray diffraction measurements performed by Professor Sigmund Kyrre Ås at the Department of Marine Technology at NTNU .....	54
Figure 34: Residual stress components acting in a MCTS wall element based on cylindrical coordinate directions .....	55
Figure 35: Tube (1 – 2) seen from the front.....	56
Figure 36: Tube (2 – 2) seen from the front.....	56
Figure 37: FEA process [42] .....	57
Figure 38: S4R element [24] .....	61
Figure 39: S3R element [24] .....	62
Figure 40: Shear locking of a fully integrated linear element [24] .....	63
Figure 41: Hourglassing of a first order reduced integration element [24].....	63
Figure 42: General contact [24] .....	65
Figure 43: Contact pairs [24] .....	66
Figure 44: Typical 3D model view of an annular MCTS .....	73
Figure 45: NX tool “Expressions” enabling the parametrization of the annular MCTS 3D model.....	74
Figure 46: Typical 3D model view of a helical MCTS.....	75
Figure 47: Helix inclination angle (lead angle) [45] .....	76

Figure 48: NX tool “Expressions” enabling the parametrization of the helical MCTS 3D model.....	76
Figure 49: Visualization of a helical MCTS, untrimmed in one end, and at its lowest possible inclination angle, that is a lead distance comprising of $(1 \cdot P)$ .....	77
Figure 50: Visualization of a helical MCTS, untrimmed in one end, and at its highest possible inclination angle analysed within this thesis, that is a lead distance comprising of $(7 \cdot P)$ .....	77
Figure 51: Material curve X70 steel.....	79
Figure 52: Bilinear material models of AISI316L and AISI316L+Ti .....	80
Figure 53: Axial displacement boundary conditions.....	83
Figure 54: S4R mesh for $P=21\text{mm}$ and $A=3\text{mm}$ . .....	84
Figure 55: MPC beam constraint with one master node in the centre and slave nodes around the end perimeter of the MCTS .....	86
Figure 56: Method and model for calculating the required forced angular displacement .....	88
Figure 57: Global dimensions utilized for the four-point bending model.....	93
Figure 58: Tube zsymmetry and boundary conditions for the rolls .....	93
Figure 59: Tube ysymmetry .....	94
Figure 60: Smooth amplitude and boundary condition allocator .....	94
Figure 61: MCTS filled with insulation .....	95
Figure 62: Typical S4R mesh for a smooth version of tube (1 – 5 and (2 – 1) exposed to four-point bending.....	96
Figure 63: Typical S4R mesh for the corrugated version of tube (1 – 5) and (2 – 1) exposed to four-point bending.....	96
Figure 64: Visualization of 9 o’clock area in tube (1 – 2) where X-ray diffraction measurements were performed in and around the welding seam.....	98
Figure 65 X-ray diffraction measurements of residual stresses at wave crest top at the welding seam at 9 o’clock in tube (1 – 2) .....	98
Figure 66: Visualization of 1, 3 and 6 o’clock area in tube (1 – 2) where X-ray diffraction measurements were performed.....	100

Figure 67: X-ray diffraction measurements of residual stresses in tube (1 – 2) at wave crest top at 1, 3 and 6 o'clock .....	100
Figure 68: Visualization of 12 o'clock area in tube (2 – 2) where X-ray diffraction measurements were performed in and around the welding seam.....	102
Figure 69: X-ray diffraction measured residual hoop and shear stresses at wave crest top at the welding seam at 12 o'clock in tube (2 – 2) .....	102
Figure 70: X-ray diffraction measurements of residual hoop and shear stresses at wave trough overside at the welding seam at 12 o'clock in tube (2 – 2).....	104
Figure 71: X-ray diffraction measurements of residual axial and shear stresses at wave trough overside at the welding seam at 12 o'clock in tube (2 – 2).....	105
Figure 72: Visualization of 3, 6 and 9 o'clock area in tube (2 – 2) where X-ray diffraction measurements were performed.....	107
Figure 73: X-ray diffraction measurements of residual hoop and shear stresses at wave crest top at 3, 6 and 9 o'clock in tube (2 – 2) .....	107
Figure 74: X-ray diffraction measurements of residual hoop and shear stresses at wave trough overside at 3, 6 and 9 o'clock in tube (2 – 2).....	108
Figure 75: Elastic strain field development view for $A=3.0$ mm, $P=21.0$ mm and $t=0.7$ mm	109
Figure 76: Plastic strain development view for $A=3.0$ mm, $P=21.0$ mm and $t=0.7$ mm .....	109
Figure 77: A comparison of corrugation strain development (tensile side) at wave crest and wave trough area when varying the $P/A$ ratio at a constant thickness equal $0.7$ mm .....	110
Figure 78: Corrugation thickness sensitivity at the wave crest area (tensile side). The figure compares the strain ratio, that is the wave crest strain (tensile side) to the smooth tubular sheath strain, for different sheath thicknesses, at a $P/A$ ratio varying between 1 – 7 and a constant $A = 3$ mm.....	111
Figure 79: Local corrugation amplitude sensitivity at the wave crest area (tensile side) for a constant thickness equal $0.7$ mm. The figure compares the strain ratio, that is the wave crest strain (tensile side) to the smooth tubular sheath strain, at a $P/A$ ratio varying between 1 – 7 at three different $A$ -values.....	112

Figure 80: Global amplitude sensitivity, at a constant thickness equal 0.7mm. The figure when plots the ratio of maximum axial reaction force (RF), pushed back from the MCTS, to the maximum axial RF in a smooth tubular sheathing, against different P/A ratios. .... 113

Figure 81: Developed reaction force vs global nominal strain for a constant A=3mm and t=0.7mm ..... 114

Figure 82: Change of MCTS inner diameter due to axial displacement ..... 115

Figure 83: Helical inclination angle sensitivity. The plot shows how the helical inclination sensitivity alters with increasing inclination angle during axial displacement for a P/A ratio equal 2 and 7 with a constant thickness equal 0.6mm. .... 116

Figure 84: Visualization of the global tension/compression side in a MCTS during bending, and localization of the wave crest and wave trough areas along the corrugation geometry. + indicate the area of tensile strain and stress during forced angular displacement..... 117

Figure 85: Comparison of maximum tensile strain path values along the tubes global tension or compression side, during bending. The strain values are obtained at each wave crest or wave trough, along either the global tension side or global compression side, depending on where the highest tensile strains are localized. The plot compares P/A=2 (A=5mm) and P/A=7 (A=3mm), at a constant thickness equal 0.6mm and with varying inclination angles..... 118

Figure 86: A comparison of vertical displacement at the middle of the MCTS models during forced angular displacement. The compared models are P/A=2 (A=5mm) and P/A=7 (A=3mm), with varying inclination angles at a constant thickness equal 0.6mm. .... 120

Figure 87: A visualization of the MCTS helical inclination sensitivity when exposed to forced angular displacement. The compared models are P/A=2 (A=5mm) and P/A=7 (A=3mm), with varying inclination angles and a constant thickness equal 0.6mm..... 121

Figure 88: The ratio of shear strain at the area of maximum total true strain, at the middle of the MCTS models exposed to forced angular displacement. The compared models in the plot are P/A=2 (A=5mm) and P/A=7 (A=3mm), with varying inclination angles and a constant thickness equal 0.6mm. .... 122

Figure 89: Ovality measurement ..... 123

Figure 90: Tube (1 – 5) exposed to static bending analysis ..... 124

Figure 91: Tube (2 – 1) exposed to static bending analysis ..... 125

Figure 92: Tube (1 – 5) at a vertical deflection of 29mm caused by four-point bending ..... 127

Figure 93: Tube (2 – 1) at a vertical deflection of 59mm caused by four-point bending .....	127
Figure 94: Smooth tubular version of tube (1 – 5) at a vertical deflection of 29mm caused by four-point bending.....	128
Figure 95: Smooth tubular version of tube (2 – 1) at a vertical deflection of 59mm caused by four-point bending.....	129
Figure 96: Tube (1 – 5) at a vertical deflection of 29mm caused by four-point bending .....	130
Figure 97: Tube (2 – 1) at a vertical deflection of 59mm caused by four-point bending .....	131
Figure 98: Smooth version of tube (1 – 5) including an internal insulation, not visualized, at a vertical deflection of 29mm caused by four-point bending .....	132
Figure 99: Smooth version of tube (2 – 1) including an internal insulation, not visualized, at a vertical deflection of 59mm caused by four-point bending. ....	132
Figure 100: Force-displacement curves for tube (1 – 5), extracted from the quasi-static four-point bending analysis.....	133
Figure 101: Force-displacement curves for tube (2 – 1), extracted from the quasi-static four-point bending analysis.....	134
Figure 102: Kinetic energy (ALLKE) in tube (1 – 5) vs Internal energy (ALLIE) in tube (1 – 5), extracted from the quasi-static four-point bending analysis. ....	136
Figure 103: Kinetic energy (ALLKE) in tube (2 – 1) vs Internal energy (ALLIE) in tube (2 – 1), extracted from the quasi-static four-point bending analysis. ....	137
Figure 104: Kinetic energy (ALLKE) in smooth version of tube (1 – 5) vs Internal energy (ALLIE) in smooth version of tube (1 – 5), extracted from the quasi-static four-point bending analysis.....	138
Figure 105: Possible local residual stress pattern along the corrugation geometry in a MCTS exposed to a global moment causing a permanent global bended curvature, causing local plasticity along the corrugation geometry. – indicate compressive residual stress while + indicate tensile residual stress. ....	142
Figure 106: Suggested set-up of full-scale fatigue testing .....	152

# List of Tables

Table 1: Parameters influencing the mechanical loading of a dynamic HV submarine power cable after installation [3]..... 9

Table 2: The purpose of the various HV submarine power cable layers [9]..... 12

Table 3: Recent Norwegian offshore projects, Gjøa [3] and Goliat [12], including a dynamic HV submarine power cable and utilization of a MCTS ..... 14

Table 4: Technical sheet UNIWEMA® HV [19] ..... 21

Table 5: Minimum bending diameter..... 30

Table 6: Thin-walled pressure vessel assumptions [32]..... 37

Table 7: Signs for axial/bending stress/strain components. Tensile is indicated by +, and compression is indicated by -..... 38

Table 8: A summarized comparison of some of the most common methods utilized for residual stress measurement of metallic materials [40, 41] ..... 48

Table 9: Material properties of test tubes..... 52

Table 10: Local geometrical parameters for the delivered test tubes..... 52

Table 11: Global geometrical test tube measurements..... 53

Table 12: Stress verification of the performed X-ray diffraction measurements..... 55

Table 13: Comparison of the typical nonlinearities exposing a structure and/or its assembly [43] ..... 59

Table 14: Energy definitions in Abaqus [24] ..... 69

Table 15: Utilized unit-system during the FEA process in Abaqus..... 78

Table 16: X70 elastic properties and density ..... 79

Table 17: Material properties for the various AISI316-materials obtained from Nexans ..... 80

Table 18: XLPE elastic material properties [46-48] ..... 80

Table 19: Assumptions and choices made for the axial analysis ..... 81

Table 20: Design input for the axial analysis of the MCTS..... 82

Table 21: Typical mesh properties for one quarter of the MCTS during axial analysis ..... 83

Table 22: Design input bending analysis ..... 85

Table 23: Design input with respect to variation of inclination angle (lead angle) .....	85
Table 24: Calculated required angular displacement .....	87
Table 25: Description of mesh properties for some of the MCTS models exposed to bending analysis .....	89
Table 26: Visualization of mesh properties for some of the MCTS models exposed to static bending analysis .....	89
Table 27: Maximum load rates (minimum time periods) .....	92
Table 28: Calculated required angular displacement of test tubes .....	92
Table 29: Typical mesh properties utilized for the various models exposed to four-point bending analysis .....	96
Table 30: Arithmetic mean residual stress ratio [%] of material yield strength at wave crest top at 1, 3 and 6 o'clock in tube (1 – 2) .....	101
Table 31: Arithmetic mean residual hoop and shear stress ratio [%] of the material yield strength at the wave crest top at 12 o'clock in tube (2 – 2).....	103
Table 32: Arithmetic mean residual axial and shear stress ratio [%] of the material yield strength at the welding seam at the wave crest top at 12 o'clock in tube (2 – 2).....	106
Table 33: Summarized findings from Figure 79 .....	112
Table 34: Summarized findings from Figure 80 .....	113
Table 35: Summarized findings from Figure 82 .....	115
Table 36: Visualization of strain development fields, caused by forced angular displacement, in helical MCTSs with a constant thickness equal 0.6mm and a P/A=2 (A=5mm) and P/A=7 (A=3mm). The visualized models are half longitudinal sections relative to the original length, that is from the right end towards the middle of the MCTS. ....	119
Table 37: Modal analysis results .....	125
Table 38: Selected load rates and computational time for the quasi-static bending analysis	135



## Abbreviations

AC	Alternating Current
AISI	American Iron and Steel Institute
ALLIE	Internal Energy (for a selected part in Abaqus)
ALLKE	Kinetic Energy (for a selected part in Abaqus)
AMS	Automatic Multi-level Substructuring
BC	Boundary Condition
BM	Base Metal
CAD	Computer-Aided Design
Comp. side	Compression side
DC	Direct Current
Deg	Degree (Angle)
DOF	Degree of Freedom
FBD	Free-Body Diagram
FEA	Finite Element Analysis
FEM	Finite Element Method
FPSO	Floating Production, Storage and Offloading
FZ	Fusion Zone
HAZ	Heat Affected Zone
HV	High Voltage
HVAC	High Voltage alternating Current
HVDC	High Voltage Direct Current
LE	Logarithmic strain (Abaqus notation)

LE <sub>12</sub>	Logarithmic shear strain (Abaqus notation)
MCTS	Metallic Corrugated Tubular Sheathing
MBD	Minimum bending diameter
MPC	Multipoint Constraint
No.	Number
No. of WL within HL	Number of wavelengths within helix lead
PE	PolyEthylene
PLM	Product Lifecycle Management
PVC	Polyvinylchloride
RBE	Rigid Body Element
RF	Reaction Force
RPM	Revolutions Per Minute
SINTEF	Stiftelsen for Industriell og Teknisk Forskning (The Foundation for Scientific and Industrial Research)
Ti	Titanium
TIG	Tungsten inert gas
UNIWEMA	UNIversal WElding Machine
ViV	Vortex induced Vibration
XLPE	Cross-Linked PolyEthylene

## Nomenclature

Symbol	Unit	Description
$A$	mm	Amplitude
$A$	mm <sup>2</sup>	True cross-sectional area
$A_o$	mm <sup>2</sup>	Original cross-sectional area
$a$	mm	Circular helix radius
$b$		Defines the slope ( $b/a$ ) of a circular helix
<b>C</b>		Damping matrix
$c$		Denotes the middle line, in a general sine function, where the sine curve fluctuates around
$C_d$	m/s	Acoustic wave speed in a material
$D$	mm	Corrugation depth
$D$	m	Estimated deflection in the impact direction (for calculating impact velocity for a quasi-static FEA)
$D_i$	mm	Inner diameter tubular sheath
$D_m$	mm	Mean diameter tubular sheath
$D_o$	mm	Outer diameter tubular sheath
$d$	mm	Interplanar lattice spacing
$d_o$	mm	Original stress free interplanar lattice spacing
$d_m$	mm	Mean diameter of circular helix
$E$	MPa	Young's modulus
$F$	N	Applied load
$f_1$	Hz	First natural eigenfrequency

$g$	$\text{m/s}^2$	Gravitational acceleration
$H$	mm	Calculated height/deflection of test tube curvature
$h$	m	Height (parallel to the direction of gravity)
$hkl$		Miller indices (a notation system for crystallographic planes)
$I$	$\text{mm}^4$	Second moment of area about the neutral axis
<b>I</b>		<i>Identity matrix</i> , when calculating the principal stresses; <i>Internal force vector</i> , when dealing with the condition of dynamic equilibrium
$I_1, I_2, I_3$		Stress invariants
<b>K</b>		Stiffness matrix
$k$		A positive variable used to describe a general sine function
$L$	mm	Change of length
$L_o$	mm	Original length
$L_{\text{Axial}}$	mm	Total axial length of tube section
$l$	mm	Helix lead
$L_1$	mm	Tensile length of the curved test tubes
$L_2$	mm	Compressive length of the curved test tubes
$L^e$	m	Characteristic length of the smallest utilized element in an explicit analysis in Abaqus
$M$	Nm	Moment about the neutral axis
<b>M</b>		Mass matrix
<b>M<math>\ddot{\mathbf{i}}</math></b>		Material inertia force vector
$N$		Number of cycles to failure (logarithmic scale)

$\mathbf{n}_i$		Principal stress directions (eigenvectors)
$n$		A positive integer used in Bragg's law for X-ray diffraction
OD	mm	Outer diameter of the whole cable cross section
P	mm	Corrugation Pitch
$\mathbf{P}$		External force vector
$p$	Pa	Pressure
$p_i$	Pa	Internal pressure
$p_H$	Pa	Hydrostatic pressure
$p_0$	Pa	Zero-reference point of the pressure
$p_o$	Pa	Ambient external pressure
$\mathbf{Q}$		Global dynamic load vector
R	mm	Radius
$\mathbf{R}$		Load vector
$\mathbf{r}$		Displacement vector
T	s	Time period
t	mm	Sheath thickness
W	mm	Test tube width
$\omega$	rad/s	Angular eigenfrequency
y	mm	Perpendicular distance to the neutral axis
$\sigma$	MPa	Cauchy stress
$\boldsymbol{\sigma}$	MPa	Cauchy stress tensor
$\sigma_b$	MPa	Bending stress

$\sigma_m$	MPa	Membrane stress
$\sigma_{mean}$	MPa	Mean stress
$\sigma_o$	MPa	Engineering stress
$\sigma_P$	MPa	Principal stress tensor
$\sigma_r$	MPa	Residual stress
$\sigma_1, \sigma_2, \sigma_3$	MPa	Principal stresses
$\sigma_x, \sigma_y, \sigma_z;$	MPa	Normal stresses
$\sigma_{xx}, \sigma_{yy}, \sigma_{zz};$		
$\sigma_{11}, \sigma_{22}, \sigma_{33}$		
$\tau_{xy}, \tau_{xz}, \tau_{yz}$	MPa	Shear stresses
$(x, \theta, r)$		Cylindrical coordinates
$\sigma_{\theta\theta}$	MPa	Hoop stress (when utilizing cylindrical coordinates)
$\sigma_{xx}$	MPa	Axial stress (when utilizing cylindrical coordinates)
$\tau_{\theta x}$	MPa	Hoop shear stress (when utilizing cylindrical coordinates)
$\tau_{x\theta}$	MPa	Axial shear stress (when utilizing cylindrical coordinates)
$\varepsilon$		Engineering strain
$\varepsilon_{global}$		Global engineering strain
$\varepsilon_l$		Logarithmic strain
$\varepsilon_p$		0.2% offset strain value
$\boldsymbol{\varepsilon}$		Cauchy strain tensor
$\varepsilon_x, \varepsilon_y, \varepsilon_z;$		Normal strains
$\varepsilon_{xx}, \varepsilon_{yy}, \varepsilon_{zz};$		

$\varepsilon_{11}, \varepsilon_{22}, \varepsilon_{33}$		
$\varepsilon_1, \varepsilon_2, \varepsilon_3$		Principal strains
$\gamma_{xy}, \gamma_{xz}, \gamma_{yz}$		Shear strains
$\nu$		Poisson's ratio
$\kappa$	$\text{mm}^{-1}$	Curvature of a circle
$\rho$	$\text{Kg/m}^3$	Density
$\lambda$	m	Wavelength of incident wave in X-ray diffraction
$\sin \theta$		$\theta$ is the scattering angle in X-ray diffraction
$\Delta t_{\text{cr}}$	s	Critical time step
$\phi$		Eigenvector (vibration mode)
$\varphi$		Describes the phase displacement in a sine function
$\alpha$	rad	Required angular displacement at each end of tube





# 1 Introduction

## 1.1 Background and Motivation

Today there is an increasing demand to supply offshore oil and gas installations with shore-generated environmentally friendly power. In the search and production of new hydrocarbons, oil and gas installations are driven further from shore and at deeper depths causing the need for not only subsea production units but also floating moving transient platforms. Also, marine renewable energy installations including tidal and wave technologies, which are transient moving installations, are in a rapid development. Last but not least, windmills, which only a few years ago was unthinkable to have installed offshore, but now has become a regular sight in a marine environment. This has led to an increasingly demand for dynamic HV subsea power cables, from ocean bottom to sea level, in collaboration with a static HV subsea power cable, along the ocean floor.

A HV subsea power cable consist of several different layers with different purposes. One layer is a metallic tubular sheathing with the main purpose to act as a moisture-blocking barrier to prevent ingress of water into the inner cable core where the current is transmitted through the cable.

A dynamic HV subsea power cable, unlike a static cable, is exposed to various hanging configurations and fatigue loading due to transient platform motion, current, wave and wind forces. This calls for a flexible but also fatigue resistant tubular sheathing for a dynamic cable. Hence, metallic corrugated tubular sheathing (MCTS) has been applied, due to its flexibility but also good mechanical and fatigue strength.

However, the usage of MCTS within a dynamic HV subsea power cable is relatively new and the competition within the subsea power business is high, meaning that there exist little or no information regarding scientific research and development advance on the specific theme. Therefore, the need for more knowledge arose from the power cable company Nexans, which is about to join the dynamic HV subsea power cable business. Nexans, in collaboration with SINTEF, wanted to research MCTS which led to this thesis.

I found this specific thesis and topic interesting and motivating because it untouched a new product for Nexans, not yet on the market, that I could help research and develop further. Another motivator and reason for my interest in this specific thesis was the possibility to dive into my professional interests, which are advanced simulations in the form of non-linear finite element analysis, and technical challenges related to fatigue.

## 1.2 Problem Description

### 1.2 Problem Description

Nexans and SINTEF, in collaboration with undersigned, agreed that the thesis should investigate and analyse how various geometrical parameters of a MCTS, that is corrugation pitch, height, sheath thickness and helical inclination angle (given a helical MCTS), influence on its fatigue properties. This led to the following challenge to be addressed in this master's thesis:

*What is the most suitable corrugation geometry design, in comparison with a smooth tubular sheathing, for fatigue life based on both local and global strain development fields in the corrugation?*

### 1.3 Project Scope

The scope of work for this thesis was to examine the impact of various geometrical parameters on the fatigue properties of MCTS. The focus was put on 3D finite element simulations, while test tubes was provided from Nexans for characterization and residual stress measurements.

#### 1.3.1 Objectives

The scope of work, described above, was sectioned into the following objectives:

1. Literature study, including but not limited to: subsea HV power cable technology, corrugation effects, MCTS production method, residual stresses and fatigue theory.
2. Develop a parametrized 3D model of a MCTS; to be able to vary different geometrical parameters such as corrugation height, pitch length, sheath thickness and helical inclination angle (for a helical MCTS).
3. Perform non-linear numerical FEA of various corrugated sheaths through controlled static axial and bending analysis.
4. Report, evaluate and postprocess the obtained FEA results with primary emphasis on developed strain fields and strain values.
5. Perform residual stress measurements in the corrugated sheath surface of the received test tubes from Nexans
6. Report, evaluate and postprocess the obtained residual stress measurements
7. Establish a four-point bending model in Abaqus and perform non-linear numerical FEA of selected test tubes received from Nexans, to predict how real experimental testing could be performed at a later stage for further work.
8. Report the obtained, evaluated and postprocessed FEA results.

## 1.4 Thesis Structure

### 1.4 Thesis Structure

The rest of the thesis is structured as follows.

**Chapter 2**, deals with basic theory regarding a subsea power cable, including, but not limited to the difference between a static and a dynamic cable, how a typical HV subsea power cable is layered, why corrugation is needed and what effect it adds within a dynamic cable, what type of materials are commonly utilized in a smooth and corrugated sheathing, different corrugation shapes and effects such a geometry holds, and how a MCTS is manufactured especially by Nexans. Chapter 2 also defines and visualize the corrugation profile utilized in the finite element method part of the thesis.

**Chapter 3**, describes typical material behaviour of the commonly utilized MCTS materials described in chapter 2, with emphasis on stress, strain and strain hardening.

**Chapter 4**, describes typical load impacts and fatigue of a MCTS, with emphasis on reeling and the operational life offshore of a whole dynamical HV subsea power cable. This chapter also discuss among other factors, friction and its significance to the MCTS fatigue properties, hydrostatic pressure and its impact on the MCTS when water depths increases, residual stresses inherited from production and its significance to the MCTS fatigue properties. One also familiarize with the commonly utilized residual stress measurement tools available, with specific emphasise on the X-ray diffraction technique.

**Chapter 5**, Introduce the experimental approach and experimental work performed in this thesis, which was residual stress measurement by utilizing X-ray diffraction. Further, it characterizes the received test tube specimens from Nexans before eventually presenting basic X-ray diffraction theory.

**Chapter 6**, introduce theory and chosen FEA tools utilized during the finite element method of this thesis.

**Chapter 7**, describes the pre-processing, evaluation and simulation part of the finite element method of this thesis. This chapter provides a detailed description of how the 3D models of the MCTS was modelled and parametrized, what material models were utilized and a thoroughly detailed description of the FEA approach, considering the various analyses performed and assumptions made.

**Chapter 8**, presents the experimental results from the X-ray diffraction measurements discussed in chapter 5.

**Chapter 9**, presents the achieved finite element method results based on the work discussed and performed in, respectively, chapter 6 and 7.

**Chapter 10**, lead into a discussion, evaluating the obtained results presented in chapter 8 and 9.

**Chapter 11**, presents a summary of the main results and findings before a conclusion is presented with emphasis on the problem description in chapter 1. This chapter also presents recommendations for further work.

1.4 Thesis Structure

## 2 High Voltage Submarine Power Cables

### 2.1 General

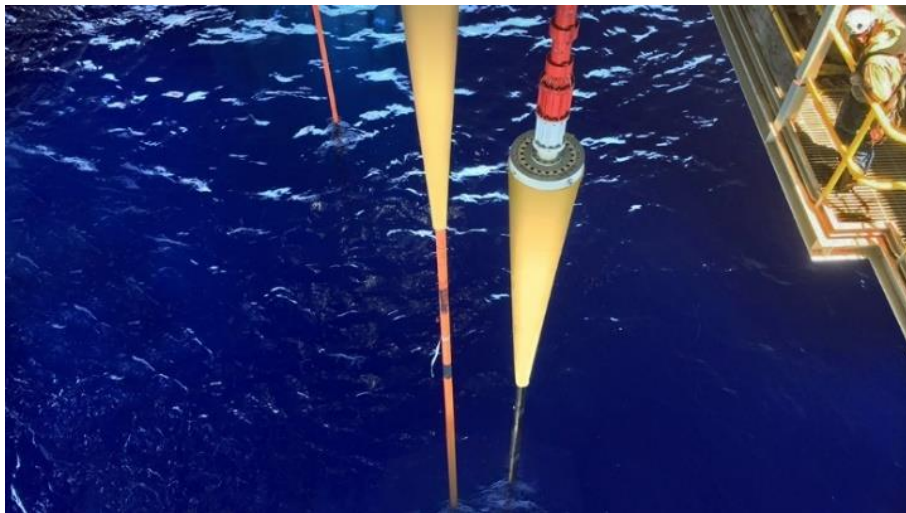
A subsea power cable is often functioning both above and beneath the sea level, giving rise to the more frequently used industry name: submarine power cable, which will be employed further in the thesis.

#### 2.1.1 Static Cables

A power cable installed along the ocean floor is called a static submarine power cable. It is referred to as static due its minimal exposure to movement and fatigue loading during its lifetime [1].

#### 2.1.2 Dynamic Cables

A power cable installed and allowed to move between two fixed supports, one support at the ocean floor and one at the sea level, is referred to as a dynamic submarine power cable due to its exposure to dynamical movement and fatigue loading. The fixed support at sea level is usually a floating installation where the cable is attached through a bending stiffener, shown in Figure 1.



*Figure 1: Bending stiffener [2]*

The bending stiffener provides a smooth transition between the rigid fixed upper support, holding a high stiffness, and the lower stiff power cable. By utilizing a bending stiffener, bending forces, caused by external forces including wind, waves and current, exposing the upper part of the submarine power cable, are decreased [3]. Typical dynamic submarine power cable hanging configurations, between two fixed supports, are visualized in Figure 2.

2.1 General

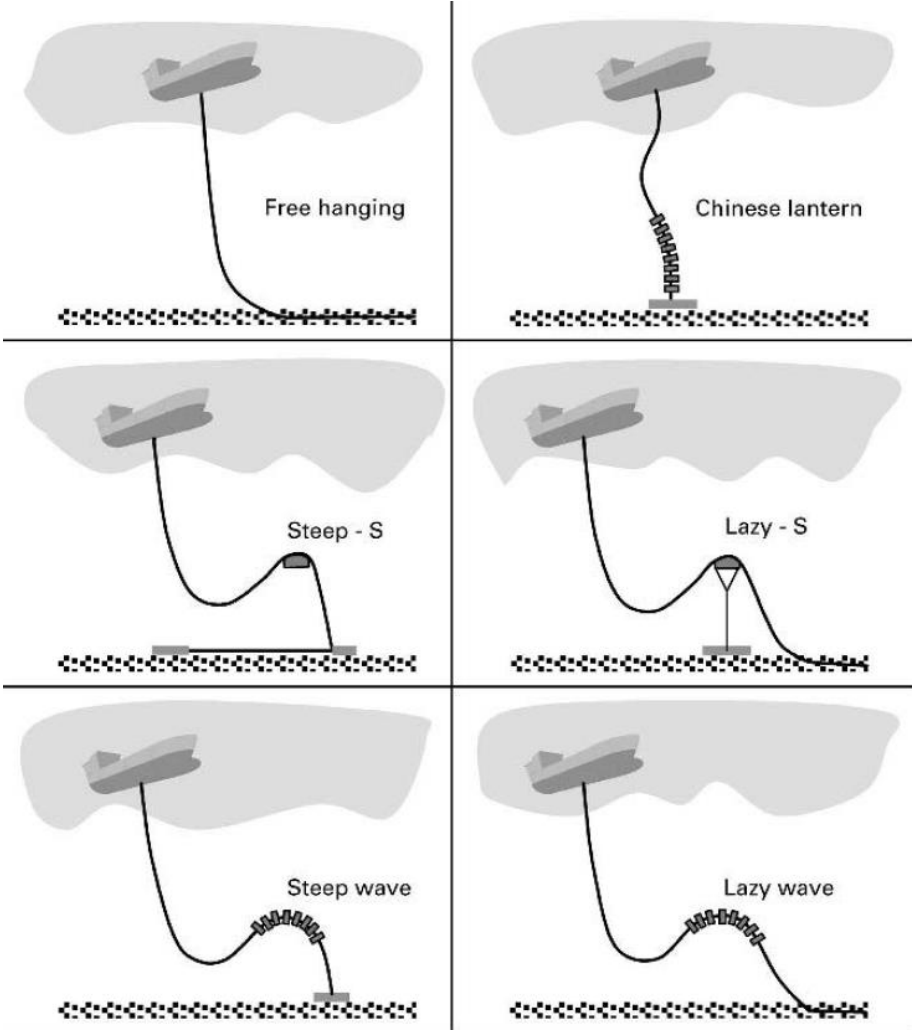


Figure 2: Various dynamic HV submarine power cable hanging configurations [4]

Dynamic submarine power cables are considerably more exposed to external forces compared to the static cable type, and the mechanical loading varies as a function of several parameters including, but not limited to the parameters visualized in Figure 3, and listed in Table 1.



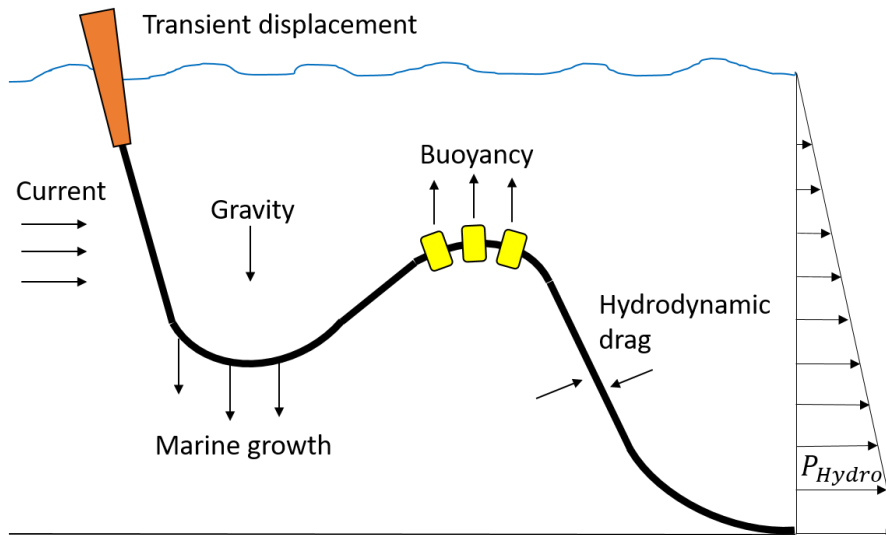


Figure 3: Parameters exposing a dynamic HV submarine power cable after installation [3]

Table 1: Parameters influencing the mechanical loading of a dynamic HV submarine power cable after installation [3]

Parameter	Impact/consideration
Cable design	How the cable is configured with respect to, inter alia, weight, geometry and length.
Marine growth	Increases the cable weight both globally and locally and hence increase axial tension and bending forces
Sea current	Can induce hydrodynamic drag forces and ViV and give rise to fatigue of the cable
Transient displacement of installation at sea level	Inducing both horizontal and vertical cable motion that can give rise to fatigue of the cable
Buoyancy force (if buoyancy modules are installed between the two fixing points)	Usually installed to accommodate for horizontal and vertical movement of a moving installation at sea level. The modules induce bending forces on the cable, but reduces axial forces along the cable.
Hydrostatic pressure	The hydrostatic pressure on the cable increases with increasing depth

## 2.2 Types and Structure

### 2.2 Types and Structure

#### 2.2.1 HVAC and HVDC

The most common types of submarine power cables that we have today is for HVAC and HVDC, presented in Figure 4. Most of the electrical power, usually, is consumed as AC. However, transmitting AC subsea, for instance, over longer distances, will in many circumstances prove to be a disadvantage due to economic and technical reasons. Then an advantage is to transmit DC instead [5].

When electrical power is transmitted over a longer distance, a feasible approach is to increase the voltage to reduce power losses within the cable. A major drawback with a HVAC submarine power cable is its limitation with respect to transmitting electrical power over longer distances, that is around 70 – 100km. The reason for this limitation is mainly due to its high electrical capacitance<sup>1</sup> which induces a capacitive charging current within the cable. The capacitive charging current, which increases with a higher voltage, absorbs the current carrying capacity within the cable. A HVDC cable does not share the same limitation as a HVAC cable, but a typical drawback is the need for converters to change AC to DC and back, which is costly. A HVDC submarine cable is the usual cable choice for distances (normally) over 100km [7].

A submarine power cable including HVAC, transmit AC through three conductors. A HVDC submarine cable only needs one conductor to transmit DC, but is dependent of having a return path either through another conductor or by using an anode/cathode through the ocean [8].

---

<sup>1</sup> Capacitance is the ability to collect or store electrical charge [6].

2.2.2 Cable Layering

The structure and design of a HV submarine power cable depends on many variables, including, but not limited to inter alia: location, cable length, transmitting power and whether it is for static or dynamic use. Figure 4, visualize how a static HVDC and HVAC submarine power cable can be layered and structured, while Table 2, describes the different layers' mission within the cable. A HVAC submarine power cable is almost structured in the same way as an HVDC type, except that the cable consists of three cores instead of one, shown in Figure 4, which introduce free space within the cable. The space is usually filled with polymeric ropes or extruded PVC/PE to maintain a circular cross section of the cable [9].

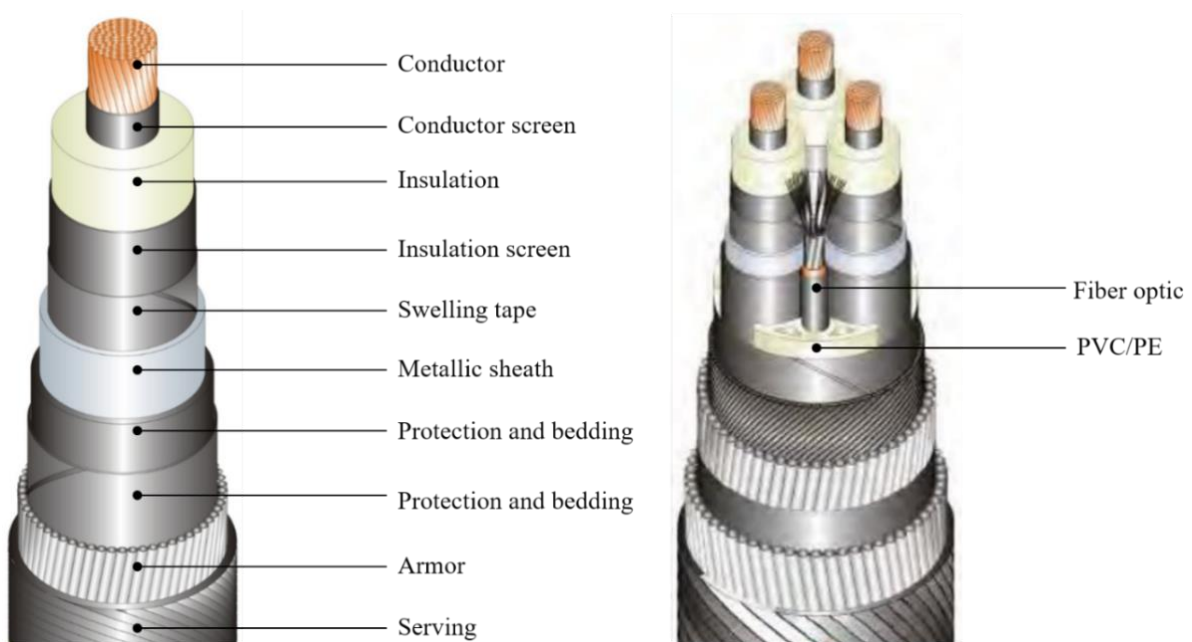


Figure 4: Static HV submarine power cable - HVDC (left) [10] and HVAC (right) [11]

## 2.2 Types and Structure

*Table 2: The purpose of the various HV submarine power cable layers [9]*

<b>Layer</b>	<b>Purpose</b>
Conductor	The conductor allows current to flow through the cable. Its material is usually copper or aluminium.
Conductor screen, insulation and insulation screen	<p>The conductor screen, insulation and insulation screen makes up the dielectric system;</p> <p>Both screens are often semi-conductive and usually made from XLPE;</p> <p>The conductor screen hinders local stresses between the conductor and insulation and therefore also helps maintaining the insulation dielectric properties;</p> <p>The insulation, commonly XLPE, function as a barrier between the potential differences, that is between the inner core of the cable and the outer layers.</p>
Swelling tape	If swelling tape is used, its main function is to suck in moisture that diffuse into the cable, especially from the longitudinally welding seam.
Metallic sheath	<p>The majority of all HV submarine power cables are equipped with a moisture-blocking tubular metallic sheath to hinder ingress of moisture and hence maintain the integrity of the dielectric system;</p> <p>In a static HV submarine power cable, usually, a smooth sheath is applied;</p> <p>In a dynamic HV submarine power cable, usually, a corrugated sheath is applied but smooth sheaths are also applicable.</p>
Protection and bedding	<p>Protection and bedding is applied beneath the armor to protect the moisture-blocking sheath from the armouring;</p> <p>The protection and bedding is often made from tape and provide some compressibility.</p>
Armor	Armor provides structural integrity for the cable with emphasis on tension and protection from mechanical loading. The common material choice is steel.

Serving	Serving acts as a protective outer layer, hindering external stresses from deteriorating the corrosion protection of the armor. Typical choice of material to utilize as serving is a type of polymer.
---------	--

2.3 Metallic Corrugated Tubular Sheathing within a Dynamic HV Submarine Power Cable

2.3 Metallic Corrugated Tubular Sheathing within a Dynamic HV Submarine Power Cable

2.3.1 Usage

The usage of a MCTS as a moisture-blocking barrier within a dynamic HV submarine power cable, visualized in Figure 5, has become an increasingly popular and preferred solution due to its flexibility and strength.



Figure 5: Dynamic HV submarine power cables with corrugated sheathing [11]

Recent Norwegian offshore projects which included the usage of dynamic HV submarine power cables with a MCTS are listed in Table 3.

Table 3: Recent Norwegian offshore projects, Gjøa [3] and Goliat [12], including a dynamic HV submarine power cable and utilization of a MCTS

Year	Field	Depth [m]	Platform type	Submarine cable	Sheath type	Cable length [km]	Company
2013	Goliat	≈380	FPSO	HVAC static	Smooth Cu	105.0	ABB
				HVAC dynamic	Corrugated Cu	1.5	
2010	Gjøa	≈350	Semi-submersible rig	HVAC static	Smooth Lead	98.5	ABB
				HVAC dynamic	Corrugated Cu	1.5	

Common material choices for a static cable sheath is often lead, while for a MCTS, different metallic materials are applicable, including, but not limited to: aluminium, copper and stainless steel [9].

### 2.3.2 Lead Sheath

A sheath consisting of lead, commonly manufactured by extrusion, is completely moisture impermeable, if well-produced. Also, the high density of lead adds an increased cable weight providing stability for a static cable along the ocean floor. However, lead alloys are soft and therefore vulnerable to mechanical loading and fatigue which is a major drawback considering a lead sheaths' candidature for a dynamic cable. Thermal cycling, moreover, can cause the lead alloy to recrystallize, leading to crystal-boundary growth causing initiation of micro-cracks leading to a degradation of its impermeable moisture properties [9].

### 2.3.3 Aluminium Sheath

An aluminium sheath can be manufactured in several ways, commonly extruded, welded or laminated.

Extruded cable sheaths of aluminium alloys, smooth or corrugated, were employed within submarine cables earlier, but not anymore, due to severe corrosion problems. An aluminium sheath, welded and thereafter corrugated, can be made of much better corrosion resistant alloys compared to an extruded and subsequently corrugated sheath.

Worzyk [9, p. 32] formulates the manufacturing process for welded aluminium sheaths as follows:

For the welded sheath, aluminium strips in the range of 0.5mm up to 4.0mm thickness are folded around the cable with a set-up of rolls. The strip edges are trimmed to correct dimensions and welded longitudinally forming a tube. The tube-like sheath can be corrugated after welding to improve the flexibility.

### 2.3.4 Copper Sheath

Welded and corrugated copper sheaths are one of the more preferred alternatives for usage within a dynamic HV submarine power cable, because of its advantageous fatigue and corrosion properties, and its impermeability. The copper sheaths are usually formed and manufactured the same way as the already described way of welded aluminium sheaths above [9].

## 2.3 Metallic Corrugated Tubular Sheathing within a Dynamic HV Submarine Power Cable

### 2.3.5 Stainless Steel Sheath

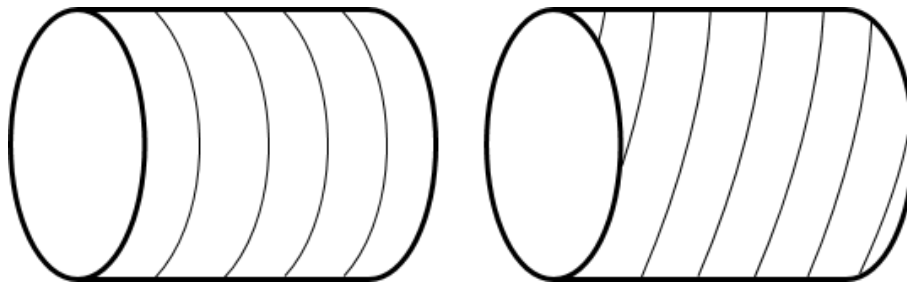
Nexans have broad experience with utilizing corrugated austenitic stainless steel as material within their cryogenic<sup>2</sup> dynamic transfer line systems for liquefied nitrogen, helium, oxygen, hydrogen and natural gas [13].

Austenitic stainless steel holds good mechanical and fatigue properties, weldability, corrosion resistance and impermeability [14]. If one also take into consideration Nexans extensive experience with the material and the corrugation of it, austenitic stainless steel is a possible candidate for usage as MCTS within a dynamic HV submarine power cable.

However, there exists some weaknesses for these alloys. Austenitic stainless steels are vulnerable to SCC if exposed to static stresses, a corrosive environment and passive oxide layer damage. Further, austenitic stainless steels hold a fatigue endurance limit<sup>3</sup> of approximately 30% of their tensile strength simultaneously as their thermal expansion coefficient is quite high. This combination make austenitic stainless steels receptive to thermal fatigue if exposed to large variations in temperature [16].

### 2.3.6 Corrugation shapes

A MCTS, to be used as a moisture barrier within a HV submarine power cable, is manufactured with a wave structure consisting of either an annular or helical pattern as presented in Figure 6.



*Figure 6: An annular pattern to the left and a helical pattern to the right*

The waves can be formed into various shapes, inter alia: sinusoidal and U-shaped, and the various shapes offers different properties with respect to bending, fatigue and pressure resistance, both internal and external [9]. The report focus further on a sinusoidal wave geometry, which will be defined later in the report.

---

<sup>2</sup> Cryogenics comprises the production and behaviour of materials at very low temperatures.

<sup>3</sup> Fatigue limit or endurance limit is defined as a distinct stress level, in a S-N curve, for typical ferrous metals and titanium where no fatigue failure will occur, given normal conditions [15].



## 2.3.7 Corrugation Profile Definition

A typical MCTS holding a sinusoidal shaped corrugation is visualized in Figure 7.

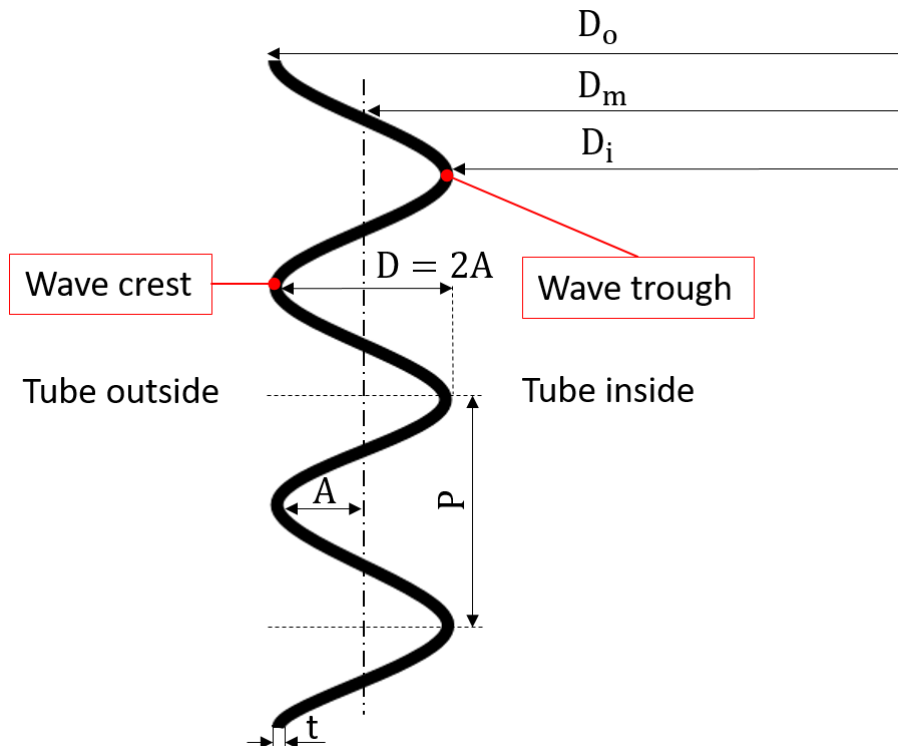


Figure 7: Corrugation profile definition

## 2.3.8 Corrugation Effects

A corrugated sheath, curved along its corrugation, adds flexibility, not necessarily, without compromising on strength. Norman, et al. [17, p. 1] states the following regarding the corrugation effect of thin sheets given an initially curved corrugation:

Thin sheet materials of low bending stiffness but high membrane stiffness are often corrugated in order to achieve improvements of several orders of magnitude in bending stiffness with only minimal increases in weight and cost. If these corrugated sheets are initially curved along the corrugations, much of this stiffness gain is lost. In return, the sheets are then capable of significant elastic changes in shape overall, including large changes in overall Gaussian curvature.

Also, a benefit from turning a smooth sheath into a curved corrugated sheath is its given ability to transform into various shapes without stretching the surface at local areas. Norman, et al. [17, p. 5], also states the following purpose of corrugating a thin sheet:

One purpose of corrugating sheets is to increase their bending stiffness along the corrugations, since such bending must then involve either large stretching and compressive strains in the top and bottom surfaces or total buckling of the corrugations if the cross-sectional shape cannot distort.

## 2.3 Metallic Corrugated Tubular Sheathing within a Dynamic HV Submarine Power Cable

A curved, for example, sinusoidal corrugated tubular sheath is further situated within the so-called category of “compliant” structures, that is, according to Norman, et al. [18, p. 3]:

“Compliant” structures are structures which undergo large deformations within their working life, typically remaining within the elastic limits of the material. Thus, they can undergo large changes of shape without hinges or mechanisms. If such a structure is also ‘multistable’, it can ‘lock’ into various shapes, giving the potential for large improvements in cost, weight, complexity, reliability and lifespan. Specifically, a corrugated shell structure can combine light weight with high strength, offering a wide scope for the designer to tailor the stiffness properties to the required behaviour.

To summarize, the effect of corrugating a tubular sheath, compared to a smooth tubular sheath, lies in its ability to undergo large deformations, without exceeding the material yield point with respect to both stress and strain, without necessarily compromising on its overall strength. It is further no doubt, with reference to Figure 2 and Table 2, that a MCTS within a dynamic HV submarine power cable can be exposed to large deformations depending on both hanging configuration and mechanical loading. Therefore, a curved corrugated tubular sheath-surface can contribute to a more robust overall cable configuration.

## 2.4 Nexans Production Line for Sheathing of Submarine Power Cable

### 2.4.1 UNIWEMA® HV

Nexans UNIWEMA® HV, visualized in Figure 8, can form, weld, and corrugate if needed, metallic tubular sheaths for HV submarine power cable usage. UNIWEMA® can take on cable core diameters ranging from 50 – 300mm.

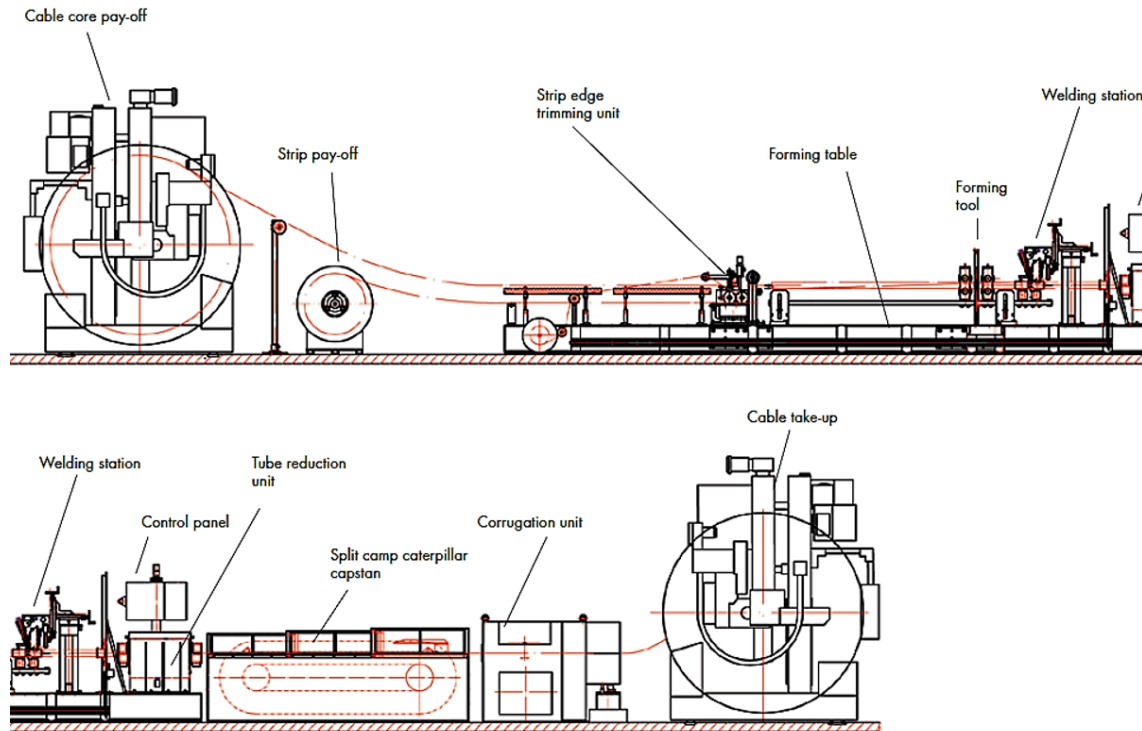


Figure 8: UNIWEMA® HV manufacturing layout [19]

A metallic strip is led into the machine where it goes over a forming table where its edges are trimmed and folded around the cable core, shown in Figure 9.



Figure 9: Forming table [19]

## 2.4 Nexans Production Line for Sheathing of Submarine Power Cable

Afterwards, the sheath is led into a welding station, shown in Figure 10, where the edges are TIG welded.



*Figure 10: Welding station [19]*

Downstream the welding station, a split clamp capstan pulls the sheathed cable through the UNIWEMA<sup>®</sup> HV, shown in Figure 11.



*Figure 11: Split clam caterpillar capstan [19]*

The cable sheathing can be transported to a corrugation chamber, if corrugation is needed, before final cable take-up [19].

### 2.4.2 Corrugation Unit

In the corrugation chamber, the MCTS is lubricated and cooled before a desired wave shape is created by the corrugation unit shown in Figure 12. Both helical and annular waves can be manufactured, helical corrugation is standard while annular corrugation production requires a special tool [19].



Figure 12: Corrugation unit [19]

The corrugation unit consists of a freely rotating corrugation tool located inside a rotationally driven corrugator head. The corrugation tool, which is an annular disk, is supported eccentrically to the longitudinal MCTS axis. The corrugation tool is set to an angle less than 90 degrees to the longitudinal MCTS axis. A continuous helical corrugation occurs when the inner surface of the annular disk rolls over the sheath surface and is forced into the sheath wall due to the eccentric support [20].

The corrugation unit is driven by a separate motor from the one that drives the split clamp caterpillar capstan. Hence, the corrugation RPM can independently be adjusted from the production speed, making it possible to produce corrugations with various shape and corrugation pitch. Also, the corrugation RPM adapts automatically to the capstan speed keeping a constant pitch during the MCTS production [19].

#### 2.4.3 Technical Data

Table 4, describes the most important technical parameters for a standard UNIWEMA<sup>®</sup> HV.

Table 4: Technical sheet UNIWEMA<sup>®</sup> HV [19]

<b>Outer diameter</b>	Smooth tubular sheath	50.0 - 200.0 [mm]
	Corrugated tubular sheath	50.0 - 200.0 [mm]
<b>Standard wall thickness</b>	Steel	0.5 - 1.5 [mm]
	Copper	0.5 - 2.0 [mm]
	Aluminium	0.5 - 2.5 [mm]
<b>Production speed</b>	Line speed range	2.0 - 8.0 [m/min]
	Corrugation speed	800.0 [1/min]

2.4 Nexans Production Line for Sheathing of Submarine Power Cable

### 3 Material Behaviour of a Metallic Corrugated Tubular Sheathing

This chapter presents typical stress and strain concepts which can be used to characterize typical material behaviour of the metallic materials described in section 2.3.3 – 2.3.5, which all three are potentially candidates as a MCTS material. Tensors, matrices and vectors are noted in bold.

#### 3.1 Stress

Stress,  $\sigma$ , can be defined as the internal forces acting in a material during deformation.

True normal stress, also known as Cauchy stress, is defined as:

$$\sigma = \frac{F}{A} \quad (3.1)$$

Engineering stress, also called nominal normal stress is defined as:

$$\sigma_o = \frac{F}{A_o} \quad (3.2)$$

##### 3.1.1 Cauchy Stress Tensor

To completely describe a true stress state within a material during deformation, the second order Cauchy stress tensor is employed [21]. It can be written in matrix form as:

$$\boldsymbol{\sigma} = \boldsymbol{\sigma}_{ij} = \begin{vmatrix} \sigma_{xx} & \sigma_{yx} & \sigma_{zx} \\ \sigma_{xy} & \sigma_{yy} & \sigma_{zy} \\ \sigma_{xz} & \sigma_{yz} & \sigma_{zz} \end{vmatrix} = \begin{vmatrix} \sigma_{11} & \sigma_{12} & \sigma_{13} \\ \sigma_{21} & \sigma_{22} & \sigma_{23} \\ \sigma_{31} & \sigma_{32} & \sigma_{33} \end{vmatrix} = \begin{vmatrix} \sigma_x & \tau_{yx} & \tau_{zx} \\ \tau_{xy} & \sigma_y & \tau_{yx} \\ \tau_{xz} & \tau_{yz} & \sigma_z \end{vmatrix} \quad (3.3)$$

Where the subscripts  $i = j$  denotes normal stresses, and  $i \neq j$  denotes shear stresses, indicated in Figure 13.

### 3.1 Stress

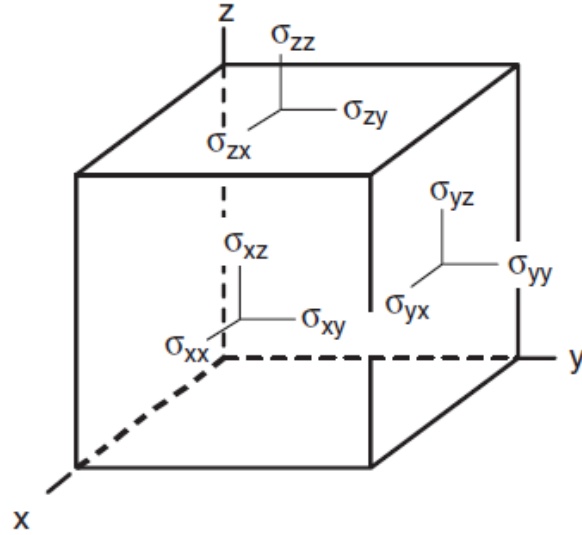


Figure 13: The stress components acting on a solid 3D infinite small element [22]

#### 3.1.2 Principal Stress

For any stress state, a set of axes (1,2,3), also called the principal axes, can be found where the shear stress components become zero. This means that one can rotate the element in Figure 13 such that only the normal stresses acts on it. For this case, the normal stresses  $\sigma_x$ ,  $\sigma_y$  and  $\sigma_z$  is denoted  $\sigma_1$ ,  $\sigma_2$  and  $\sigma_3$ , and called principal stresses,  $\sigma_p$  [22].

The principal stresses can be determined through the following eigenvalue problem:

$$(\boldsymbol{\sigma} - \sigma_p \mathbf{I}) \mathbf{n}_i = 0 \quad (3.4)$$

Where  $\boldsymbol{\sigma}$  is the Cauchy stress tensor,  $\mathbf{I}$  is the identity matrix and  $\mathbf{n}_i$  ( $i=1,2,3$ ) is the principal stress directions (eigenvectors), giving a set of three linear equations. To determine a non-trivial solution to system (3.5), the determinant of the coefficient matrix is set equal to zero [21]. This gives the following equation:

$$\sigma_p^3 - I_1 \sigma_p^2 - I_2 \sigma_p - I_3 = 0 \quad (3.5)$$

Where  $I_1$ ,  $I_2$  and  $I_3$  comprises of constant coefficients for the given stress state because they are independent of axis orientation. Hence,  $I_1$ ,  $I_2$  and  $I_3$  are called stress invariants [22]. The principal stress tensor can be written in matrix form as:

$$\boldsymbol{\sigma}_p = \begin{vmatrix} \sigma_1 & 0 & 0 \\ 0 & \sigma_2 & 0 \\ 0 & 0 & \sigma_3 \end{vmatrix} \quad (3.6)$$

Where the principal stresses can be determined by finding the roots of equation (3.5).



### 3.2 Strain

According to Irgens [21, pp. 133], strain is about: “*local deformation in a material, that is deformation in the neighbourhood of a particle. Strain represents change in material lines, angles, and volume.*”

For small strain, the strain tensor can, analogues to the Cauchy stress tensor, be treated as a tensor and written in matrix form as:

$$\boldsymbol{\varepsilon} = \boldsymbol{\varepsilon}_{ij} = \begin{vmatrix} \varepsilon_{xx} & \varepsilon_{yx} & \varepsilon_{zx} \\ \varepsilon_{xy} & \varepsilon_{yy} & \varepsilon_{zy} \\ \varepsilon_{xz} & \varepsilon_{yz} & \varepsilon_{zz} \end{vmatrix} = \begin{vmatrix} \varepsilon_{11} & \varepsilon_{12} & \varepsilon_{13} \\ \varepsilon_{21} & \varepsilon_{22} & \varepsilon_{23} \\ \varepsilon_{31} & \varepsilon_{32} & \varepsilon_{33} \end{vmatrix} = \begin{vmatrix} \varepsilon_{xx} & \frac{1}{2}\gamma_{yx} & \frac{1}{2}\gamma_{zx} \\ \frac{1}{2}\gamma_{xy} & \varepsilon_{yy} & \frac{1}{2}\gamma_{zy} \\ \frac{1}{2}\gamma_{xz} & \frac{1}{2}\gamma_{yz} & \varepsilon_{zz} \end{vmatrix} \quad (3.7)$$

For large strains, the tensor definition does not apply and the strains cannot be transformed between different axis systems. The reason for this is the existence of angular deflection between the material directions due to the deformation, which is neglectable for small strains [22].

The strain deformation is typically subdivided into two theories:

- **Finite strain theory**, is utilized for the presence of deformations including large rotations and large strains. Thus, enabling an exactly measure of changes in dimensions and angles for a nonlinear behaviour.
- **Infinite strain theory**, is utilized for linearized finite strain or when small strains are present.

For finite strains there exists several strain measures including but not limited to: Lagrangian strain, Eulerian strain and Hencky strain. Hencky strain is also called logarithmic or true strain. These various finite strain measures have one thing in common, namely that they converge towards the infinite strain measure value at low strains, that is for magnitudes  $\ll 1$  [23].

#### 3.2.1 Logarithmic Strain

Logarithmic strain (LE) is the default strain measure output for Abaqus/Explicit, and for Abaqus/Standard, given a geometrically non-linear analysis employing elements supporting finite strains [24].

The conventional strain,  $\varepsilon$ , also called engineering strain, is valid for infinite small strains and is defined as the change of length,  $L$ , per unit length of original length,  $L_0$ , and is defined as:

## 3.2 Strain

$$\varepsilon = \frac{L - L_0}{L_0} \quad (3.8)$$

While logarithmic strain is defined as:

$$\varepsilon_l = \int_0^{\varepsilon_l} d\varepsilon = \int_0^{\varepsilon_l} \frac{dL}{L} = \ln L - \ln L_0 = \ln \frac{L}{L_0} = \ln(1 + \varepsilon) \quad (3.9)$$

Where Irgens [21, p. 3] notes that “ $d\varepsilon$ , expresses the incremental change of length,  $dL$ , per unit of the present length,  $L$ , that is the length of the specimen prior to the increment. The logarithmic strain represents a sum of the strain increments” [21].

### 3.2.2 Principal Strain

The strain tensor can, analogues to how the principal stress was found in 3.1.2, be rotated in such a way that the shear strain components become zero and the principal axes (1,2,3) is found [22]. Hence, the normal strain components are denoted as the principal strain components  $\varepsilon_1$ ,  $\varepsilon_2$ ,  $\varepsilon_3$  and presented in matrix form as:

$$\boldsymbol{\varepsilon} = \begin{vmatrix} \varepsilon_1 & 0 & 0 \\ 0 & \varepsilon_2 & 0 \\ 0 & 0 & \varepsilon_3 \end{vmatrix} \quad (3.10)$$

### 3.3 Strain Hardening

Work hardening, also called strain hardening, is the process of strengthening a metallic material by plastically deforming it. Pelleg [25, p. 195] notes that “*Plastic deformation is associated with the motion of a relatively large number of dislocations. Strengthening is the consequence of dislocation motion and interactions with other dislocations and features present in the material.*” Strain hardening will be induced in the MCTS at wave crest and wave trough during the cold forming<sup>4</sup> corrugation process described in subsection 2.4.2.

#### 3.3.1 Isotropic

Isotropic hardening can be defined as an isotropic expansion of a material yield strength due to plastic deformation. This means that the initial yield strength is increased, equally in all directions in the yield locus<sup>5</sup>, with increasing stress shown in Figure 14. The isotropic hardening model is adequate for describing changes in the load path with subsequent large strains [22].

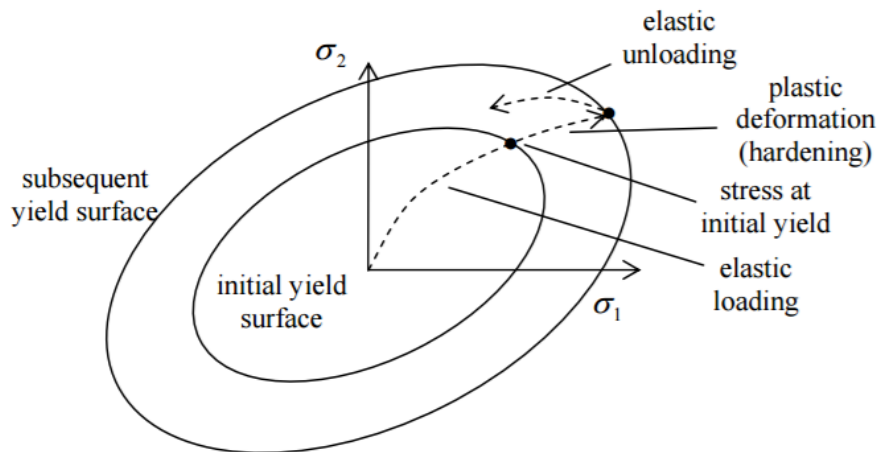


Figure 14: The effect of an isotropic strain hardening on the yield locus [27]

#### 3.3.2 Kinematic

The kinematic hardening model, dissimilar to the isotropic model, holds the yield locus shape and size constant during plastic deformation, but shifts it in the loading path direction. A large shift might cause plastic deformation during unloading. The kinematic model is adequate for describing changes in the load path with subsequent small strains [22].

<sup>4</sup>Cold forming (working) is, According to Wang and Gong [26, p.141], defined as a forming process or plastic deformation operation carried out at temperatures below the recrystallization temperature of the workpiece material, but more often it is simply referred to as the forming process at room or ambient temperature.

<sup>5</sup>“A yield locus is the surface of a body in three-dimensional stress space. Stress states on the locus will cause yielding. Those inside the locus will not cause yielding” [22, p. 81].

### 3.3 Strain Hardening

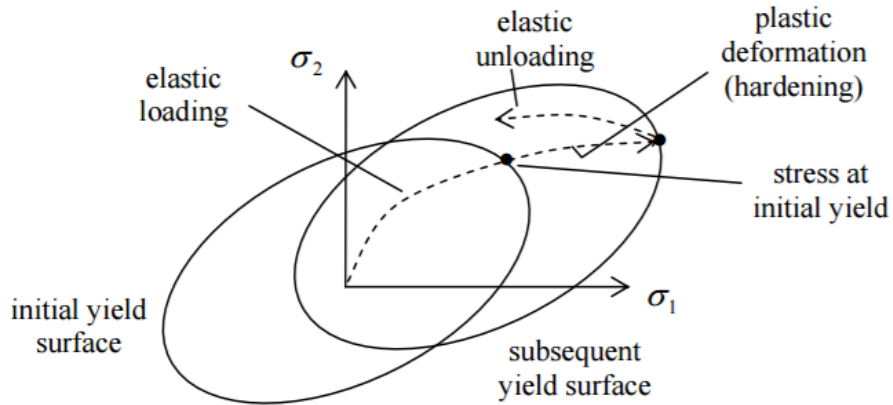


Figure 15: The effect of a kinematic strain hardening on the yield locus [27]

An effect that can be interpreted as a shift in the kinematic model is the so-called Bauschinger effect. This effect appears when, for instance, a loading path changes significantly or when a material yield strength increases simultaneously as its compressive yield strength decreases after a tension-compression loading. One of several reasons for the Bauschinger effect is dislocation-pile up at obstacles within the material visualized in Figure 16. When switching from tension to compression loading, dislocations can easily flow away from the barrier [22].

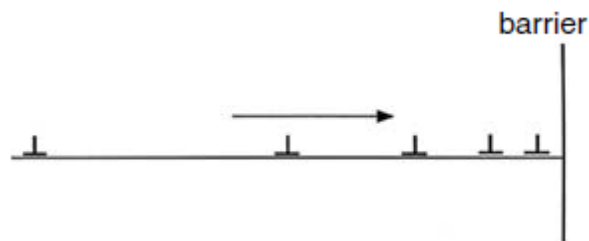


Figure 16: Dislocation pile-up [22]

## 4 Load Impact and Fatigue of Metallic Corrugated Tubular Sheathing

Load and fatigue analysis of a HV submarine power cable, and therefore also a MCTS, should comprise of load cycles including, but not limited to: reeling, handling, installation, operational lifetime and unplanned events, like a reinstallation. However, this thesis, only consider reeling and operational lifetime offshore.

Initially, this chapter will introduce how a MCTS behaves when exposed to axial and bending displacement before the focus shifts to the cable reeling followed by dynamical impact and fatigue loading during a MCTS operational lifetime offshore. Typically, the highest bending curvature a dynamic HV submarine power cable is exposed to occurs during reeling, therefore the FE bending analysis of the MCTS in ABAQUS FEA will be based on this.

### 4.1 Global Behaviour

A MCTS exposed to global axial displacement will behave according to Figure 17. Global stress and strain can be calculated from the equations found in section 3.1 and 3.2.

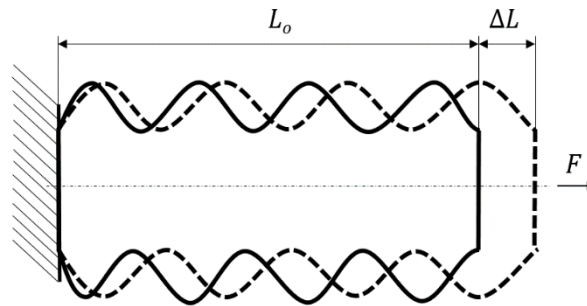


Figure 17: Global axial displacement

A MCTS exposed to global bending will behave according to Figure 18.

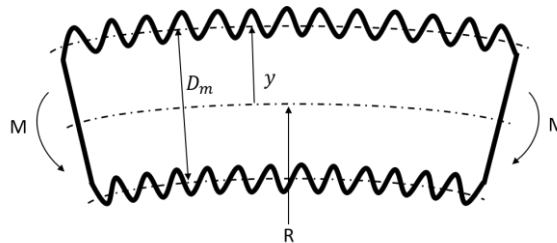


Figure 18: Global tube bending

The imposed global engineering strain can be approximated by beam element theory [28]:

$$\varepsilon_{global} = \kappa y = \frac{1}{R} y = \frac{1}{R} \frac{D_m}{2}, \quad \frac{1}{R} = \frac{M}{EI} \quad (4.1)$$

4.2 Minimum Bending Radius

4.2 Minimum Bending Radius

When handling a power cable in the workshop during reeling or when installing the cable offshore by utilizing a chute, precautions must be taken with respect to the cable maximum bending radius (MBR) visualized in Figure 19. MBR is the lowest bending radius the cable is permitted to be bent around, and a smaller MBR implies an enhanced cable material flexibility.

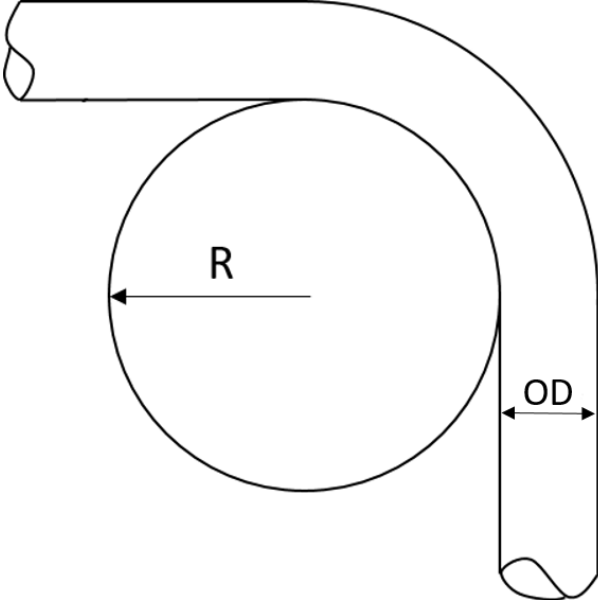


Figure 19: Minimum bending radius

Exceeding the MBR could result in kinks, damage of the cable internal layers, plastic deformation of the MCTS and subsequent fatigue life reduction. A rule of thumb is typically to maintain a minimum bending diameter (MBD)  $\geq 2.5$  times the outer cable diameter (OD) [9]. Table 5, describes the MBD utilized by Nexans.

Table 5: Minimum bending diameter

Load aspect	MBD
Without tension	$30 \cdot OD$
With tension	$25 \cdot OD$

### 4.3 Dynamical Bending, Axial and Friction Forces

A dynamic HV submarine power cable is especially exposed to global dynamical bending during its operational lifetime. The global dynamical bending acting on the whole cable induces both axial tension, bending and friction stresses within the cable and therefor also to the MCTS. Hence, an important design factor is to reduce the amount of global dynamic bending forces from being transmitted to the MCTS during its operational lifetime.

The bending response of a cable, consisting of several layers in contact, is complicated due to the presence of relative motion between the layers. ISO 13628-5 [29, p. 127] states the following regarding the bending response of a layered dynamical cable:

For small tension and torsion loads, the internal reaction forces and the associated friction resistance against relative motions are normally small and the structural response due to bending is dominated by the elastic deformation of each component. However, for deep-water and ultra-deep-water dynamic applications with high associated top tensions, the contact pressure and friction resistance can become large and can, hence, induce significant additional axial stresses as well as wear and fretting effects that it is necessary to take into account in fatigue evaluations.

Further, according to ISO 13628-5 [29, p. 128], the physical behaviour in bending of a layered cable can be divided into two regimes:

**Stick regime**, where plane surfaces remain plane as in traditional beam theory; this behaviour governs until the shear stress between components at the neutral axis of the umbilical exceeds the frictional resistance governed by the friction coefficient and the internal reaction forces from tension and torsion or external loads.

**Slip regime**, where the friction resistance is exceeded and relative displacements occur; for the constantly curved case, this means that helical components move by relative displacement from the compressive side towards the tensile side of the umbilical.

A three phase HVAC cable, for example, will behave stiff when exposed to only a small amount of bending. This is because the various layer-interactions lies within the stick regime. A high friction coefficient between the layers means the cable holds a high bending stiffness. Increasing the bending means, eventually, that the stick regime switches to stick-slip or slip. This occurs when the friction forces are not capable of withstanding the bending forces, resulting in a decreasing bending stiffness of the cable. Jeroense, et al. [30, p. 3] states the following:

A low bending gives a high bending stiffness and a high bending gives a low bending stiffness. The transition point between these two levels of bending stiffness depends on the level of friction between the different layers in the cable.

### 4.3 Dynamical Bending, Axial and Friction Forces

A cable holding a high bending stiffness results in more bending forces being transmitted to the different cable layers giving rise to higher local stresses present within the cable and therefore also to the MCTS. By keeping a low bending stiffness, the local stresses exposing the MCTS are diminished [30].

#### 4.3.1 Friction Reducing Layer

One way to diminish the global bending forces influence on the internal cable parts is to introduce friction reducing layers between the MCTS and its touching layers. By installing at least one friction reducing layer between the sheathing and the outer touching layer, improved bending resistance is obtained, and the risk for cracks to initiate on the sheath surface reduces considerably [30].

According to Jeroense, et al. [30], the necessary friction coefficient between the protective sheath and the friction reducing layer should lie in the range of 0.05 – 0.40, and preferably between 0.10 – 0.30. Further, the thickness of the layer should be in the range of 0.01 – 1.00mm, but preferably within the range of 0.05 – 0.30mm. According to Jeroense, et al. [30], the layer could comprise of one of the following materials as a main constituent:

- A polymer including one or several of the following materials: PP, HDPE, Teflon, silicone or polyester. This layer could either be a polymer tape wounded around the MCTS or an extruded tubular polymer.
- A liquid comprising of either: Oil, graphite, grease or wax.



#### 4.4 Hydrostatic Pressure

A dynamic HV submarine power cable submerged in the sea is exposed to a hydrostatic pressure increasing with an increasing depth. Hydrostatic pressure is defined as:

$$p_H = p_0 + \rho gh \quad (4.2)$$

When utilizing a MCTS in a dynamic HV submarine power cable, at a certain water depth, a critical hydrostatic pressure is reached where it is probable that the MCTS could be damaged or experience buckling. The critical water depth is dependent on, but not limited to: the cable geometry, layering and the MCTS geometry. A MCTS can be utilized within a dynamic HV submarine power cable down to water depths ranging up to 400 – 600m without having to counteracting the external ambient pressure [31].

However, there are ways to overcome the challenges when utilizing MCTS at deeper water depths. During manufacturing, the internal MCTS surface could either be arranged close to the external insulation surface, meaning that they partly abut one another, or an annular space could be arranged between the two layers. Anyway, a void arises, either solely along the internal MCTS corrugation, or additionally also due to the arranged annular space. The void could be filled with a dielectric liquid to counteract the external ambient pressure and hence, maintain the MCTS shape and its geometrical, mechanical and fatigue properties. Preferably, the dielectric liquid should be hydrophobic, meaning it repels water molecules, or it should be hydrophilic, meaning it is attracted to water molecules [31].

For the above discussed cable arrangement, a helical corrugation is preferable compared to an annular corrugation, especially if the internal MCTS surface is installed close to the external insulation surface or abuts it. This is because the liquid can be added post-corrugation of the MCTS since the helical geometry allows the liquid to flow through the helical corrugation path. If an annular space is arranged between the internal MCTS surface and the external insulation surface, spacers could be installed. The spacers should be radially compressible but also axially permeable or perforated. The spacers will maintain a circular space and allow liquid to flow axially within the space [31].

The conductor current loading might vary due to a fluctuating demand for electricity during the cable operational lifetime. A high demand for electricity magnifies the conductor current load and might increase heat emission from the conductor. An increasing heat emission can cause thermal expansion of the dielectric liquid and induce a pressure build-up within the corrugated sheath. A potential pressure build-up can be mitigated by installing a fluid reservoir topside at

## 4.4 Hydrostatic Pressure

the cable end, which can be used to equalize a potential pressure build-up. The liquids increase the MCTS collapse resistance simultaneously as it maintains the MCTS degree of freedom within the cable. By employing the above discussed cable arrangement, a MCTS can be utilized within a dynamic HV submarine power cable down to water depths ranging from 1000 – 4000m [31].

However, a solution including a fluid reservoir topside to equalize any pressure build-up within the MCTS is not preferable due to cost and possible installation complexity. Also, it is desirable to avoid any usage of potential environmentally pollutive liquid, if a potential leakage occur. A preferable solution is to maintain both collapse resistance and maximum degree of freedom by utilizing a more solid filler element, that is an incompressible elastic polymer filler for instance. One drawback with this solution is the increased production and installation complexity, because the filler is preferably more solid. The filler element should be installed within the MCTS without compromising on, among other factors, production effectiveness.

### 4.4.1 Hoop Stress

A MCTS exposed to ambient external hydrostatic pressure alone, or in an interaction with a counteracting internal pressure from a liquid or a polymer filler, hoop and longitudinal stresses arises in the wall. If the external pressure is higher than the internal pressure, the MCTS is also vulnerable to elastic/inelastic wall-buckling. These produced stresses and wall-buckling must be calculated for and considered during the design phase of the MCTS. The following stress derivation is only valid for thin-walled pressure theory and detailed assumptions are described in Table 6 and visualized in Figure 20, that is a thin-walled smooth sheathing or an annular MCTS.

When two planes of a smooth tubular sheath, that is internally pressurized, an analysis of an infinite small element, visualized in Figure 20, with respect to stresses can be performed.

#### 4 Load Impact and Fatigue of Metallic Corrugated Tubular Sheathing

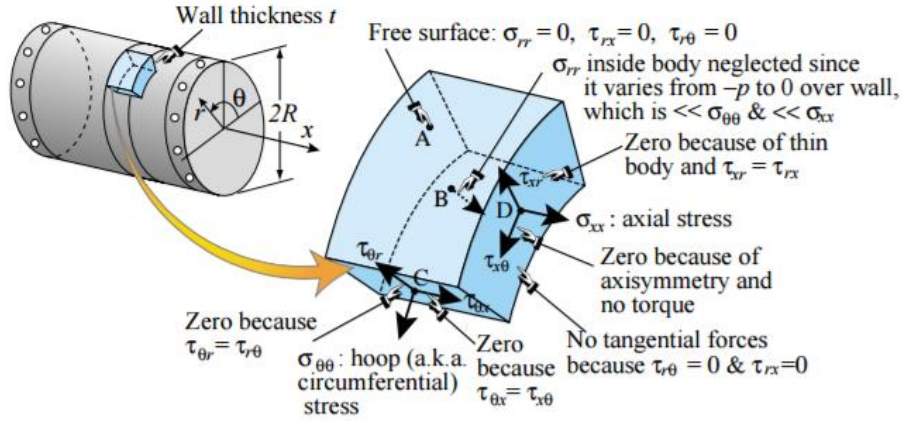


Figure 20: Wall element of a pressurized thin-walled cylinder [32]

The wall stress state of the element can be transferred into matrix form, utilizing cylindrical coordinates  $(x, \theta, r)$ , as:

$$\boldsymbol{\sigma} = \boldsymbol{\sigma}_{ij} = \begin{vmatrix} \sigma_{xx} & \tau_{x\theta} & \tau_{xr} \\ \tau_{\theta x} & \sigma_{\theta\theta} & \tau_{\theta r} \\ \tau_{rx} & \tau_{r\theta} & \sigma_{rr} \end{vmatrix} \quad (4.3)$$

The outer surface, where  $r = R$ , is assumed stress free because of the assumptions of a free surface and a thin wall:

$$\sigma_{rr} = \tau_{rx} = \tau_{r\theta} = 0 \text{ for } r = R \quad (4.4)$$

Along the inner tube surface, where  $r = R - t$ , the assumption of a thin wall is applicable excluding the tangential shear stresses. However, a compressive normal stress ( $\sigma_{rr} = -p$ ) is present to equalize the internal pressure. The compressive normal stress is moreover small relative to the axial and circumferential (hoop) normal stress, and therefore it is reasonable to neglect it.

$$\sigma_{rr} \approx \tau_{rx} = \tau_{r\theta} = 0 \text{ for } r \in [R-t, R] \quad (4.5)$$

Further, because of the symmetric assumption, described in Table 6:

$$\begin{aligned} \tau_{\theta x} &= \tau_{x\theta} = 0 \\ \tau_{rx} &= \tau_{xr} = 0 \\ \tau_{\theta r} &= \tau_{r\theta} = 0 \end{aligned} \quad (4.6)$$

This gives the following plane stress state matrix for the wall:

$$\boldsymbol{\sigma} = \boldsymbol{\sigma}_{ij} = \begin{vmatrix} \sigma_{xx} & 0 & 0 \\ 0 & \sigma_{\theta\theta} & 0 \\ 0 & 0 & 0 \end{vmatrix} \quad (4.7)$$

#### 4.4 Hydrostatic Pressure

A free body diagram (FBD) of the plane stress state is presented in Figure 21.

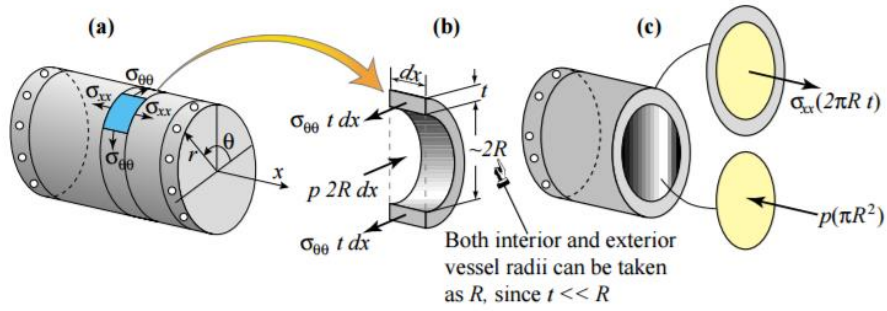


Figure 21: Free body diagram of a thin-walled pressurized cylinder [32]

The FBD and an equilibrium criterion gives the following characteristic equations [32]:

$$\sigma_{\theta\theta} = \frac{pR}{t} \quad (4.8)$$

$$\sigma_{xx} = \frac{pR}{2t} = \frac{1}{2} \sigma_{\theta\theta}$$

Maximum in-plane and out-of-plane shear stress on the inner and outer surface occur on  $45^\circ$  rotated planes about the principal axes (1, 2, 3), which was defined in section 3.1.2. These stresses are equal for the inner and outer surface, when the thin walled assumption is valid, and can be calculated from [33]:

Maximum in-plane shear stress:

$$\tau_{\max_z} = \frac{(\sigma_1 - \sigma_2)}{2} = \frac{(\sigma_{xx} - \sigma_{\theta\theta})}{2} = \frac{\sigma_{xx}}{4} = \frac{pr}{4t}$$

Maximum out-of-plane shear stress: (4.9)

$$\tau_{\max_x} = \frac{(\sigma_1 - \sigma_3)}{2} = \frac{(\sigma_{xx} - \sigma_{rr})}{2} = \frac{\sigma_{xx}}{2} = \frac{pr}{2t}$$

$$\tau_{\max_y} = \frac{(\sigma_2 - \sigma_3)}{2} = \frac{(\sigma_{\theta\theta} - \sigma_{rr})}{2} = \frac{\sigma_{\theta\theta}}{2} = \frac{pr}{4t}$$

With the presence of an ambient external pressure in addition to an internal pressure, equation (4.8) alters to:

$$\sigma_{\theta\theta} = \frac{(p_i - p_o)R}{t}$$

$$\sigma_{xx} = \frac{(p_i - p_o)R}{2t} = \frac{1}{2} \sigma_{\theta\theta} \quad (4.10)$$

## 4 Load Impact and Fatigue of Metallic Corrugated Tubular Sheathing

Table 6: Thin-walled pressure vessel assumptions [32]

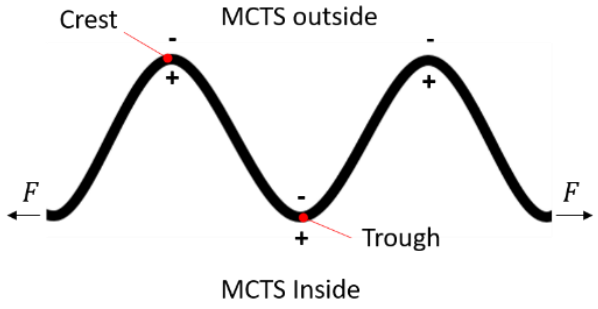
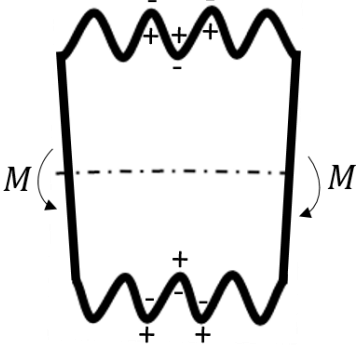
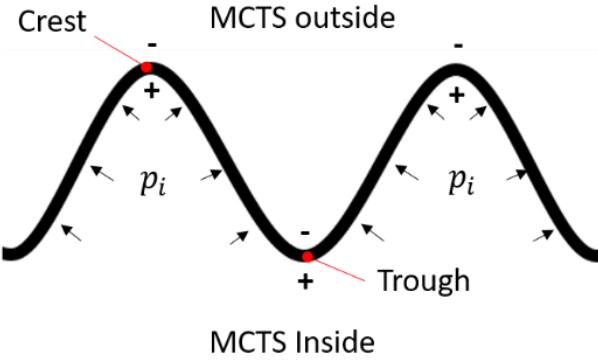
<b>Assumptions</b>	<b>Comments</b>
Wall thickness is thin compared to other dimensions	Valid if: $\frac{R}{t} > 10$ . It is reasonable to assume uniform stresses across the MCTS wall if this criterion is fulfilled.
Cylindrical symmetry is present with respect to geometry and loading	This assumption is only valid for a smooth tubular sheath and an annular MCTS. The symmetry vanishes when introducing helical corrugation.
The pressure is uniform along the MCTS surface	If external pressure is higher than the internal pressure the MCTS is vulnerable to wall-buckling. If this is the case, the equations should be utilized with caution, since elastic/inelastic wall buckling is a more probable failure mode.
End effects are ignored	
The material is linear-elastic and isotropic	

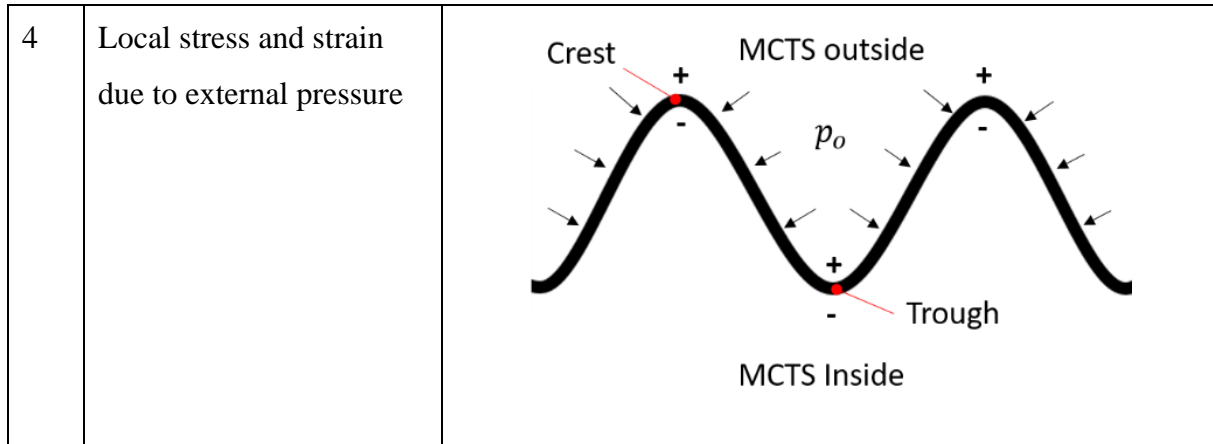
4.5 Stress and Strain Component Signs

4.5 Stress and Strain Component Signs

Different stress and strain components with respect to tension/compression occur when displacing a MCTS axially, by bending or by an internal or external pressure. Table 7, sums up the different cases with respect to tension/compression signs along the corrugation geometry.

Table 7: Signs for axial/bending stress/strain components. Tensile is indicated by +, and compression is indicated by -.

No.	Loading type	Sign
1	Local stress and strain due to global axial displacement	
2	Local stress and strain due to global bending	
3	Local stress and strain due to internal pressure	



The stress and strain through the thickness of a MCTS, due to the above-mentioned loadings presuming a linear elastic behaviour, can be divided into a bending and a membrane component. Figure 22, visualize how the stress through the thickness behaves for loading situation number 1 and 3 from Table 7.

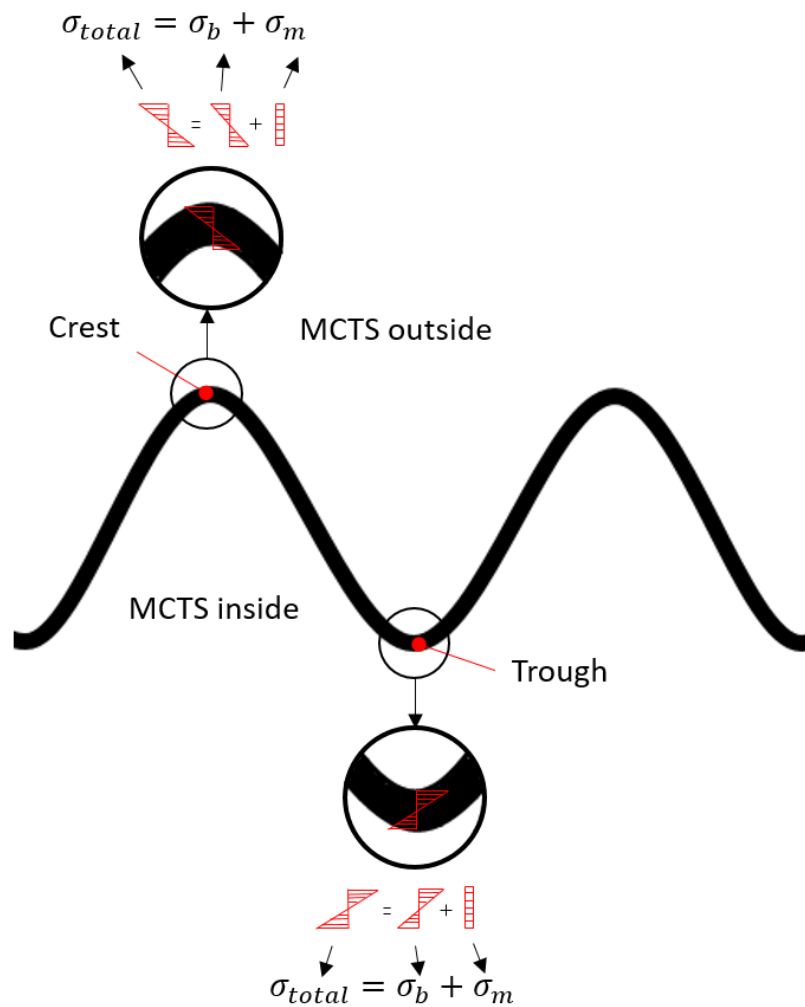


Figure 22: Stress through the MCTS wall thickness including bending stress ( $\sigma_b$ ) and membrane stress ( $\sigma_m$ )

## 4.6 Fatigue

### 4.6 Fatigue

#### 4.6.1 Fatigue Loads

During operation, the highest fatigue loads a dynamic HV submarine power cable is exposed to are commonly occurring at a water depth between 0 – 30m. Dynamic forces created by a moving floating platform and external forces created by currents and wind are in general exposing the cable at their highest value around this depth. [34].

#### 4.6.2 Fatigue Resistance

The fatigue resistance of a MCTS is dictated by several parameters: material, surface roughness, sheath thickness (t) and corrugation geometry. When it comes to the corrugation geometry, the most important parameters are the corrugation pitch (P), corrugation amplitude (A) and corrugation depth (D), all indicated on Figure 7, in section 2.3.7 [34].

#### 4.6.3 Strain-based Fatigue Approach

According to Dowling [15, p. 745]: “*The strain-based approach to fatigue considers the plastic deformation that may occur in localized regions where fatigue cracks begin, as at edges of beams and at stress raiser*”. Further, Dowling [15, p. 745] states:

This procedure permits detailed consideration of fatigue situations where local yielding is involved, which is often the case for ductile metals at relatively short lives. However, the approach also applies where there is little plasticity at long lives, so that it is a comprehensive approach that can be used in place of a stress-based approach.

The situation with little plasticity at long lives applies specially for a MCTS used in a dynamic HV submarine power cable.

#### 4.6.4 Strain vs Life Curves

A strain-based fatigue approach utilizes a strain vs life ( $\epsilon - N$ ) curve to estimate fatigue life, meaning that it plots strain amplitude vs number of cycles to failure, visualized in Figure 23.



#### 4 Load Impact and Fatigue of Metallic Corrugated Tubular Sheathing

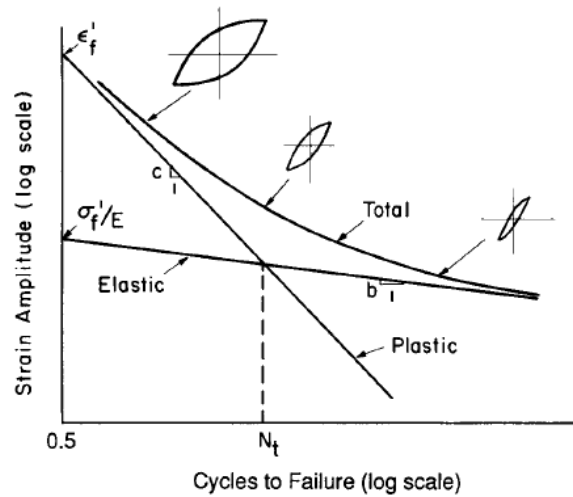


Figure 23: Elastic, plastic and total strain amplitudes vs number of cycles  $N$  [35]

Factors affecting the strain-life curves for a MCTS includes, but are not limited to the following parameters [15]:

**Environment:** If a MCTS is exposed to a hostile environment, for example if seawater reach the sheath surface or temperatures turns high, the number of cycles to failure can be expected to decrease. If a crack is present, the fatigue crack growth rate, usually increases with higher temperatures. Hostile chemical environments can both cause crack initiation, from pitting corrosion for instance, and speed up the fatigue crack growth rate.

**Surface finish:** A rough surface finish is congruent with a decreasing fatigue strength, since fatigue cracks usually initiates at the surface.

**Mean stress:** If the material is exposed to a mean stress during fatigue loading, its completely reversed loading ( $\epsilon - N$ ) curve must be lowered, visualized in Figure 24.

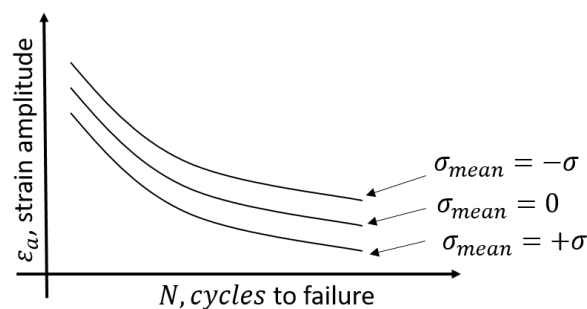


Figure 24: Mean stress effect [15]

**Residual stresses:** Dowling [15, p. 446] states: “Internal stresses in the material, called residual stresses, have an effect similar to an applied mean stress. Hence, compressive residual stresses are beneficial”.

## 4.7 Residual Stresses

### 4.7 Residual Stresses

Residual stresses, within a material, may arise for instance, from uneven heating and cooling of various regions and cold working during metal-forming, and can be defined as the locked-in stresses after removing external loading or thermal gradient.

The amount of, and location of induced residual stresses within a material, that is compression or tension, varies. However, force and moment equilibrium within a material must be satisfied, meaning that tensile residual stresses in one area must be compensated by an equal amount of compressive residual stresses in another area. Figure 30, indicates how residual stresses varies across an imaginary cut,  $\overline{AB}$ , through a material, and equation (4.11) expresses the force equilibrium along  $\overline{AB}$ .

$$\int \sigma_x w(z) dz = 0 \quad (4.11)$$

Where,  $w$  is the material width in the  $y$ -direction, depending on  $z$ .

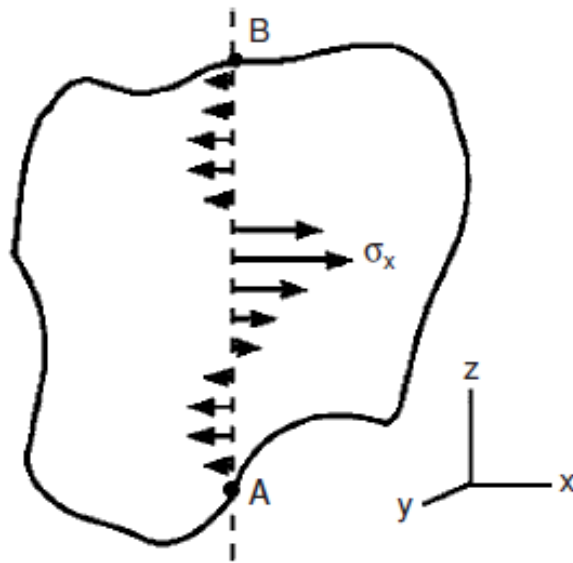


Figure 25: Force and moment equilibrium on a cut  $\overline{AB}$  through a material [22]

At a material micro/macro scale, dislocation-pile ups near barriers and grain size variations can induce varying residual stresses within a grain. For polycrystalline materials, like the mentioned metallic materials in section 2.3.2 – 2.3.5, the grain orientation typically varies from grain to grain and can hence, give rise to stress differences between the grains during tension and compression loading of the material, which again can induce various residual stresses within different grains.

#### 4 Load Impact and Fatigue of Metallic Corrugated Tubular Sheathing

When a polycrystalline material is plastically deformed during tensile loading and unloading, slip will occur at lower stresses for favourably orientated grains compared to those less favourably oriented. During the stress relief, the elastic contraction for all the grains must be equal, and the favourably oriented grains will be left with compressive residual stresses. The situation will be opposite for the less favourable oriented grains, which will experience tensile residual stresses after unloading. This is visualized in Figure 26.

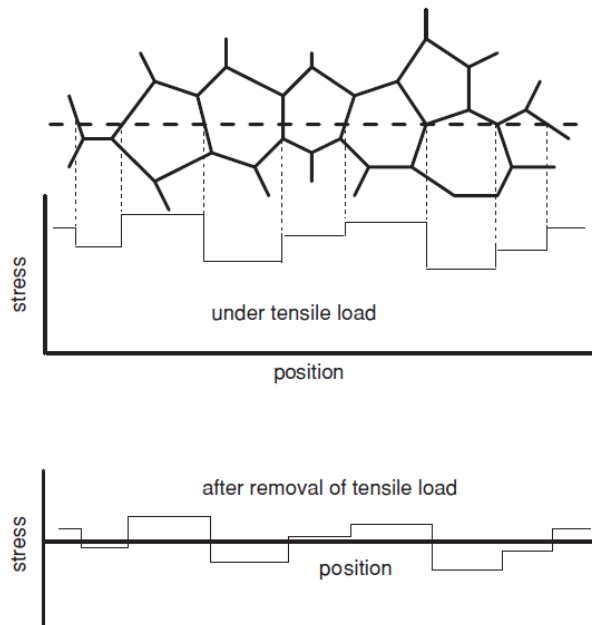


Figure 26: Residual stresses within grains in a polycrystalline material deformed plastically during tensile loading [22]

Another source of stress variations between different grains after unloading is the orientation dependency with respect to elastic moduli. During unloading, stresses will alter more for a grain with a high elastic moduli compared to a grain with a lower value [22].

The process of making a metallic flat strip into a MCTS involves several sources which can induce residual stresses, both axially and circumferentially (hoop), in the MCTS wall. Also, any plastic deformation during reeling/unreeling of the whole power cable in the workshop, and during installation offshore, can give rise to residual stresses within the MCTS, which again can lower the sheathings fatigue limit. Further this report will only go into residual stresses occurring from welding and the cold forming corrugation process, both described within section 2.4.

## 4.7 Residual Stresses

### 4.7.1 Welding

Dowling [15, p. 447] notes: “Welding results in geometries that involve stress raisers, and residual stresses often occur as a result of uneven cooling from the molten state. Unusual microstructure may exist, as well as porosity or other small flaws”. Hence, the presence of welds reduces fatigue strength, aggravate crack effects and requires special attention.

During the TIG welding of a MCTS, the tubular sheathing is welded longitudinally which may give rise to residual stresses in and around the welding seam. When welding is performed, visualized in Figure 27, the fusion zone (FZ)<sup>6</sup>, especially, and the heat affected zone (HAZ)<sup>7</sup> is hot, simultaneously as the base metal (BM) is cold.

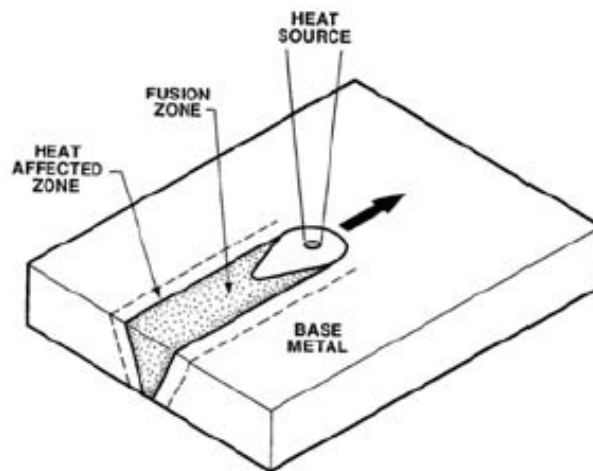


Figure 27: Heat source and three distinct weldment regions in a fusion weld, that is FZ, HAZ and BM [36]

When FZ and HAZ cools, its thermal contraction is resisted by adjacent colder material. This resistance give rise to tensile residual stresses in the FZ especially, but also in HAZ. The adjacent base material must experience compressive residual stresses; this is shown in Figure 28 [22].

---

<sup>6</sup> FZ is known as the weld metal, and it experiences melting and solidification during the weldment [36].

<sup>7</sup> HAZ is the adjacent region to FZ. HAZ is not experiencing melting during the weldment, but it is exposed to such large amount of heat that its microstructure and mechanical properties changes [36].

## 4 Load Impact and Fatigue of Metallic Corrugated Tubular Sheathing

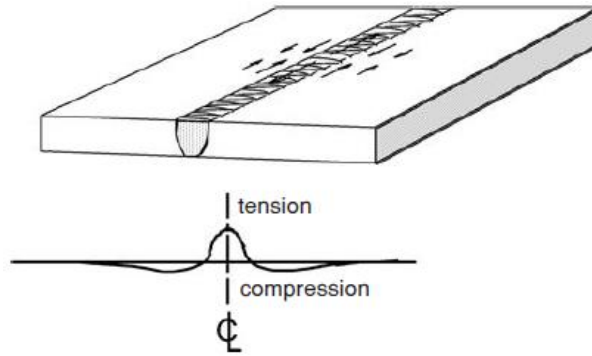


Figure 28: Typical residual stress pattern in a welded plate [22]

### 4.7.2 Cold Working

During the corrugation process, corrugated geometry is formed by the rotating corrugated tool, that is cold forming, introducing strain hardening and residual stresses. Figure 29, presents a typical residual stress distribution pattern when bending a sheet plastically by cold forming.

Wang and Gong [26, p. 145] states two important aspects from the figure:

First, for equilibrium, the effect of tension must be balanced by that of compression; second, the surface that originally plastically extended finally remains in compression, while that which was plastically compressed is left in tension.

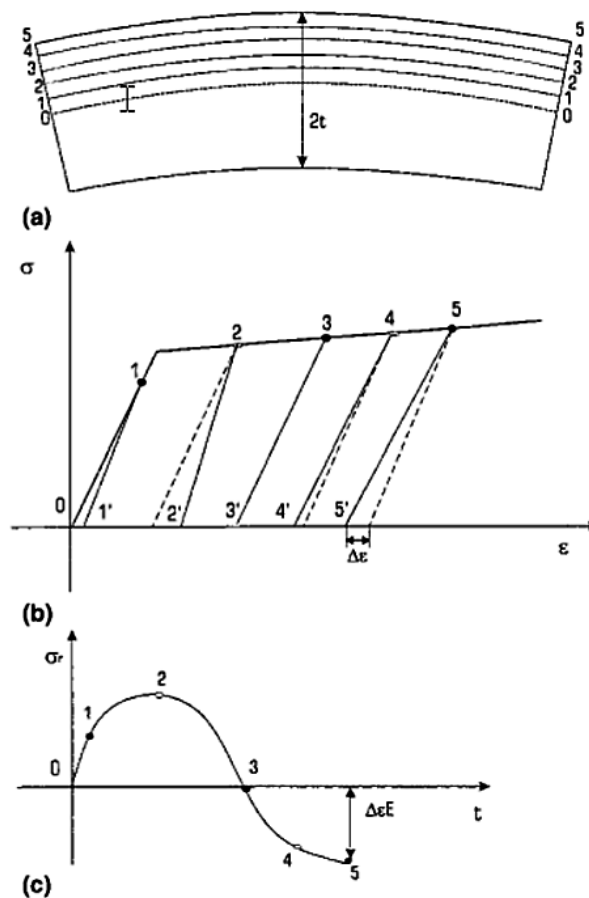
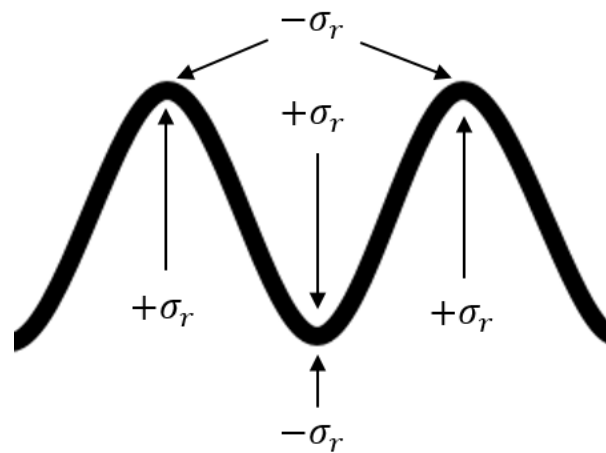


Figure 29: Residual stress pattern after plastically sheet bending [26]

## 4.7 Residual Stresses

We may draw a parallel between Figure 29 and the corrugation cold forming process of the MCTS, meaning that there might arise unfavourable tensile residual stresses after forming, considering the MCTS fatigue strength during both axial and bending fatigue loading. When the corrugation tool is cold forming the tubular sheathing into a MCTS, the sheath wall is bended or forced plastically into a corrugated geometry. When unloading, a spring-back effect may occur, possibly leaving tensile residual stresses and compressive residual stresses as indicated on Figure 30, that is the corrugation crest and trough [26].



*Figure 30: Residual stresses that might arise from the corrugation cold forming process*

### 4.7.3 Stress Relief

Residual stresses can be removed or relieved from a material by converting the plastic strains into elastic strains by annealing or other stress relieving procedures, but this is both time consuming and costly. It is also possible to introduce compressive residual stresses in the material surface by performing shot-peening, this technique is commonly utilized in conjunction with weldment. As regards the cold forming, one might tweak the cold forming parameters to better control the deformation zone and hence, reduce or avoid “bad” residual stresses – this is however difficult [26].

### 4.7.4 Measurement – X-ray Diffraction

There exist several various techniques for measuring residual stresses within a material. The different methods can be divided into three main methods, that is non-destructive, semi-destructive and destructive. Table 8, describes the most commonly used techniques for residual stress measurement and their accuracy and penetration through the material.

The X-ray diffraction technique is one of the most commonly used non-destructive methods, but it functions only as a surface technique. It bases its residual stress calculation on the change

of interplanar lattice spacing,  $d$ , from the stress-free state and original spacing distance,  $d_0$ , between crystallographic planes by utilizing Bragg's law, presented in equation (4.12) and visualized in Figure 31.

$$n\lambda = 2d \sin \theta \quad (4.12)$$

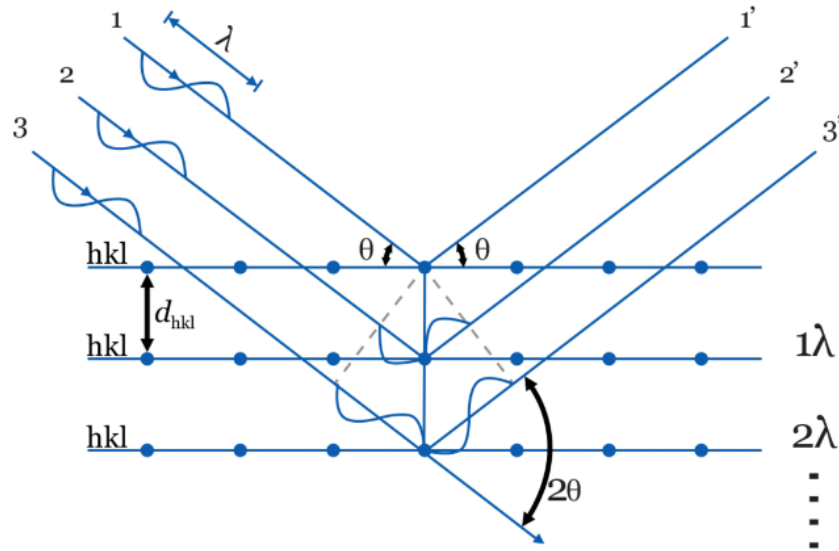


Figure 31: X-ray diffraction of crystallographic planes characterized by Bragg's law of reflection [37]

The altering space, dependent of the prior loading situation, between the planes reflects the engineering elastic strain, which by use of X-ray diffraction measurements can obtain the normal strains in the surface of the material. The stress state can subsequently be found by utilizing Hooks law [22, 38].

To acquire deeper knowledge of how the stress state is calculated by use of X-ray diffraction the reader is recommended to read the work done by Prevey [38]. Also, to understand the differences between the different methods mentioned in Table 8, the reader is recommended to read the work included, but not limited to Rossini, et al. [39], Withers and Bhadeshia [40] and Huang, et al. [41].

## 4.7 Residual Stresses

Table 8: A summarized comparison of some of the most common methods utilized for residual stress measurement of metallic materials [40, 41]

Method	Penetration	Spatial resolution	Accuracy	Comments
Hole drilling (distortion caused by stress relaxation)	~ 1.2 x hole diameter	50 $\mu\text{m}$ length	$\pm 50$ MPa	Three-dimensional stress by in-plane point measurement; Semi-destructive method; Economical
Sectioning	Specimen thickness/length	$> 1 \text{ mm}^3$	$\pm 1.38$ MPa (for three measurements)	Accurate and economical when only the longitudinal stress is important; Creates irreversible destruction
Layer removal	10 mm	0.05 of thickness	Limited by minimum measurable curvature	Three-dimensional stress layer to layer removal; Can be time consuming
Magnetic (variations in magnetic domains with stress)	10 mm	1 mm	10 %	Non-destructive for magnetic materials only; Economical device; In-plane stress measurement



#### 4 Load Impact and Fatigue of Metallic Corrugated Tubular Sheathing

X-ray diffraction (atomic strain gauge)	< 50 $\mu\text{m}$ (Al), < 5 $\mu\text{m}$ (Ti), < 1 mm (with layer removal)	1 mm diameter 20 $\mu\text{m}$ depth	$\pm 20$ MPa	Non-destructive only as a surface technique; In-plane stress; Sensitive to surface roughness; Costly equipment
Ultrasonic	> 10 cm	5 mm	$\pm 50 \times 10^{-6}$ strain	Non-destructive; Sensitive to microstructures and defects; Limited by reliability of stress free references
Raman spectroscopy	< 1 $\mu\text{m}$	< 1 $\mu\text{m}$ approx.	$\pm 50$ MPa ( $\equiv \Delta\lambda \approx 0.1 \text{ cm}^{-1}$ )	Sensitive to surface roughness; Costly equipment

## 4.7 Residual Stresses

## 5 Experimental Work

During the master's thesis, ten MCTS lengths, of approximately 1m each, were transported from Nexans in Germany to NTNU in Trondheim for testing and examination. The intention was to perform both material tests, that is tensile tests, and residual stress measurements of various areas along the corrugation geometry, especially at the wave crest and wave trough. The goal with the tests was to better understand the significance, considering material properties, welding and cold forming constituted during production. By extracting tensile specimens along the corrugation geometry and subsequently perform material tests, obtaining stress-strain curves and strain hardening parameters, altered material properties from the original strip properties along the corrugation geometry could be implemented in Abaqus for FEA comparison purposes. However, residual stress measurement was merely possible before thesis delivery. The main reason for this was because of late delivery of test tubes and a challenging tensile specimen extraction process due to the complex MCTS geometry.

### 5.1 Material and geometrical characterization of test tubes

All the tubes were made of austenitic stainless steel and their outer tube surfaces were covered with a polymer protection material. Five of the tubes, that is tube (1 – i) where  $i \in [1 - 5]$ , inherit the material properties of AISI316L and an own set of geometric parameters. The other five tubes, that is tube (2 – i) where,  $i \in [1 - 5]$ , inherit the properties of AISI316L+Ti and an own set of geometric parameters. The material properties are summarized in Table 9, and are the properties obtained from standard tensile tests of the strips which the MCTSs were produced from.

As presented in Appendix B, the test tubes where delivered with a plastic deformation, a global curvature, most likely obtained during the reeling process after production in workshop. The induced curvature and plastic deformation could be a potential drawback considering the resulting values that would be obtained during testing at NTNU. However, it was clear that the testing would provide interesting and useful results even though.

## 5.1 Material and geometrical characterization of test tubes

Table 9: Material properties of test tubes

Tube $i \in [1 - 5]$	Material	Pos.	Yield strength 0.2% [MPa]	Yield strength 1.0% [MPa]	UTS [MPa]	Elongation (A80%)
(1 - i)	AISI316L	Top	334.0	361.0	607.0	52.0
		Bottom	364.0	364.0	606.0	51.5
(2 - i)	AISI316L +Ti	Top	290.0	317.0	626.0	53.1
		Bottom	310.0	340.0	646.0	52.0

The delivered MCTSs were missing both local and global geometrical parameters. Hence, a selection of tube type 1 and 2 were measured to qualitatively evaluate the local geometrical parameters. This measurement was also performed to verify that there were only two different local tube geometries. The result is presented in Table 10.

Table 10: Local geometrical parameters for the delivered test tubes

Tube	t [mm]	Measured A [mm]	Calculated A [mm]	P [mm]	D <sub>o</sub> [mm]	D <sub>i</sub> [mm]	Inclination angle [degree]
(1 - 1)	0.800	2.300	2.275	12.000	109.200	98.500	2.000
(1 - 2)	0.800	2.300	2.275	12.000	109.200	98.500	2.000
(2 - 1)	0.600	1.800	1.750	9.000	109.200	101.000	1.500
(2 - 2)	0.600	1.800	1.750	9.000	109.200	101.000	1.500

Also, a global measurement was performed of all the tubes, where the measured parameters are visualized in Figure 32, and the obtained result is presented in Table 11. In Table 11, the radius, R, is calculated according to equation (4.13).

$$R = \frac{H}{2} + \frac{W^2}{8H} \quad (4.13)$$

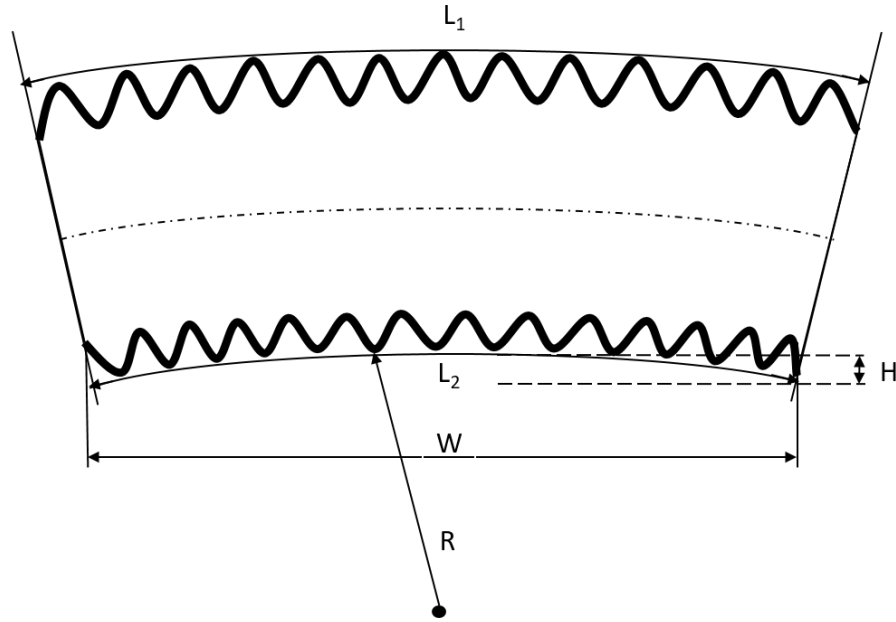


Figure 32: Visualization of measured global geometrical test tube parameters

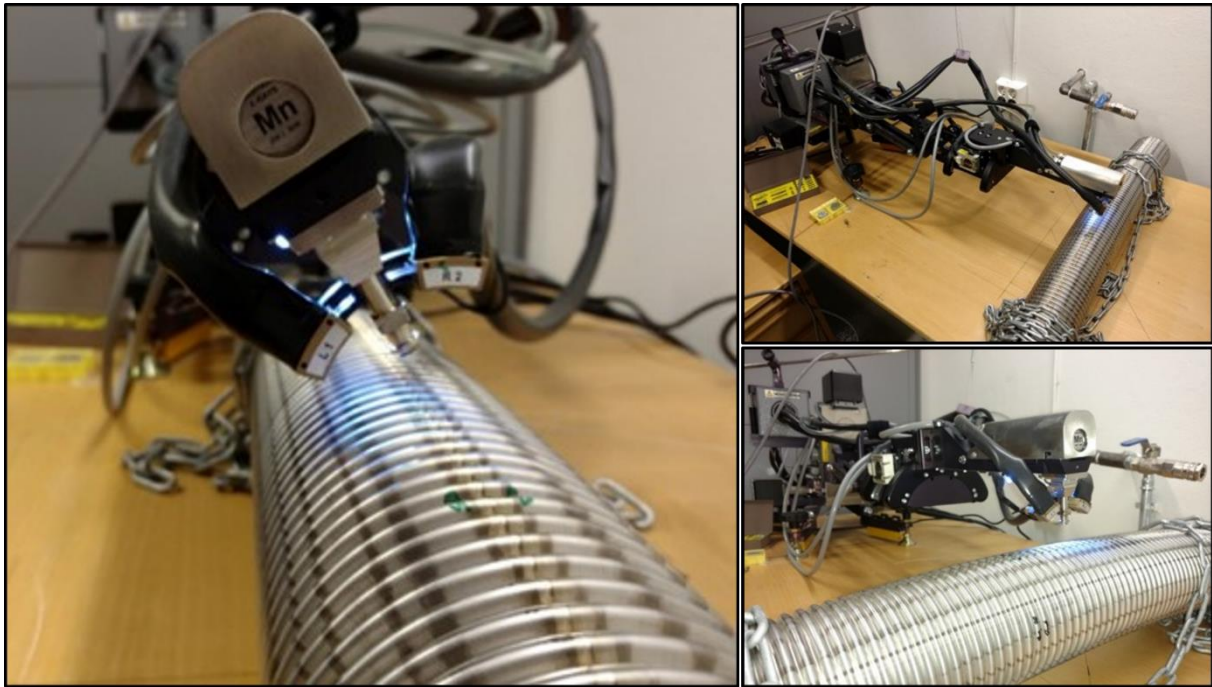
Table 11: Global geometrical test tube measurements

Tube	Measured H [mm]	Measured L <sub>1</sub> [mm]	Measured L <sub>2</sub> [mm]	Measured W [mm]	Calculated R [mm]	Calculated $\kappa$ [mm <sup>-1</sup> ]
(1 – 1)	28.800	990.000	968.000	965.000	4056.175	2.465E-04
(1 – 2)	33.800	1010.000	985.000	980.000	3568.675	2.802E-04
(1 – 3)	29.100	1010.000	989.000	986.000	4190.650	2.386E-04
(1 – 4)	29.800	1008.000	979.000	977.000	4018.797	2.488E-04
(1 – 5)	29.000	1018.000	998.000	1002.000	4342.103	2.303E-04
(2 – 1)	59.700	1100.000	1055.000	1049.000	2333.872	4.285E-04
(2 – 2)	59.900	1101.000	1057.000	1049.000	2326.279	4.299E-04
(2 – 3)	71.800	1113.000	1060.000	1050.000	1955.294	5.114E-04
(2 – 4)	66.800	1133.000	1085.000	1076.000	2199.897	4.546E-04
(2 – 5)	66.100	1112.000	1065.000	1057.000	2145.851	4.660E-04

## 5.2 X-ray Diffraction

### 5.2 X-ray Diffraction

For the measurement of residual stresses within the MCTS test tubes, X-ray diffraction, discussed in subsection 4.7.4, was selected as measurement technique. The main reason for this was because of its non-destructive and relatively efficient technique. Tube (1 – 2) and (2 – 2) were thereafter brought to NTNU at Tyholt in Trondheim, at the Department of Marine Technology, where Professor Sigmund Kyrre Ås performed the measurements on behalf of the undersigned, shown in Figure 33.



*Figure 33: X-ray diffraction measurements performed by Professor Sigmund Kyrre Ås at the Department of Marine Technology at NTNU*

The measurements were performed assuming a plane stress state, described in section 4.4.1, and by measuring the change of atomic lattice spacing, explained in section 4.7.4, in one direction at a time. Afterwards, the stress state, visualized in Figure 34, in each direction was calculated by assuming uniaxial tension. This means that when measuring in axial direction, values were obtained for  $\sigma_{11} = \sigma_{xx}$  and  $\sigma_{12} = \tau_{x\theta}$ , while  $\sigma_{22} = \sigma_{\theta\theta} = \tau_{\theta x} = 0$ . In real, the stress state is biaxial independent of measuring direction, meaning that both hoop and axial stresses is present, because of the plastic deformation caused by the corrugation cold forming process in both axial and hoop direction. The shallow penetration depth of the X-rays caused the X-ray diffraction technique to only be capable of measuring in-plane stresses. This means that we assumed the stress components in the normal direction to be equal zero, that is plane

stress. This was reasonable to assume throughout the thickness in this case, due to the thin wall thickness.

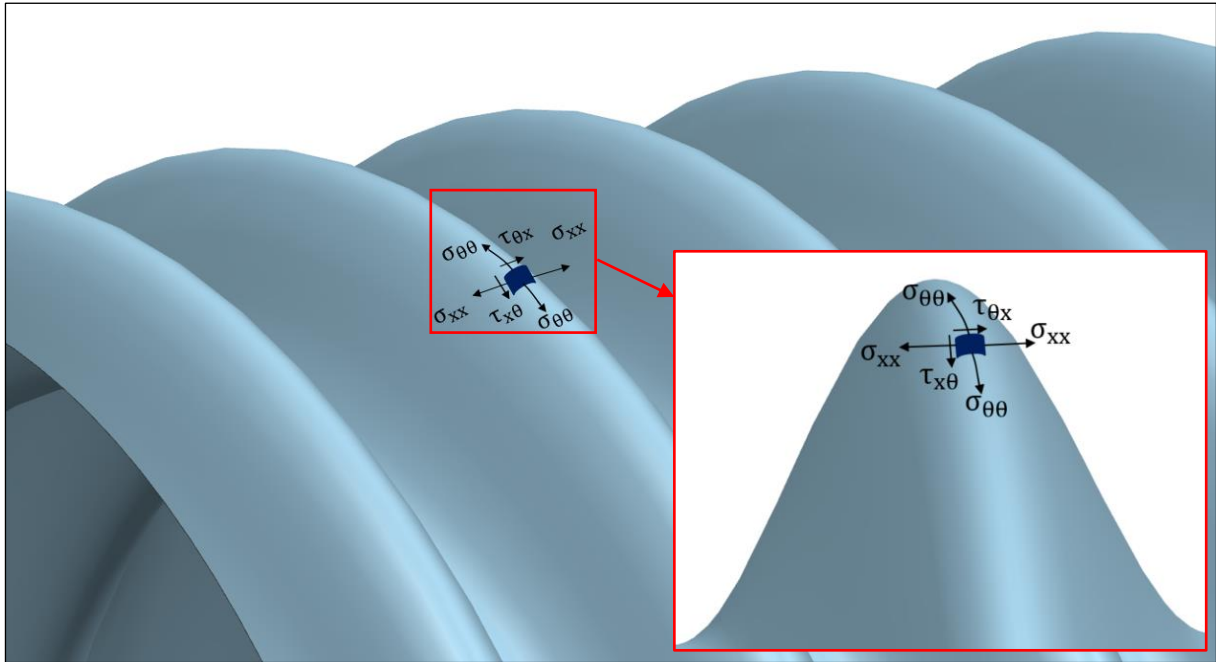


Figure 34: Residual stress components acting in a MCTS wall element based on cylindrical coordinate directions

Prior to the performed X-ray diffraction measurements various parameters and settings had to be adjusted and considered. The various utilized X-ray diffraction parameters can be found in Appendix C. To sum up, among other things, noise and background radiation was subtracted by measuring the gain from a Ti plate, since Ti does not have any diffraction peaks within the measured range of tilted X-ray angles. During the measurements, a total of 9 tilt angles were used. The stress verification was performed for low stresses on low-stress samples made of AISI316 powder, and for high stresses on high-stress shot-peened AISI316 samples. The stress verification resulted in various  $\pm$  stress values, at different stress ranges, presented in Table 12. The  $\pm$  stress values are the statistical variance obtained through last squares regression method.

Table 12: Stress verification of the performed X-ray diffraction measurements

Stress sample (AISI316)	Stress [MPa]	Shear [MPa]
Low (powder)	$5.25 \pm 35.00$	$7.80 \pm 17.00$
High (shoot-peened)	$-598.00 \pm 13.00$	$30.00 \pm 6.70$

5.2 X-ray Diffraction

During the measurements, it proved to be difficult to measure the axial stress components in the wave trough area. The reason for this was mainly due to the small space available in the area due to the convex and sharp cornering. Also, several unforeseen problems related to the stress calibration and X-ray tube focus occurred during the measurements. This entailed that the various measurements had to be performed several times before the correct values could be obtained, which led to time-related problems considering thesis delivery. Because of this, various stress components at some areas around the two tube surfaces were omitted from the X-ray diffraction measurements.

The various measurements were performed at four different locations on each tube. Tube (1 – 2) was measured at 1, 3, 6 and 9 o'clock, visualized in Figure 35, while tube (2 – 2) was measured at 12, 3, 6 and 9 o'clock, visualized in Figure 36. As mentioned, the two test tubes were delivered with a global inherent curvature. Tube (1 – 2) was max global convex over the 1 o'clock location, while tube (2 – 2) was max global convex over the 12 o'clock location.

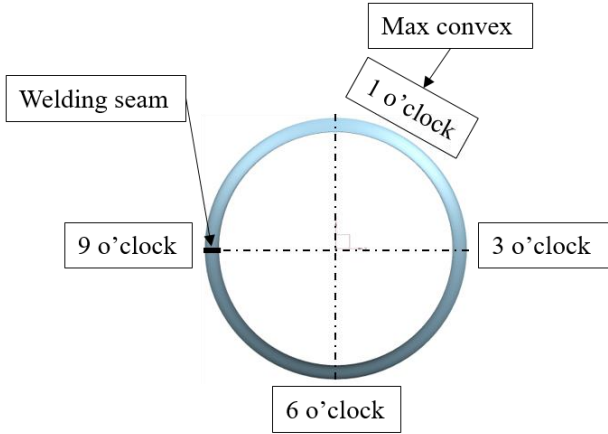


Figure 35: Tube (1 – 2) seen from the front

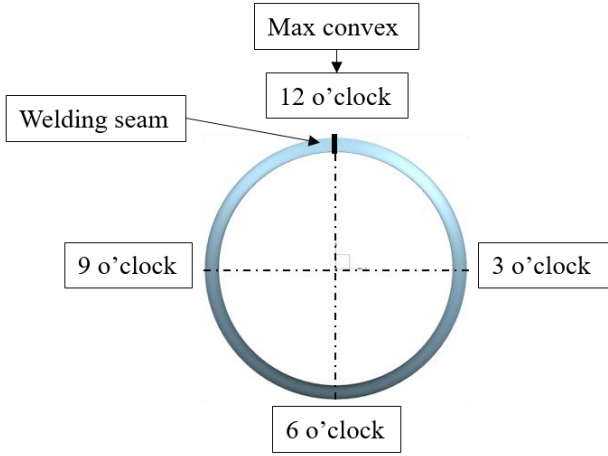


Figure 36: Tube (2 – 2) seen from the front



## 6 Finite Element Method – Theory and Utilized Tools

### 6.1 Software

The different MCTS 3D models were mainly pre-processed by utilization of NX 10 and 11 CAD software, but also by the FEA software Abaqus. For evaluation and simulation of the various 3D models, Abaqus was the preferred software. The result postprocessing was also performed in Abaqus in collaboration with Excel.

#### 6.1.1 NX

NX 10 and 11 is a Product Lifecycle Management (PLM) software from developed by Siemens. From the PLM software, various technologies and functions are available. One of them was the chosen CAD software, NX 10 and 11.

#### 6.1.2 Abaqus FEA

Abaqus FEA is a Dassault software package, consisting of different modules for FEA. For some of the pre-processing and post-processing (in collaboration with Excel) Abaqus/CAE version 6.14-1 was utilized. For the evaluation and simulation both Abaqus/Standard (implicit integration solver) and Abaqus/Explicit (explicit integration solver) was utilized. A general overview of the FEA process is visualized in Figure 37.

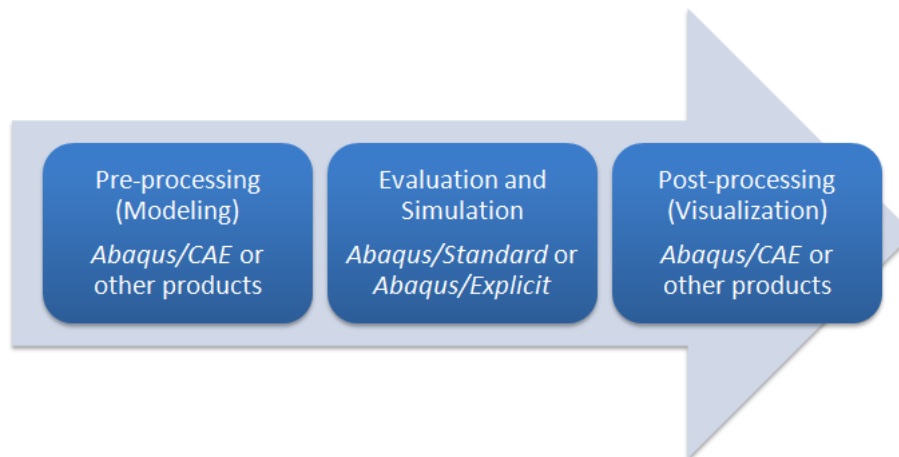


Figure 37: FEA process [42]

## 6.2 General

### 6.2 General

There exists a large amount of literature that deals with the theory behind and the use of finite element method (FEM). This report will not go further into basic background material, considering FEM, and it is therefore assumed that the reader is familiar with this type of subject.

#### 6.2.1 Governing Equations

For a static analysis, the following global matrix equation yields, including all degrees of freedom involved in the analysis:

$$\mathbf{R} = \mathbf{K}(\mathbf{r})\mathbf{r} \quad (6.1)$$

Where,  $\mathbf{R}$  is the load vector,  $\mathbf{K}$  is the stiffness matrix and  $\mathbf{r}$  is the displacement vector.

For dynamic analysis, the following global matrix equation typically yields, including all degrees of freedom involved in the analysis:

$$\mathbf{M}\ddot{\mathbf{r}} + \mathbf{C}\dot{\mathbf{r}} + \mathbf{K}\mathbf{r} = \mathbf{Q}(t) \quad (6.2)$$

Where,  $\mathbf{M}$  is the mass matrix,  $\mathbf{C}$  is the damping matrix,  $\mathbf{K}$  and  $\mathbf{r}$  is the same as for the static equation (6.1) and  $\mathbf{Q}(t)$  is termed the global dynamic load vector.

The mentioned equations can both involve linear and nonlinear behaviour.

### 6.3 Nonlinear FEM

A structure alone or a structural assembly can experience four types of nonlinear behaviour during a structural analysis, that is:

- Material
- Geometrical
- Force boundary condition
- Displacement boundary condition

For a MCTS exposed to axial displacement and/or bending the material and geometrical nonlinearity is the most likely behaviours to occur, if plasticity is present and/or the corrugated geometry changes considerably during loading. In real applications, displacement boundary condition nonlinearities also yield, considering contact between the MCTS and its touching layers within the HV power cable. Table 13, summaries the four different nonlinearities characterizations and differences [43].

*Table 13: Comparison of the typical nonlinearities exposing a structure and/or its assembly [43]*

<b>Nonlinearity</b>	<b>Physical source</b>	<b>Applications</b>
Material	The behaviour of the material is determined by the current deformation state and possibly the past deformation history	Structures experiencing nonlinear elasticity, plasticity etc.
Geometrical	The deformation of the structure, and therefore the change of geometry, is considered when calculating the equilibrium and strain-displacement equations	Slim structures; Forming of metals and plastics; Stability analysis; Tensile structures like cables and inflatable membranes
Force boundary condition	The applied force is dependent on deformation	Pressure loads of fluids

6.3 Nonlinear FEM

Displacement boundary condition	Dependent on the structural deformation	Contact problems, that is dynamical contact, including a condition of non-enforced interpenetration simultaneously as the extent of contact area is unknown
---------------------------------	---	---

## 6.4 Elements

Shell theory is appropriate to utilize for structural problems if the thickness is thin compared to characteristic surface dimensions. By using shell theory, a 3D continuum problem can be approximated with 2D theory, which is computationally effective during FEA.

A smooth and corrugated tubular sheath is produced with a relatively slim thickness, noted in subsection 2.4.3, compared to a characteristic surface dimension of the tube, that is length or circumference. Hence, the models utilized during the FEAs in this thesis were meshed with shell elements, that is the general-purpose conventional shell elements S4R, especially, but also S3R.

### 6.4.1 General-Purpose Conventional Shell Elements

The general-purpose conventional shell elements allow shear deformation through the thickness. These elements follow the thick shell theory formulation of Mindlin-Reissner when thickness increases, allowing shear deformation. However, when thickness decrease, these elements become discrete Kirchhoff thin shells, which not account for shear deformation [24].

#### S4R

S4R, visualized in Figure 38, is a conventional stress/displacement (S), robust 4-node, quadrilateral shell element including linear interpolation, reduced integration (R), hourglass control and a finite-strain formulation. S4R is available in both Abaqus/Standard and Abaqus/Explicit and it is applicable for many different applications [24].

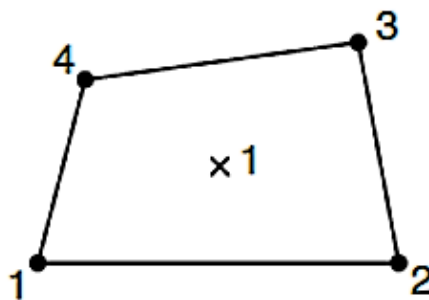


Figure 38: S4R element [24]

#### S3R

S3R, visualized in Figure 39, is a conventional stress/displacement (S), 3-node, triangular shell element including linear interpolation, reduced integration (R), hourglass control and a finite-strain formulation [24].

## 6.4 Elements

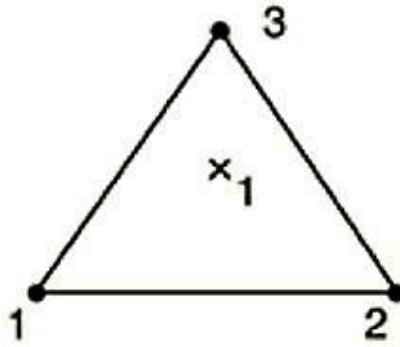


Figure 39: S3R element [24]

S3R provides a satisfactory result in most loading situations. However, it is worth to notice that the S3R elements approximates constant bending and membrane strain, meaning that a high mesh refinement often is required to provide accurate results for loading situations involving pure bending or high strain gradients [24].

### 6.4.2 Reduced Integration

For fully integrated first-order elements, like S4 and S3, reduced integration lowers the amount of integration points down to only one point, without reducing the integration accuracy of the mass matrix and distributed loadings. In many situations, reduced integration proves to improve computational time and often provides more accurate results than without, given that elements are not either distorted or exposed to in-plane bending [24].

### 6.4.3 Hourglassing

A fully integrated first-order element, not employing reduced integration, exposed to dominant bending loading, do not hourglass but can experience both shear and volumetric locking.

The volumetric locking phenomenon can occur for first-order fully integrated elements assigned an almost incompressible material behaviour, hyperelastic materials for instance. Hence, this phenomenon is not of any importance for the performed FEAs in this thesis. However, when this phenomenon is present, spurious pressure stresses evolves at the integration points, making the element behave artificial stiff. Then, the element is unable to bend without changing its volume at each integration point for a deformation where no volume change should be necessary. For first-order fully integrated elements, this phenomenon can be avoided by employing reduced integration [24].

The shear locking phenomenon, tends to form the first-order element into a trapezoidal form, visualized in Figure 40.

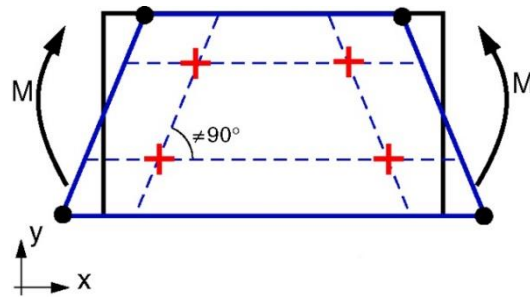


Figure 40: Shear locking of a fully integrated linear element [24]

Shear locking generates shear strains at the integration points that not exist, also called parasitic shear, making the element behave artificial stiff during bending [24]. In Abaqus, shear locking can be avoided by employing reduced integration, visualized in Figure 41.

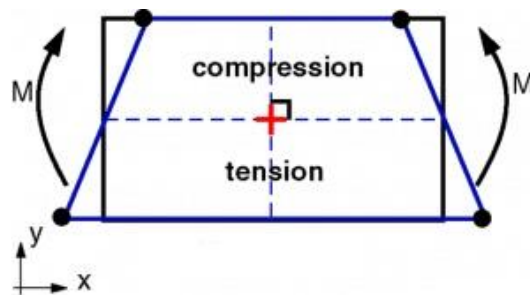


Figure 41: Hourglassing of a first order reduced integration element [24]

However, a first-order element employing reduced integration cannot obtain strains at the interpolation point in the element centre during pure bending, this phenomenon is called hourglassing, shown in Figure 41. In Abaqus, hourglassing can be avoided or counteracted by refining the mesh or employing hourglass control, which in Abaqus comprises off several various algorithms. In general the hourglass control in Abaqus introduces an “artificial” stiffness to the element to restrict this “stress free” mode of deformation [24].

## 6.5 Multipoint Constraint

### 6.5 Multipoint Constraint

During the FEAs involving bending of the MCTS, multipoint constraint (MPC) type beam was utilized in each end of the tube to transmit forced angular displacement. This boundary condition is described in section 7.6.2. This section intends to present an overview of theory behind this constraint.

The two most common rigid body elements (RBE) existing in FEM is the RBE2 and RBE3. They are both typical MPC elements and are commonly used to connect one node to one or several node(s).

The main difference between these formulations is that RBE2 involves one independent node while the rests DOFs are dependent of that node, that is a master-slave relationship. RBE3 formulation, on the other hand, is similar, but allows one dependent node and one or several independent node(s), where DOFs can be selected/unselected both at the dependent and independent node(s). Also, in the RBE3 formulation, various DOFs can be selected/unselected for the independent nodes, which is different from RBE2 where only one determined set of DOFs is transmitted to the dependent nodes by the chosen master node. A RBE2 constraint behaves infinitely stiff, this is not the case for a RBE3 [44].

In Abaqus, RBE2 is called MPC beam, while RBE3 is called Coupling. The MPC beam constraint in Abaqus constrain the displacement and rotation at a selected master node to the displacement and rotation of one or several slave nodes. A rigid beam will be established between the master and slave nodes, making the slave nodes behave according to the given rotation and/or displacement of the master node [24].



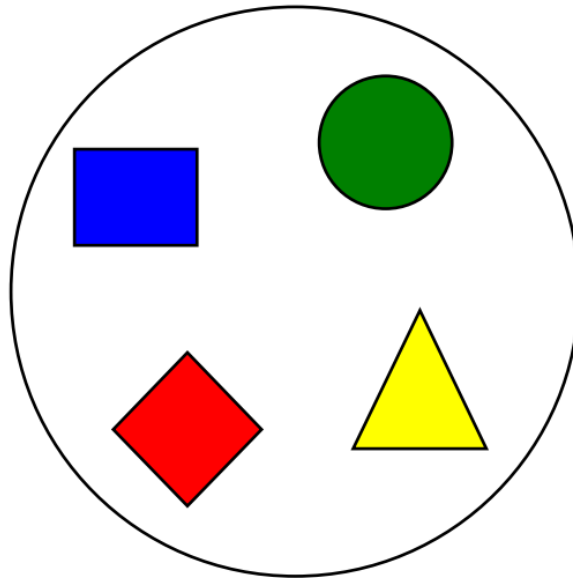
## 6.6 Contact Interaction

During the FEAs for the four-point bending model, detailed described in section 7.7, involves contact interaction. This section intends to present a brief introduction to the chosen contact interaction algorithm. For a deeper understanding, the reader is recommended to study the contact literature described by Dassault Systemes [24].

Contact is the most discontinuous nonlinearity form that can be present within a FEM analysis. Abaqus offer two different interaction algorithms for contact modelling, which both can be used within Abaqus/Standard and Abaqus/Explicit:

- General contact
- Contact pair

General contact algorithm, requires only one single interaction definition to define contact between regions. The possibly interacting surfaces comprises of the contact domain, visualized in Figure 42, and can include many various disconnected regions. When using the general contact algorithm, master/slave roles automatically is assigned to the surfaces.



*Figure 42: General contact [24]*

Contact pair algorithm, requires a precise contact definition between every surface that might come in contact interaction, or is in contact interaction from the beginning of the simulation. This is visualized in Figure 43. When using the contact pair algorithm, the surfaces in each contact pair that is, or might come in contact during the analysis must be assigned master/slave roles manually.

6.6 Contact Interaction

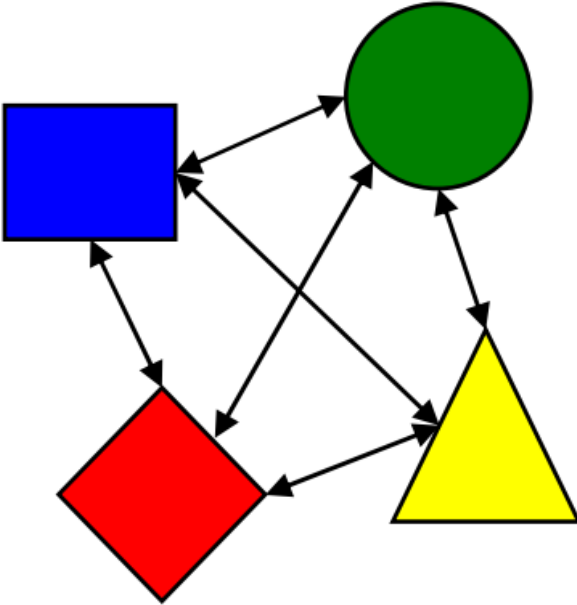


Figure 43: Contact pairs [24]

The general contact algorithm applies the penalty method for contact constraints, while contact pairs offers the choice between penalty and kinematic compliance method. When choosing algorithm for the four-point bending analysis, described in section 7.7, the main criterions were simplicity and computational time. General contact algorithm is reckoned to, usually, be faster than the contact pair algorithm and to be better for models involving complex topology, which the corrugated geometry could be considered as. Hence, general contact algorithm was chosen [24].

## 6.7 Abaqus/Standard vs Abaqus/Explicit

Abaqus/Standard can analyse problems including, but not limited to:

- Linear and nonlinear static
- Linear dynamic
- Low speed (low frequency response) nonlinear dynamic

In Abaqus/Standard an implicit time integration is utilized.

Abaqus/Explicit can analyse problems including, but not limited to:

- High speed (short duration) dynamics
- Large nonlinear quasi-static analyses
- Post buckling and collapse simulations that is highly discontinuous

In Abaqus/Explicit an explicit time integration is utilized [24].

### 6.7.1 Time Integration

For dynamic FEM analysis, the condition of dynamic equilibrium can be written as:

$$\mathbf{P} - \mathbf{I} = \mathbf{M}\ddot{\mathbf{r}} \quad (6.3)$$

Where  $\mathbf{P}$  is the external force vector,  $\mathbf{I}$  is the internal force vector and  $\mathbf{M}\ddot{\mathbf{r}}$  is the material inertia force vector. When material inertia forces are small, or constant with time, equation (6.2) forms into the static equilibrium equation (6.1) [24].

The implicit time integration typically not include inertial effects, which means that equation (6.2) turns into equation (6.1), that is static equilibrium.

Implicit time integration solves for increment,  $(t + \Delta t)$ , without knowing it, by guessing the state at  $(t + \Delta t)$  and using  $t$ . The guessing of the later system state could entail several iterations to reach equilibrium condition. The implicit time integration is unconditionally stable and a large time step is possible, but for nonlinear problems the stiffness matrix needs to be inverted, many equations needs to be solved and small iterative steps are probably required to obtain convergence. For highly nonlinear situations, like contact interaction for instance, convergence is not guaranteed [24].

The explicit time integration, on the other hand, solves for increment,  $(t + \Delta t)$ , based on the information already known in  $t$ , that is the system state at the current time. At the end of each increment, the explicit time integration calculates a new stiffness matrix based on changes in geometry and/or material, before the next increment of load/displacement is applied [24].

## 6.7 Abaqus/Standard vs Abaqus/Explicit

The explicit method employs elements using a lumped<sup>8</sup> mass matrix, which makes it easy to determine nodal accelerations:

$$\ddot{\mathbf{r}} \Big|_{(t)} = \mathbf{M}^{-1}(\mathbf{P} - \mathbf{I}) \Big|_{(t)} \quad (6.4)$$

Further, the explicit time integration utilizes the central difference method of integration, to update velocities and displacement, without the need for any iteration. A drawback of an explicit time integration is that it is unconditionally stable, which means that it becomes unstable when the time steps is too large [24].

In this thesis, both nonlinear static problems and highly nonlinear contact problems were analysed. For the nonlinear static problems, Abaqus/Standard, that is implicit time integration, was chosen as method, due to its unconditionally stability and possibility of employing large time steps. For the nonlinear contact problems, Abaqus/Explicit, that is explicit time integration, was chosen as method, due to computational efficiency considering the high nonlinearity that contact interaction impose.

### 6.7.2 Explicit – Stability

To maintain stability in an explicit analysis, it is important to always ensure that the time step,  $\Delta t$ , is smaller than the critical time step,  $\Delta t_{cr}$ . If this stability criterion is not maintained, the model could experience an oscillation response and become unstable. Critical time step,  $\Delta t_{cr}$ , for an undamped model can be defined as:

$$\Delta t_{cr} \leq \frac{L^e}{c_d}, \text{ (Damping will reduce } \Delta t_{cr} \text{)} \quad (6.5)$$

Where,  $L^e$ , is the characteristic length of the smallest utilized element in the model, and  $c_d$  is the acoustic wave speed in the material.  $c_d$ , can, for a linear elastic material (with  $\nu = 0$ ), be determined from:

$$c_d = \sqrt{\frac{E}{\rho}} \quad (6.6)$$

Where,  $E$  and  $\rho$  is respectively the material young's modulus and density. Decreasing the,  $L^e$ , or increasing,  $c_d$ , will lower the stable time increment, which implies that mesh size, among other factors, is an important parameter in a numerical explicit analysis. A mesh refinement will lead to an increased number of necessary time increments for the analysis to maintain

---

<sup>8</sup> Mass is distributed to the element nodes which creates a diagonal mass matrix

stability which again will increase the computational time. Hence, the stability criterion is very important to consider [24].

### 6.7.3 Explicit – Energy Balance

A small time step does not necessarily mean that an explicit analysis will provide meaningful results. One must in addition ensure that the energy balance of the system is satisfactory, that is tolerably constant throughout the analysis. This means that no energy should disappear or be added to the system.

For validity check of the energy balance in an explicit analysis, the energy balance equation (6.7), could be utilized. The variables are further described in Table 14.

The most useful indications when evaluating an explicit analysis and its validation, is the “artificial” strain energy,  $E_{AE}$ , and the amount of kinetic energy,  $E_{KE}$ . The “artificial” strain energy,  $E_{AE}$ , which is a measure on the “artificial” added stiffness, mentioned in subsection 6.4.3, is used by Abaqus to suppress hourglass modes. This energy output should not exceed 1 – 2% of the internal energy,  $E_I$ . In a quasi-static analysis, which the four-point bending analysis described in section 7.7 is, the kinetic energy,  $E_{KE}$ , should not exceed 5 – 10% of the internal energy,  $E_I$  [24].

$$E_I + E_{VD} + E_{FD} + E_{KE} - E_W = E_{TOT} = \text{constant} \quad (6.7)$$

Table 14: Energy definitions in Abaqus [24]

Variable	Definition
$E_{TOT}$	Total energy in the system
$E_W$	Work done by external forces
$E_{KE}$	Kinetic energy
$E_{FD}$	Frictional dissipation energy
$E_{VD}$	Amount of absorbed energy by viscous dissipation
$E_I$	Internal energy comprising of elastic, $E_{SE}$ , inelastic, $E_{PD}$ , and “artificial” strain energy, $E_{AE}$ .

### 6.8 Quasi-Static Analysis in Abaqus/Explicit

A highly nonlinear static problem, involving contact and large deformation for instance, can be handled efficiently by using the explicit solver in Abaqus and solve the problem by a quasi-static approach. This means that motions are made slow, such that inertia forces are neglected or insignificant.

When the dynamic explicit solver is utilized, solving a quasi-static problem, considerations with respect to approaching the problem in a computationally efficient way is specially required. The system's natural time period, that is during a real test/simulation, would require a large amount of time increments, leading to an uneconomical computational time. However, in Abaqus, it is possible to artificially speed up the simulation process and hence, obtain an economical solution. This can be done by either increasing the load rates, or scale the mass of the model [24]. By increasing the load rate, the time scale is artificially lowered which can cause an artificially high material strain rate if the material is strain rate sensitive.

Mass scaling, on the other hand, increases the stable time increment and allows for utilization of the system's natural time scale during the quasi-static analysis. This approach is especially appropriate when dealing with a strain rate sensitive material [24].

Both methods, increasing the load rate or scaling the mass, provides the same effect, that is fewer increments are needed to complete the analysis. However, speeding up the simulation, means that inertia forces become more dominant because the state of static equilibrium gradually alters into a state of dynamic equilibrium [24].

For the quasi-static analysis performed in this thesis, that is the four-point bending model described in section 7.7, the load rate method was chosen.

#### 6.8.1 Load Rate

When performing a quasi-static analysis, the goal is to perform the simulation as fast as possible while simultaneously keeping the inertia forces at a low level.

A rule of thumb, considering the highest possible load rate which can approximately be performed during a quasi-static analysis, is to calculate the natural eigenfrequencies of the model. The first structural mode will be the dominant response. Afterwards, the first natural eigenfrequency,  $f_1$ , can be used to calculate the time period,  $T$ , by the following equation:

$$T = \frac{1}{f_1} \quad (6.8)$$

The impact velocity in the simulation can be estimated by the following equation:

$$V = \frac{D}{T} \quad (6.9)$$

Where,  $D$  is the estimated deflection in the direction of impact. It is recommended to keep the impact speed less than 1% the acoustic wave speed of the material, which for most metals is approximately 5000 m/s [24].

### 6.8.2 Modal Analysis

The natural frequency is the frequency at which an undamped system/model tend to oscillate. The natural frequencies can be found, based on equation (6.2), from the following equation:

$$\left(-\omega^2\mathbf{M} + \mathbf{K}\right)\phi = 0 \quad (6.10)$$

Where,  $\omega$ , denotes the angular eigenfrequency and  $\phi$ , is the corresponding eigenvector (vibration mode) [24]. Abaqus offers three different methods of extracting the natural eigenfrequencies from a model, that is:

- Lanczos
- Automatic multi-level substructuring (AMS)
- Subspace iteration

The reader can acquire information about the different solvers by reading the Dassault Systemes [24]. In this thesis, the modal analysis was performed by utilizing the AMS solver.

6.8 Quasi-Static Analysis in Abaqus/Explicit



## 7 Finite Element Method – Pre-processing, Evaluation and Simulation

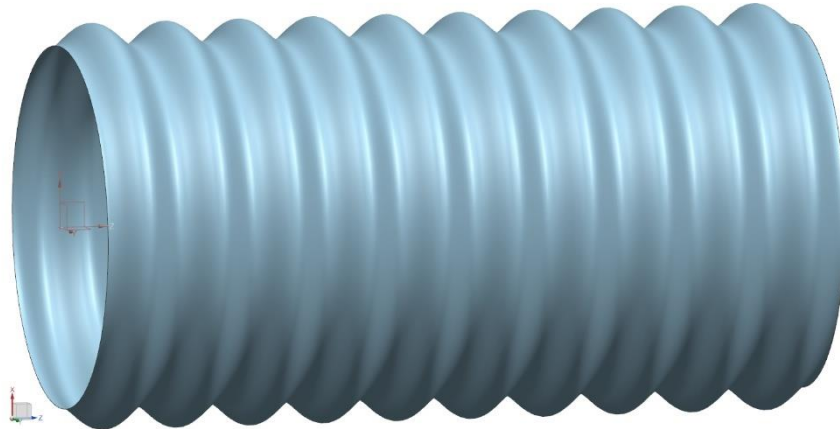
For the 3D models of the MCTS and the subsequently FEAs in this thesis, a sinusoidal corrugation wave geometry was chosen and applied. This type of wave geometry was chosen because of the easy sinusoidal function definition, which made it easy to parametrize the 3D models. A parametrization of the utilized 3D models was important, to simplify the process of varying the various corrugation wave geometry parameters, visualized in subsection 2.3.7. The utilized sinusoidal corrugation wave geometry can be defined by the following equation:

$$f(i) = A \cdot \sin(ki + \varphi) + c \quad (7.1)$$

Where,  $i = (x, y \text{ or } z)$  dependent of choice of revolving axis,  $A$  (amplitude) and  $k$  are positive variables and  $\varphi$  describes the phase displacement. Parameter  $c$ , denotes the middle line where the sine curve values fluctuates around.

### 7.1 3D model – Annular Metallic Corrugated Tubular Sheathing

A typical view of a 3D model of an annular MCTS, modelled in NX, is presented in Figure 44.



*Figure 44: Typical 3D model view of an annular MCTS*

#### 7.1.1 Parametrization

The 3D model parametrization of the annular MCTS was based on the “law curve” tool in NX, making it possible to draw a parametrized spline in the XY plane that further could be revolved around the axial axis to create a tubular sheathing. The “law curve” was parametrized based on the sinus equation defined in equation (7.1). Figure 45, shows and describes the parametrization of the annular MCTS in NX, enabled by the tool “Expressions”.

7.1 3D model – Annular Metallic Corrugated Tubular Sheathing

The screenshot shows the 'Expressions' window in NX software. It features a 'Listed Expressions' section with a search filter set to 'Named'. Below this are three checkboxes: 'Show Groups' (unchecked), 'Show Active Group Only' (unchecked), and 'Show Locked Formula Expressions' (unchecked). The main area contains a table with the following data:

Name	Formula	Value	Units	Type	Up t...	Comment
A	8	8	mm	Num...	✓	Amplitude
OR	50+A	58	mm	Num...	✓	Outer radius of corrugated tubular sheathing
P	56	56	mm	Num...	✓	Corrugation pitch (P)
Periods	2	2		Num...	✓	Number of corrugated periods
t (Law Defined Spline(2) X Law: Function Parameter)	0	0		Num...	✓	
xt (Law Defined Spline(2) X Law: Function Equation)	$A \cdot \sin(\text{Periods} \cdot 360 \cdot t - 90) + \text{OR}$	50		Num...	✓	Phase displacement of 90 degrees
yt (Law Defined Spline(2) Y Law: Function Equation)	$P \cdot (\text{Periods} \cdot t)$	0		Num...	✓	
zt (Law Defined Spline(2) Z Law: Function Equation)	0	0		Num...	✓	

Figure 45: NX tool “Expressions” enabling the parametrization of the annular MCTS 3D model

## 7.2 3D model – Helical Metallic Corrugated Tubular Sheathing

A typical view of a 3D model of a helical MCTS, modelled in NX, is presented in Figure 46.

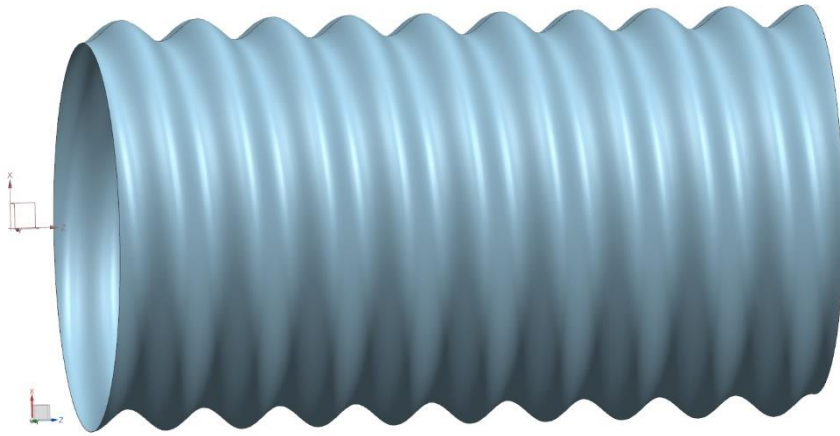


Figure 46: Typical 3D model view of a helical MCTS

### 7.2.1 Parametrization

The 3D model parametrization of the helical MCTS was partly built on the same principle as for the annular MCTS described above, in subsection 7.1.1. However, to enable a helical wave pattern, a new “law curve” was established, that is a spline-formed helix. A helix is characterized as a smooth three-dimensional space curve with the property of having a constant inclination angle with the chosen axial axis. Mathematically, a circular helix can be parametrized by the following parameters:

$$\begin{aligned} x(t) &= a \cos(t) \\ y(t) &= a \sin(t) \\ z(t) &= bt \end{aligned} \tag{7.2}$$

Where,  $a$  is the radius and  $b$  defines the slope. The inclination angle, also called lead angle, is the angle between the helix curve and the plane of rotation, and can be defined as:

$$\text{Inclination angle (lead angle)} = \arctan\left(\frac{l}{\pi d_m}\right) \tag{7.3}$$

Where,  $l$ , is the helix lead, visualized in Figure 47, and  $d_m$ , is the mean diameter of the helix [45].

## 7.2 3D model – Helical Metallic Corrugated Tubular Sheathing

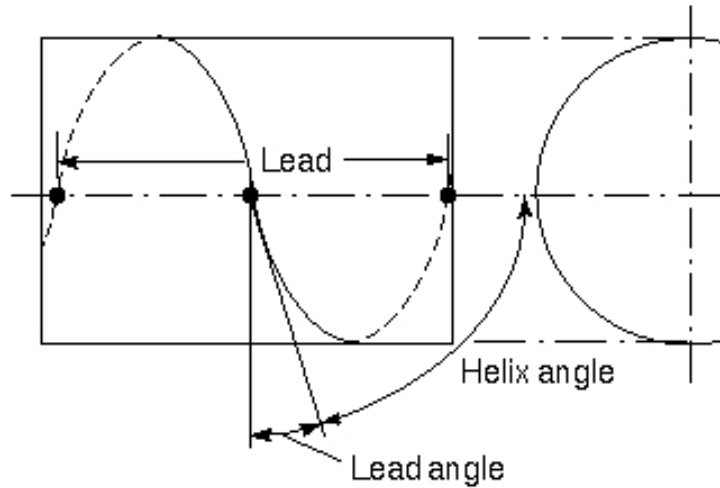


Figure 47: Helix inclination angle (lead angle) [45]

Hence, the parametrized sinusoidal “law curve” could be swept along the helix path, enabling the establishment of a helical MCTS, as shown in Figure 46. The helix was parametrized based on the mathematical definition noted in equation (7.2), allowing the variation of inclination angle of the helical corrugation wave pattern. Figure 45, shows and describes the parametrization of the helical MCTS in NX, enabled by the tool “Expressions”.

Name	Formula	Value	Units	Type	Up t...	Comment
A	3	3	mm	Num...	✓	Amplitude
Inclination_angle	$\text{atan}(\frac{P * \text{Inclination\_nothes}}{\pi * 2 * \text{radius}})$	3.824251...	degr...	Num...	✓	Inclination angle (lead angle) with the plane of rotation
Inclination_nothes	1	1		Num...	✓	The number of axial pitch-lengths within the lead of the helix
no_turns	1	1		Num...	✓	
OR	radius+A	53	mm	Num...	✓	
P	21	21	mm	Num...	✓	Corrugation pitch (P)
Periods	110	110		Num...	✓	Number of corrugated periods
radius	50	50	mm	Num...	✓	
t_helix (Law Defined Spline(1) X Law: Function Parameter)	0	0		Num...	✓	
t_sine (Law Defined Spline(2) X Law: Function Parameter)	0	0		Num...	✓	
teta	360	360	degr...	Num...	✓	
xt_helix (Law Defined Spline(1) X Law: Function Equation)	$\text{radius} * \cos(\text{teta} * \text{t\_helix} * \text{no\_turns})$	50		Num...	✓	
xt_sine (Law Defined Spline(2) X Law: Function Equation)	$A * \sin(\text{Periods} * 360 * \text{t\_sine} - 90) + \text{OR}$	50		Num...	✓	Phase displacement of 90 degrees
yt_helix (Law Defined Spline(1) Y Law: Function Equation)	$\text{radius} * \sin(\text{teta} * \text{no\_turns} * \text{t\_helix})$	0		Num...	✓	
yt_sine (Law Defined Spline(2) Y Law: Function Equation)	0	0		Num...	✓	
zt_helix (Law Defined Spline(1) Z Law: Function Equation)	$P * \text{no\_turns} * \text{Inclination\_nothes} * \text{t\_helix}$	0		Num...	✓	
zt_sine (Law Defined Spline(2) Z Law: Function Equation)	$P * (\text{Periods} * \text{t\_sine})$	0	mm	Num...	✓	

Figure 48: NX tool “Expressions” enabling the parametrization of the helical MCTS 3D model

The helical inclination angle defined in the NX 3D model is dependent on the helix lead,  $l$ , visualized in Figure 47, which is the advance of the helix during a complete rotational turn ( $360^\circ$ ). This advance is, for the 3D model, a function of the corrugation pitch (P) and the number of corrugated wavelengths, where one wavelength equals the distance of one P. This is, visualized in Figure 49 and Figure 50.

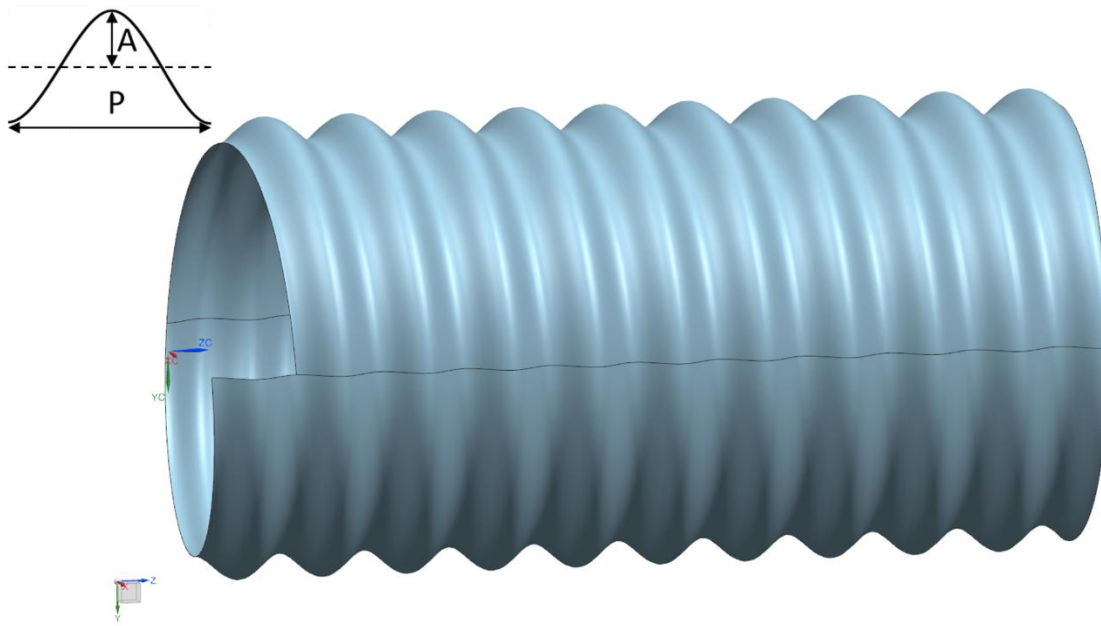


Figure 49: Visualization of a helical MCTS, untrimmed in one end, and at its lowest possible inclination angle, that is a lead distance comprising of  $(1 \cdot P)$ .

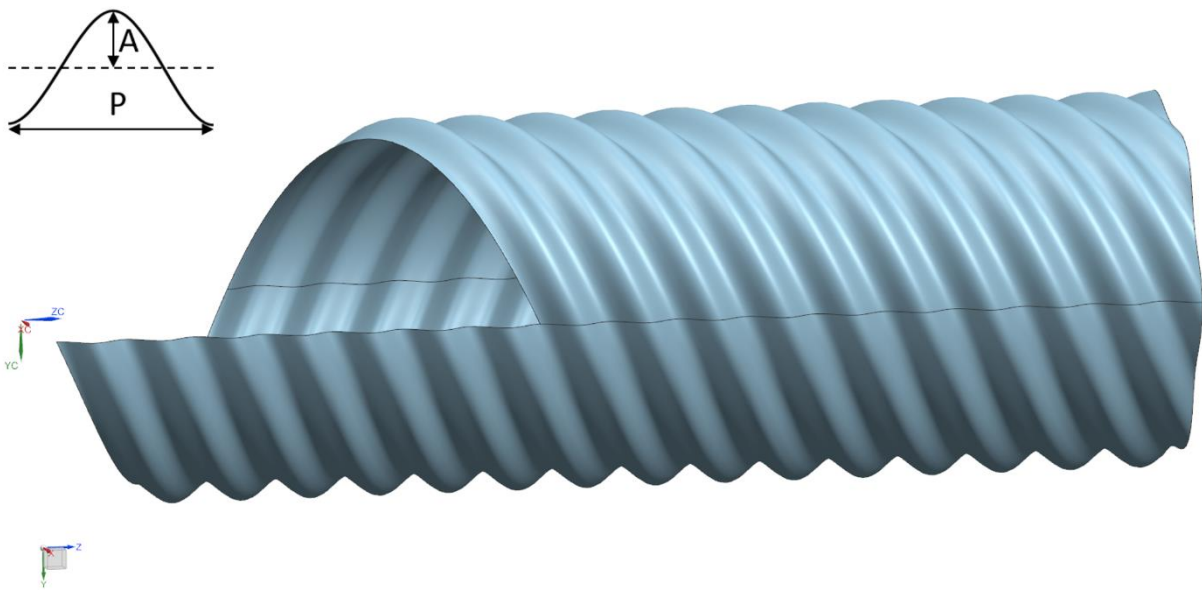


Figure 50: Visualization of a helical MCTS, untrimmed in one end, and at its highest possible inclination angle analysed within this thesis, that is a lead distance comprising of  $(7 \cdot P)$ .

## 7.3 Units

### 7.3 Units

Abaqus has no built-in units, except the rotational DOFs (expressed as radians) and angle measures (expressed in degrees). Hence, the operator must choose a consistent unit system and follow this throughout the FEA process. Table 15, notes the chosen units in Abaqus.

*Table 15: Utilized unit-system during the FEA process in Abaqus*

<b>Quantity</b>	Length	Force	Mass	Time	Stress	Energy	Density
<b>Unit</b>	mm	N	$\text{kg} \cdot 10^3$	<i>s</i>	MPa	$\text{J} \cdot 10^{-3}$	$\frac{\text{kg} \cdot 10^3}{\text{mm}^3}$

## 7.4 Material Models

### 7.4.1 X70 Steel

Proper material properties were missing when performing the static axial and bending analysis for the MCTS. Hence, a temporary steel material, that is X70 steel, was used to be able to receive an impression of how plasticity affected the results. The plastic effect was assumed to give the same trend using one of the other materials discussed in section 2.3.3 – 2.3.5. The material properties were given by SINTEF and included elastic-plastic properties, presented in Table 16 and Figure 51.

Table 16: X70 elastic properties and density

<b>E [MPa]</b>	<b><math>\nu</math></b>	<b><math>\rho</math> [Kg/m<sup>3</sup>]</b>
196000.0	0.3	7800.0

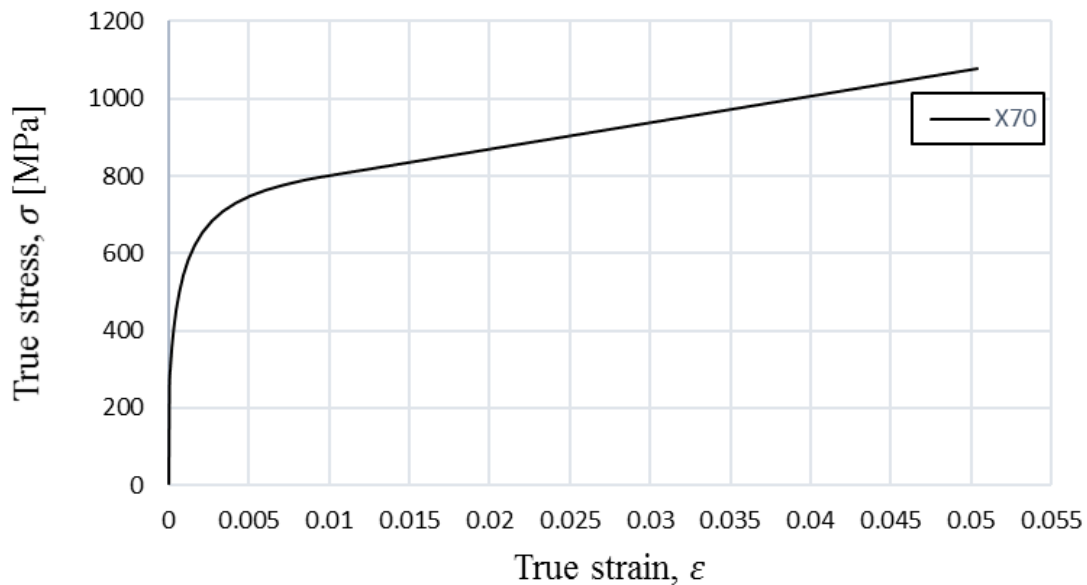


Figure 51: Material curve X70 steel

### 7.4.2 AISI316

The four-point bending analysis, described in section 7.7, was performed with two different AISI316 sheath materials, that is AISI316L and AISI316L+Ti. Both materials are described further in section 5.1. From the received material data, two elastic-plastic bilinear models, presented in Table 17 and Figure 52, were created and utilized in Abaqus.

## 7.4 Material Models

Table 17: Material properties for the various AISI316-materials obtained from Nexans

Material	E [MPa]	$\nu$	$\rho$ [Kg/m <sup>3</sup> ]
AISI316L	167000.0	0.3	8000.0
AISI316L+Ti	150000.0	0.3	8000.0

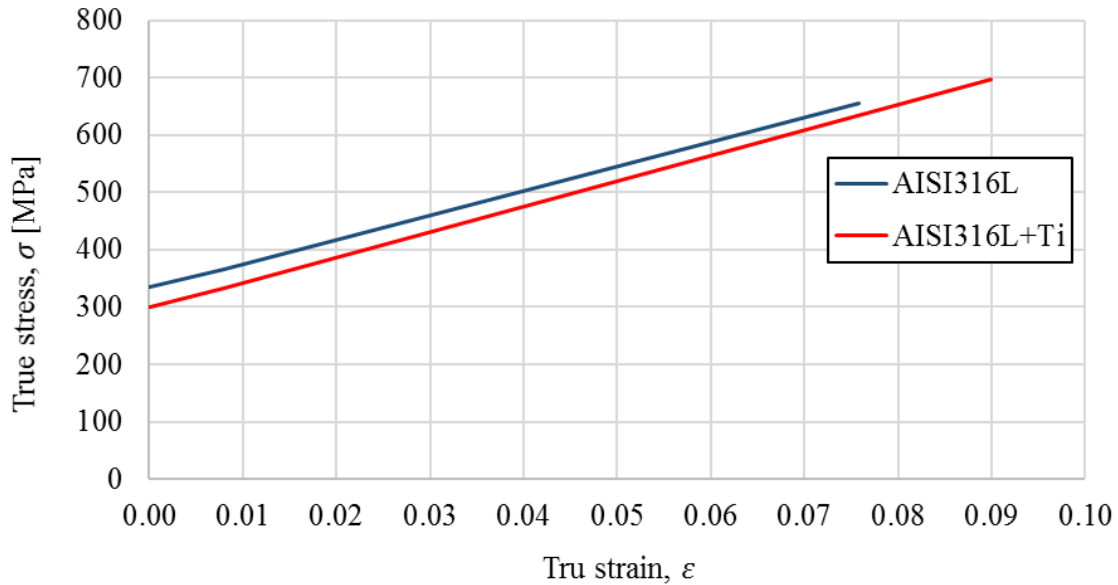


Figure 52: Bilinear material models of AISI316L and AISI316L+Ti

### 7.4.3 XLPE

During the four-point bending analysis described in 7.7, insulation was added inside the tubes for comparison purposes. The insulation was assigned elastic material properties only. The utilized material properties are presented in Table 18.

Table 18: XLPE elastic material properties [46-48]

E [MPa]	$\nu$	$\rho$ [Kg/m <sup>3</sup> ]
350.0	0.4	930.0

### 7.4.4 Strain Hardening Model

For every FEA done in this thesis, the isotropic strain hardening model, discussed in section 3.3.1, was assumed and utilized in Abaqus.



## 7.5 Static Axial Analysis

In chapter 4, it was discussed and mentioned that a dynamic HV subsea power cable, and thus a MCTS, especially is exposed to global bending forces both during reeling/unreeling and during its operational lifetime offshore. The global forces induce both axial and bending forces. Hence, these stress factors were of interest to analyse. First and foremost, axial analysis of the MCTS was performed, where the main goal was to research the significance of varying the geometrical parameters, presented in section 2.3.7, considering strain development along the corrugation wave geometry.

Prior to the axial analysis, several assumptions were made for simplicity, both considering the modelling point of view but also with respect to the FEA computational efficiency. Assumptions made and applied are listed in Table 19.

*Table 19: Assumptions and choices made for the axial analysis*

<b>Parameter</b>	<b>Assumptions/choices</b>	<b>Comments</b>
Wave pattern	Annular wave pattern was applied, meaning that a helical wave pattern was neglected	An annular corrugation wave pattern was chosen due to computational efficiency. The error made under this assumption was assumed neglectable, as the corrugation pitch was short relative to the tubular sheathing diameter;  To validity check the above-mentioned assumption and to analyse the helical inclination angle sensitivity during axial displacement, a helical MCTS, with two different P/A ratios, was analysed for comparison purpose
Number of corrugation wavelengths along the tubular sheathing	Two wavelengths of annular sinusoidal corrugated wave geometry were applied for modelling and FEA simplicity	In terms of the number of wavelengths required, several wavelengths were considered, but after a FEA comparison of specimens with various numbers of wavelengths, an annular MCTS with two sinusoidal wavelengths were chosen

## 7.5 Static Axial Analysis

Modelling technique	Surface modelling was applied	Surface modelling was applied due to the thin sheath thicknesses, in order to decrease the FEA computational time
Geometrical symmetry	Due to symmetry, one quarter of the whole circular cross section of the MCTS was modelled and applied throughout the FEA	Symmetry was applied to simplify the 3D-modelling and reduce the possibly time consuming FEA

### 7.5.1 Design Input

The design input for the MCTS during the axial analysis, that is  $D_i$  and MCTS thicknesses,  $t$ , is presented in Table 20. Combinations of  $P$  and  $A$ , that is different  $P/A$  ratios, applied in the FEA is found in Table 20.

Table 20: Design input for the axial analysis of the MCTS

MCTS $D_i$ [mm]	MCTS thickness [mm]	$P$ [mm]	$A$ [mm]	$P/A$
100.0	0.7 – 1.0	3.0 – 56.0	3.0 – 8.0	1.0 – 7.0

### 7.5.2 Boundary conditions

The FEA of the axial analysis was performed by inducing a controlled axial displacement of 5% of axial length of each specimen defined by the following equation:

$$\Delta U_{axially} = 0.05 \cdot (\text{axial length}) = 0.05 \cdot ((\text{number of wavelengths}) \cdot P) \quad (7.4)$$

Figure 53, shows the utilized axial displacement boundary condition. Each specimen was fixed in rotational DOF at both ends and free in the radial direction at both ends. One end, that is the bottom edge visualized in Figure 53, was fixed in the axial direction, while the other end, that is the top edge, visualized Figure 53, was introduced to the controlled axial displacement mentioned above and defined in equation (7.4).

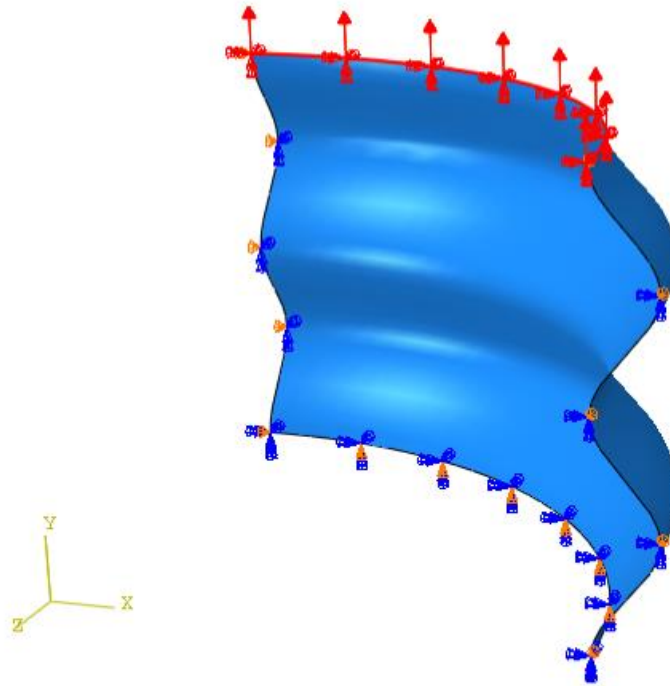


Figure 53: Axial displacement boundary conditions

For comparison purpose, a smooth tubular sheathing was modelled and introduced to the same type of boundary conditions as the annular MCTS. Also, as mentioned in Table 19 considering the assumptions, a helical MCTS, with a whole cross-section, was introduced to the same boundary conditions as the annular MCTS for validity check.

### 7.5.3 Mesh

All the one-quarter 3D models were meshed in Abaqus prior to the FEA. The helical, whole cross-section, MCTSs were meshed in NX and subsequently exported to Abaqus.

The shell element applied for the MCTS during the axial analysis was S4R. This element type was described in detail in section 6.4.1. Table 21 and Figure 54, presents and visualize typical utilized mesh properties for a one quarter MCTS.

Table 21: Typical mesh properties for one quarter of the MCTS during axial analysis

<b>P [mm]</b>	<b>A [mm]</b>	<b>Shell element</b>	<b>No. of nodes</b>	<b>No. of elements</b>
21	3	S4R	4658	4488

7.5 Static Axial Analysis

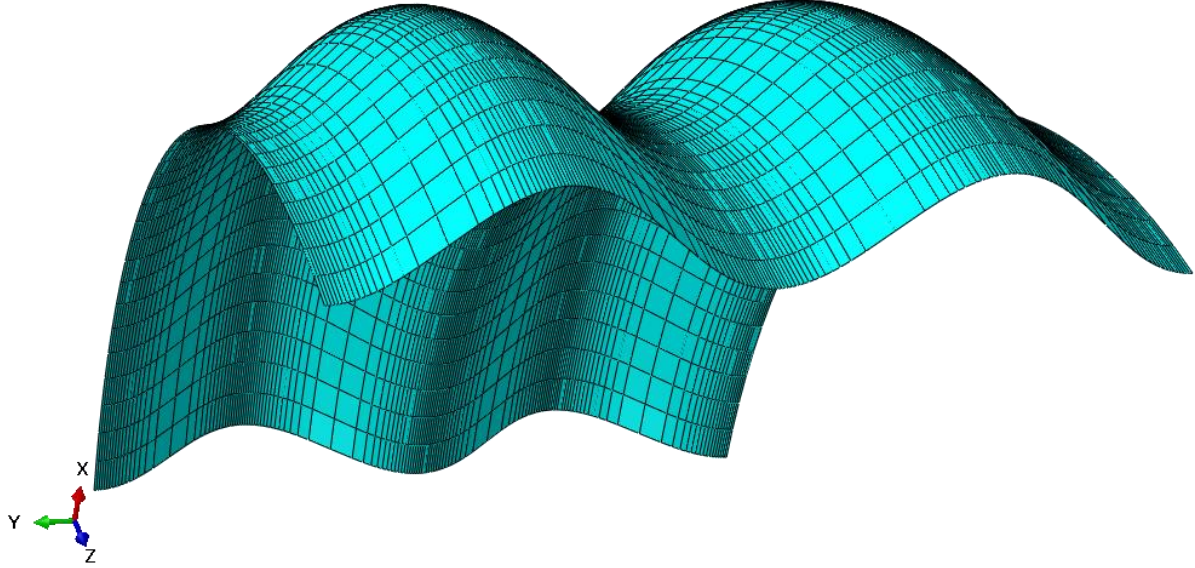


Figure 54: S4R mesh for  $P=21\text{mm}$  and  $A=3\text{mm}$ .

## 7.6 Static Bending Analysis

Subsequent to the axial analysis, it was of interest to build on the extracted axial results by perform bending analysis of the MCTS. The main goal for the bending analysis was to check whether variation of inclination angle had any significance on the strain development along the corrugated geometry during bending.

The introduction of helical wave pattern eliminated the possibility of utilizing any form of symmetry, considering the MCTS 3D model. Hence, the whole cross section of the model had to be considered during the FEA. This increased the required number of mesh elements and nodes leading to a decreased computational efficiency.

### 7.6.1 Design input

Prior to the performed bending analysis, it was decided to analyse two different P/A ratios that had a certain range in between them. Based on the results from the axial analysis, and input from Nexans, the various geometrical parameters presented in Table 22 were selected as design input.

*Table 22: Design input bending analysis*

<b>Model</b>	<b>MCTS <math>D_i</math> [mm]</b>	<b>t [mm]</b>	<b>P [mm]</b>	<b>A [mm]</b>	<b>P/A</b>
1	100.0	0.6	10.0	5.0	2.0
2	100.0	0.6	21.0	3.0	7.0

Table 23, describes the design input for the bending analysis with respect to variation of the helix inclination angle (lead angle) for the two chosen MCTS models. The various inclination angles were calculated by utilizing equation (7.3).

*Table 23: Design input with respect to variation of inclination angle (lead angle)*

<b>No. of wavelengths within helix lead</b>	<b>Helix lead [mm]</b> <b>(No. of wavelengths within helix lead · P)</b>		<b>Inclination angle (lead angle) [degree]</b>	
	<b>Model 1</b>	<b>Model 2</b>	<b>Model 1</b>	<b>Model 2</b>
0	Annular MCTS	Annular MCTS	Annular MCTS	Annular MCTS

7.6 Static Bending Analysis

1	10.00	21.00	1.82	3.82
2	20.00	42.00	3.64	7.61
3	30.00	63.00	5.45	11.34
4	40.00	84.00	7.26	14.97
5	50.00	105.00	9.04	18.48
6	60.00	126.00	10.81	21.85
7	70.00	147.00	12.56	25.08

7.6.2 Boundary Conditions

When deciding which method to enable for the bending analysis, the main criterions were simplicity, reproducibility and computational efficiency. A bending analysis involving contact interaction for instance, was reckoned to decrease the computational efficiency. Hence, the contact interaction approach was brushed aside. Another approach, not involving any contact interaction, was to utilize a MPC beam, described in section 6.5 and visualized in Figure 55, at each end of the MCTS to transmit an angular forced displacement to the whole MCTS. After some trial and error, this approach was chosen, due to its simplicity, reproducibility and computational efficiency, compared to the contact interaction approach.

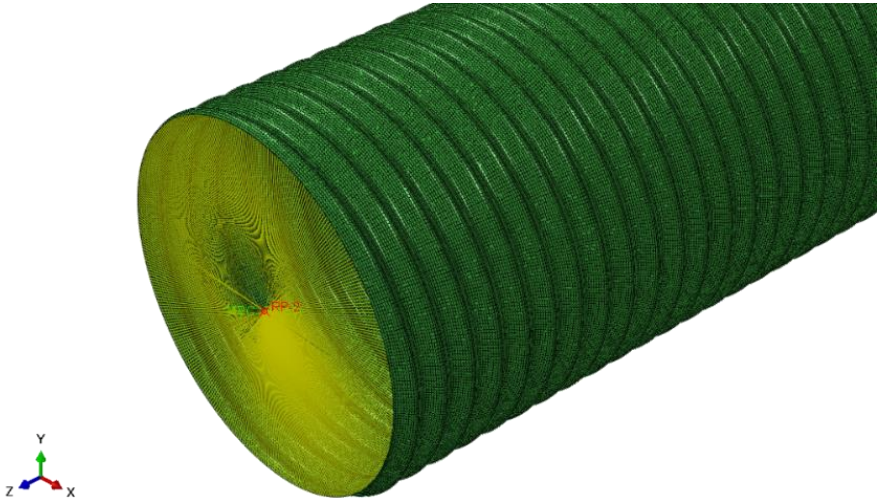


Figure 55: MPC beam constraint with one master node in the centre and slave nodes around the end perimeter of the MCTS

As mentioned in section 6.5, an MPC beam constraint transmits infinite stiffness. This infinite stiffness which the MPC beam transmitted in each end of the tubes proved to create a somewhat

artificial local stress and strain concentration close to the tube ends. This artificial localization turned out to decrease and level out the longer MCTS length that was analysed. However, a longer MCTS length resulted in an increased computational time, since the number of elements and nodes would increase with an increasing length. Hence, a compromise had to be made considering the choice of maximum MCTS length to be analysed. After some trial and errors, a maximum MCTS length of 35 wavelengths, that is an axial length of  $35 \cdot P$ , was decided.

Afterwards, a simple model to calculate the amount of forced angular displacement at each tube end was created. The most conservative bending radius a MCTS (probably) will experience during its lifetime is occurring during the cable drum reeling in the workshop. Hence, the created model was based on the maximum bending radius discussed in section 4.2.

The created model assumed both an elastic behaviour and the same amount of generated contraction/extension for the compressive/tensile side of the MCTS during the bending process. By employing these assumptions, equation (7.5) was utilized for calculating the required angular displacement to enable the MCTS to follow the cable drum curvature.

$$\alpha = \arcsin \left( \frac{\frac{L_{\text{Axial}}}{2}}{\frac{25 \cdot \text{OD}}{2} + \frac{\text{OD}}{2}} \right) \quad (7.5)$$

Where,  $\alpha$  is the required angle in each MCTS end, while OD was assumed to be 150mm and  $L_{\text{Axial}}$  was decided to be equal  $35 \cdot P$ . The created model is visualized in Figure 56, and the utilization of a MPC beam constraint is presented in Figure 55. Table 24, presents the calculated required angular displacements utilized in the various static bending analyses.

*Table 24: Calculated required angular displacement*

<b>Model</b>	<b><math>\alpha</math> [Degree]</b>	<b><math>\alpha</math> [rad]</b>	<b><math>L_{\text{Axial}}</math> [mm]</b>
1	5.15	0.09	350.00
2	10.86	0.19	735.00

## 7.6 Static Bending Analysis

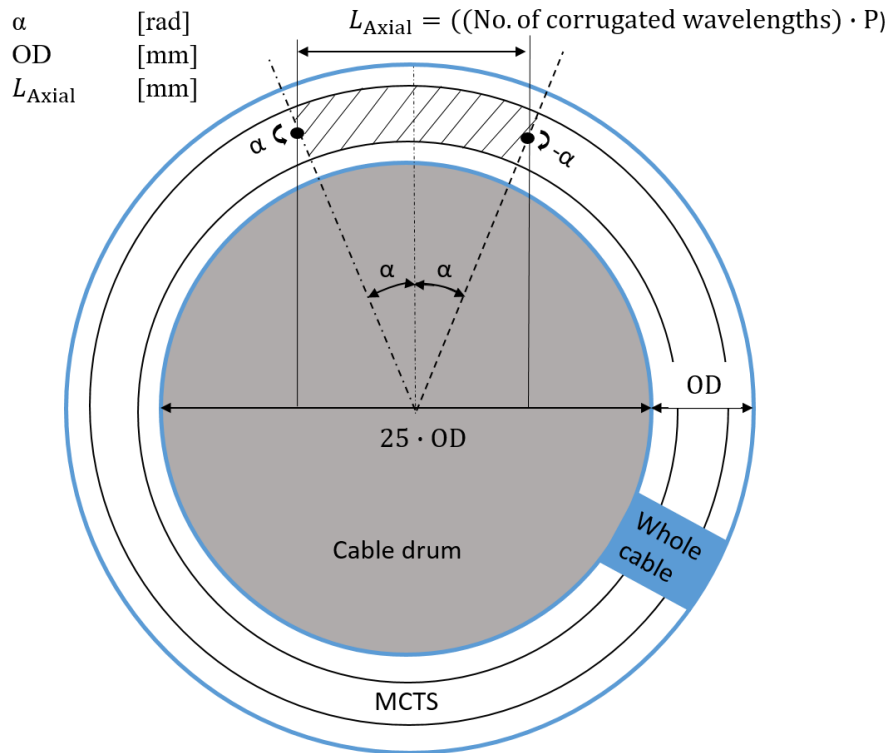


Figure 56: Method and model for calculating the required forced angular displacement

### 7.6.3 Mesh

All the models exposed to bending analysis were meshed within the NX software and subsequently exported into Abaqus.

The shell element applied for the MCTS during the bending analysis was both S4R and S3R, both described in section 6.4.1.

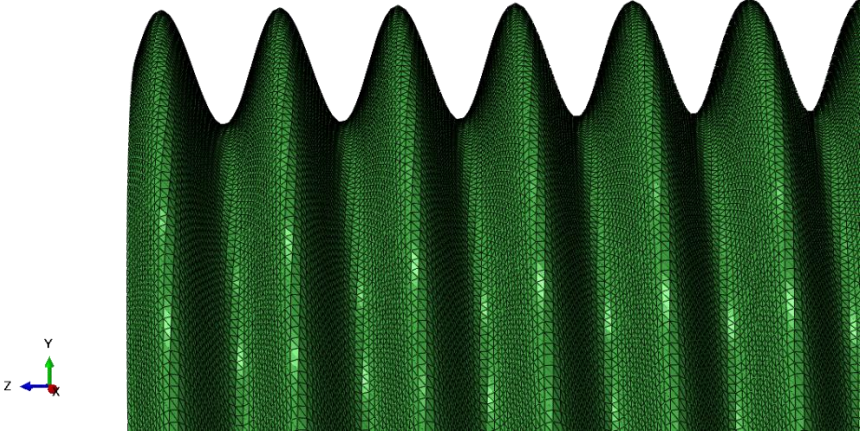
Model 1, had an aggressive and sharp corrugation which required a refined mesh if utilizing S4R, which again would create a comprehensive number of elements and nodes that would drastically reduce computational efficiency. Hence, a refined S3R mesh was utilized for model 1. Model 2, contained a less aggressive corrugation, which enabled the possibility to utilize a refined S4R mesh without necessarily compromising on computational efficiency. However, at higher angles of helical inclination, warping of some S4R elements occurred. Hence, it was decided to weave in more and more S3R elements the greater the angle of inclination was to remove the warping warnings. Table 25 and Table 26, respectively, describes and visualizes the utilized mesh properties for some of the models exposed to the bending analysis.



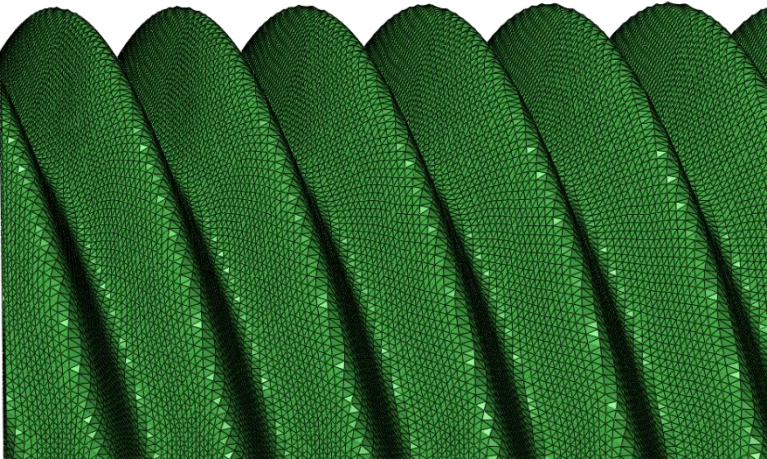
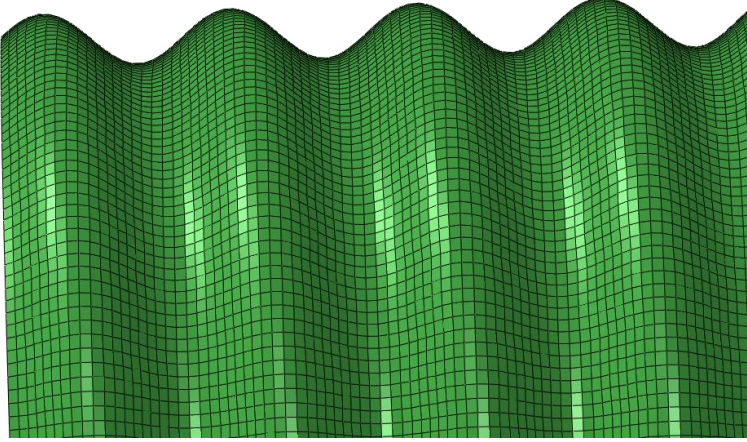
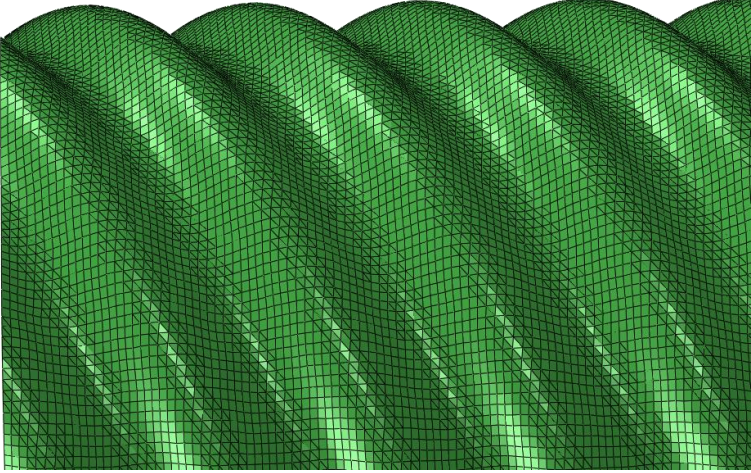
Table 25: Description of mesh properties for some of the MCTS models exposed to bending analysis

Model	Inclination angle (lead angle) [degree]	Shell element	No. of nodes	No. of elements
1	1.82	S3R	402906	805070
	12.56	S3R	393816	786656
2	3.82	S4R	157920	157696
	25.08	S3R	190060	148556
		S4R		115522

Table 26: Visualization of mesh properties for some of the MCTS models exposed to static bending analysis

Model	Inclination angle [deg]	Mesh
1	1.82	

7.6 Static Bending Analysis

1	12.56	 <p>A 3D finite element mesh plot showing a periodic structure with sharp, rounded peaks. The mesh is colored in shades of green. A small 3D coordinate system is visible in the bottom-left corner, with the Y-axis pointing up, the X-axis pointing right, and the Z-axis pointing out of the page.</p>
2	3.82	 <p>A 3D finite element mesh plot showing a periodic structure with smooth, rounded waves. The mesh is colored in shades of green. A small 3D coordinate system is visible in the bottom-left corner, with the Y-axis pointing up, the X-axis pointing right, and the Z-axis pointing out of the page.</p>
2	25.08	 <p>A 3D finite element mesh plot showing a periodic structure with sharp, rounded peaks, similar to the first plot. The mesh is colored in shades of green. A small 3D coordinate system is visible in the bottom-left corner, with the Y-axis pointing up, the X-axis pointing right, and the Z-axis pointing out of the page.</p>

## 7.7 Quasi-Static Four-Point Bending Analysis

The intention and main goal of establishing a four-point bending model in Abaqus was to compare virtual results from FEAs with real test results in the workshop if time allowed. However, the experimental part lapsed due to lack of time to be a part of this thesis. Anyhow, the establishment of the four-point bending model would be complimentary for any potentially further work within this topic. Also, by performing virtual four-point bending analysis in Abaqus, one could predict and suggest how to perform the real testing of corrugated tubes in workshop at a later stage, both full scale static bending and fatigue testing.

It was decided to analyse both smooth and corrugated versions of the two different tube types inherent with the most conservative curvature. From Table 11, this proved to be tube (1 – 5) and (2 – 1). Additionally, for comparison purposes, it was decided to expose the corrugated tubes to static bending analysis, in the same way as described in section 7.6.2.

The bending analysis results, presented in section 9.2, indicated that variation of inclination angle during bending had low significance on developed strain, at least for smaller P/A ratios and small inclination angles. Hence, an annular model was utilized for the quasi-static bending analysis. This assumption enabled the utilization of symmetry, which increased the computational efficiency.

### 7.7.1 Design Input

Tube (1 – 5) and (2 – 1) were modelled with the local geometrical values presented in Table 10, and a global axial length based on the mean value of their  $l_1$  and  $l_2$ , presented in Table 11.

### 7.7.2 Modal Analysis

Prior to the quasi-static four-point bending analysis, modal analysis of the involved models were performed, as discussed in section 9.3.2.

When performing the modal analysis, it was important to analyse the whole models without any use of symmetry to extract any unsymmetrical modes. The first resulting natural eigenfrequency and respectively mode shape of the analysed models is presented in section 9.3.2, Table 37. The resulting eigenfrequencies of the different models resulted in the maximum load rates, that is the minimum time period, which is presented in Table 27.

## 7.7 Quasi-Static Four-Point Bending Analysis

Table 27: Maximum load rates (minimum time periods)

<b>Tube</b>	<b>Maximum load rate (minimum time period) [s]</b>
Smooth version of (1 – 5)	0.0052
Smooth version of (2 – 1)	0.0077
(1 – 5)	0.0137
(2 – 1)	0.0167

### 7.7.3 Boundary Conditions

The static bending analysis of the corrugated models of tube (1 – 5) and (2 – 1) were conducted by adding an angular displacement in each MPC master node in each tube end, allowing the tubes to follow the radius of curvature calculated in section 5.1. To determine the required angular displacement, equation (7.5) was utilized. The required angular displacements are presented in Table 28.

Table 28: Calculated required angular displacement of test tubes

<b>Tube</b>	<b><math>\alpha</math> [Degree]</b>	<b><math>\alpha</math> [rad]</b>	<b><math>L_{\text{Axial}}</math> [mm]</b>
(1 – 5)	2.7721	0.0484	420.0000
(2 – 1)	3.8700	0.0675	315.0000

The FEA of the four-point bending model was performed by inducing a controlled vertical forced displacement of the various models corresponding to the measured heights,  $H$ , of tube (1 – 5) and (2 – 1) found in Table 11. This approach made it possible to evaluate how the elastic-plastic strain developed along the corrugation geometry when bending the tubes into the same type of global curvature which the test tubes inherit from the reeling process after production.

Because of symmetric geometry and deformation, the models were split in half both longitudinally and vertically, which also was computationally efficient considering the post FEA. This also meant that the four rolls, for support at the ends and transmitting displacement

at the middle, could be reduced to only two. The rolls were modelled as discrete rigid parts, meaning that they were assumed rigid and hence, undeformable. Figure 57, indicates the utilized set-up and global dimensions for the four-point bending model.

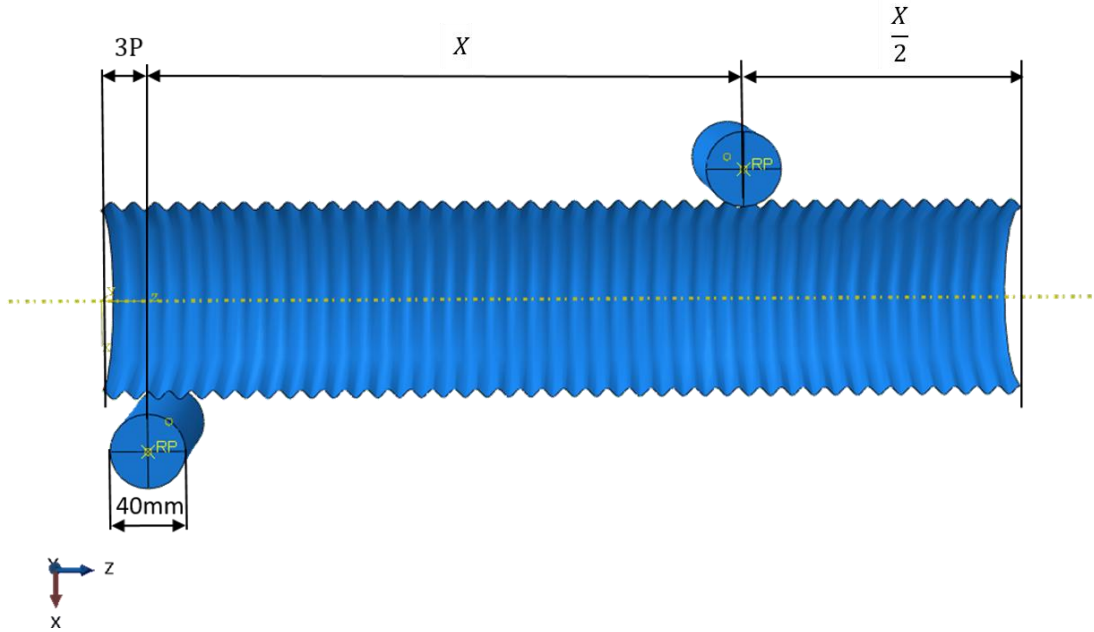


Figure 57: Global dimensions utilized for the four-point bending model

The lower roll was fixed in all DOFs while the upper roll was forced to translate in X-direction (U1) with a given displacement. The vertical split of the model was assigned symmetry properties in Y-direction, while the longitudinal split at the middle was assigned symmetry properties in Z-direction. Figure 58 and Figure 59, describes the utilized symmetries and BC.

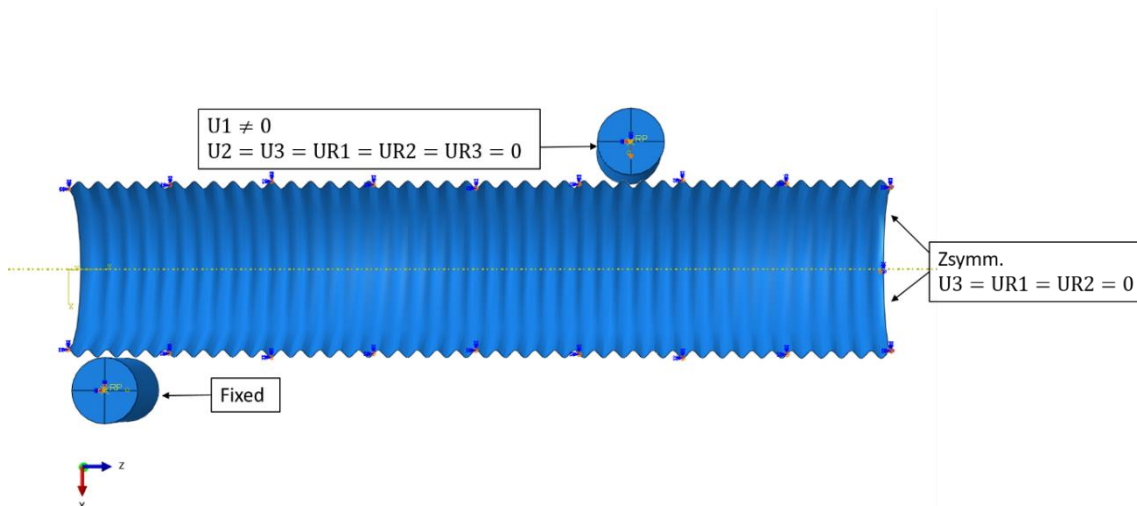


Figure 58: Tube zsymmetry and boundary conditions for the rolls

## 7.7 Quasi-Static Four-Point Bending Analysis

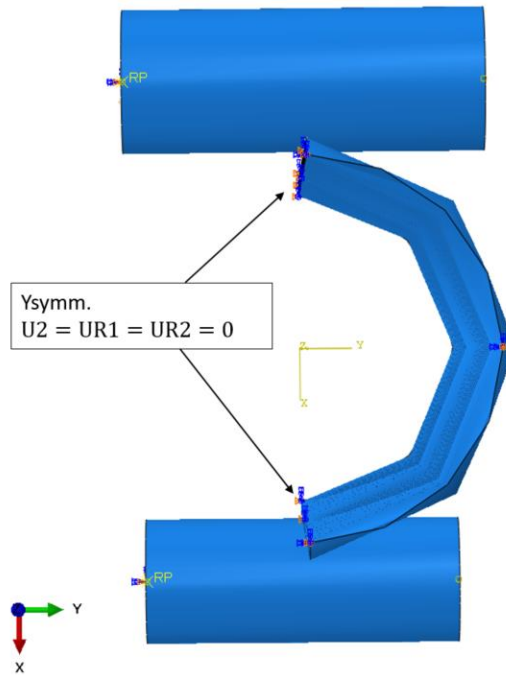


Figure 59: Tube ysymmetry

The forced vertical displacement of all the models were introduced by utilizing the tools: smooth amplitude and BC allocator in Abaqus, visualized in Figure 60.

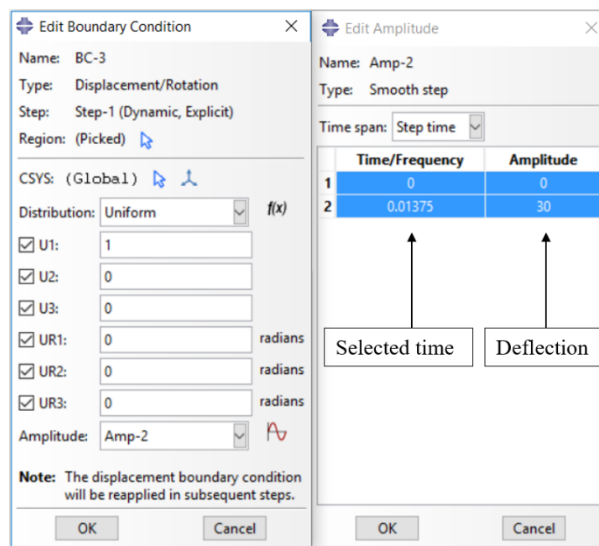


Figure 60: Smooth amplitude and boundary condition allocator

As an addition for comparison purpose, the various tubes were also analysed by four-point bending when filled internally with insulation, visualized in Figure 61. For simplicity and computational efficiency, the conductor and various screens were neglected. The insulation was assigned the same symmetry conditions as the MCTS.

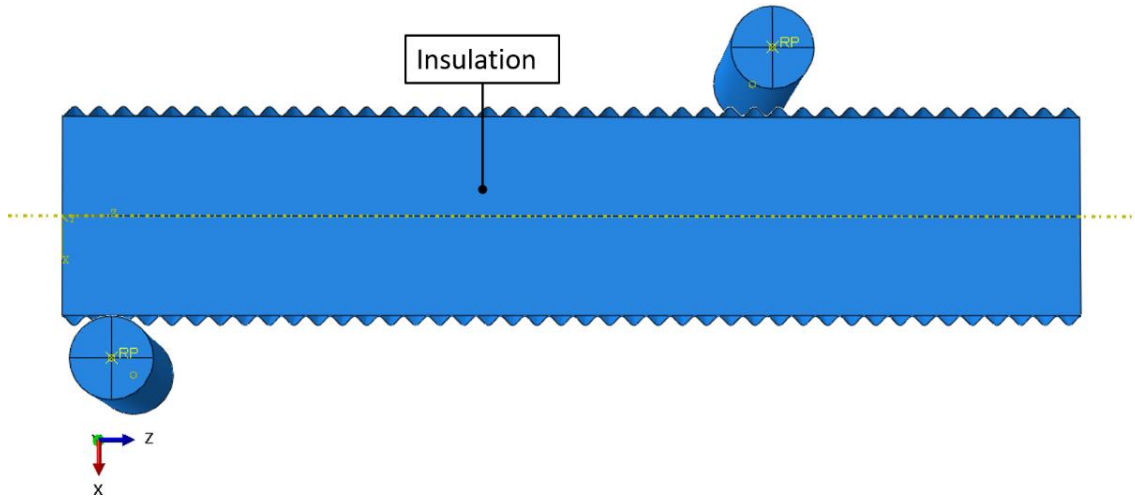


Figure 61: MCTS filled with insulation

#### 7.7.4 Contact

To represent the real-life physical interaction, between the tube/rolls and tube/insulation, during the four-point bending analysis, the general contact algorithm, described in section 6.6, was used. This algorithm automatically identified the possible contact pairs in the model. During the bending of the MCTS models, both tangential and normal contact properties had to be defined. “Hard contact” was chosen as the normal behaviour, while a frictionless formulation was chosen for the tangential behaviour to mimic the actual rotational roller behaviour.

For the contact interaction between the insulation and the sheathing, the same above mentioned normal and tangential behaviour was utilized. The reason for the frictionless choice of tangential behaviour was due to computational efficiency and because it was of interest to only compare and understand how the MCTS reacted when stabilization was added internally during four-point bending.

#### 7.7.5 Mesh

The different 3D models were modelled in NX and subsequently exported into Abaqus where they were meshed. The insulation was meshed with 3D hexahedral elements, that is general linear reduced integration C3D8R elements. The various sheath-models were meshed with S4R elements. Table 29, describes typical mesh properties utilized for the analysed sheaths. Figure 62 and Figure 63, shows a typical mesh for respectively a smooth tube and a corrugated tube.

7.7 Quasi-Static Four-Point Bending Analysis

Table 29: Typical mesh properties utilized for the various models exposed to four-point bending analysis

Tube	Shell element	No. of nodes	No. of elements
Smooth versions	S4R	5080	4914
(1 – 5)	S4R	197349	195936
(2 – 1)	S4R	245203	243520

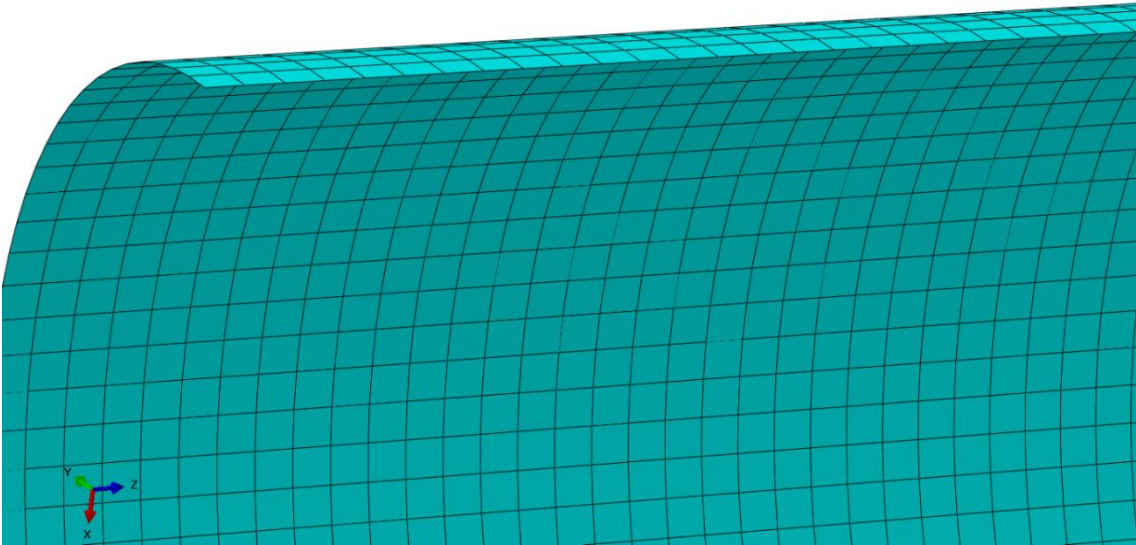


Figure 62: Typical S4R mesh for a smooth version of tube (1 – 5 and (2 – 1) exposed to four-point bending

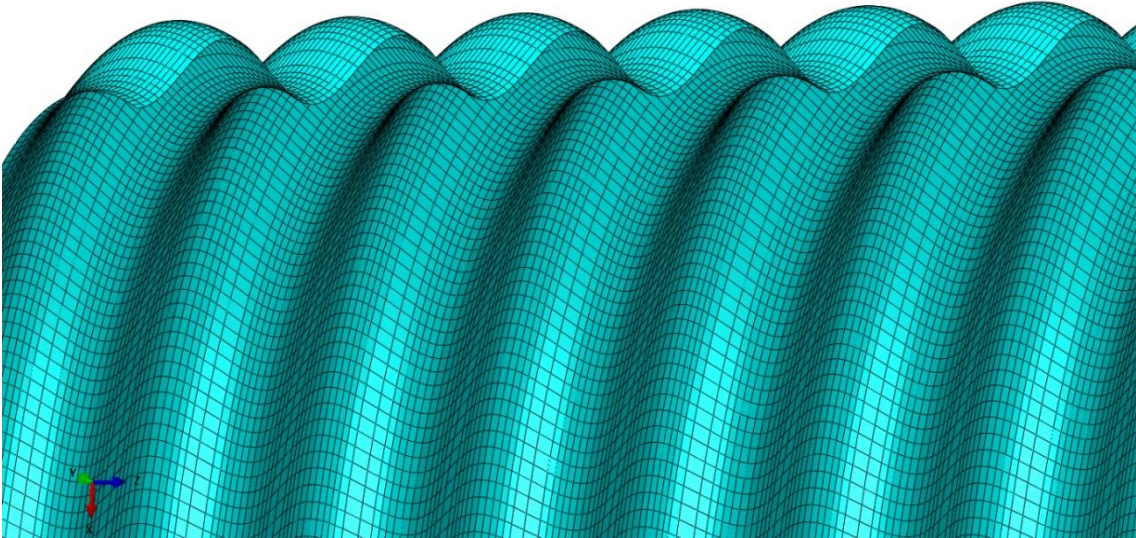


Figure 63: Typical S4R mesh for the corrugated version of tube (1 – 5) and (2 – 1) exposed to four-point bending



## 8 X-ray Diffraction – Results

This chapter presents the results from the X-ray diffraction measurements of residual stresses in tube (1 – 2) and (2 – 2), described in chapter 5. The notation of –, indicates a compressive stress behaviour.

### 8.1 Tube (1 – 2)

#### 8.1.1 Welding Seam – Residual Stresses at Wave Crest Top

Figure 65, presents the X-ray diffraction measurements of residual stresses at the welding seam at the wave crest top at 9 o'clock, visualized in Figure 64, in tube (1 – 2).

The residual hoop stresses ( $\sigma_{\theta\theta}$ ) are scattering, ranging from –15% to 35% of the material yield strength, and it is difficult to predict a trend. However, the plot indicates a relatively high portion of  $\sigma_{\theta\theta}$ , in and around the welding seam, ranging from 21 – 35% of the material yield strength.

The plot indicates a smooth and nearly constant impact of residual hoop shear stresses ( $\tau_{\theta x}$ ) in and around the welding seam. Its values constitute of approximately 15% of the material yield strength.

Considering the residual axial stresses ( $\sigma_{xx}$ ), the appurtenant values are scattered, and the stress values are ranging from –25% to 47% of the material yield strength. However, the plot indicates a relatively high portion of  $\sigma_{xx}$ , in and near the welding seam, ranging from 47% to 27%.

Considering the residual axial shear stresses,  $\tau_{x\theta}$ , the plot indicates a trend where the residual stresses peak in the welding seam (15% of material yield strength), decreasing right outside the welding seam (5 – 6% of material yield strength), subsequently stabilizing at a level in between farther away from the welding seam (9 – 11% of material yield strength).

## 8.1 Tube (1-2)

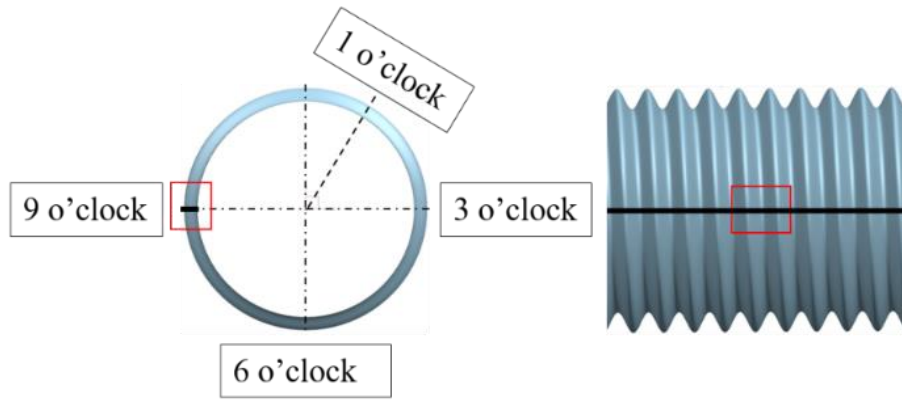


Figure 64: Visualization of 9 o'clock area in tube (1 – 2) where X-ray diffraction measurements were performed in and around the welding seam

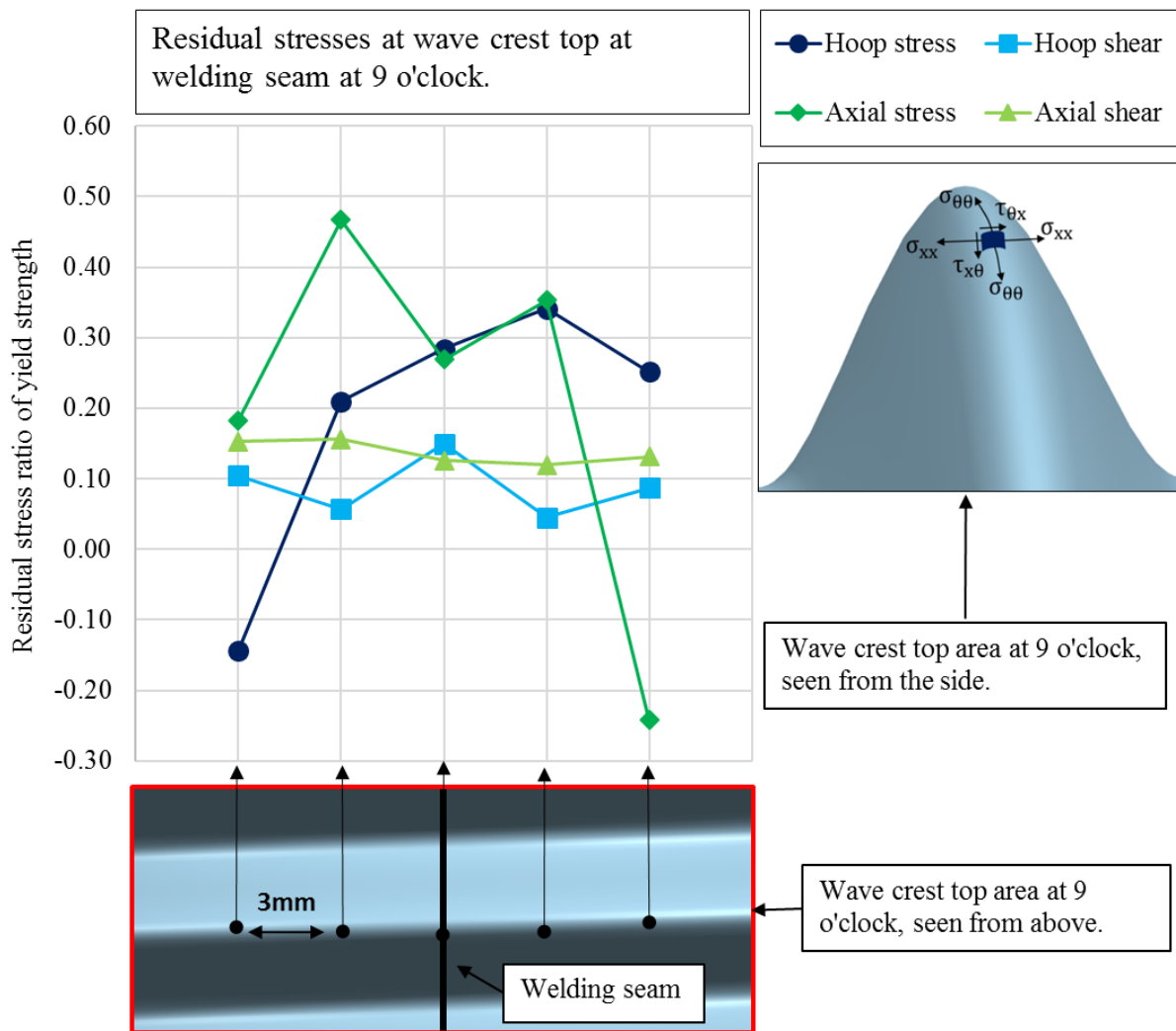


Figure 65 X-ray diffraction measurements of residual stresses at wave crest top at the welding seam at 9 o'clock in tube (1 – 2)

## 8.1.2 Weld-free Areas – Residual Stresses at Wave Crest Top

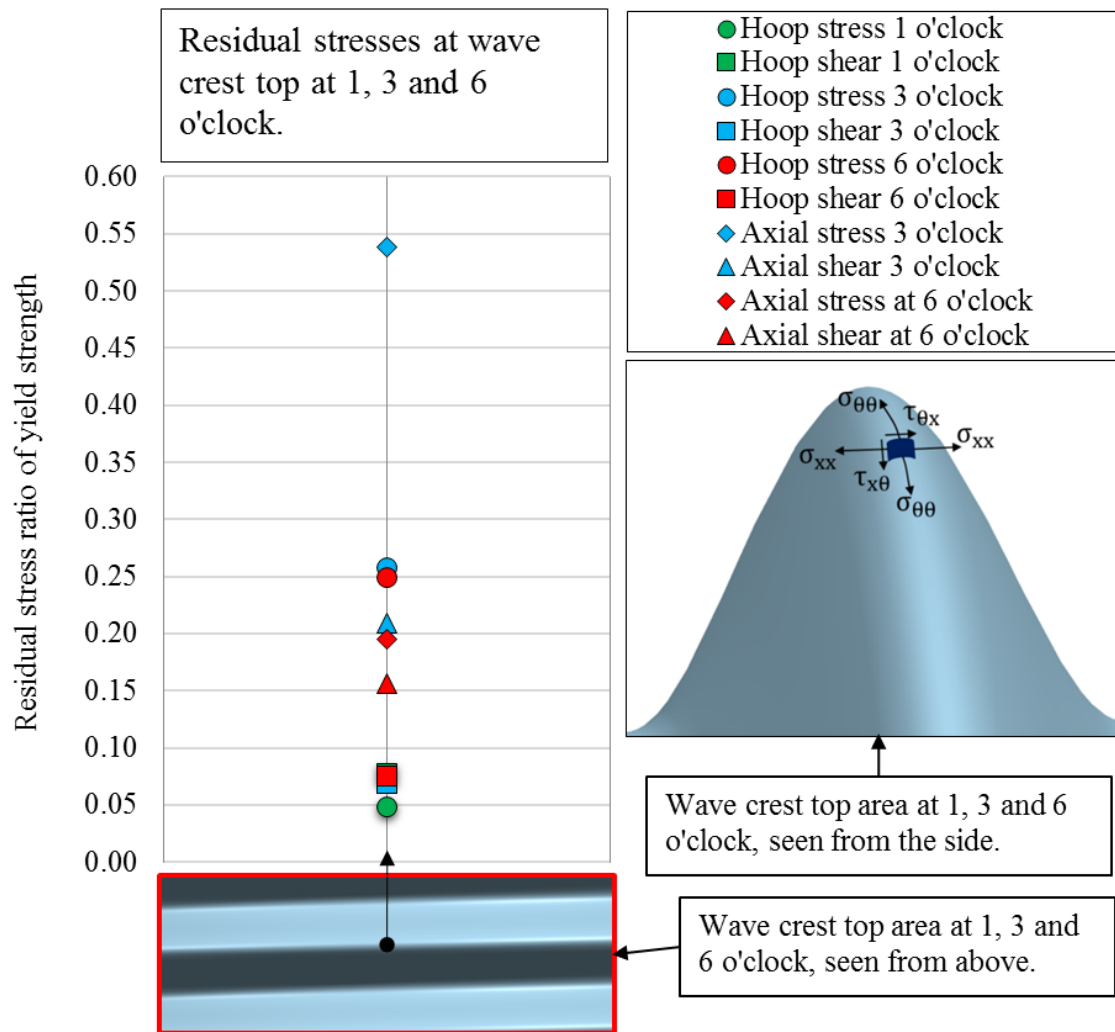


Figure 67: X-ray diffraction measurements of residual stresses in tube (1 – 2) at wave crest top at 1, 3 and 6 o'clock

Figure 67 and Table 30, presents the X-ray diffraction measured residual stresses in the weld-free areas in the tube surface at three different locations in tube (1 – 2). The plot shows the residual stress impact at the wave crest top at 1, 3 and 6 o'clock, visualized in Figure 66.

The plot indicates a low impact of hoop shear stress ( $\tau_{\theta x}$ ) at all three clock locations.  $\tau_{\theta x}$ , constitutes approximately 8% of the material yield strength. Considering the hoop stresses ( $\sigma_{\theta\theta}$ ) the plot indicates a somewhat higher impact relative to  $\tau_{\theta x}$ . The values obtained for  $\sigma_{\theta\theta}$ , represent approximately between 5 – 26% of the material yield strength.

The axial shear stress values ( $\tau_{x\theta}$ ) at 3 and 6 o'clock constitutes approximately 15 – 20% of the material yield strength. The axial stress values ( $\sigma_{xx}$ ) at 3 and 6 o'clock are relatively more scattered. These values represent a higher arithmetic mean residual stress ratio relative to the

## 8.1 Tube (1-2)

other stress components at all three clock locations. The  $\sigma_{xx}$  values constitutes approximately between 19 – 54% of the material yield strength.

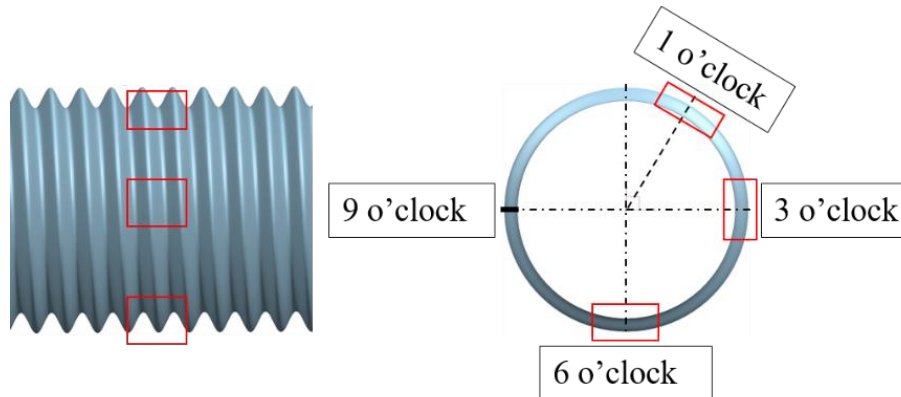


Figure 66: Visualization of 1, 3 and 6 o'clock area in tube (1-2) where X-ray diffraction measurements were performed

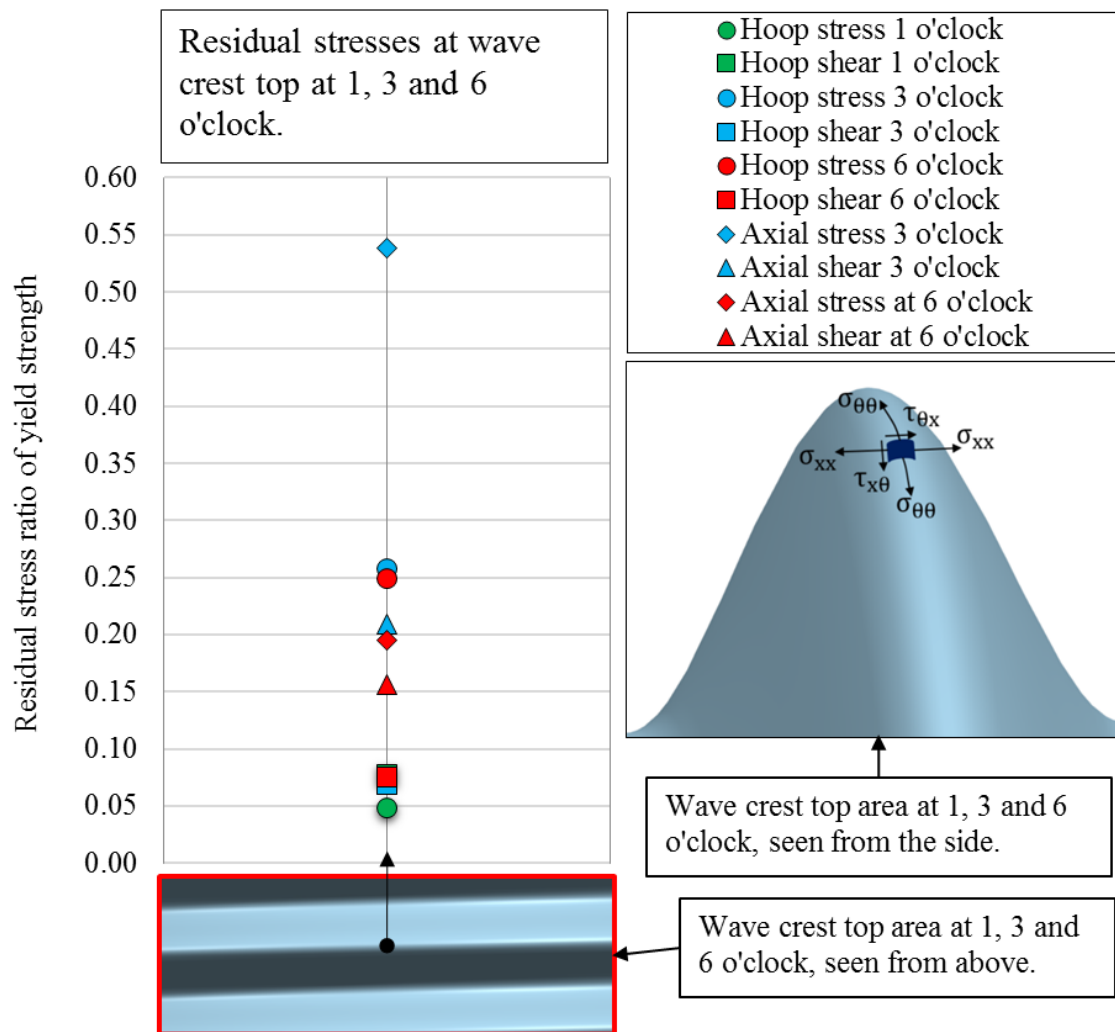


Figure 67: X-ray diffraction measurements of residual stresses in tube (1-2) at wave crest top at 1, 3 and 6 o'clock

Table 30: Arithmetic mean residual stress ratio [%] of material yield strength at wave crest top at 1, 3 and 6 o'clock in tube (1 – 2)

Clock location	Residual stress component	Arithmetic mean ratio of yield strength [%]
1, 3 and 6	$\sigma_{\theta\theta}$	18.5
1, 3 and 6	$\tau_{\theta x}$	7.4
3 and 6	$\sigma_{xx}$	36.7
3 and 6	$\tau_{x\theta}$	18.3

## 8.2 Tube (2 – 2)

### 8.2.1 Welding Seam – Residual Hoop and Shear Stresses at Wave Crest and Wave Trough

Figure 69, presents the X-ray diffraction measurements of residual hoop and shear stresses at the welding seam at the wave crest top at 12 o'clock, visualized in Figure 68, in tube (2 – 2). The measurements are obtained at three different wave crests, that is at number 1, 2 and 3, visualized in Figure 69.

The residual hoop stress ( $\sigma_{\theta\theta}$ ) ratio of the material yield strength, in the welding seam, considering all three wave crests, range from 10 – 14%. At the area beside the welding seam at wave crest number 1 and 2, the measured values of  $\sigma_{\theta\theta}$  scatter. At wave crest number 2, the  $\sigma_{\theta\theta}$  ratio of the material yield strength on both sides of the welding seam proves to be constant with a value of approximately 7%. At wave crest number 1, the  $\sigma_{\theta\theta}$  ratio of the material yield strength range from –4% to 12%.

The residual hoop shear stress ( $\tau_{\theta x}$ ) ratio of the material yield strength, in the welding seam, considering all three wave crests, range from –9% to 2%. At the area beside the welding seam, at wave crest number 1 and 2, the measured values of  $\tau_{\theta x}$  scatter. At wave crest number 2, the  $\tau_{\theta x}$  ratio of the material yield strength range from –6% to 5%, from one side to the other. At wave crest number 1, the  $\tau_{\theta x}$  ratio of the material yield strength range from –9% to 11%, from one side to the other.

Since many of the measured values in Figure 69 scatter, making a possible trend difficult to predict, the resulting measurements are summarized by utilizing the arithmetic mean value in Table 31.

## 8.2 Tube (2-2)

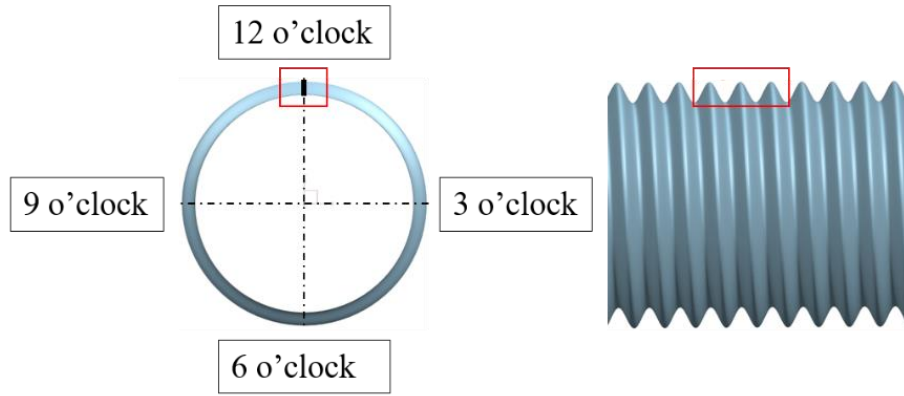


Figure 68: Visualization of 12 o'clock area in tube (2-2) where X-ray diffraction measurements were performed in and around the welding seam

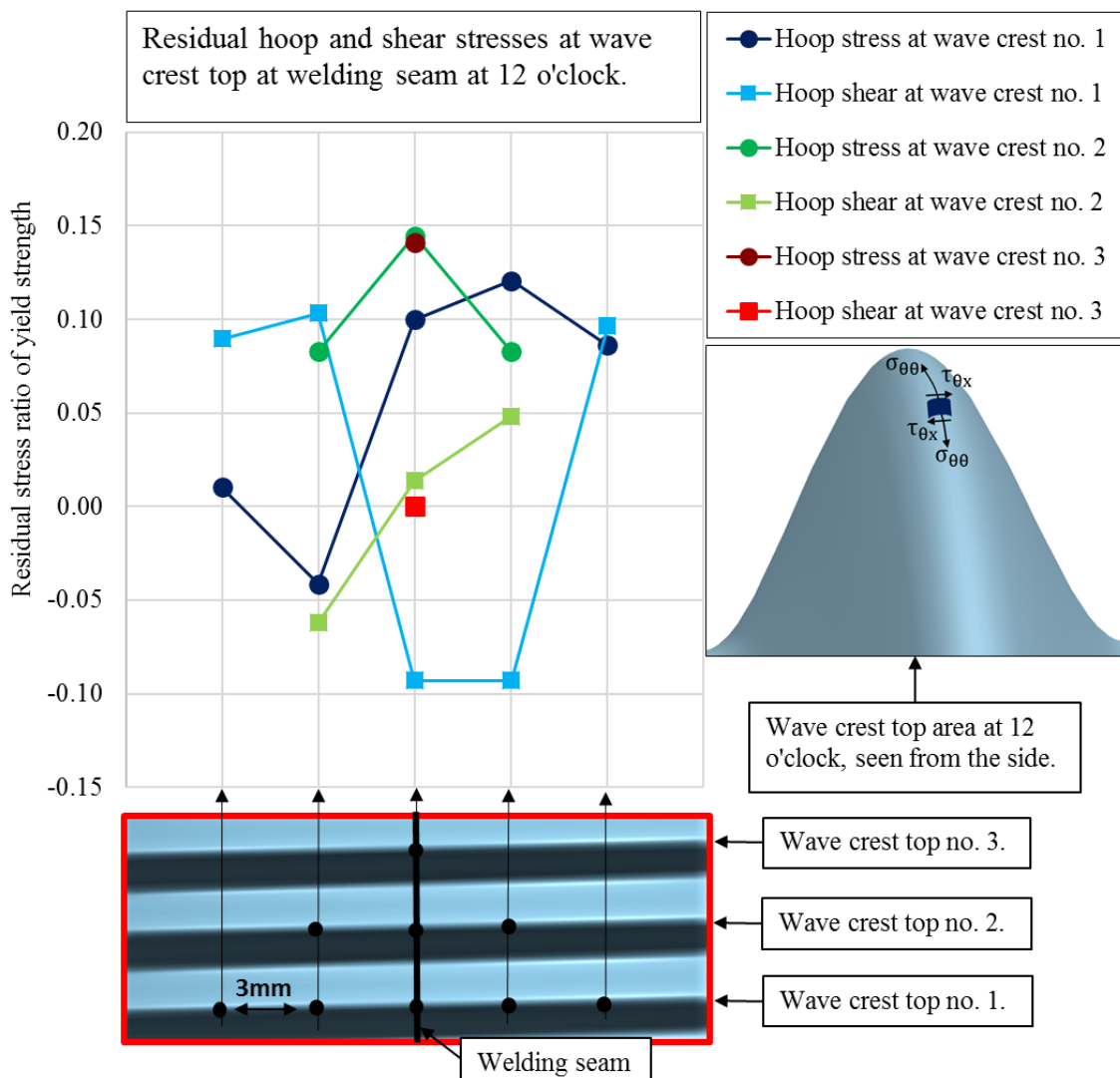


Figure 69: X-ray diffraction measured residual hoop and shear stresses at wave crest top at the welding seam at 12 o'clock in tube (2-2)

Table 31: Arithmetic mean residual hoop and shear stress ratio [%] of the material yield strength at the wave crest top at 12 o'clock in tube (2 – 2)

Point of measurement	Contributing wave crests	Residual stress component	Arithmetic mean ratio of yield strength [%]
In the welding seam	1, 2 and 3	$\sigma_{\theta\theta}$	12.7
		$\tau_{\theta x}$	-4.0
3mm from the welding seam (both sides)	1 and 2	$\sigma_{\theta\theta}$	6.0
		$\tau_{\theta x}$	0.0
6mm from the welding seam (both sides)	1	$\sigma_{\theta\theta}$	5.0
		$\tau_{\theta x}$	9.5

Figure 70, presents the X-ray diffraction measurements of residual hoop and shear stresses at the welding seam at the wave trough overside area at 12 o'clock, visualized in Figure 68, in tube (2 – 2).

The residual hoop stress ( $\sigma_{\theta\theta}$ ) ratio of the material yield strength, across the welding seam, range from  $-3\%$  to  $9\%$ . The corresponding arithmetic mean  $\sigma_{\theta\theta}$  ratio of the material yield strength is approximately  $5\%$ .

The residual hoop shear stress ( $\tau_{\theta x}$ ) ratio of the material yield strength, across the welding seam, range from  $-3\%$  to  $11\%$ . The corresponding arithmetic mean  $\tau_{\theta x}$  ratio of the material yield strength is approximately  $5\%$ .

## 8.2 Tube (2-2)

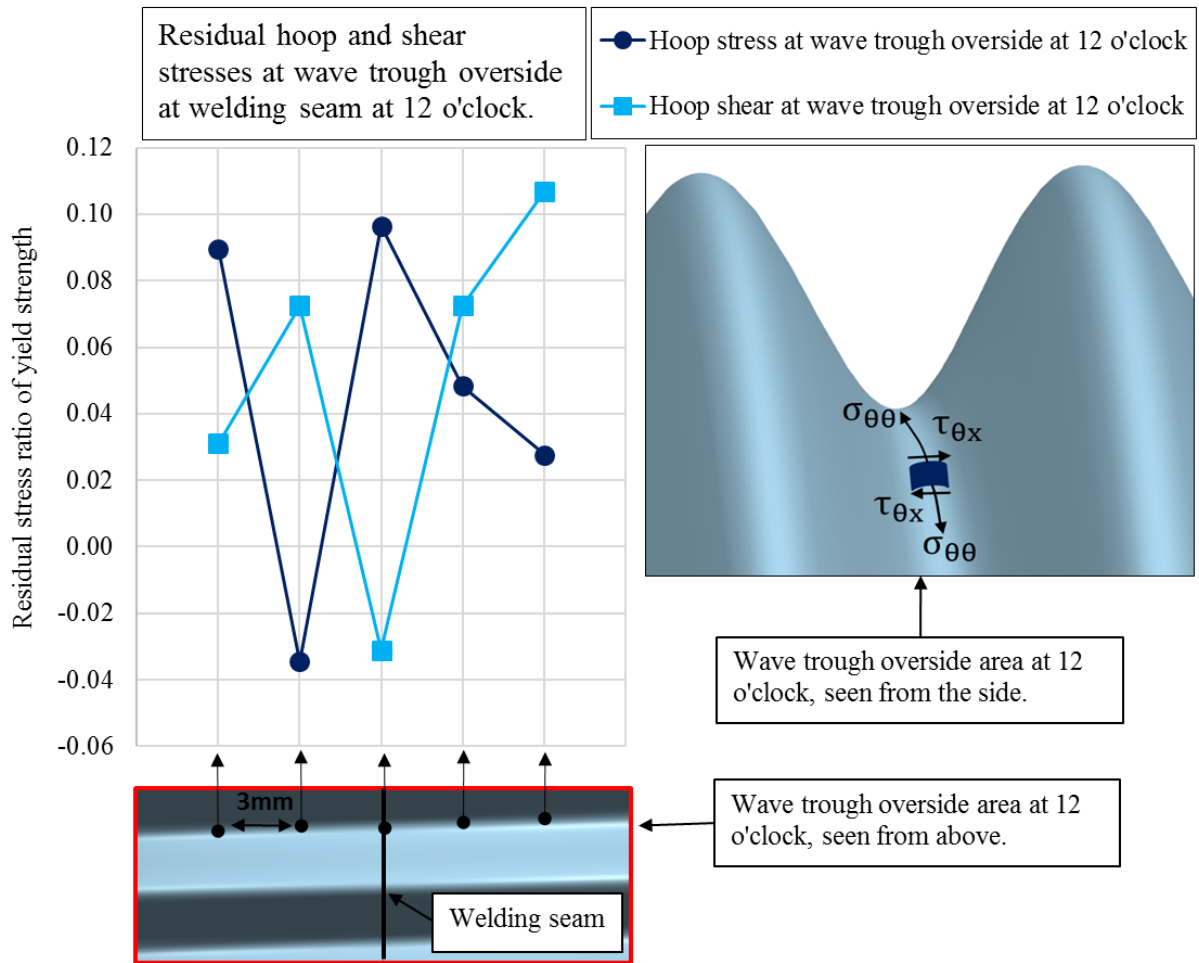


Figure 70: X-ray diffraction measurements of residual hoop and shear stresses at wave trough overside at the welding seam at 12 o'clock in tube (2-2)

Figure 71, presents the X-ray diffraction measurements of residual axial and shear stresses at the welding seam at the wave crest top at 12 o'clock, visualized in Figure 68, in tube (2-2). The measurements are obtained at three different wave crests, that is 1, 2 and 3, visualized in Figure 71.

The residual axial stress ( $\sigma_{xx}$ ) ratio of the material yield strength, in the welding seam, considering all three wave crests, are scattered and range from -8% to 23%. At the areas beside the welding seam, at wave crest number 1 and 2, the measured values of  $\sigma_{xx}$  is also scattered. At wave crest number 2, the  $\sigma_{xx}$  ratio of the material yield strength range from 3 – 23%. At wave crest number 1, the  $\sigma_{xx}$  ratio of the material yield strength range from 13 – 25%.

The residual axial shear stress ( $\tau_{\theta x}$ ) ratio of the material yield strength, in the welding seam, considering all the wave crests, range from 6 – 19%. At the areas beside the welding seam, at wave crest number 1 and 2, the measured values of  $\tau_{x\theta}$  scatter. At wave crest number 2, the  $\tau_{x\theta}$  ratio of the material yield strength range from -19% to 5%, from one side to the other. At



wave crest number 1, the  $\tau_{\theta x}$  ratio of the material yield strength range from 14 – 20%, from one side to the other.

Since many of the measured values in Figure 71 scatter, making a possible trend difficult to predict, the resulting measurements are summarized by utilizing the arithmetic mean value in Table 32.

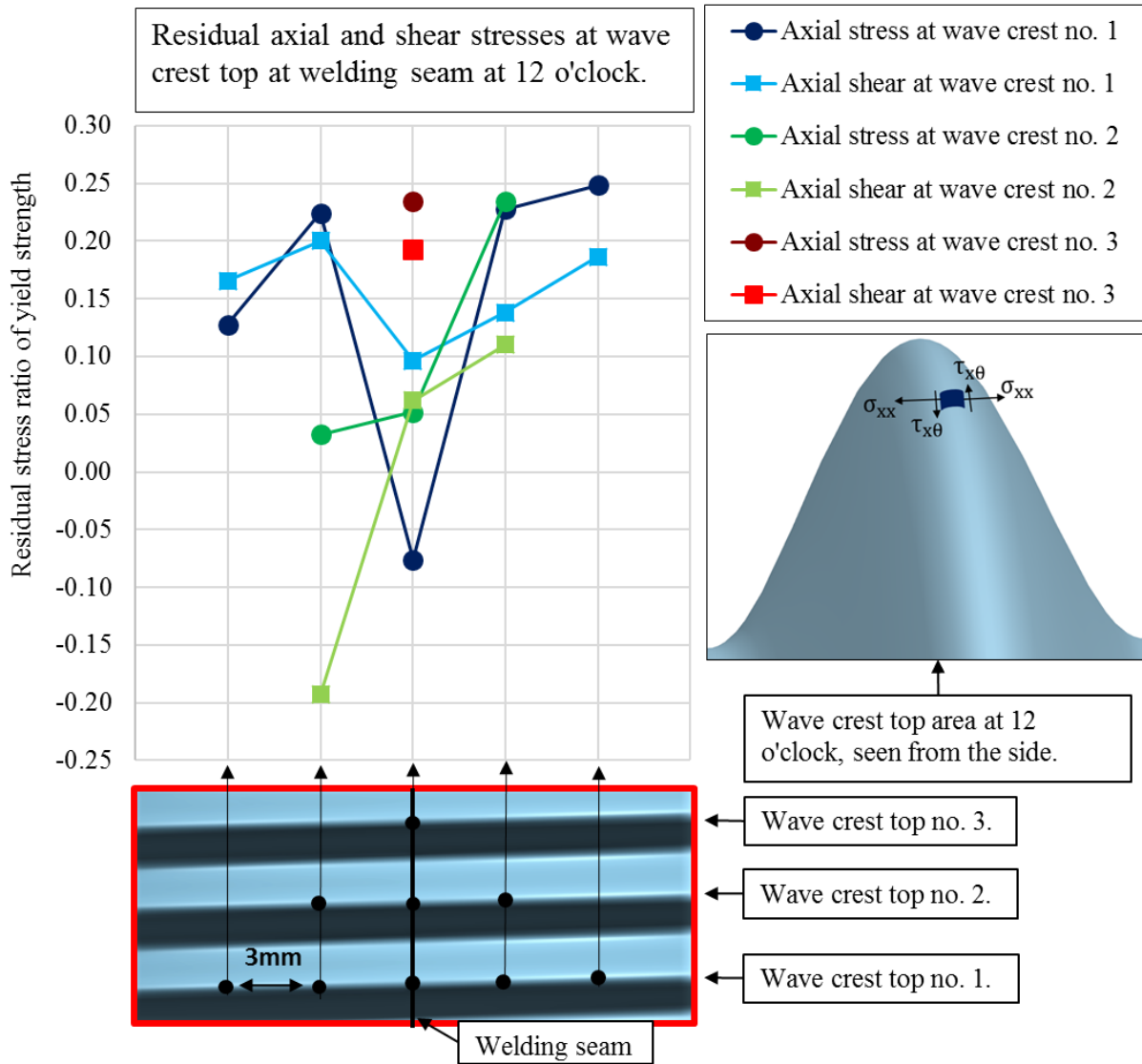


Figure 71: X-ray diffraction measurements of residual axial and shear stresses at wave trough overside at the welding seam at 12 o'clock in tube (2 – 2)

## 8.2 Tube (2-2)

Table 32: Arithmetic mean residual axial and shear stress ratio [%] of the material yield strength at the welding seam at the wave crest top at 12 o'clock in tube (2 – 2)

Point of measurement	Contributing wave crests	Residual stress component	Arithmetic mean ratio of yield strength [%]
In the welding seam	1, 2 and 3	$\sigma_{xx}$	7.0
		$\tau_{x\theta}$	12.0
3mm from the welding seam (both sides)	1 and 2	$\sigma_{xx}$	18.0
		$\tau_{x\theta}$	6.5
6mm from the welding seam (both sides)	1	$\sigma_{xx}$	25.5
		$\tau_{x\theta}$	18.0

### 8.2.2 Weld-free Areas – Residual Hoop and Shear Stresses at Wave Crest Top

Figure 73, presents the X-ray diffraction measurements of residual hoop and shear stresses at the weld-free wave crest top areas at 3, 6 and 9 o'clock, visualized in Figure 68, in tube (2 – 2).

The residual hoop stress ( $\sigma_{\theta\theta}$ ) ratio of the material yield strength, considering all three clock locations, range from 25 – 49%. The highest ratios are located at 6 o'clock, holding a ratio of 46%, and at 9 o'clock, holding a ratio of 49%. The corresponding arithmetic mean ratio of the material yield strength considering all three clock locations, is approximately 40%.

The residual hoop shear stress ( $\tau_{\theta x}$ ) ratio of the material yield strength, considering all three clock locations, range from 10 – 13%. The corresponding arithmetic mean  $\tau_{\theta x}$  ratio of the material yield strength, considering all three clock locations is approximately 12%.

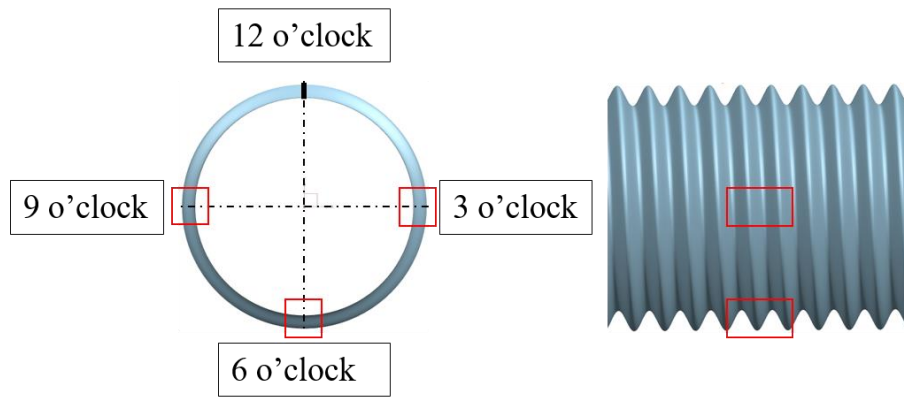


Figure 72: Visualization of 3, 6 and 9 o'clock area in tube (2 – 2) where X-ray diffraction measurements were performed

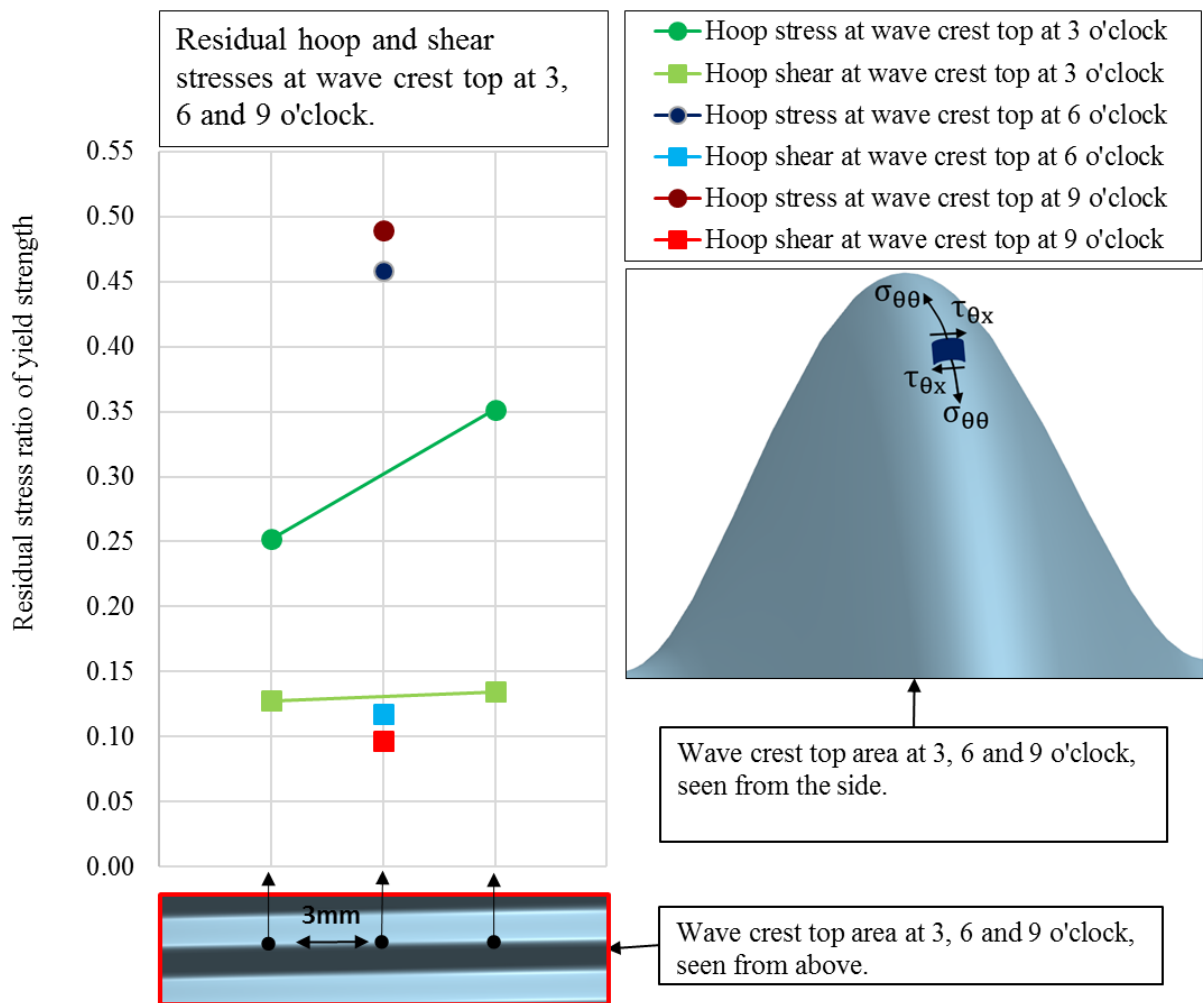


Figure 73: X-ray diffraction measurements of residual hoop and shear stresses at wave crest top at 3, 6 and 9 o'clock in tube (2 – 2)

Figure 74, presents the X-ray diffraction measurements of residual hoop and shear stresses at the weld-free wave trough overside areas at 6 and 9 o'clock, visualized in Figure 68, in tube (2 – 2).

## 8.2 Tube (2-2)

The residual hoop stress ( $\sigma_{\theta\theta}$ ) ratio of the material yield strength, considering both clock locations, range from 15%, at 9 o'clock, to 32%, at 3 o'clock. The arithmetic mean residual hoop stress ratio of the material yield strength, considering both clock locations, is approximately 26%.

The residual hoop shear stress ( $\tau_{\theta x}$ ) ratio of the material yield strength, considering both clock locations, range from 3%, at 9 o'clock, to 11%, at 3 o'clock. The arithmetic mean residual hoop shear stress ratio of the material yield strength, considering both clock locations, is approximately 7%.

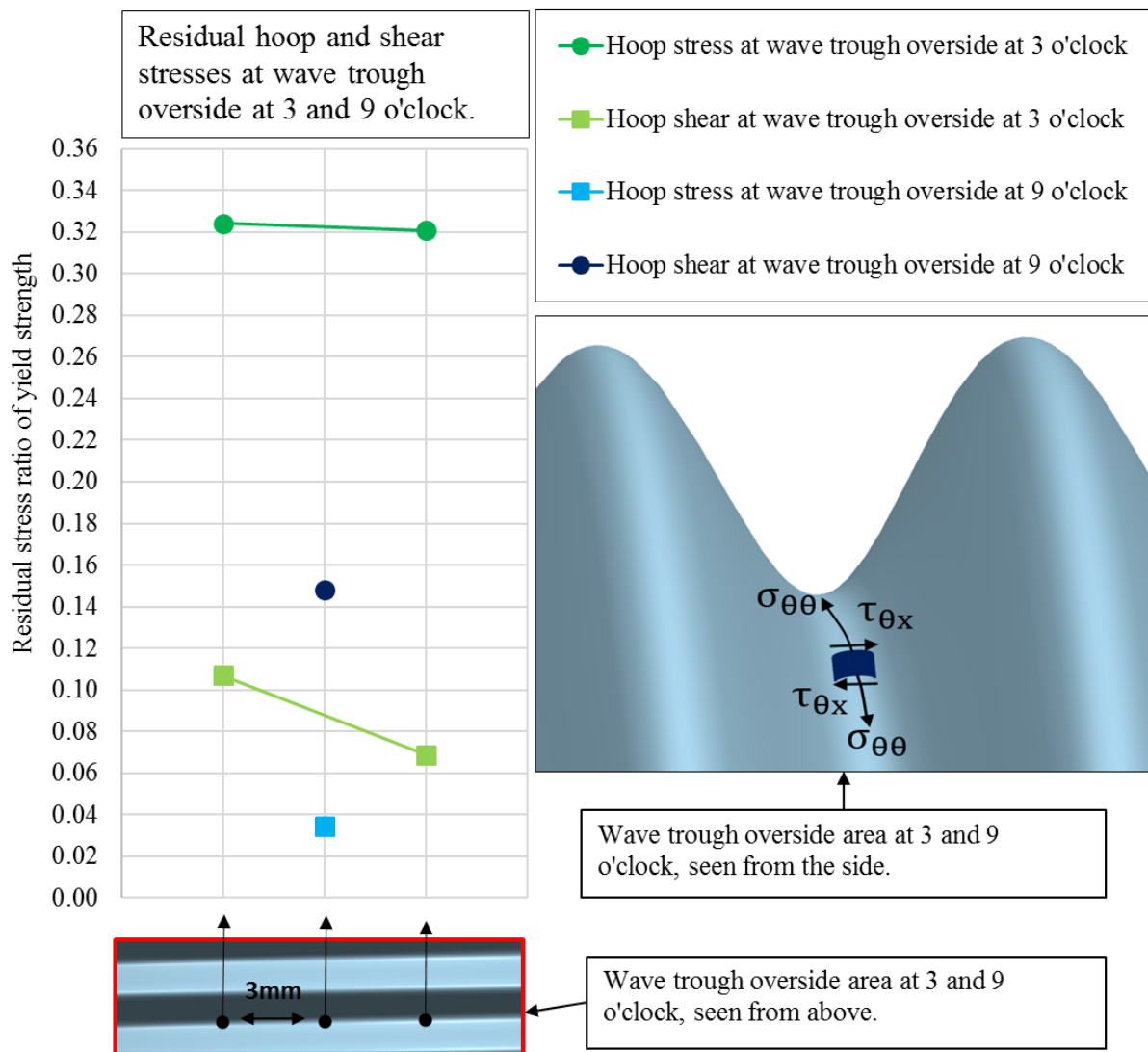


Figure 74: X-ray diffraction measurements of residual hoop and shear stresses at wave trough overside at 3, 6 and 9 o'clock in tube (2-2)

## 9 Finite Element Method – Postprocessing and Results

### 9.1 Static Axial Analysis

#### 9.1.1 Strain Development

Figure 75 and Figure 76, presents, respectively, typical elastic and plastic strain development fields for a MCTS with  $A = 3\text{mm}$  and  $P = 21\text{mm}$ . The figures indicate that the highest strain occur at the wave crest area, tensile side.

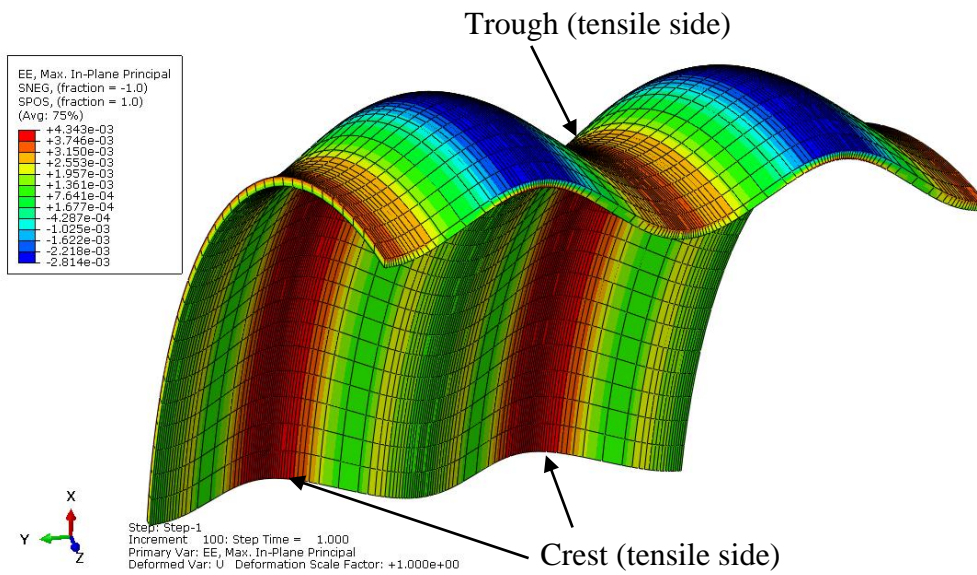


Figure 75: Elastic strain field development view for  $A=3.0\text{ mm}$ ,  $P=21.0\text{ mm}$  and  $t=0.7\text{mm}$

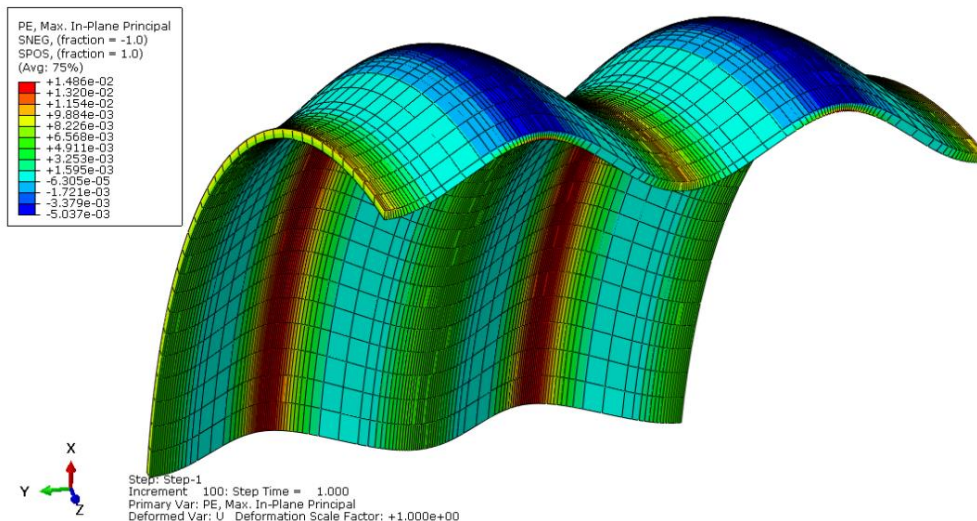


Figure 76: Plastic strain development view for  $A=3.0\text{mm}$ ,  $P=21.0\text{mm}$  and  $t=0.7\text{mm}$

## 9.1 Static Axial Analysis

### 9.1.2 Wave Crest vs Wave Trough

Figure 77, presents a comparison between maximum in-plane corrugated tensile strain for the area of wave crest and wave trough, when varying the  $P/A$  ratio at a constant thickness equal 0.7mm. For  $A = 3\text{mm}$ , the trough tensile strain is higher for a  $P/A < 4$ , compared to the crest tensile strain. For  $A = 5\text{mm}$ , the trough tensile strain is higher for a  $P/A < 2$  compared to the crest tensile strain. For  $A = 8\text{mm}$ , the crest tensile strain tends to be larger all the time.

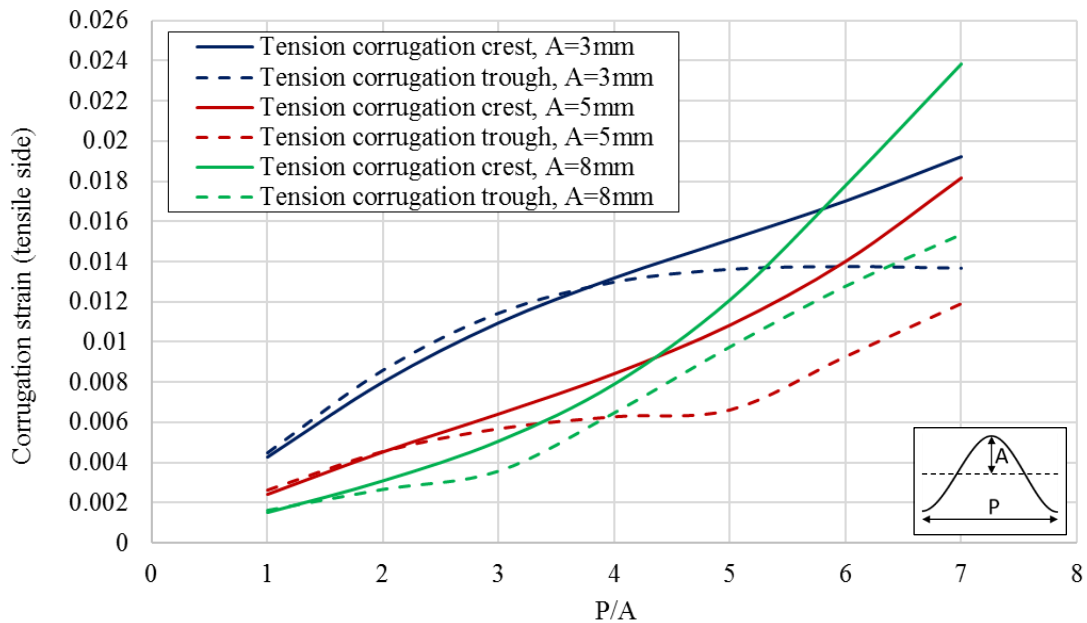


Figure 77: A comparison of corrugation strain development (tensile side) at wave crest and wave trough area when varying the  $P/A$  ratio at a constant thickness equal 0.7mm

### 9.1.3 Thickness Sensitivity

Figure 78, presents the corrugation thickness sensitivity at the wave crest area (tensile side). The figure compares the strain ratio, that is the wave crest strain (tensile side) to the smooth tubular sheath strain, for different sheath thicknesses, at a  $P/A$  ratio varying between 1 – 7 and a constant  $A = 3\text{mm}$ . The plot indicates that lower thickness decreases local corrugated strain development in the wave crest area (tensile side).

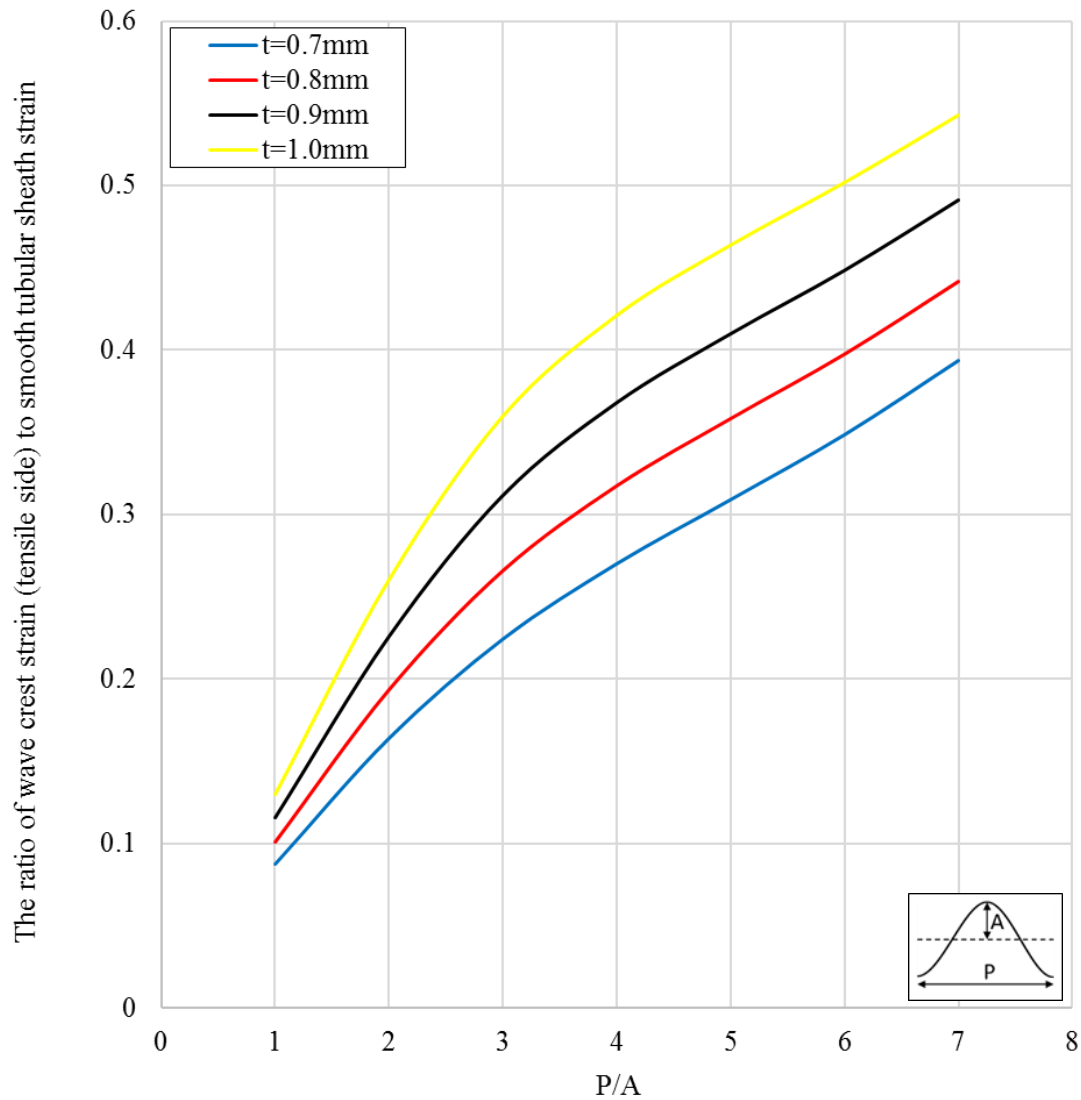


Figure 78: Corrugation thickness sensitivity at the wave crest area (tensile side). The figure compares the strain ratio, that is the wave crest strain (tensile side) to the smooth tubular sheath strain, for different sheath thicknesses, at a  $P/A$  ratio varying between 1 – 7 and a constant  $A = 3\text{mm}$ .

#### 9.1.4 Amplitude Sensitivity

Figure 79, presents the corrugation amplitude sensitivity at the wave crest area (tensile side) for a constant thickness,  $t = 0.7\text{mm}$ . The figure compares the strain ratio, that is the wave crest strain (tensile side) to the smooth tubular sheath strain, at a  $P/A$  ratio varying between 1 – 7 at three different  $A$ -values. The plot indicates that a higher amplitude is favourable at lower  $P/A$  ratios, while smaller amplitudes are more favourable at higher  $P/A$  ratios. At an  $A = 3\text{mm}$  and a  $P/A = 7$ , the MCTS develop 61% less strain than a smooth tubular sheath, and approximately 4 times more strain than a MCTS with a  $P/A = 2$  and  $A = 5\text{mm}$ .

9.1 Static Axial Analysis

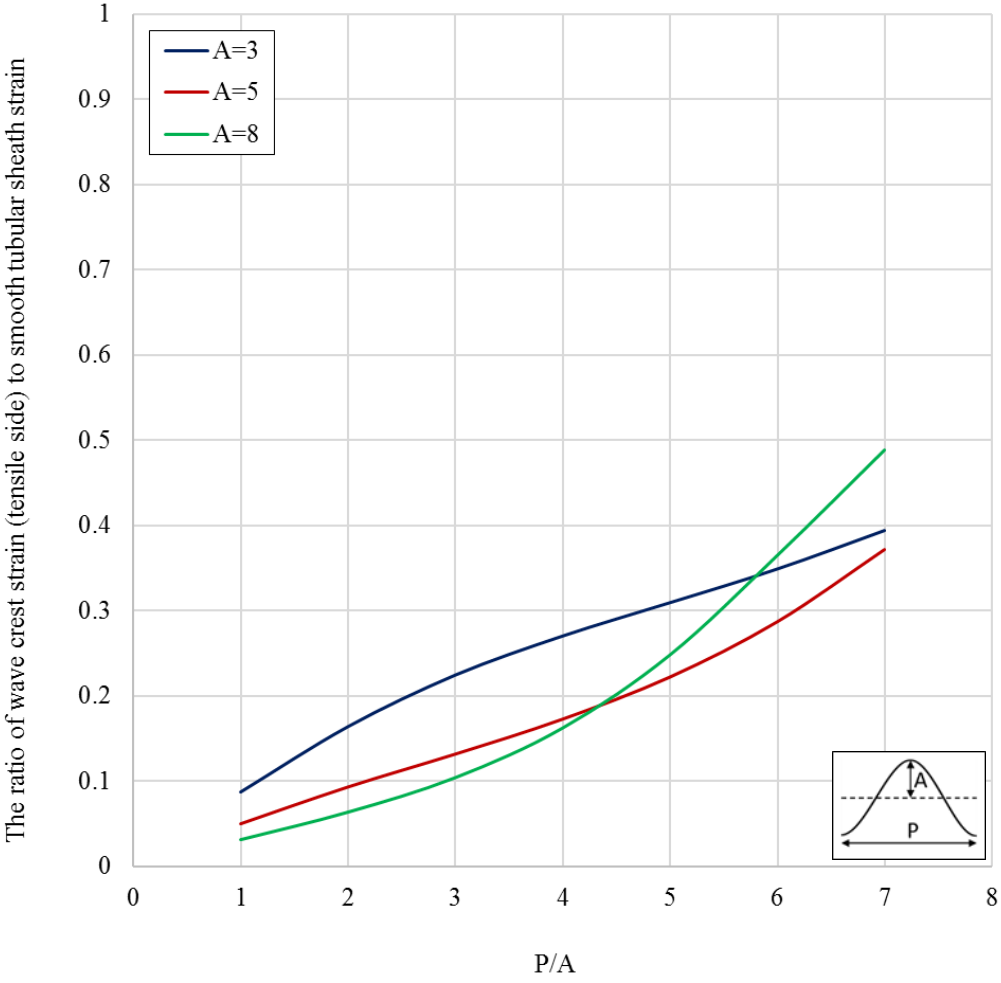


Figure 79: Local corrugation amplitude sensitivity at the wave crest area (tensile side) for a constant thickness equal 0.7mm. The figure compares the strain ratio, that is the wave crest strain (tensile side) to the smooth tubular sheath strain, at a P/A ratio varying between 1 – 7 at three different A-values.

Table 33, summarizes the finding from Figure 79.

Table 33: Summarized findings from Figure 79

P/A ratio range	Comments
$P/A \leq 4.3$	A = 8mm more favourable
$4.3 < P/A \leq 5.8$	A = 5mm more favourable
$P/A > 5.8$	A = 3mm more favourable

Figure 80, presents the global amplitude sensitivity, at a constant  $t = 0.7\text{mm}$ , when plotting the ratio of maximum axial reaction force (RF), pushed back from the MCTS, to the maximum axial RF in a smooth tubular sheathing, against different P/A ratios.



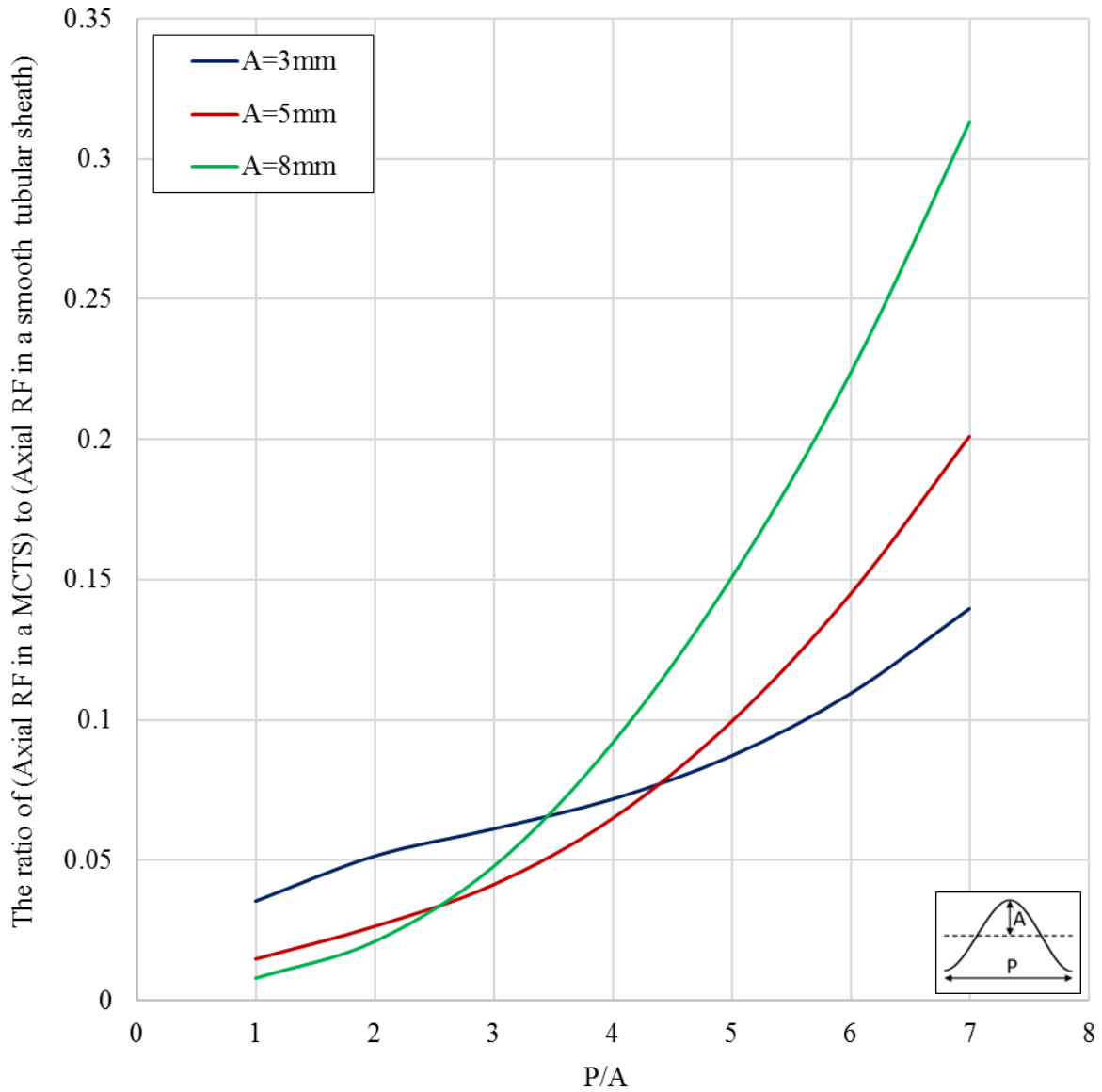


Figure 80: Global amplitude sensitivity, at a constant thickness equal 0.7mm. The figure when plots the ratio of maximum axial reaction force (RF), pushed back from the MCTS, to the maximum axial RF in a smooth tubular sheathing, against different P/A ratios.

Table 34, summarizes the findings from Figure 80.

Table 34: Summarized findings from Figure 80

<b>P/A ratio range</b>	<b>Comments</b>
$P/A \leq 2.6$	A = 8mm more favourable
$2.6 < P/A \leq 4.4$	A = 5mm more favourable
$P/A > 4.4$	A = 3mm more favourable

## 9.1 Static Axial Analysis

### 9.1.5 Reaction Force

Figure 81, compares the axial reaction force (RF), pushed back from the MCTS, with different P-values at an  $A = 3\text{mm}$  and  $t = 0.7\text{mm}$ , against global nominal strain,  $\Delta U_{\text{Axial}}/L$ . Higher reaction force means the geometry is stiffer and less flexible and absorbs less strain before reaching yield at wave crest tensile side, indicated with  $\epsilon_p = 0.2\%$ .

The plot indicates that a low P/A ratio is most favourable considering the induced strain on the wave crest tensile side. However, the plot indicates that only a small corrugation provides a relatively large positive outcome considering the strain development in the MCTS. At a P/A ratio equal 7, approximately 20.9% more global strain can be induced before reaching  $\epsilon_p = 0.2\%$ , compared to a smooth tubular sheathing.

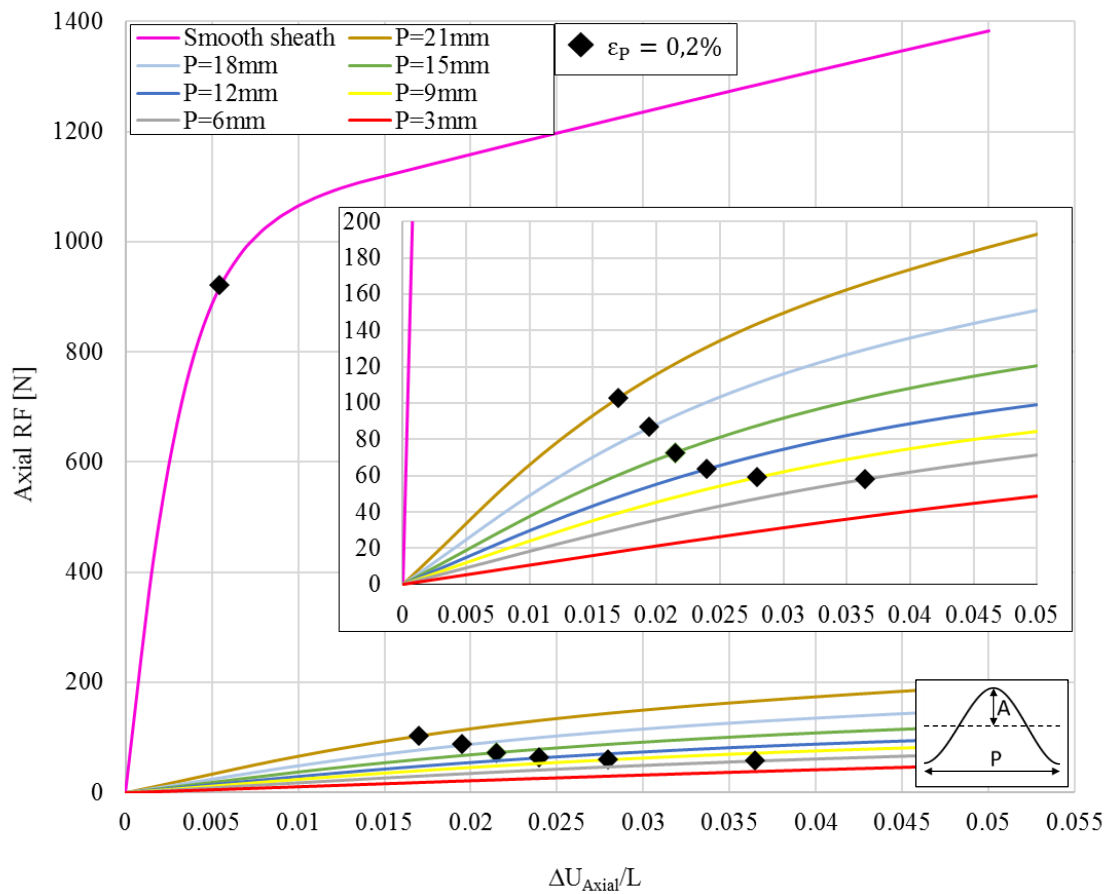


Figure 81: Developed reaction force vs global nominal strain for a constant  $A=3\text{mm}$  and  $t=0.7\text{mm}$

9.1.6 Diameter Variation

Figure 82 and Table 35, shows how the MCTS inner diameter,  $D_i$ , alters due to the axial displacement at  $P/A = 1$  and 7. The plot indicates that the change in  $D_i$ , is negligible at lower  $P/A$  ratios. At higher  $P/A$  ratios,  $D_i$ , increases. However, it is though insignificant low compared to the original  $D_i$ .

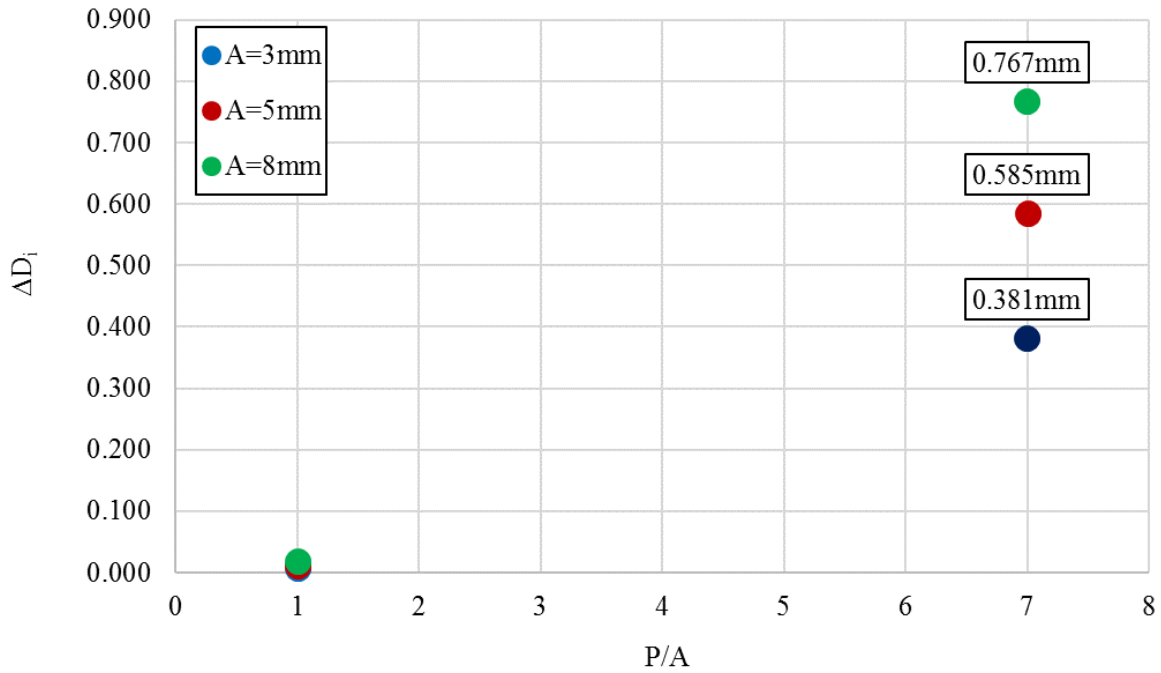


Figure 82: Change of MCTS inner diameter due to axial displacement

Table 35: Summarized findings from Figure 82

Amplitude [mm]	Percentage change of inner diameter, $\Delta D_i$
3.000	0.381
5.000	0.585
8.000	0.767

9.1 Static Axial Analysis

9.1.7 Helical Inclination Angle Sensitivity

Figure 83, shows how the helical inclination sensitivity alters with increasing inclination angle during axial displacement for a P/A ratio equal 2 and 7 with a constant  $t = 0.6\text{mm}$ . The plot indicates a minimal sensitivity at a low P/A ratio. At a high P/A ratio, the sensitivity increases. However, the enhancement is minor. At  $P = 21\text{mm}$  and  $A = 3\text{mm}$ , the change in tensile strain at wave crest area is approximately 16%, when increasing the inclination angle from  $0 - 25.08^\circ$ .

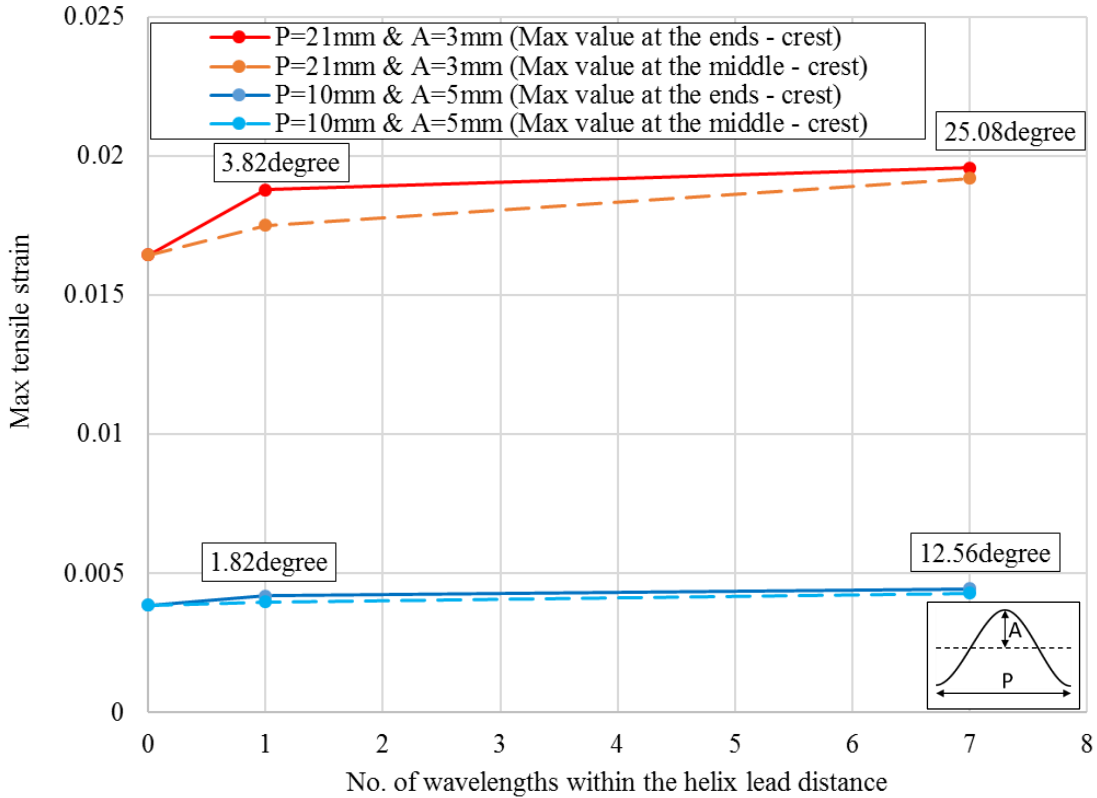


Figure 83: Helical inclination angle sensitivity. The plot shows how the helical inclination sensitivity alters with increasing inclination angle during axial displacement for a P/A ratio equal 2 and 7 with a constant thickness equal 0.6mm.

## 9.2 Static Bending Analysis

### 9.2.1 Strain Development

Figure 85, compares maximum tensile strain path values along the tubes global tension or compression side, during bending. The strain values are obtained at each wave crest or wave trough, along either the global tension side or global compression side, depending on where the highest tensile strains are localized, visualized in Figure 84.

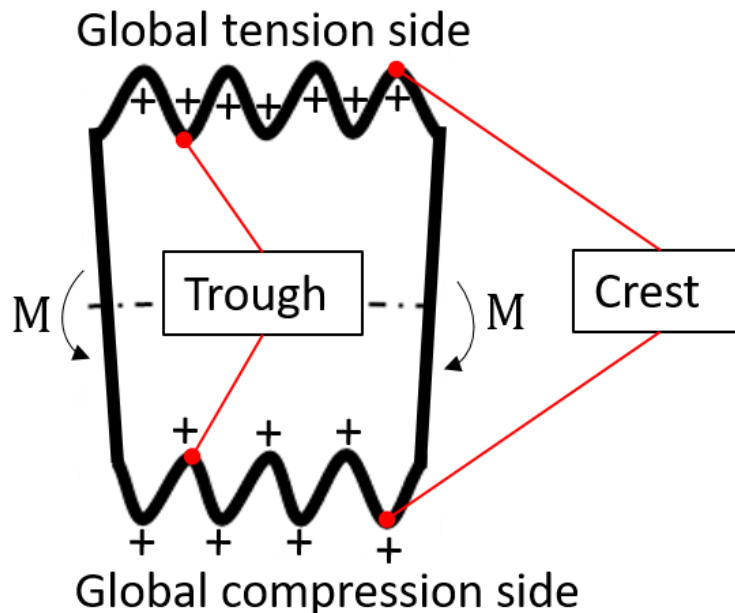


Figure 84: Visualization of the global tension/compression side in a MCTS during bending, and localization of the wave crest and wave trough areas along the corrugation geometry. + indicate the area of tensile strain and stress during forced angular displacement.

All the analysed models had an inherent wall thickness of 0.6mm. The plot indicates that a MCTS with  $P/A = 7$  and  $A = 3\text{mm}$ , develop approximately 3.5 times more strain than a MCTS with a  $P/A = 2$  and  $A = 5\text{mm}$ . This ratio nearly coincides with the indicated result for the same corrugation geometry in Figure 79, during forced axial displacement. The plot also indicates a local accumulation of strain at the MCTS ends. This event is especially conspicuous when increasing the  $P/A$  ratio and the helical inclination angle.

Table 36, visually compares the strain development, for model  $P = 21\text{mm}$  and  $A = 3\text{mm}$ , and model  $P = 10\text{mm}$  and  $A = 5\text{mm}$ , when varying the inclination angle. The models found in Table 36, are visualized as half longitudinal sections relative to the original length, that is from one end to the middle, for a larger and better visualization.

## 9.2 Static Bending Analysis

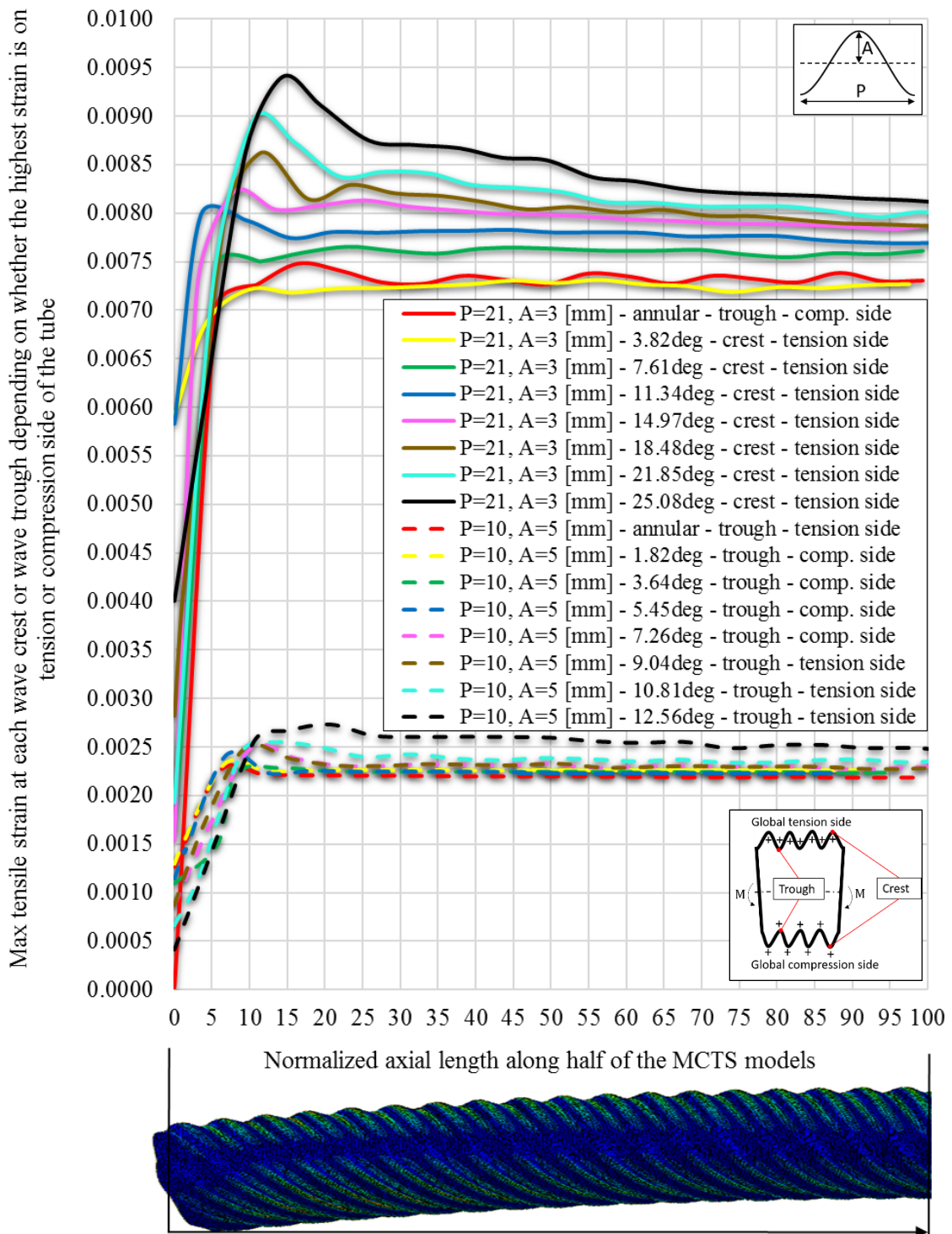
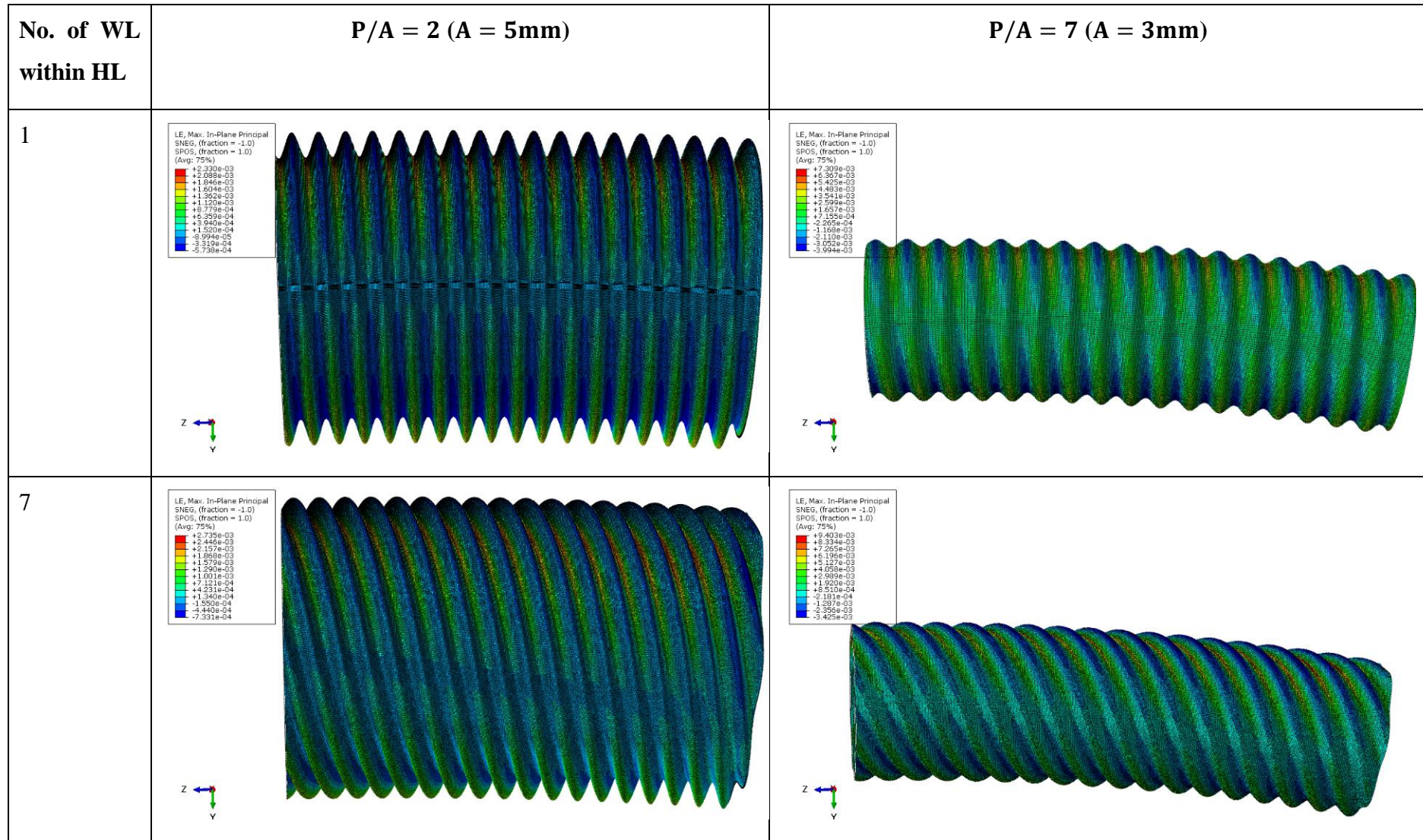


Figure 85: Comparison of maximum tensile strain path values along the tubes global tension or compression side, during bending. The strain values are obtained at each wave crest or wave trough, along either the global tension side or global compression side, depending on where the highest tensile strains are localized. The plot compares  $P/A=2$  ( $A=5\text{mm}$ ) and  $P/A=7$  ( $A=3\text{mm}$ ), at a constant thickness equal  $0.6\text{mm}$  and with varying inclination angles.

Table 36: Visualization of strain development fields, caused by forced angular displacement, in helical MCTSs with a constant thickness equal 0.6mm and a  $P/A=2$  ( $A=5\text{mm}$ ) and  $P/A=7$  ( $A=3\text{mm}$ ). The visualized models are half longitudinal sections relative to the original length, that is from the right end towards the middle of the MCTS.



### 9.2 Static Bending Analysis

Figure 86, compares the vertical displacement at the middle of the various models analysed during the bending analysis. The plot indicate that the vertical displacement is constant at lower P/A ratios, while at higher P/A ratios, the model tends to stiffen at higher inclination angles. This stiffening can also be noticed in the results presented in Figure 85, where the model  $P = 21\text{mm}$  and  $A = 3\text{mm}$ , at higher inclination angles, suffers of a localized strain congestion at the tube ends.

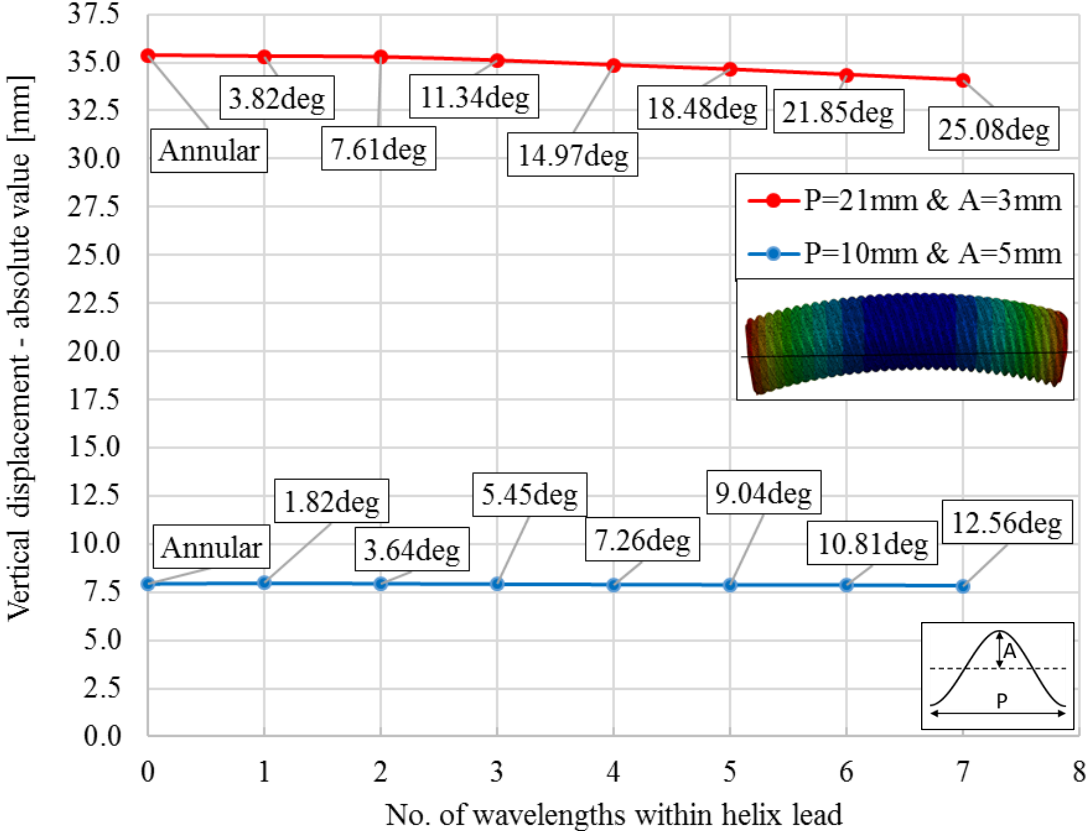


Figure 86: A comparison of vertical displacement at the middle of the MCTS models during forced angular displacement. The compared models are  $P/A=2$  ( $A=5\text{mm}$ ) and  $P/A=7$  ( $A=3\text{mm}$ ), with varying inclination angles at a constant thickness equal  $0.6\text{mm}$ .



9.2.2 Helical Inclination Angle Sensitivity

Figure 87, presents the MCTS helical inclination sensitivity when exposed to forced angular displacement. The compared models in the plot are  $P/A=2$  ( $A=5\text{mm}$ ) and  $P/A=7$  ( $A=3\text{mm}$ ), with varying inclination angles and a constant wall thickness equal  $0.6\text{mm}$ . Maximum tensile strain values were obtained from both the MCTS middle, and at the MCTS ends where the localized strain congestion accumulated. The plot indicates a low sensitivity at lower inclination angles. However, at higher inclination angles the sensitivity increases, especially at a higher  $P/A$  ratio. At higher  $P/A$  ratios and inclination angles, the local congestion of strain at each MCTS end noticeably increase relative to the strain value obtained at the middle.

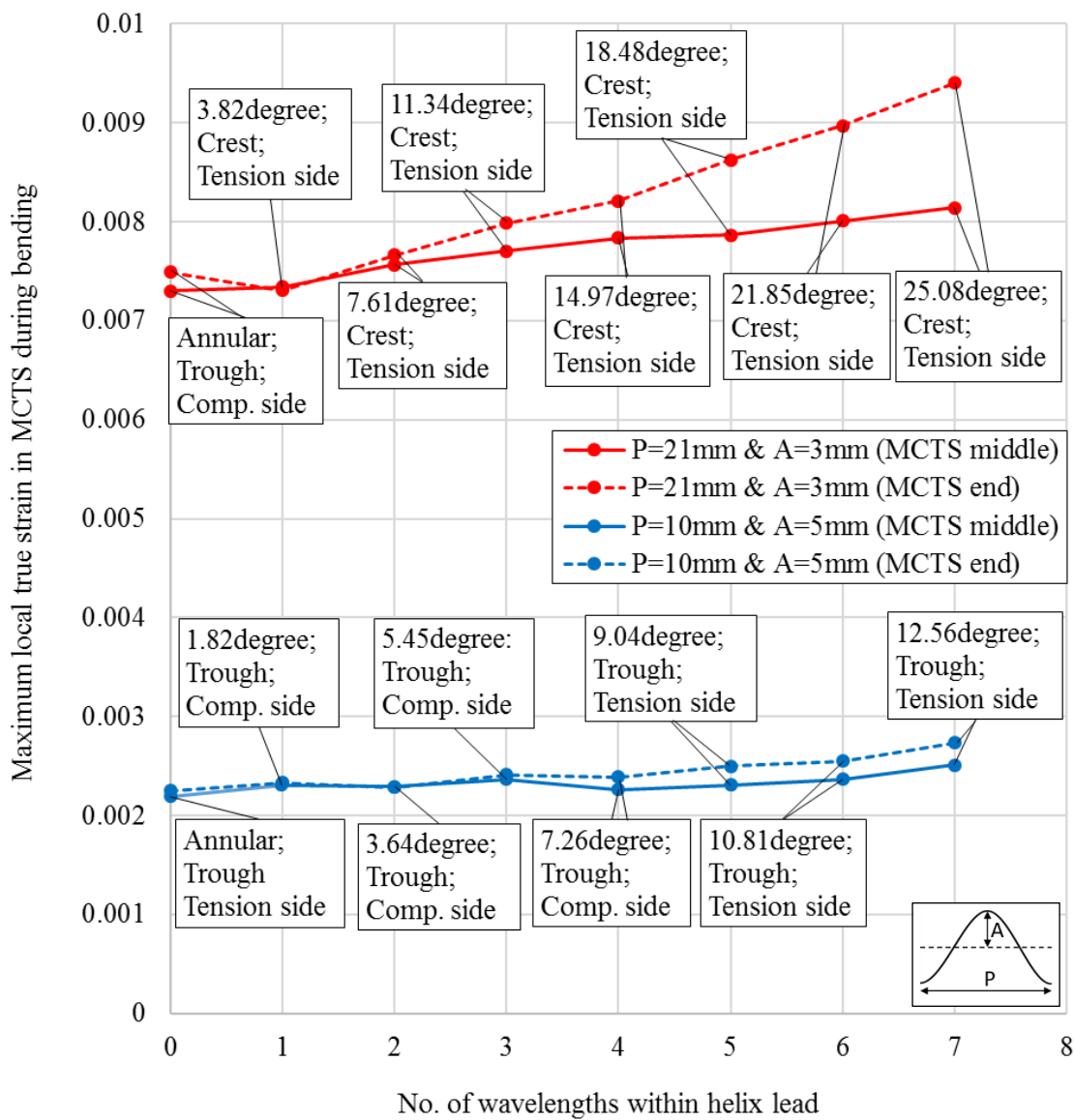


Figure 87: A visualization of the MCTS helical inclination sensitivity when exposed to forced angular displacement. The compared models are  $P/A=2$  ( $A=5\text{mm}$ ) and  $P/A=7$  ( $A=3\text{mm}$ ), with varying inclination angles and a constant thickness equal  $0.6\text{mm}$ .

## 9.2 Static Bending Analysis

### 9.2.3 Shear Strain Sensitivity

Figure 88, presents the shear strain sensitivity for a MCTS consisting of  $P/A=2$  ( $A=5\text{mm}$ ) and  $P/A=7$  ( $A=3\text{mm}$ ), with varying inclination angles at a constant wall thickness equal  $0.6\text{mm}$ . The plot indicates that the portion of shear strain increases almost linearly. The shear strain portion is approximately 2.4 times higher for a  $P/A=7$  ( $A=3\text{mm}$ ) compared to a  $P/A=2$  ( $A=5\text{mm}$ ), at a helical inclination angle  $\theta$  by a helix lead consisting of the same number of wavelengths. An increased proportion of shear strain is proportional to increasing torsional forces. This means that torsional forces have a growing present when inclination angles are increasing, especially at higher  $P/A$  ratios, shown in Figure 88. An increasing amount of torsional forces implies an increased amount of twisting of the MCTS during bending.

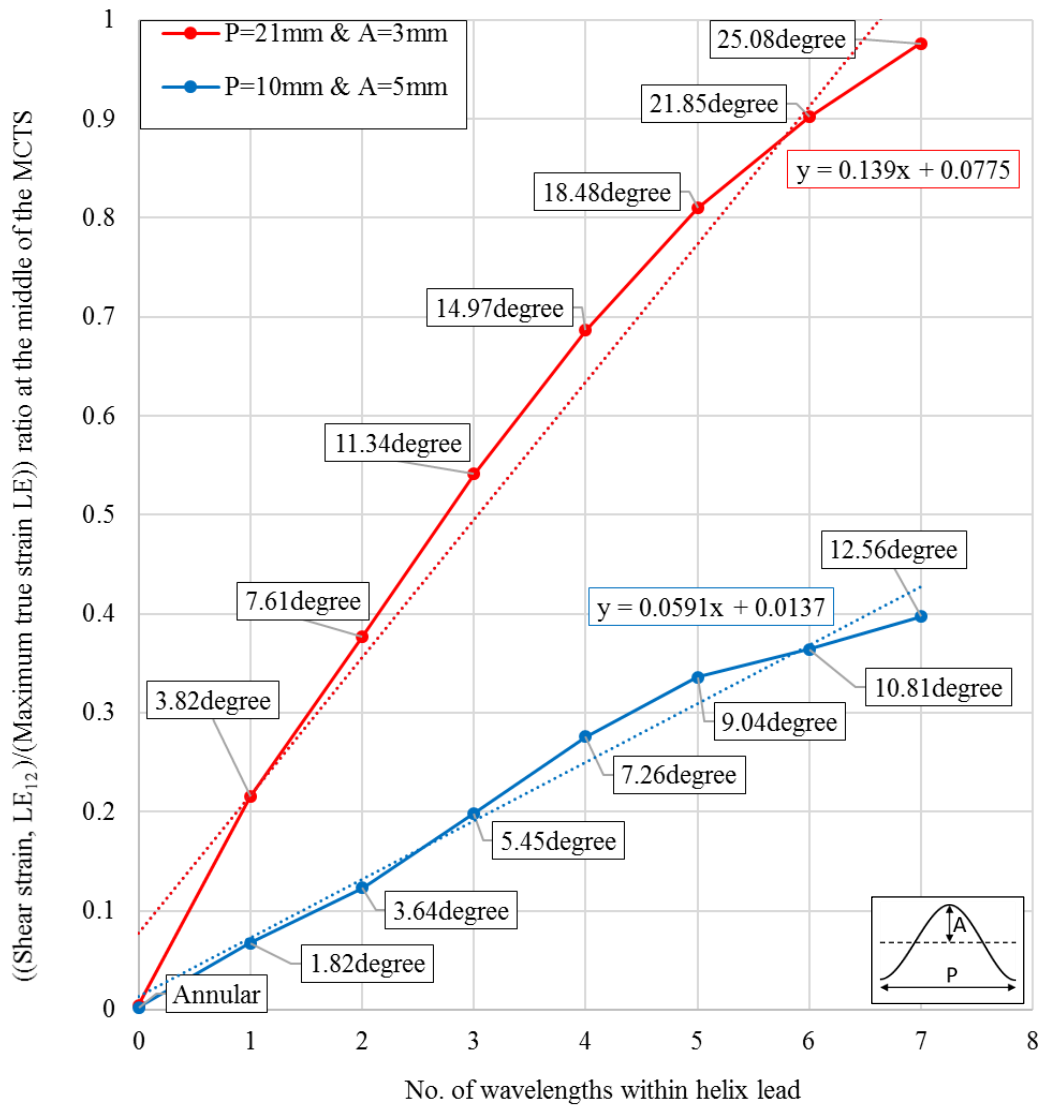
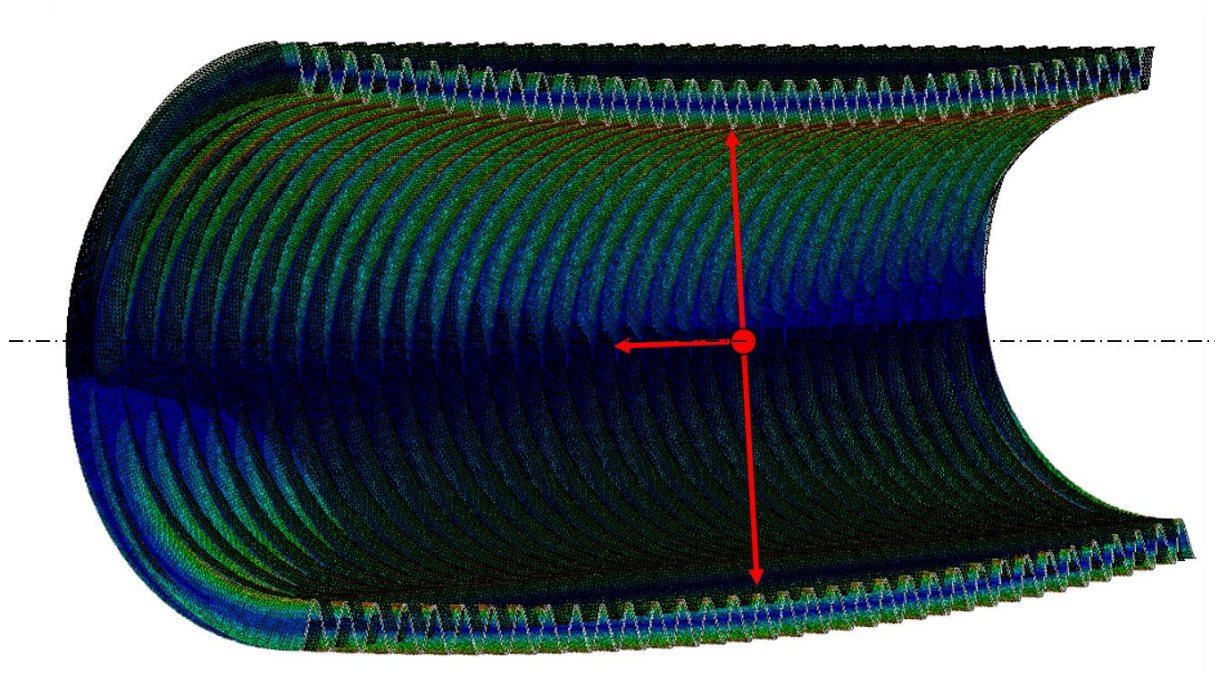


Figure 88: The ratio of shear strain at the area of maximum total true strain, at the middle of the MCTS models exposed to forced angular displacement. The compared models in the plot are  $P/A=2$  ( $A=5\text{mm}$ ) and  $P/A=7$  ( $A=3\text{mm}$ ), with varying inclination angles and a constant thickness equal  $0.6\text{mm}$ .

9.2.4 Ovality

After each MCTS bending FEA, a measurement of ovality was performed, visualized in Figure 89. The measurements indicated a negligible ovality, meaning a value lower than 0.2% for each model.



*Figure 89: Ovality measurement*

9.3 Quasi-Static Four-Point Bending

9.3 Quasi-Static Four-Point Bending

9.3.1 Static Bending Analysis

Figure 90 and Figure 91 presents the strain development fields for respectively tube (1 – 5) and tube (2 – 1) when exposed to static bending analysis. The figures indicate that tube (2 – 1) generates approximately 2.40 times higher strain value than tube (1 – 5). It is however important to notice that the various tubes are forced to follow two different curvatures. Tube (2 – 1) is forced to follow a curvature holding a 1.86 times larger radius than the curvature that tube (1 – 5) is forced to follow.

A comparison of the tubes at an equal angular displacement was also performed. This was achieved by finding the required angular displacement required for tube (2 – 1) to follow the same radius as calculated for tube (1 – 5). When tube (2 – 1) followed the same radius as tube (1 – 5), it generated approximately a tensile strain value on the tube middle of 0.0041. This strain value is approximately 11% lower than the generated tensile strain value at the same angular displacement in tube (1 – 5), on the tube middle.

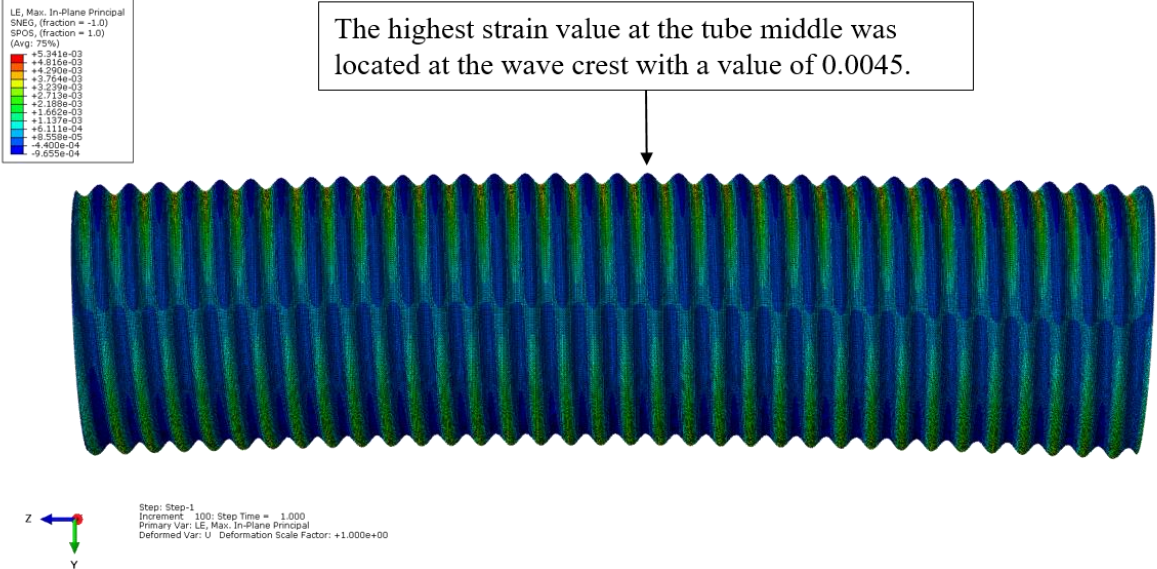


Figure 90: Tube (1 – 5) exposed to static bending analysis

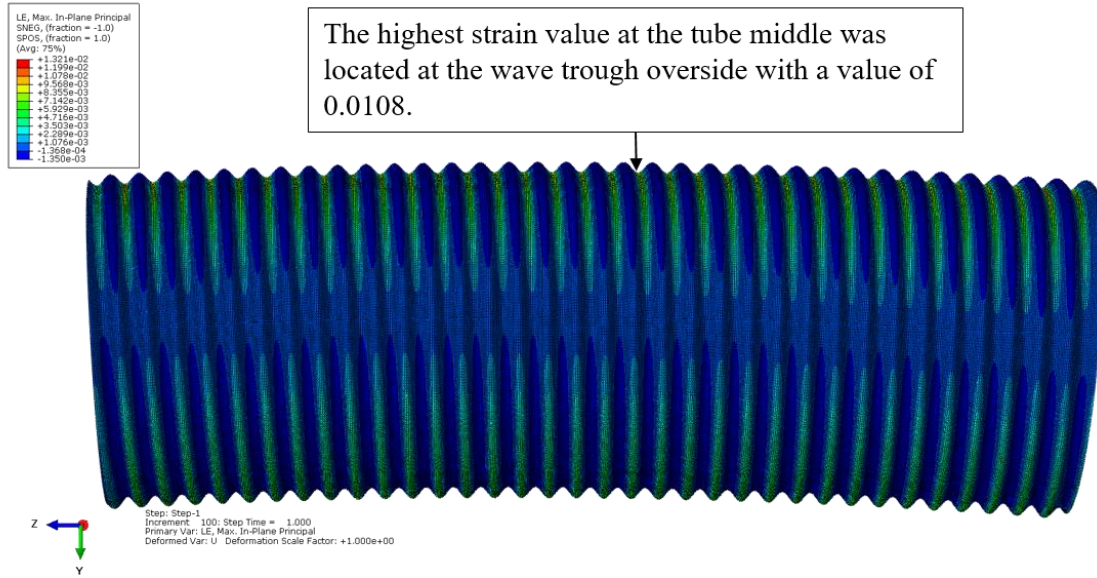


Figure 91: Tube (2 – 1) exposed to static bending analysis

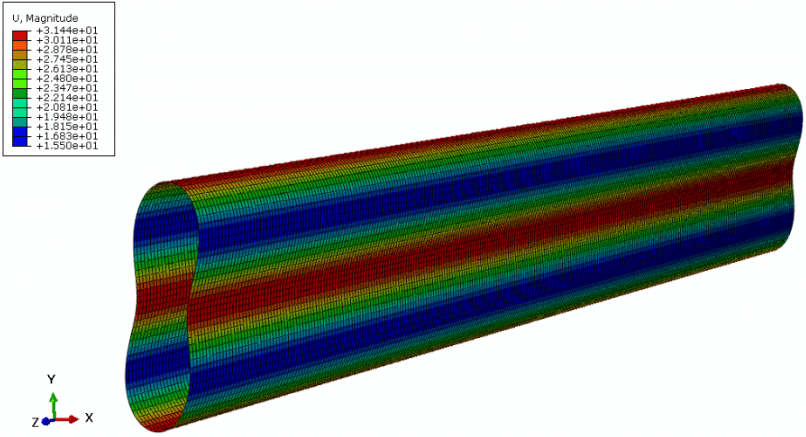
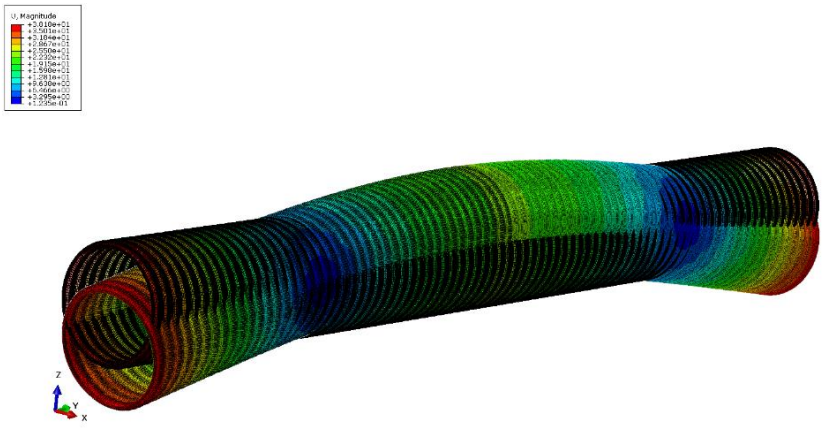
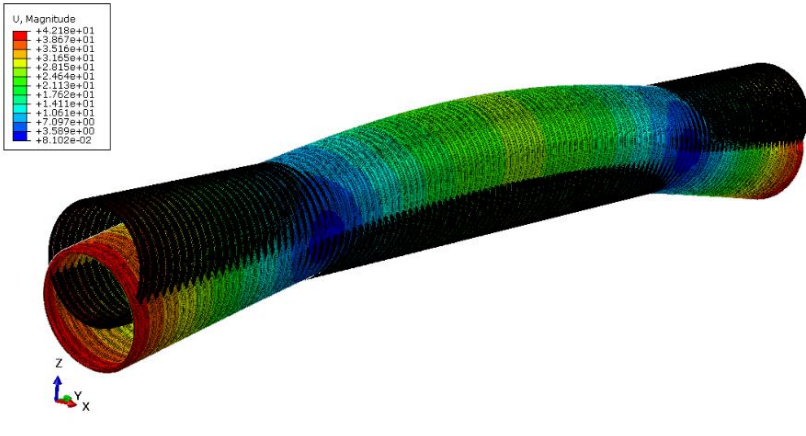
9.3.2 Modal Analysis

Table 37, summarizes the first natural eigenfrequency and corresponding mode shape appurtenant to the tubes that was exposed to four-point bending analysis.

Table 37: Modal analysis results

Tube	$f_1$ [s <sup>-1</sup> ]	Mode shape (Deformation scale = 1)
Smooth version of (1 – 5)	192.11	

9.3 Quasi-Static Four-Point Bending

<p>Smooth version of (2 – 1)</p>	<p>130.47</p>	
<p>(1 – 5)</p>	<p>72.95</p>	
<p>(2 – 1)</p>	<p>57.95</p>	

9.3.3 Strain Development without Insulation

Figure 92 and Figure 93, respectively, show the strain development for tube (1 – 5) and (2 – 1), at a deflection that coincide with the calculated height, H, presented in Table 11.

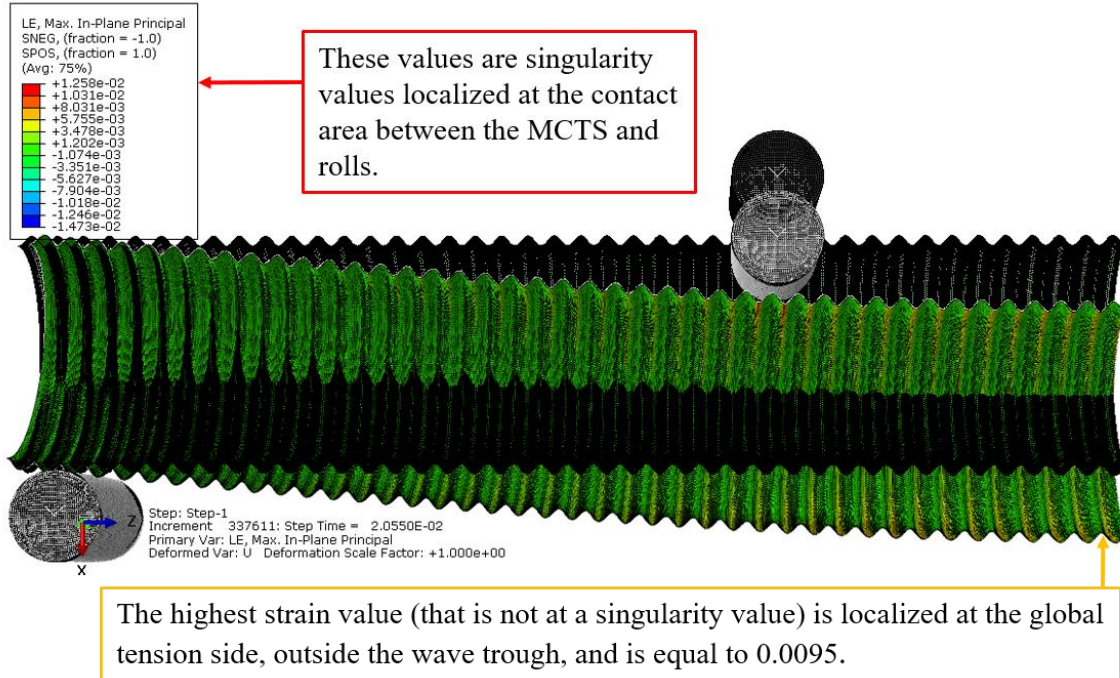


Figure 92: Tube (1 – 5) at a vertical deflection of 29mm caused by four-point bending

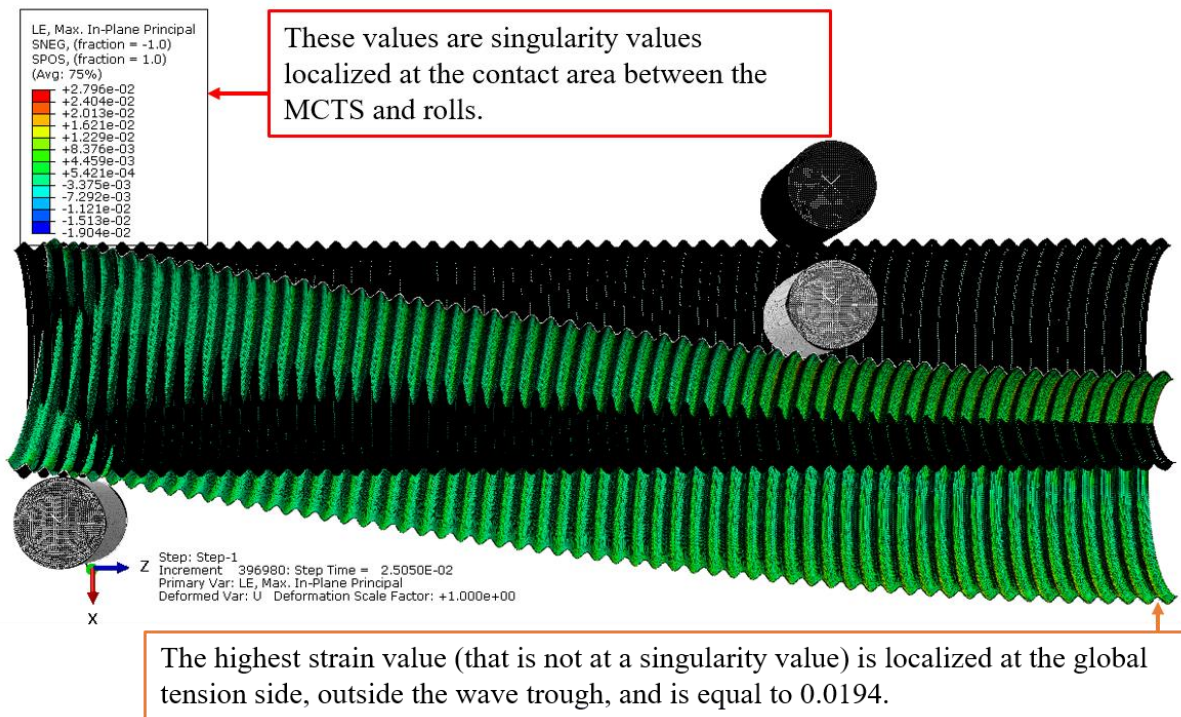


Figure 93: Tube (2 – 1) at a vertical deflection of 59mm caused by four-point bending

### 9.3 Quasi-Static Four-Point Bending

When comparing the two tubes at an equal deflection, that is at a deflection equal to 29mm, tube (2 – 1) experienced an accumulated strain value of 0.0091 outside the wave trough area presented in Figure 93. This strain value is approximately 4% lower relative to the strain value present in tube (1 – 5) at the same deflection.

Figure 94 and Figure 95, respectively, shows the strain development for the smooth versions of tube (1 – 5) and (2 – 1), at a deflection coinciding with the calculated height, H, presented in Table 11. The tubes experience local wall collapse at the contact area, between the fixed roll and sheath surface. Local wall collapse at the sheath area in contact with the outer roll started to develop after only 5mm vertical displacement of both models.

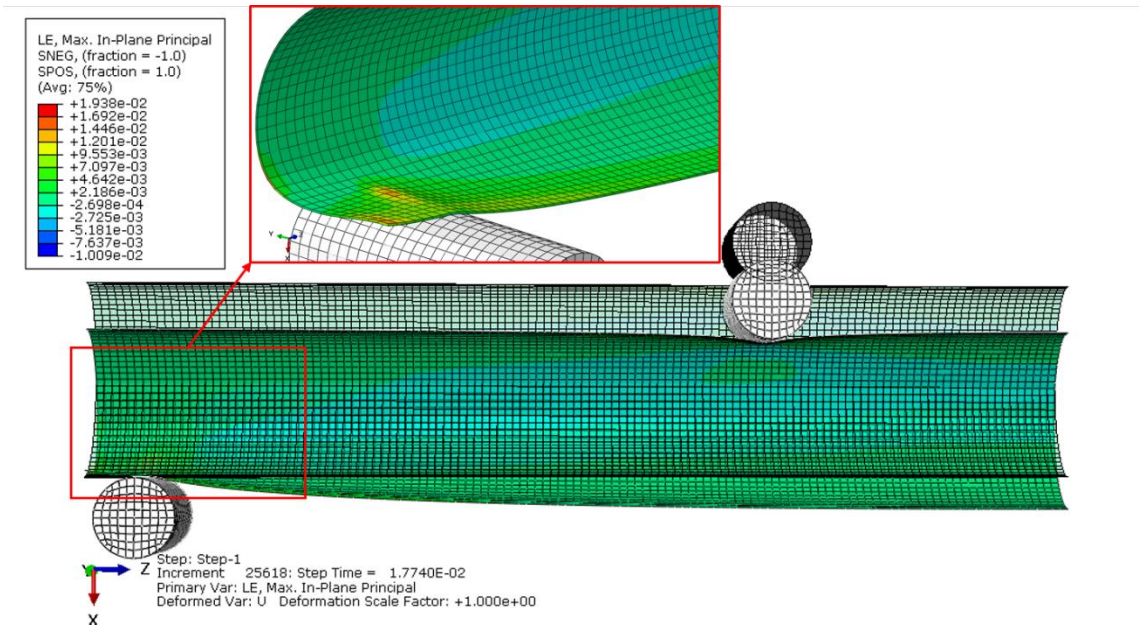


Figure 94: Smooth tubular version of tube (1 – 5) at a vertical deflection of 29mm caused by four-point bending



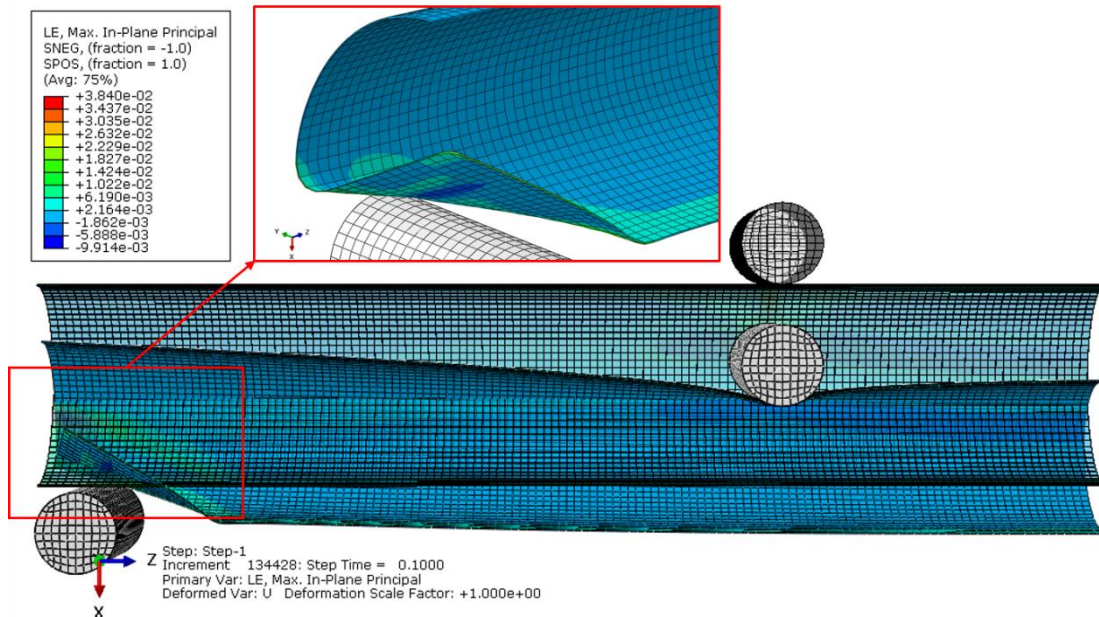


Figure 95: Smooth tubular version of tube (2 – 1) at a vertical deflection of 59mm caused by four-point bending

To avoid local wall collapse, the tubes were divided into two different sections. The section in contact with the fixed roll were assigned elastic material properties only. The other section inherited the initially assigned material properties. Afterwards, a new FEA was performed. However, the attempt turned out to be unsuccessful.

Then, the section in contact with the fixed roll was assigned an artificially high Young's modulus, subsequently followed by a new FEA. However, this attempt also proved to be unsuccessful.

Either way, the tubes tended to experience local wall collapse, either at the sheath surface in contact with the fixed roll, or at the sheath surface in contact with the middle roll. Hence, it was challenging to extract valid and useful strain values from the smooth tubes.

#### 9.3.4 Strain development with insulation

Figure 96 and Figure 97, respectively, shows the strain development for tube (1 – 5) and (2 – 1), filled with insulation, at a deflection coinciding with the calculated height,  $H$ , presented in Table 11. The highest strain value occurs at the same location as for the MCTSs deflected without internal insulation. Tube (1 – 5) experience approximately a 5.3% lower maximum tensile strain value when filled internally with insulation. Tube (2 – 1) experience approximately a 17.5% lower maximum tensile strain value when filled internally with insulation.

### 9.3 Quasi-Static Four-Point Bending

When comparing the two tube types at an equal deflection, that is at a deflection equal to 29mm, tube (2 – 1), with insulation, experienced an accumulated strain value of 0.0058 outside the wave trough area visualized in Figure 93. This strain value is approximately 35.5% lower relative to the strain value present in tube (1 – 5), with insulation, at the same deflection.

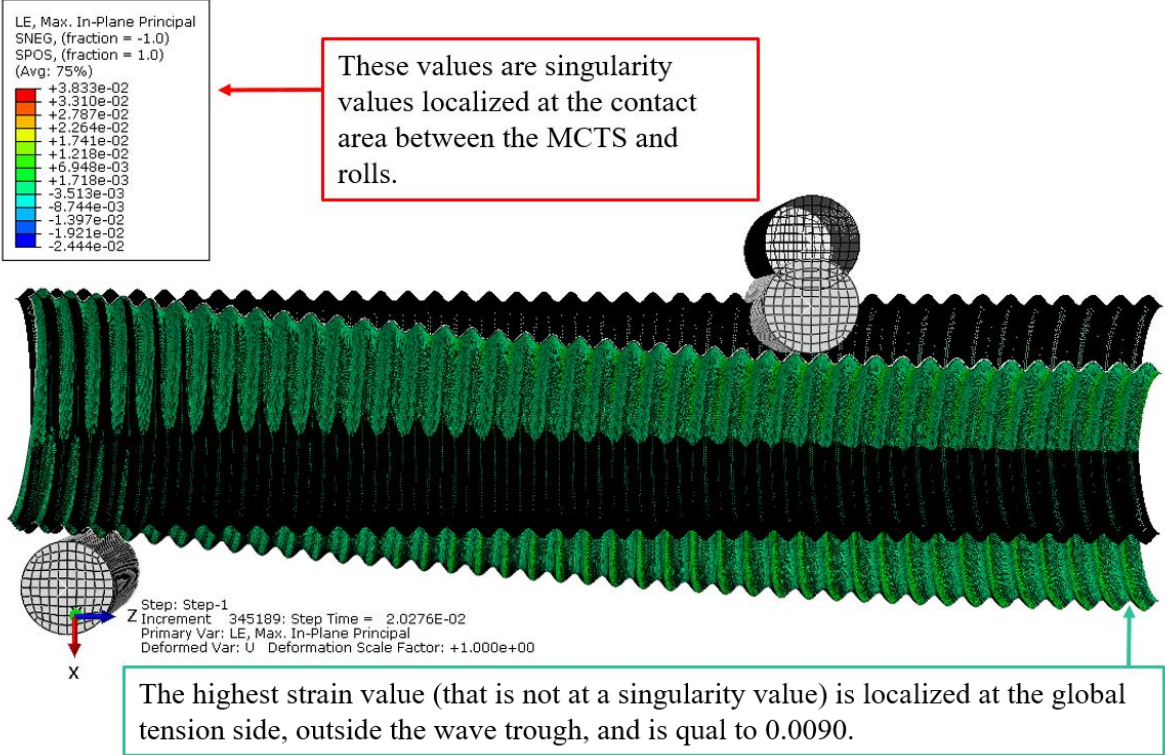


Figure 96: Tube (1 – 5) at a vertical deflection of 29mm caused by four-point bending

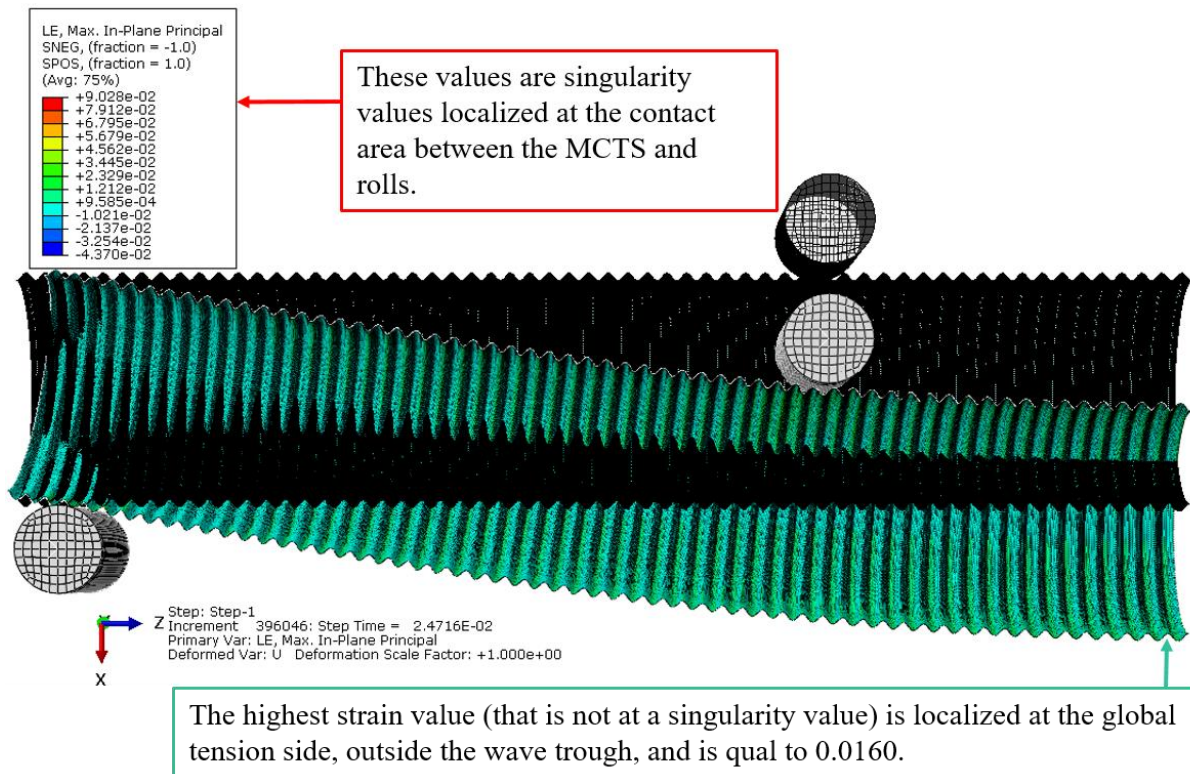


Figure 97: Tube (2 – 1) at a vertical deflection of 59mm caused by four-point bending

Figure 98 and Figure 99, respectively, shows the strain development for the smooth versions of (1 – 5) and (2 – 1), filled internally with insulation at a deflection coinciding with the calculated height, H, presented in Table 11. The figures indicate a local wrinkle/kink effect at the global compressive tube side close to the tube middle. These local areas experience a congestion of stress and strain.

A comparison of the two smooth tube versions at an equal deflection, that is at a deflection equal to 29mm, indicated differences in accumulated strain. The smooth version of tube (2 – 1) generated a maximum tensile strain value on the global tension side of the tube equal to 0.0160. This value is approximately 18.5% lower than the generated strain value in the smooth version of tube (1 – 5) at the same deflection.

### 9.3 Quasi-Static Four-Point Bending

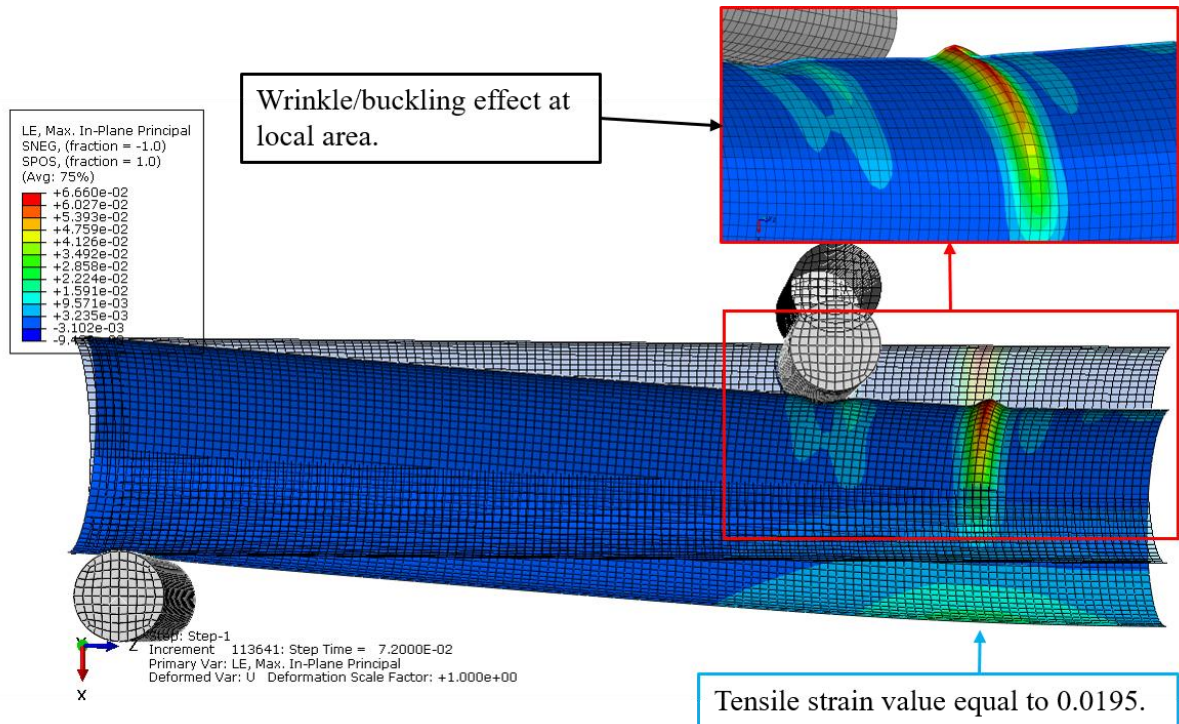


Figure 98: Smooth version of tube (1 – 5) including an internal insulation, not visualized, at a vertical deflection of 29mm caused by four-point bending

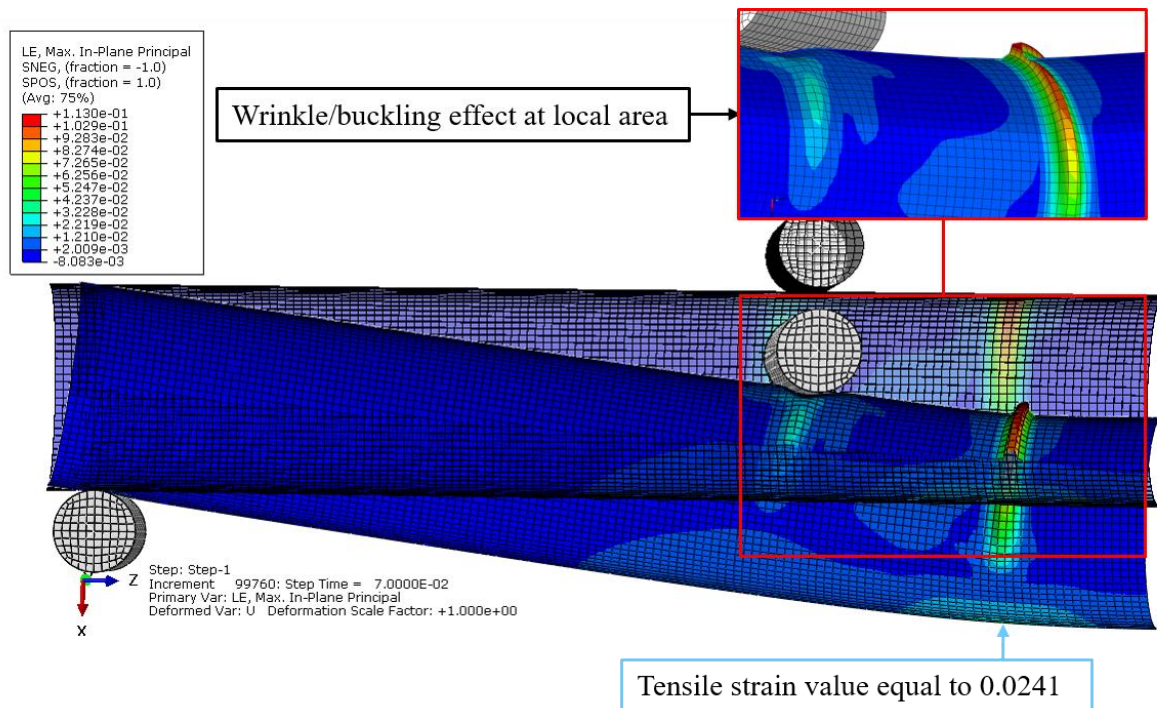


Figure 99: Smooth version of tube (2 – 1) including an internal insulation, not visualized, at a vertical deflection of 59mm caused by four-point bending.

## 9.3.5 Force-Displacement

Figure 100 and Figure 101, presents various force-displacement curves for tube (1 – 5) and (2 – 1), when forced vertically into a, respectively, 29mm and 59mm deflection. The plotted data was extracted from a reference point centred in the middle rigid roll that was forced into vertical motion during the quasi-static simulations.

In the plots, textboxes are utilized to explain important aspects related to the various curve behaviour. In general, the present oscillating behaviour of the curves relates to both a sliding-stop-sliding effect, but also due to varying impact behaviour and local defects occurring at the contact areas between the rolls and the sheathing.

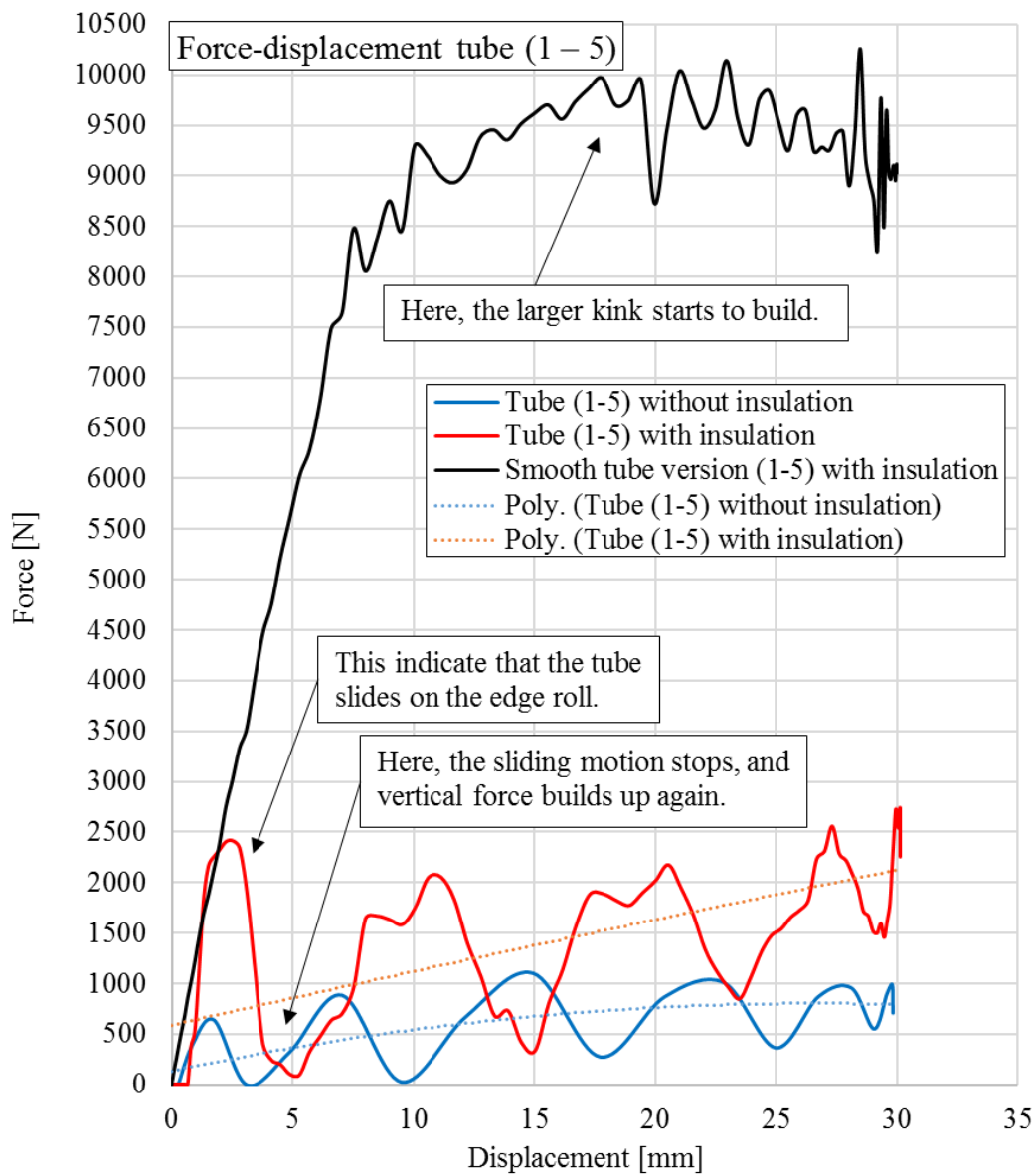


Figure 100: Force-displacement curves for tube (1 – 5), extracted from quasi-static four-point bending analysis.

### 9.3 Quasi-Static Four-Point Bending

Figure 100, indicates that the smooth version of tube (1 – 5), with insulation, requires a 4 times higher vertical force relative to tube (1 – 5), with insulation, to reach the given vertical deflection. The plot also indicates that tube (1 – 5), without insulation, requires approximately 2.5 times more vertical force, relative to the same tube model without internal insulation, to reach the given vertical deflection.

Figure 101, indicates that the smooth version of tube (2 – 1), with insulation, requires approximately 2.4 times more vertical force, relative to the corrugated tube (2 – 1), with insulation, to reach the given vertical deflection. The plot also indicated that tube (2 – 1), without insulation, requires approximately a 7 times higher vertical force, relative to the same tube model without internal insulation, to reach the given vertical deflection.

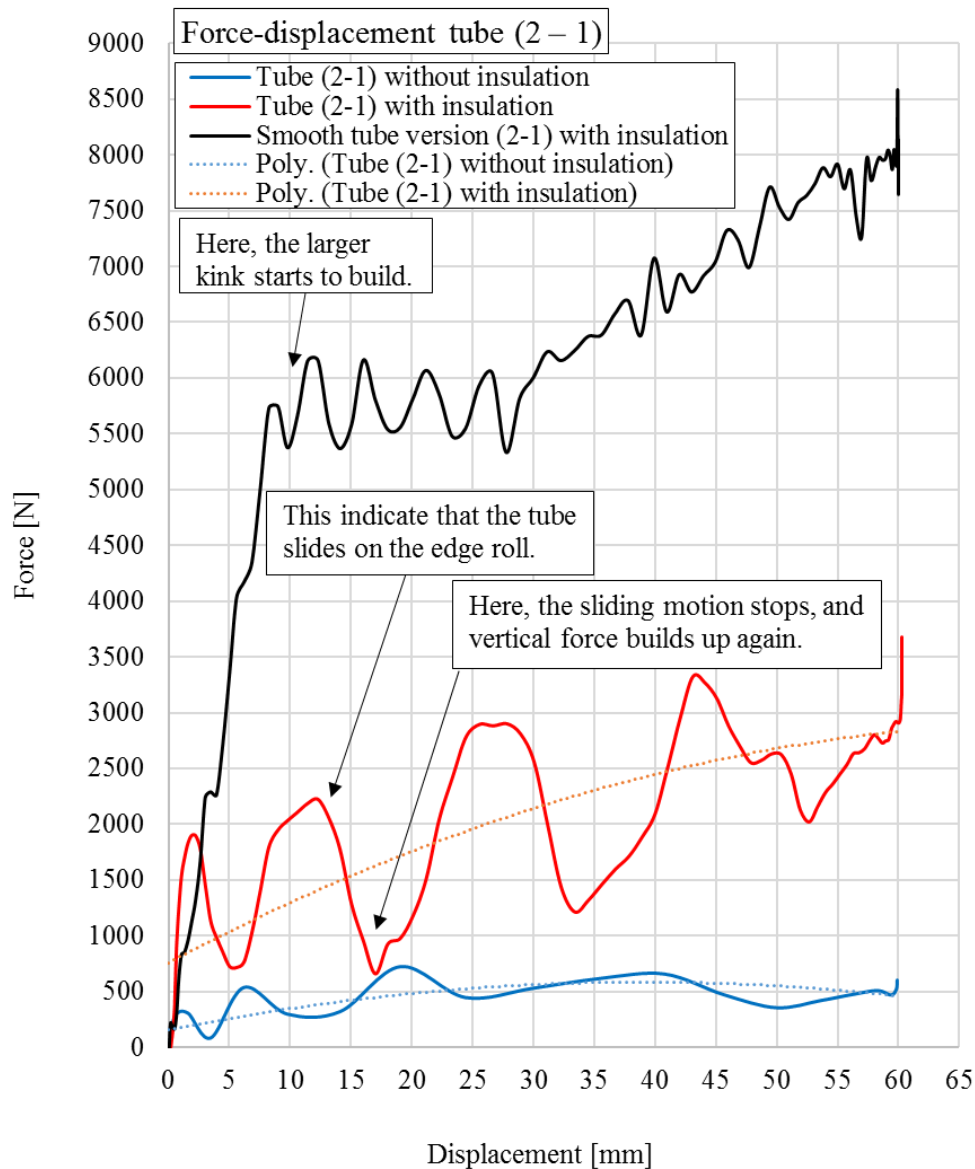


Figure 101: Force-displacement curves for tube (2 – 1), extracted from quasi-static four-point bending analysis.

## 9.3.6 Internal vs Kinetic Energy

As mentioned in section 6.7.3, the most valuable quality check of a quasi-static analysis is to check the development of artificial strain energy and the relationship between developed kinetic and internal energy. For the performed quasi-static analysis in this thesis, the development of artificial strain energy was negligibly small, that is below 1% of the internal energy developed in the various tube models.

About the ratio of developed kinetic and internal energy, within the various tube models, a trial and error approach had to be performed. The reason for this approach was to find a load rate large enough to run the analysis in a cost-effective manner but at the same time low enough to bring the kinetic energy down to an acceptable low level, that is approaching a max 10% ratio of the kinetic to internal energy. The trial and error approach was based on the obtained natural eigenfrequencies for the two different tube models, mentioned and discussed in section 6.8.2 and corresponding results presented in section 9.3.2. Based on the calculated “max” load rates, several simulations were performed with continuously decreasing the load rates, while simultaneously checking the ratio of developed kinetic and internal energy. In the end, a compromise had to be made.

Figure 102, Figure 103 and Figure 104, presents the ratio between developed kinetic and internal energy within the various tube models for the final selected load rates, presented in Table 38.

*Table 38: Selected load rates and computational time for the quasi-static bending analysis*

<b>Tube</b>	<b>Maximum load rate (minimum time period) [s]</b>	<b>Final chosen load rate [s]</b>	<b>Computational time [hr]</b>
(1 – 5) without insulation	0.0137	0.0274	20
(1 – 5) with insulation	Not available	0.0274	24
(2 – 1) without insulation	0.0167	0.0334	28
(2 – 1) with insulation	Not available	0.0334	31

9.3 Quasi-Static Four-Point Bending

Smooth version of (1 – 5) with insulation	0.0052	0.1	2
Smooth version of (2 – 1) with insulation	0.0077	0.1	3

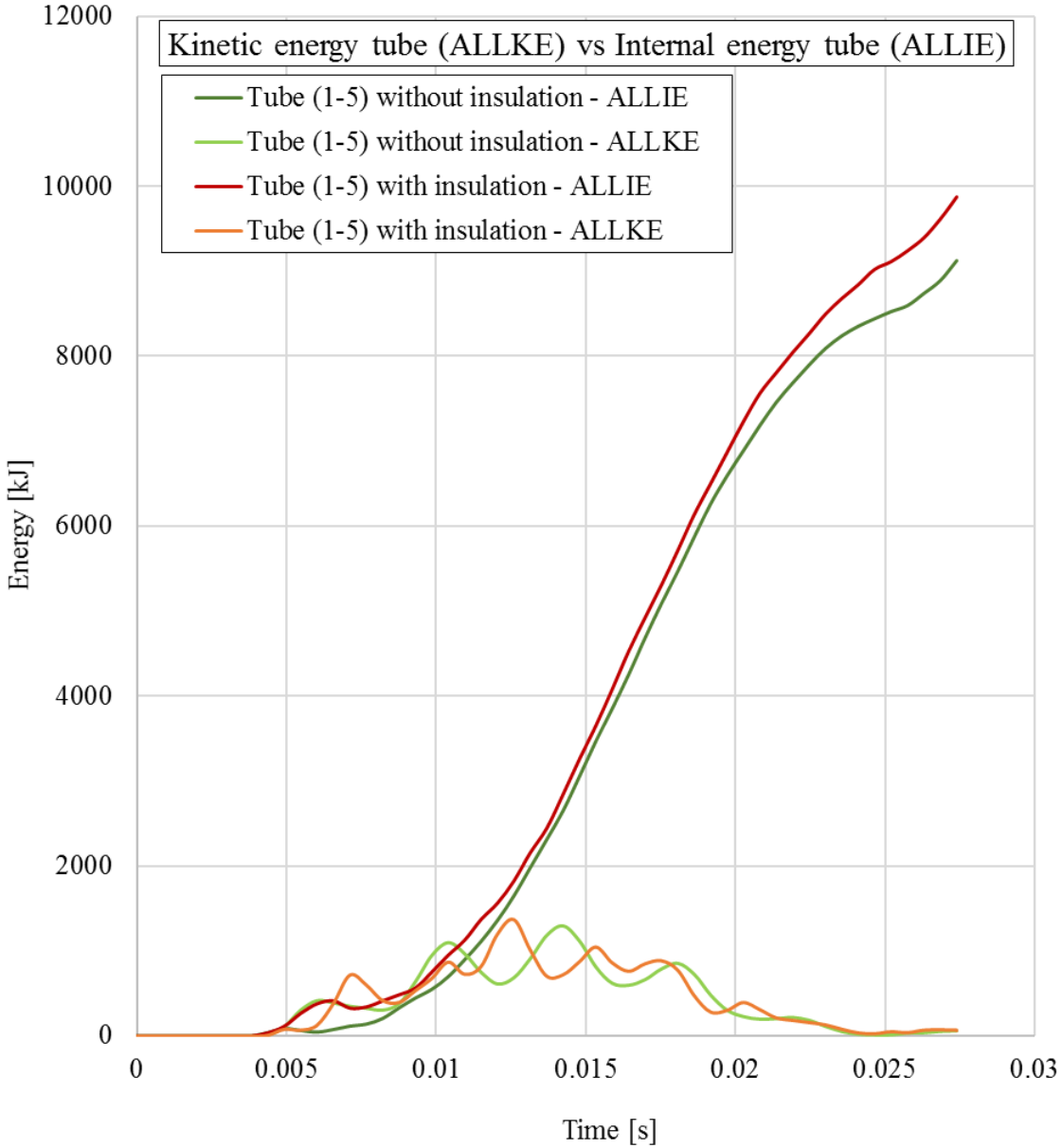


Figure 102: Kinetic energy (ALLKE) vs Internal energy (ALLIE) in tube (1 – 5), extracted from quasi-static four-point bending analysis.



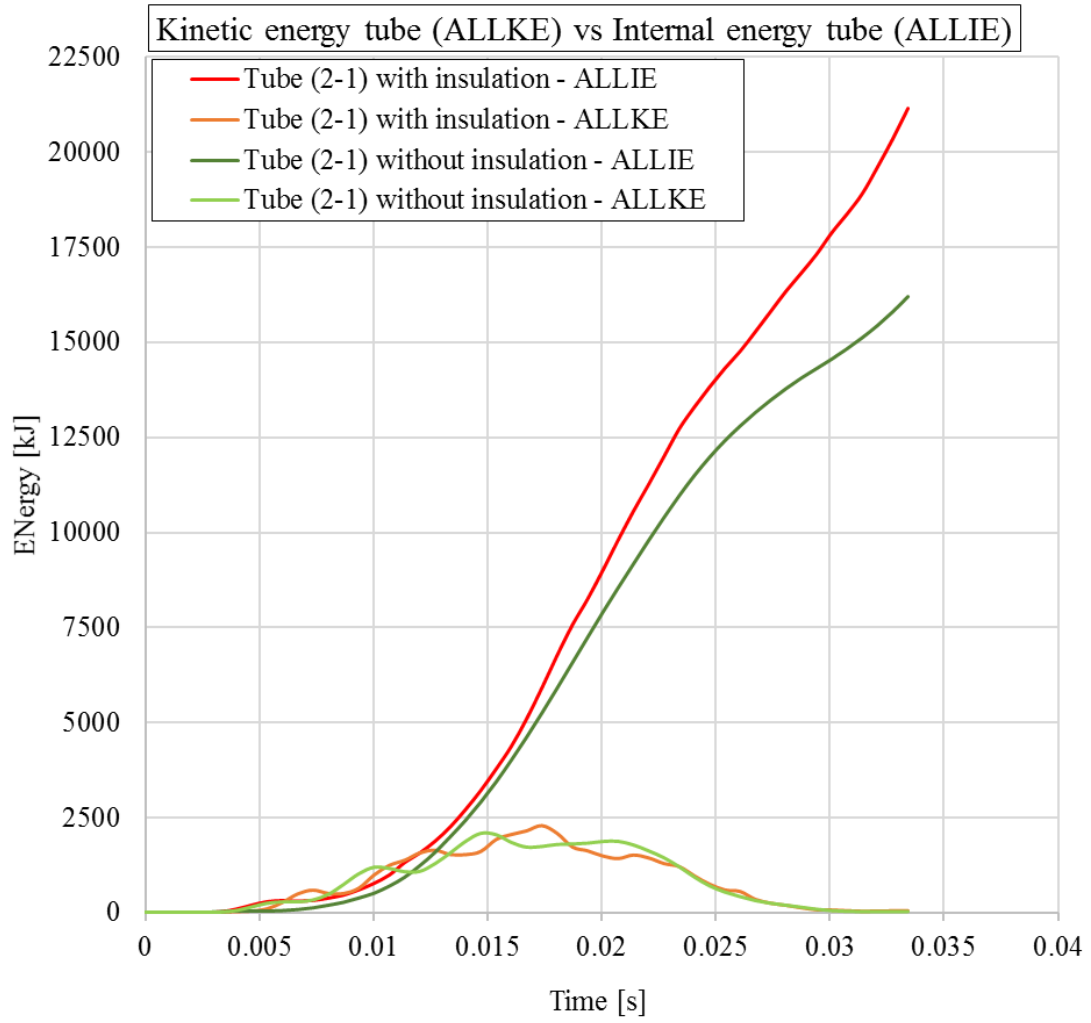


Figure 103: Kinetic energy (ALLKE) vs Internal energy (ALLIE) in tube (2 – 1), extracted from quasi-static four-point bending analysis.

9.3 Quasi-Static Four-Point Bending

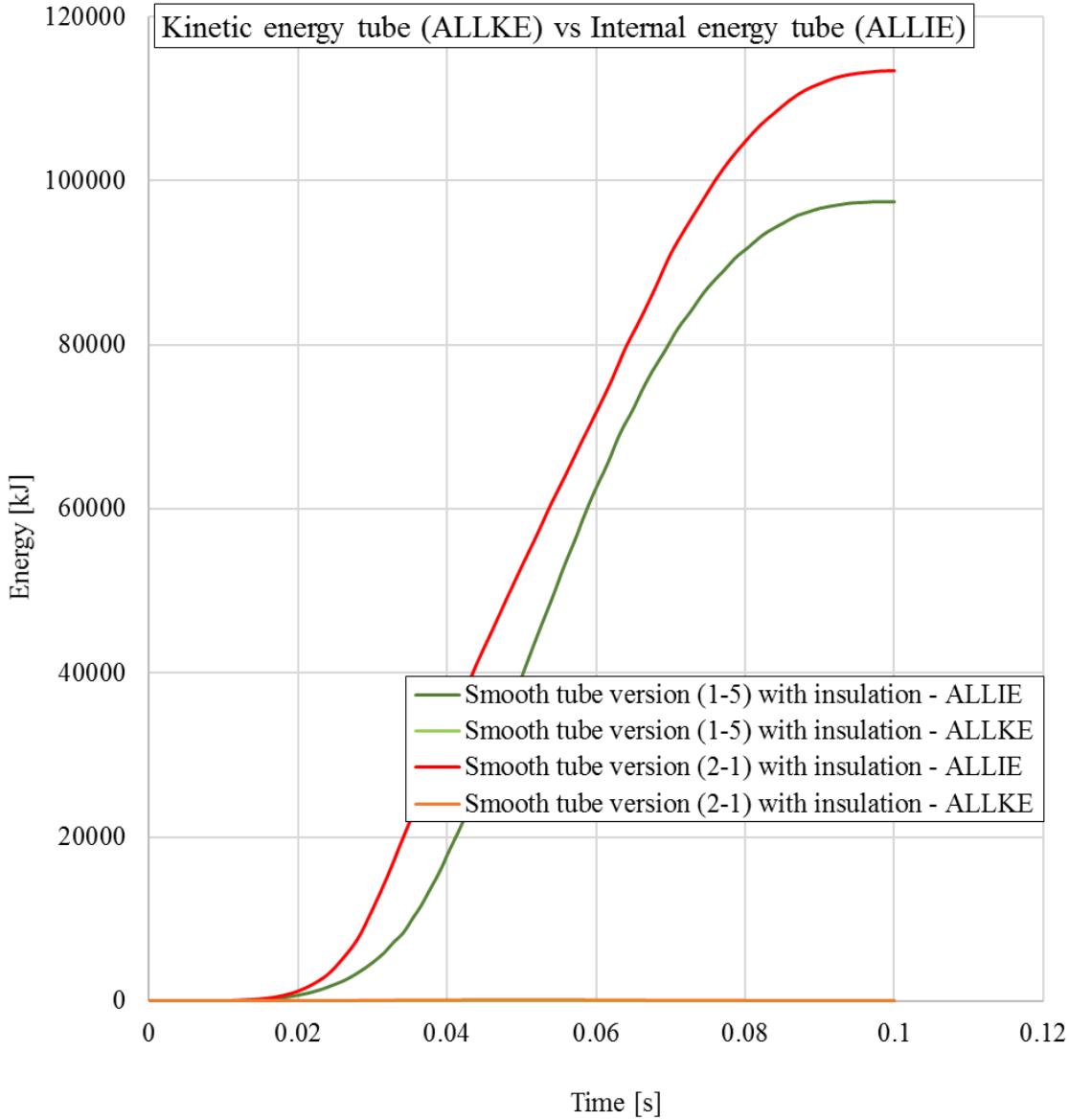


Figure 104: Kinetic energy (ALLKE) vs Internal energy (ALLIE) in smooth versions of tube (1 – 5) and tube (2 – 1), with insulation, extracted from quasi-static four-point bending analysis.

## 10 Discussion

### 10.1 Experimental Work

#### 10.1.1 Choice of Measurement Technique

When it came to decide which technique to use for the residual stress measurements, several techniques were discussed and thought of. The main criteria for the choice of technique were simplicity, time-effectiveness, cost-saving and non-destructiveness (if possible).

All the mentioned techniques, described in section 4.7.4, in Table 8, were possible candidates. However, the techniques involving dissection were disregarded. The reason for this was mainly because of its destructive technique, but also since such techniques function better for gross residual stress development over a larger sheet/depth in a simple geometry. On the one hand, it was conceivable that there existed gross residual stress values in the MCTS surface, but on the other hand, the MCTS geometry was complex, leading to a possible residual stress pattern that irrespectively would change rapidly along the corrugations.

The hole drilling technique is a destructive method, and would offer a relatively low accuracy. However, on one hand the hole drilling method was quite economical, but on the other hand it also, somewhat in the same way as the dissection techniques, functions better for uniformly developed residual stresses over an area larger than the dimension of the drilled hole. It was highly conceivable that both the residual stress development and residual stress magnitude was uneven along the MCTS surface. The mentioned arguments all ended with a conclusion to disregard the hole drilling method for the residual stress measurement in this thesis.

X-ray diffraction, ultrasonic, magnetic and Raman spectroscopy, all mentioned in Table 8, were all possible non-destructive candidates. Table 8, indicates that Raman Spectroscopy offers a relatively low accuracy. Both the ultrasonic and magnetic method shared the same limitation with respect to errors caused by material orientation, grain size and amount of cold work performed. However, these techniques could offer a relatively better accuracy. The X-ray diffraction technique required an expensive apparatus which would be limited to a workshop specific area. This technique could only measure a shallow surface layer in a polycrystalline fine grained material. However, the required measurement time was relatively low and the MCTS was made of a polycrystalline fine grained material which made it susceptible for X-ray diffraction.

In the end, it was decisive what equipment was available on the NTNU campus with respect to time and cost. Since the Department of Marine Technology at NTNU at Tyholt was in

## 10.1 Experimental Work

possession of an X-ray diffraction apparatus which Professor Sigmund Kyrrre Ås had experience of making use of for residual stress measurement, the X-ray diffraction method was selected as technique.

### 10.1.2 Measurement Results

On a general basis, the stress measurement results from tube (1 – 2) and (2 – 2) indicated a significant amount of tensile residual stresses around the MCTS outside circumference. In the welding seam, tensile axial stresses tend to be most prominent while in the weld-free areas, all the different stress components, to various extent, are present. However, it is difficult to draw a definitive picture of the residual stresses field development since axial stress measurements are missing from some locations at the wave crest top and are totally absent in the wave trough area.

In general, the perceived residual stress variations in both tubes, for small shifts in hoop and axial direction and somewhat scattering, can be explained by several reasons. One explanation could be due to the surface curvature, which vary from one wave crest and wave trough to another around the tube circumference. It is conceivable that this could interfere the obtained residual stress measurements. Another explanation could be that there actually exist stress variations and various in-depth stress gradients for small location changes. It is also possible that the crystallographic texture is altered from one location to the other, and the X-ray diffraction technique is somewhat dependent of measuring a refined grain size, and variations in grain orientations could lead to at least small variations. Also, for small stress and strain values, the relative accuracy is quite poor.

In section 4.7.2, a possible residual stress pattern, emerged from cold working, at wave crest and wave trough area were discussed and suggested. At the wave crest top, it was assumed a negative residual stress component, mainly due to a possible spring-back effect after performing the corrugation cold working process. However, the stress measurements indicate the opposite, and not only at some clock locations, but it proves to be consistently around the whole tube circumference for both tubes. It is therefore conceivable that this is a result of the corrugation process alone, and not from any other external interfering source, for instance the global plastic deformation, that is the visible global curvature of the tubes. A reasonable explanation for this phenomenon is difficult to predict in this thesis, since one does not know enough about the specific corrugation process and its significance with respect to the occurrence of residual stresses through the thickness of the thin wall of the MCTS. One can therefore conclude that

the corrugation process is complex and needs a deeper investigation with respect to its impact on the MCTS surface and residual stress significance.

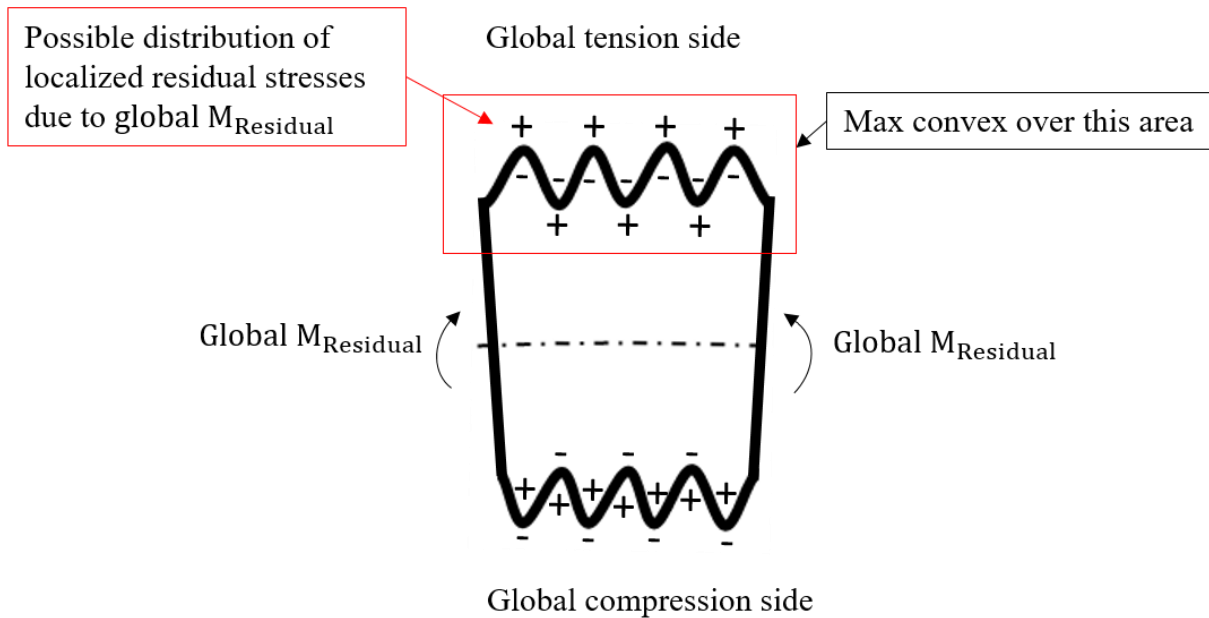
In the weld-free areas around the two tube types outer circumference, the measurements indicate that tube (2 – 2) holds a somewhat higher hoop stress and hoop shear stress magnitude compared to tube (1 – 2), although some scattering exist. There could be several reasons for this.

Based on the two created bilinear material curves described in section 7.4.2, it is conceivable that tube (2 – 2) has experienced a somewhat higher amount of strain hardening than tube (1 – 2) based on both their various yield strength and especially the slope of the plastic curves, which is somewhat higher for tube (2 – 2). This might call for a somewhat higher relatively residual stress value present in tube (2 – 2). However, tube (2 – 2) holds a relatively lower thickness, which might call for a higher flexibility. Another possible explanation can lie in their different local corrugation geometry, that is the value of A and P. On the one hand tube (1 – 2) holds a relatively larger value of A and P, on the other hand the P/A ratio for both tubes are almost similar, which might cancel out the reciprocal difference of P and A. It is however difficult to make any form of conclusion based on this aspect. Hence, it is conceivable that the different material properties can be the main cause for the small variation in residual stress magnitude around the two tubes outer circumference in the weld-free areas.

In the welding seam area, considering both tubes, the residual stress measurements indicate some differences. Tube (1 – 2) proves to hold a relatively higher residual stress magnitude in and across the welding seam compared to tube (2 – 2). One explanation may be the fact that tube (1 – 2) holds a higher wall thickness, which might require higher heat input to the weld area to achieve the same amount of burnout compared to tube (2 – 2), which holds a thinner wall thickness. This might increase FZ and HAZ, giving rise to a possibly higher residual stress magnitude in tube (1 – 2), compared to what tube (2 – 2) will be in possession of. Another explanation could be the presence of the tubes global bended curvature. Tube (2 – 2) holds a larger bended curvature than tube (1 – 2), possibly giving rise to a larger amount of residual stresses because of the plastic deformation. For tube (2 – 2), the convex curvature peak is located over the welding seam at 12 o'clock. This is not the case for tube (1 – 2), where the welding seam is located at 9 o'clock, which is more neutrally located compared to the convex peak found at 1 o'clock. A potential residual stress pattern arising from the global curvature and the spring-back effect, where the convex peak is located over, can be seen in Figure 105. The residual stress pattern, visualized in Figure 105, could potentially interfere with the

## 10.1 Experimental Work

measured tensile residual stresses at the wave crest area in the welding seam in tube (2 – 2). The size of impact and its significance is however difficult to predict. It is therefore more likely that tube (1 – 2) holds a higher residual stress magnitude in and across the welding seam, compared to tube (2 – 2), because it may have required a higher heat input during the welding process, as discussed above.



*Figure 105: Possible local residual stress pattern along the corrugation geometry in a MCTS exposed to a global moment causing a permanent global bended curvature, causing local plasticity along the corrugation geometry. – indicate compressive residual stress while + indicate tensile residual stress.*

Anyway, the measured residual stresses may influence the tubes fatigue life during a dynamical bending loading. The tensile residual stresses indicated on the outside will cause the tubes to experience a higher loading than initially applied externally, and these stresses will have somewhat the same significant of impact as a typical mean stress value, which was discussed in section 4.7.2 and visualized in Figure 24.

## 10.2 Static and Quasi-Static Analysis

The 3D models of the MCTS, during both the static axial, static bending and quasi-static four-point bending analysis, were assigned with both homogenous material properties and thickness along the corrugation geometry, without accounting for any pre-defined strain hardening from the manufacturing process, and without the presence of a longitudinal welding seam. This is however not the case for a real MCTS. Hence, the MCTS material properties and thickness is inhomogeneous leading to variations in both axial and bending stiffness along the corrugations. Also, the fatigue strength can be decreased if unfavourable tensile residual stresses from cold forming and welding is present at the surface. This implies a limitation to the performed FEA simulations.

### 10.2.1 Static Axial analysis

The strain field development trend along the corrugations, indicated by Figure 75 and Figure 76, will not change much by introducing various material properties and thicknesses along the corrugations. But it is conceivable that the strain values will change. On the one hand the model will be stiffer due to strain hardening at the wave crest and wave trough areas, on the other hand the MCTS may be less stiff at local areas due to inhomogeneous thickness after being formed. This might in overall result in higher developed strain values at both the wave crest and wave trough for the MCTS. However, it is likely that the strain output trend comparison between the wave crest and wave trough, presented in Figure 77, will remain the same, but that again highly depends on the amount of induced strain hardening and residual stresses.

The obtained trends with respect to both thickness and amplitude sensitivity, presented in Figure 78 and Figure 79 will likely not change much, at least qualitatively, by introducing more real material properties along the corrugations. But the strain ratios plotted along the y-axis at both figures will probably indicate higher ratio values, meaning that the figures now indicate an unrealistically good result for the MCTS. It is further expected that both the thickness and amplitude sensitivity may be amplified due to higher stiffness at the wave crest. Also, it is likely that a MCTS, in reality, will push back with a higher reaction force due to an increased stiffness at local regions, meaning that both Figure 80 and Figure 81, indicates a somewhat unrealistic good result for the various P-values compared to a smooth tubular sheathing.

Prior to the axial analysis an assumption was made considering a negligible helical significance. Figure 83, proves that this assumption was valid, since the change in developed strain along the corrugation geometry tends to be relatively small. However, the result indicates an increasing

## 10.2 Static and Quasi-Static Analysis

difference between an annular and a helical wave pattern for a high  $P/A$  ratio, although the difference is small. This small change in developed strain indicates that the MCTS tends to stiffen at somewhat higher  $P/A$  ratios when subjected to axial displacements.

Even considering the limitations inherent to the utilized FEA approach for the axial analysis, the assumptions made, and results obtained, provides a useful approximation of how a MCTS reacts to axial displacement when varying its geometrical corrugation parameters. Hence, the obtained results could further be used to describe fatigue properties and predict fatigue life for a MCTS.

### 10.2.2 Static Bending Analysis

The strain field development trend along the corrugation, presented in Figure 86 and Table 36, and the helical inclination sensitivity presented in Figure 87, all indicate a phenomenon of local congestion of accumulated strain close to the tube ends during the static bending. The reason for this phenomenon is probably twofold. On the one hand the utilized MPC beams caused the MCTS to behave artificially stiff in the ends, allowing the appearance of local congestion of accumulated strain in the relatively sharp transition area between the normal tube stiffness and the artificial MPC stiffness close to the tube ends. On the other hand, it is conceivable that the MCTS stiffens independently of the MPC beams when the helical inclination angle increases, at least for high  $P/A$  ratios, which implies that the MCTS is converging towards a smooth tubular sheathing. The assertion and indication of a stiffen MCTS behaviour at higher inclination angles for higher  $P/A$  ratios are justified by Figure 86. This plot indicates that the vertical displacement drops somewhat at the tube middle for  $P/A = 7$  when increasing the inclination angle. The above discussed aspects indicate that more of the induced energy, due to a forced angular displacement and the usage of artificial stiff MPC beams, accumulate at the ends rather than distributing smoothly towards the MCTS middle. Because of this, it is conceivable that the obtained strain values from the middle of the MCTS during the static bending analysis provides an artificially good result, meaning that the strain values probably should be somewhat higher than they pretends to be. This also implies that the helical inclination sensitivity at a  $P/A = 7$ , obtained at the middle of the MCTS, actually lies somewhere between the curve obtained from the local congestion of accumulated strain values close to the tube ends, and the curve obtained from the highest strain value at the middle.

The phenomenon of local congestion of accumulated strain could have been avoided by utilizing a three-point or four-point bending method instead. However, such an approach would



involve contact interaction which again would have introduced a displacement boundary condition (highly nonlinear) and thus decreased the computationally effectiveness.

Considering the shear strain sensitivity, indicated in Figure 88, the plot indicates a relatively high sensitivity when increasing the helical inclination angle. An increased proportion of shear strain is proportional to an increase of torsional forces. This means that torsional forces have a growing present when the helical inclination angle is increased, especially at a high P/A ratio, indicated by Figure 88. An increasing amount of torsional forces implies an increased amount of twisting of the MCTS during bending. When the MCTS is functioning within an operational dynamic HV submarine power cable, it is not allowed to twist within the cable section. This implies a larger amount of internal locked-in torsional forces, not allowed to relieve itself, when applying a high helical inclination angle compared to a low one. At worst, this can significantly reduce the fatigue life of a MCTS utilized within a dynamic HV submarine power cable, when exposed to dynamical bending forces.

The indication of negligibly ovality during static bending, presented in section 9.2.4, can be explained by the fact that a MCTS is much more flexible compared to a smooth tubular sheathing. A smooth tubular sheathing holds one global tension and compression side during bending, while a MCTS distributes the global tension/compression during bending into several local tension/compression areas along the corrugation geometry. This local distribution of global forces equalizes the global tension/compression values along the sheathing adjusting the reciprocal distance between the global tension and compression side of the MCTS. Hence, ovality is avoided.

The absence of pre-strain hardening parameters in the corrugation geometry would probably have somewhat the same significance to the obtained results in the static bending analysis as it would have for the static axial analysis, discussed in section 10.2.1. It is conceivable that the various presented strain values in the various plots probably will increase consistently. At the same time, it is conceivable that the presented trends will remain tolerably unchanged.

Even considering the limitations inherent to the utilized FEA approach for the bending analysis, the assumptions made, and results obtained, provides a useful indication of how a MCTS acts when subjected to bending with both varying its geometrical corrugation parameters and helical inclination angle. This obtained results may, in collaboration with physical testing, constitute a part of a larger argumentation when determining which corrugation geometry and helical inclination angle to use in a MCTS with respect to fatigue.

## 10.2 Static and Quasi-Static Analysis

### 10.2.3 Quasi-Static Four-Point Bending Analysis

The obtained results for both the performed static bending and quasi-static bending analysis of tube (1 – 5) and (2 – 1), without insulation, all indicated a higher amount of accumulated strain values in tube (1 – 5) compared to tube (2 – 1). A reasonable explanation for this trend, could be that tube (2 – 1) holds a lower sheath thickness compared to tube (1 – 5). This calls for an increased flexibility leading to a lower amount of accumulated strain along the corrugation geometry. The same trend is found in the results for the same simulations when both the corrugated tubes and corresponding smooth tubular versions were filled with insulation. However, the difference in accumulated strain values increased when insulation was added. One explanation for this could be that tube (2 – 1) take greater advantage of being stabilized internally than tube (1 – 5), which is stiffer due to the increased wall thickness.

Both Figure 98 and Figure 99, which presents the resulting bending deformation of the smooth tubular versions of tube (1 – 5) and (2 – 1), indicates local wall collapse near the middle of the tubes. This phenomenon demonstrates the fundamental problem of utilizing a smooth tubular sheathing within a dynamic cable. The local wall buckling is catastrophic with respect to maintaining a moisture-blocking barrier within the power cable subsea. It might lead to cracks and possible rupture. This is not a result caused by fatigue, but because of a bending deflection so large that the wall become unstable at local areas and buckle.

Considering the various force-displacement curves found in section 9.3.5, it is qualitatively of importance to perform real physical experimental testing, that is full scale static bending in workshop, for comparison purposes and for verification of the obtained virtual force-displacement curves.

When analysing the obtained internal and kinetic energy behaviour for the final selected load rates in the quasi-static analysis, some instabilities can be seen in Figure 102 and Figure 103, at least in the beginning. However, the kinetic energy curves stabilize during the simulations at a level satisfying the quasi-static condition, at least to a tolerable level, meaning that the curves indicate that the performed simulations output a somewhat reasonably result. For an even better internal vs kinetic energy behaviour, it is recommended to utilize a computer inherent with a larger amount of computer resources, enabling simulations with longer time periods, which again may decrease and stabilize the kinetic energy within the tubes at an earlier stage, and at a lower level.

Even considering the limitations inherent to the utilized FEA approach for the quasi-static bending analysis, the assumptions made, and results obtained, provides a useful indication of how a MCTS acts when subjected to four-point bending. This obtained results may provide useful input for a real time experimental four-point bending process in the workshop.

## 10.2 Static and Quasi-Static Analysis

## 11 Conclusion and Further Work

### 11.1 Conclusion

When manufacturing the corrugation profile by cold forming, the X-ray diffraction measurements indicate a consistently significant presence of tensile residual stresses, both at wave crest top and wave trough overside, around the MCTS circumference. Such tensile residual stresses may act somewhat in the same way as a mean stress value and may therefore have a significantly negative impact on the MCTS fatigue life during dynamical bending loading.

By corrugating a metallic tubular sheathing, the global strain development decreases with only a small corrugation at present, which is useful both for improved flexibility and enhanced fatigue life.

The axial FEA results indicates that a low sheath thickness, is favourable with respect to local strain development and therefore increases the flexibility of a MCTS. At  $P/A = 2$ , a MCTS holding a  $t = 0.7\text{mm}$  generates approximately 10% less amount of strain compared to a MCTS inherent with a  $t = 1.0\text{mm}$ . It is further proven that for local strain development values within a MCTS, a high A-value is advantageous at smaller and medium P/A ratios, that is for  $P/A \leq 5.8$ , while a smaller A-value tends to become more favourable at a higher P/A ratio.

The bending FEA results indicates that the helical inclination sensitivity is low for smaller P/A ratios, while slightly increasing with the P/A ratio, especially when the inclination angle increases. It is further proven that the shear strain sensitivity ascends nearly linearly when increasing the helical inclination angle at both low and high P/A ratios. A small rate is generated by even the least possible angle of inclination. However, the ascending slope increases with an increasing P/A ratio. Also, the FEA indicates a negligibly appearance of ovality within a MCTS subjected to bending loading, independent of the P/A ratio and magnitude of helical inclination angle.

The quasi-static bending FEA results indicated that the MCTS flexibility increases when thickness decreases, which undergirds the obtained axial FEA results. It is also noticeable that a smooth tubular sheathing is vulnerable to local buckling/kinks when forced into only a small deflection.

Based on the results listed above, the most suitable corrugation geometry for fatigue life, based on global and local strain development fields in the corrugation during axial and angular displacement, is a MCTS consisting of:

## 11.1 Conclusion

- A thin wall thickness
- A low P/A ratio and a high A-value
- A corrugation wave pattern either annular or helical. However, a helical wave pattern should only hold a small inclination angle, that is a lead distance comprising of not more than 1-2 wavelengths, due to shear strain sensitivity.

A prime design example considering fatigue life, based on the FEA results, may be a MCTS comprising of a  $t = 0.7\text{mm}$ ,  $P/A = 2.0$ ,  $A = 5.0\text{mm}$  and a corrugation geometry holding either an annular or helical wave pattern, where the inclination angle should be kept to a minimum.

However, one should also keep in mind that a MCTS with a higher helical inclination angle and a low A-value at a high P/A ratio may be more desirable with respect to the manufacturing process. The reason for this is that it is both easier and more efficient to produce, and it may induce less amount of residual stresses. A low A-value at a high P/A ratio is also favourable considering the power cable weight and material consumption, which decreases the total overall cost.

## 11.2 Further Work

Based on the literature study, it became clear that the friction coefficients between the adjacent layers within a dynamic HV submarine power cable is highly significant considering fatigue of the MCTS. This aspect is a topic which may be looked more into during further research.

Plausibly research questions may be:

- How does the varying friction properties impact strain development of the MCTS during bending?
- How do variations in surface roughness impact the developed strain along the corrugation geometry during bending?

Based on the MCTS X-ray diffraction measurements of residual stresses, more research is needed considering the cold forming corrugation process and its impact to the development of residual stresses. A suggestion could be to research the residual stress impact both by performing more of the residual stress measurements and simultaneously compare the obtained results with FEA based work. It could be of interest to measure the amount of residual stresses before and after performing the cold forming corrugation process for comparison purposes.

Another suggestion for further research is to perform full-scale static and fatigue testing of the received test tubes and simultaneously compare the results with quasi-static bending FEA. Based on the X-ray diffraction measurements, both the welding seam and the weld-free areas around the tubes circumference are of interest with respect to crack initiation locations. This is because the measurements indicated tensile residual stresses both at the wave crest top and the wave trough overside. Figure 106, presents a suggestion for set-up of full-scale fatigue testing. Finally, a last suggestion for further work is to perform local hardness measurements in the wave crest and wave trough area, in order to understand the local hardness profiles along the tube cross section. The hardness profiles can thereafter be varied and utilized in the FEA. It can then be possible to research the pre-strain hardening induced during cold forming and its significance to the MCTS fatigue properties

11.2 Further Work

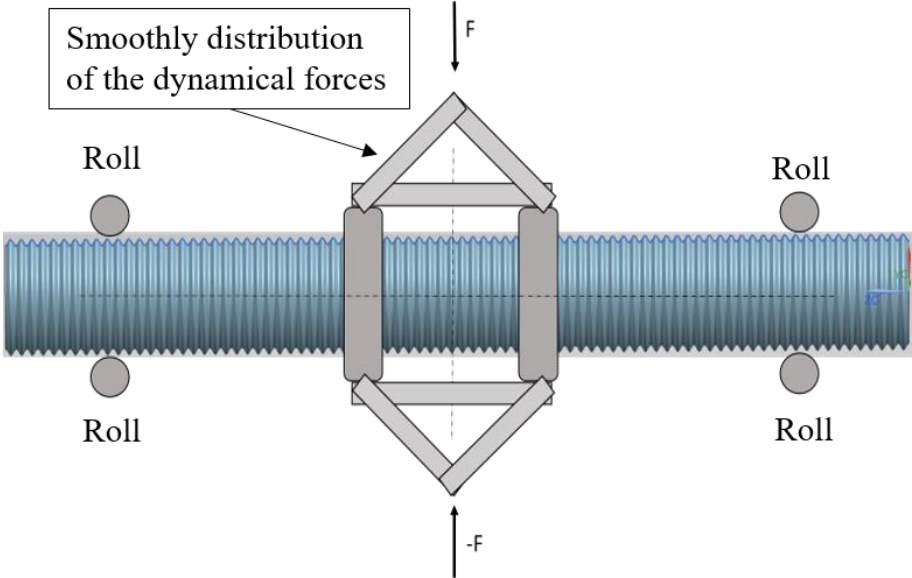


Figure 106: Suggested set-up of full-scale fatigue testing



## 12 Bibliography

- [1] C. Koelblin and F. Eggertsen, "Fatigue Resistant Metallic Moisture Barrier in Submarine Power Cable," U.S. patent no. 9 058 917 B2, 16.06, 2015.
- [2] Trelleborg. *Bending stiffener* [Picture]. Available: <http://www.trelleborg.com/offshore/~media/offshore/images--and--product--sheets/bend--control--solutions/subsea--bend--control--solutions/subsea--bend--stiffeners/subsea-bend-stiffener-installation-2-trelleborg-offshore-gallery.jpg?w=1024>
- [3] E. Eriksson, M. Jeroense, M. Larsson-Hoffstein, C. Sonesson, K.-A. Farnes, R. O. Råd, *et al.* (2011). *Submarine link - Submarine HVAC cable to the floating oil and gas platform at Gjøa*. Available: [https://library.e.abb.com/public/bbcc7542b39ba68bc125796e00527f76/48-53%204m156\\_ENG\\_72dpi.pdf](https://library.e.abb.com/public/bbcc7542b39ba68bc125796e00527f76/48-53%204m156_ENG_72dpi.pdf)
- [4] M. W. Bræstrup, J. B. Andersen, L. W. Andersen, M. Bryndum, C. J. Christensen, and N.-J. Rishøj Nielsen, *Design and installation of marine pipelines*. Oxford: Blackwell Science, 2005.
- [5] Alstom. (2010). *HVDC for beginners and beyond*. Available: [http://www.cigre.ru/research\\_commitets/ik\\_rus/b4\\_rus/library/ALSTOM\\_HVDC\\_for\\_Beginners\\_and\\_Beyond.pdf](http://www.cigre.ru/research_commitets/ik_rus/b4_rus/library/ALSTOM_HVDC_for_Beginners_and_Beyond.pdf)
- [6] M. Ardelean and P. Minnebo, *HVDC submarine power cables in the world : state-of-the-art knowledge*. Luxembourg: Luxembourg : Publications Office, 2015.
- [7] Entsoe. (2011). *Offshore Transmission Technology*. Available: [http://www.benelux.int/files/6814/0923/4514/offshore\\_grid\\_technology.pdf](http://www.benelux.int/files/6814/0923/4514/offshore_grid_technology.pdf)
- [8] J. Snyder and N. Rondorf. (2011). *About Submarine Power Cables*. Available: <https://www.iscpc.org/documents/?id=1755>
- [9] T. Worzyk, *Submarine Power Cables*. Dordrecht: Springer, 2009.
- [10] ABB AB. (2015). *525 kV extruded HVDC cable system, doubling power transmission over longer distances*. Available: [https://library.e.abb.com/public/db10262e14b5414099c9ca721964adb1/150909\\_525kV%20brochure%20\(v%209\).pdf](https://library.e.abb.com/public/db10262e14b5414099c9ca721964adb1/150909_525kV%20brochure%20(v%209).pdf)
- [11] ABB AB and M. Jeroense. (2010). *Energizing the Gjøa Oil and Gas Platform with a Dynamic Power Cable*. Available: <https://www.pesicc.org/iccWebSite/subcommittees/C/Presentations/2010Spring/C5-Spring-EnergizingtheGjoaOilandGasPlatformwithaDynamicPowerCable.pdf>
- [12] ABB AB. (2011). *World's longest most powerful dynamic AC cable, Goliat floating oil and gas platform, Barents Sea*. Available: <https://library.e.abb.com/public/46f24c5450e7d8e8c12578c0003343b6/Project%20Goliat%20123%20kV%20XLPE%20subm.pdf>
- [13] Nexans. *Transfer lines for liquefied natural gas* [Online]. Available: [http://www.nexans.de/eservice/Germany-en/navigatepub\\_315903\\_-33066/Transfer\\_lines\\_for\\_liquefied\\_natural\\_gas\\_.html](http://www.nexans.de/eservice/Germany-en/navigatepub_315903_-33066/Transfer_lines_for_liquefied_natural_gas_.html)
- [14] N. D. Insitute. (1974). *Materials for Cryogenic Service: Engineering Properties of Austenitic Stainless Steel*. [Publication]. Available: [https://www.nickelinstitute.org/~media/Files/TechnicalLiterature/MaterialsforCryogenicService\\_EngineeringPropertiesofAusteniticStainlessSteel\\_4368\\_.ashx](https://www.nickelinstitute.org/~media/Files/TechnicalLiterature/MaterialsforCryogenicService_EngineeringPropertiesofAusteniticStainlessSteel_4368_.ashx)

- [15] N. E. Dowling, *Mechanical behaviour of materials, Engineering methods for deformation, fracture and fatigue*, 4th international edition, ed.: Pearson Education Limited, 2012.
- [16] ASM International, "Austenitic Stainless Steels," in *Stainless Steels for Design Engineers*, ed: ASM International, 2008, pp. 1-10.
- [17] A. D. Norman, K. A. Seffen, and S. D. Guest, "Morphing of curved corrugated shells," *International Journal of Solids and Structures*, vol. 46, pp. 1624-1633, 4// 2009.
- [18] A. D. Norman, K. A. Seffen, and S. D. Guest, "Multistable Corrugated Shells," *Proceedings: Mathematical, Physical and Engineering Sciences*, vol. 464, pp. 1653-1672, 2008.
- [19] Nexans. (2009). *Production Line for Sheathing of High Voltage Cable UNIWEMA® HV*. Available: [http://www.nexans.de/Germany/2008/F\\_UNIWEMA\\_HV.pdf](http://www.nexans.de/Germany/2008/F_UNIWEMA_HV.pdf)
- [20] C. Frohne, M. Meyer, and F. Harten, "Method for producing longitudinally welded helically corrugated metal tubing," U.S. patent no. 6 789 318 B2, 14.09, 2004.
- [21] F. Irgens, *Continuum Mechanics*: Springer Berlin Heidelberg, 2008.
- [22] W. F. Hosford, *Mechanical behavior of materials*. Cambridge: Cambridge University Press, 2005.
- [23] C. Felippa. (2012). *Strains*. Available: <http://www.colorado.edu/engineering/CAS/courses.d/Structures.d/IAST.Lect04.d/IAST.Lect04.pdf>
- [24] Dassault Systemes. *Abaqus Analysis User's Guide (6.14 ed.)*. Available: <http://50.16.225.63/v6.14/books/usb/default.htm>,
- [25] J. Pelleg, *Mechanical Properties of Materials* vol. 190. Dordrecht: Springer, 2012.
- [26] Z. Wang and B. Gong, "Residual stress in the forming of materials," in *Handbook of Residual Stress and Deformation of Steel*, G. Totten, M. Howes, and T. Inoue, Eds., ed Materials Park: ASM International, 2002, pp. 141-149.
- [27] P. Kelly, "Strain hardening," in *Solid Mechanics Part II: Engineering Solid Mechanics - small strain*, ed. New Zealand: University of Auckland, 2012, pp. 299-313.
- [28] P. Kelly, "The Moment-Curvature Equations.," in *Solid Mechanics Part II: Engineering Solid Mechanics - small strain*, ed. New Zealand: University of Auckland, 2013, pp. 124-130.
- [29] ISO 13628-5, "Petroleum and natural gas industries. Design and operation of subsea production systems. Part 5: Subsea umbilicals. ISO 13628-5:2009," ed: Standard Norge, 2009.
- [30] M. Jeroense, C. Sonesson, and J. Ekh, "Electric power cable," U.S. patent no. 9 029 704 B2, 2015.
- [31] A. Farkas and A. Tyrberg, "Arrangement for a Dynamic High Voltage Subsea Cable and a Dynamic High Voltage Subsea Cable," U.S. patent application 2016/0217887 A1, 2016.
- [32] C. Felippa. (2013). *Thin Wall Pressure Vessels*. Available: <http://www.colorado.edu/engineering/CAS/courses.d/Structures.d/IAST.Lect03.d/IAST.Lect03.pdf>

- [33] C. Felippa. (2013). *Plane Stress Transformations*. Available: <http://www.colorado.edu/engineering/CAS/courses.d/Structures.d/IAST.Lect06.d/IAS T.Lect06.pdf>
- [34] A. Tyrberg, E. Eriksson, and J. Ekh, "Radial water barrier and a dynamic high voltage submarine cable for deep water applications," U.S. patent no. 9 171 659 B2, 27.10, 2015.
- [35] R. W. Landgraf, "The resistance of metals to cyclic deformation.," in *Achievement of High Fatigue Resistance in Metals and Alloys*, ed West Conshohocken: ASTM International, 1970, pp. 3-36.
- [36] S. A. David, S. S. Babu, and J. M. Vitek, "Welding: Solidification and microstructure," *JOM*, vol. 55, pp. 14-20, 2003.
- [37] VEQTER Ltd. *Bragg's law*. Available: <http://www.veqter.co.uk/assets/images/content-images/x-ray-diffraction/braggs-law.png>
- [38] P. S. Prevey, "X-ray diffraction residual stress techniques," *ASM International, ASM Handbook*, vol. 10, pp. 380-392, 1986.
- [39] N. S. Rossini, M. Dassisti, K. Y. Benyounis, and A. G. Olabi, "Methods of measuring residual stresses in components," *Materials & Design*, vol. 35, pp. 572-588, 3// 2012.
- [40] P. Withers and H. K. D. H. Bhadeshia, "Residual stress. Part 1 - Measurement techniques," *Materials Science and Technology*, vol. 17, pp. 355-365, 2001.
- [41] X. Huang, Z. Liu, and H. Xie, "Recent progress in residual stress measurement techniques," *Acta Mechanica Solida Sinica*, vol. 26, pp. 570-583, 2013/12/01 2013.
- [42] *Abaqus FEA software process*. Available: [https://en.wikipedia.org/wiki/Abaqus#/media/File:Abaqus\\_software\\_FEA\\_process.png](https://en.wikipedia.org/wiki/Abaqus#/media/File:Abaqus_software_FEA_process.png)
- [43] C. Felippa. (2012). *A Tour of Nonlinear Analysis*. Available: <http://www.colorado.edu/engineering/CAS/courses.d/NFEM.d/NFEM.Ch02.d/NFEM.Ch02.pdf>
- [44] SeStructures. *RBE2 vs RBE3*. Available: <https://www.sestructures.com/foundations/17-public-site/foundations/foundations-finite-element/38-foundations-rbe2-vs-rbe3>
- [45] A. N. Standards, "Gear Nomenclature, Definitions of Terms with Symbols," in *ANSI/AGMA 1012-G05*, ed. United States of America: American Gear Manufacturers Association, 2005.
- [46] Prospector. *Polyethylene (PE) Typical Properties Generic XLPE*. Available: <https://plastics.ulprospector.com/generics/27/c/t/polyethylene-pe-properties-processing/sp/25>
- [47] Omnexus. *Young Modulus*. Available: <http://omnexus.specialchem.com/polymer-properties/properties/young-modulus>
- [48] AZO materials. *Crosslinked Polyethylene - XLPE*. Available: <http://www.azom.com/article.aspx?ArticleID=855>



# Appendix A Risk Assessment

 NTNU  HMS	Kartlegging av risikofylt aktivitet			
	Utlarbeidet av	Nummer	Dato	
HMS-avd.	HMSRV2601	22.03.2011	Erstatter	
Godkjent av Rektor		01.12.2006		

**Dato:** 03.02.2017

**Enhet:** MTP

**Linjeleder:** Torgeir Welo

**Deltakere ved kartleggingen (m/ funksjon):**

(Ansv. veileder, student, evt. medveiledere, evt. andre m. kompetanse)

**Kort beskrivelse av hovedaktivitet/hovedprosess:** Masteroppgave for Bjørnar Fugløy. Fatigue properties of subsea corrugated sheathing.

**Er oppgaven rent teoretisk? (JA/NEI):**

«JA» betyr at veileder innestår for at oppgaven ikke inneholder noen aktiviteter som krever risikovurdering. Dersom «JA»: Beskriv kort aktiviteten i kartleggingskjemaet under. Risikovurdering trenger ikke å fylles ut.

**Signaturer:** Ansvarlig veileder: *Dag M. Hansen*

Student: *Bjørnar Fugløy*

ID nr.	Aktivitet/prosess	Ansvarlig	Eksisterende dokumentasjon	Eksisterende sikringstiltak	Lov, forskrift o.l.	Kommentar
01	Fatigue properties of subsea corrugated sheathing	Bjørnar Fugløy	Masterbeskrivelse	-	-	Kontorarbeid

NTNU	Risikovurdering		Utarbeidet av	Nummer	Dato
			HMS-avd.	HMSRV2501	22.03.2011
HMS			Godkjent av		Erstatter
			Rektor		01.12.2006
					

Ehnet: MTP

Dato: 03.02.2017

Linjeleder: Torger Welø

Deltakere ved kartleggingen (m/ funksjon):

(Ansv. Velleder, student, evt. medvulleder, evt. andre m. kompetanse)

Risikovurderingen gjelder hovedaktivitet: Masteroppgave for Bjørnar Fugloy. Fatigue properties of subsea corrugated sheathing.

Signaturer: Ansvartlig velleder:

*Per M. Skjold*

Student:

*Bjørnar Fugloy*

ID nr	Aktivitet fra kartleggings-skjemaet	Mulig uønsket hendelse/ belastning	Vurdering av sannsynlighet (1-5)	Vurdering av konsekvens:			Risiko-Verdi (menneske)	Kommentarer/status Forslag til tiltak	
				Menneske (A-E)	Ytre miljø (A-E)	Øk/ materiell (A-E)			Om-dørme (A-E)
01	Fatigue properties of subsea corrugated sheathing	Vond nekke og/eller ryg, sår selernuskulatur, vonda hændedd	2	B	A	A	A	B2	Øke den daglige fysiske aktiviteten

NTNU	Risikovurdering		Utlarbeidet av	Nummer	Dato
			HMS-avd.	HMSRV/2601	22.03.2011
			Godkjent av		Erstatter
			Rektor		01.12.2006



### Sannsynlighet vurderes etter følgende kriterier:

Svært liten 1	Liten 2	Middels 3	Stor 4	Svært stor 5
1 gang pr 50 år eller sjeldnere	1 gang pr 10 år eller sjeldnere	1 gang pr år eller sjeldnere	1 gang pr måned eller sjeldnere	Skjer ukentlig

### Konsekvens vurderes etter følgende kriterier:

Gradering	Menneske	Ytre miljø Vann, jord og luft	Øk/materiell	Omdømme
<b>E</b> Svært Alvorlig	Død	Svært langvarig og ikke reversibel skade	Drifts- eller aktivitetstans > 1 år.	Troverdighet og respekt betydelig og varig svekket
<b>D</b> Alvorlig	Alvorlig personskade. Mulig uførhet.	Langvarig skade. Lang restitusjonstid	Driftstans > ½ år Aktivitetstans i opp til 1 år	Troverdighet og respekt betydelig svekket
<b>C</b> Moderat	Alvorlig personskade.	Mindre skade og lang restitusjonstid	Drifts- eller aktivitetstans < 1 mnd	Troverdighet og respekt svekket
<b>B</b> Liten	Skade som krever medisinsk behandling	Mindre skade og kort restitusjonstid	Drifts- eller aktivitetstans < 1 uke	Negativ påvirkning på troverdighet og respekt
<b>A</b> Svært liten	Skade som krever førstehjelp	Ubetydelig skade og kort restitusjonstid	Drifts- eller aktivitetstans < 1 dag	Liten påvirkning på troverdighet og respekt

### Risikoverdi = Sannsynlighet x Konsekvens

Beregn risikoverdi for Menneske. Enheten vurderer selv om de i tillegg vil beregne risikoverdi for Ytre miljø, Økonomi/materiell og Omdømme. I så fall beregnes disse hver for seg.

### Til kolonnen "Kommentarer/status, forslag til forebyggende og korrigerende tiltak":

Tiltak kan påvirke både sannsynlighet og konsekvens. Prioriter tiltak som kan forhindre at hendelsen inntreffer, dvs. sannsynlighetsreducerende tiltak foran skjerpet beredskap, dvs. konsekvensreducerende tiltak.

NTNU	Risikomatrixe			Utarbeidet av	Nummer	Dato	
				HMS-avd.	HMSRV2604	08.03.2010	
HMS/MS				godkjent av		Erstatter	
				Rektor		09.02.2010	

## MATRISE FOR RISIKOVURDERINGER ved NTNU

KONSEKVENNS		SANNSYNLIGHET				
Svært alvorlig	E1	E2	E3	E4	E5	
Alvorlig	D1	D2	D3	D4	D5	
Moderat	C1	C2	C3	C4	C5	
Liten	B1	B2	B3	B4	B5	
Svært liten	A1	A2	A3	A4	A5	
	Svært liten	Liten	Middels	Stor	Svært stor	

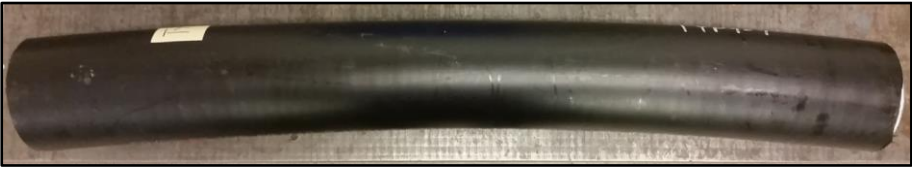

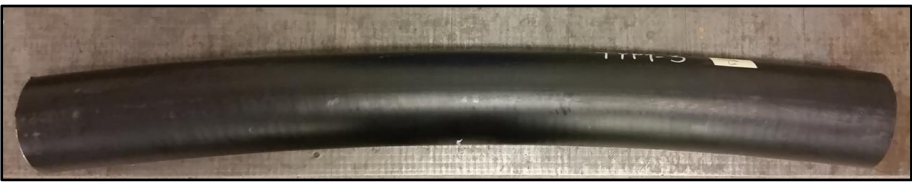
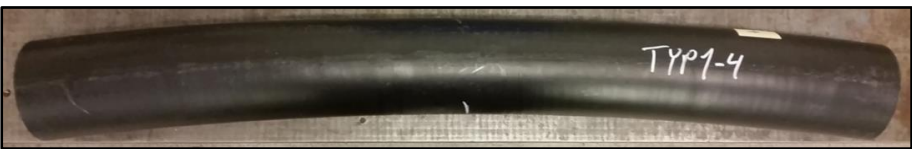

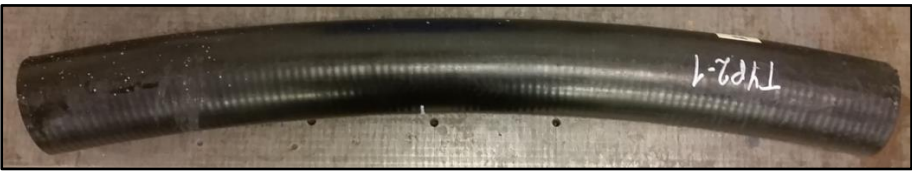

Prinsipp over akseptkriterium. Forklaring av fargene som er brukt i risikomatrixen.

Farge	Beskrivelse
Rød	Uakseptabel risiko. Tiltak skal gjennomføres for å redusere risikoen.
Gul	Vurderingsområde. Tiltak skal vurderes.
Grønn	Akseptabel risiko. Tiltak kan vurderes ut fra andre hensyn.



## Appendix B Tube specimens

Table B. 1: Delivered test tubes from Nexans

Tube	Weight [g]	Pipe curvature
(1 – 1)	3969	
(1 – 2)	4029	
(1 – 3)	4031	
(1 – 4)	3979	
(1 – 5)	4056	
(2 – 1)	3428	
(2 – 2)	3433	

(2 - 3)	3443	
(2 - 4)	3521	
(2 - 5)	3474	

## Appendix C Utilized X-ray Diffraction Parameters

Table C. 1: Utilized X-ray Diffraction parameters during the residual stress measurements

Parameters
Material: ST. STEEL - AUST. (Mn KAlpha) (FCC, hkl-311)
Tube: Mn KAlpha
Wavelength: 2.103
KV: 20.00; mA: 4.00
Beta Osc.: 0.00; Phi Osc.:0.00; X Osc. : 0.00; Y Osc.: 0.00;
Exp. time: 2.00 [s] 2.00 [s]
No. of exp.: 20 20
Aperture: 1 mm
Filters: No filters
Bragg Angle [degree]: 152.80
Peak Location: Gaussian 80%
Gain Correction: P/G(s)
Peak shifts: Absolute Peak
(1/2) S2: 7.18 E-6 [1/MPa] - S1:1.20 E-6 [1/MPa]
D spacing [Angstroms]: 1.0819055
LPA Correction: YES



# Appendix D X-ray diffraction results

## Tube (1-2)

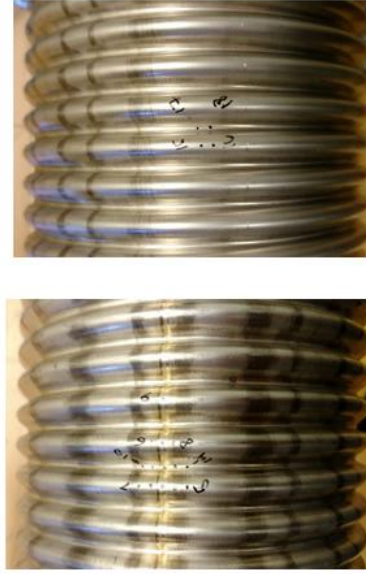
Clockpos	Point	Stress	Hoop		Stress	Axial			
			+/-	Shear		+/-	Shear		
1	1	16	12	26	6	61	23	51	11
	3	-48	37	35	18	156	20	52	9
	4	70	32	19	16	90	38	42	19
9	5 (weld)	95	53	50	26	118	22	40	11
	6	114	28	15	14	180	20	70	10
3	8	86	18	23	9	65	26	52	13
6	24	83	13	25	6	-81	20	44	9
9	27	84	9	29	5				



Figure D. 1: X-ray diffraction measurements for tube (1 – 2)

# Tube (2-2)

Clock pos	Point	Hoop		Axial	
		Stress +/-	Shear +/-	Stress +/-	Shear +/-
0	1	3	26	6	48
	2	-12	30	4	58
	3 (weld)	29	-27	11	28
	4	35	-27	5	40
	5	25	28	5	54
	6	24	-18	14	-56
	7 (weld)	42	4	10	17
	8	24	14	12	32
	9 (weld)	41	0	10	22
	10	26	9	13	
	11	-10	21	13	
3	12 (weld)	28	-9	10	
	13	14	21	12	
	14	8	31	15	
	15	73	37	5	
6	16	102	39	5	
	17	94	31	5	
9	18	93	20	5	
	19	133	34	19	34
	20	142	28	16	
	21	10	9	43	4



3 mm distance between points

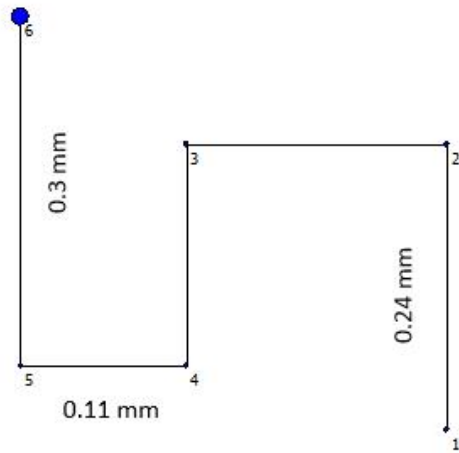
Triaxial measurement for point 19 (1 is axial direction, 2 is hoop)

S11	S22	S33	S12	S21
-9	125	0	-27	-35

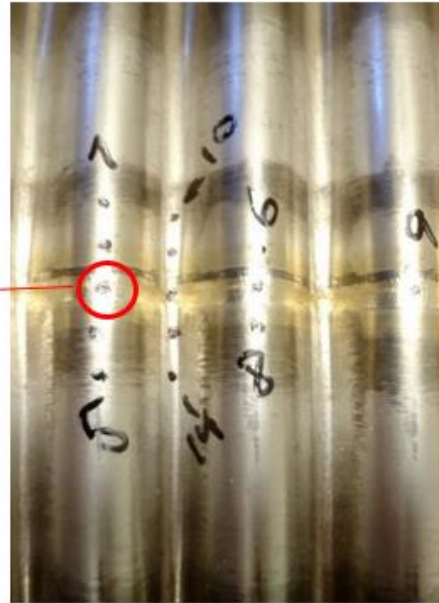
Note the difference due to biaxial stress: 125 vs 133 when uniaxial stress is assumed.  
Surface normal stress is assumed 0.

Figure D. 2: X-ray diffraction measurements for tube (2 – 2)

# Stress variations



The beam size is 1 mm in diameter.



Point	Stress	Hoop		
		+/-	Shear	+/-
1	1	16	48	8
2	21	14	43	7
3	39	25	21	12
4	28	26	21	12
5	7	26	18	13
6	24	22	21	11

Figure D. 3: A visualization of the residual stress variations at selected locations during the X-ray diffraction measurements